

Control of Electron Dynamics in Mesoscopic Quantum Circuits

Dissertation der Fakultät für Physik
der Ludwig-Maximilians-Universität München



vorgelegt von
Sergey Platonov
geboren in Mahiljou
München, Oktober 2017

Erstgutachter: PD Dr. Stefan Ludwig
Zweitgutachter: Prof. Dr. Jan von Delft
Datum der Abgabe: 16.10.17
Datum der mündlichen Prüfung: 01.12.17

Inhaltsangabe

Die zukünftige Elektronik steht vor einem Übergang von der konventionellen Technologie mit dem Fortschritt, der von Moores Gesetz vorhergesagt wird, zu einer Quantentechnologie, in der Quantentunneln und Kohärenter ballistischer Transport bedeutende Rollen spielen werden. Diese Arbeit konzentriert sich auf vier wichtige Bereiche der Quantentechnologie, die als Grundkern von Quantenschaltkreisen angesehen werden können. Wir beginnen mit einer alternativen Methode zum Maßschneiden der Potentiallandschaft in zweidimensionalen Elektronensystemen, eingebettet in GaAs/AlGaAs-Heterostrukturen im ersten Kapitel. Wir präsentieren eine Charakterisierung dieser Methode anhand von Feld-Effekt, Hall-Effekt und Aharonov-Bohm-Messungen, um elektrostatische, dynamische und kohärente Eigenschaften zu untersuchen und auch eine allgemeine Tauglichkeit unserer Methode für zukünftige Quantenanwendungen zu zeigen. Im zweiten Kapitel untersuchen wir die Optimierung des ballistischen Elektronentransports zwischen zwei entfernten Quantenpunktkontakten. Wir präsentieren eine Technik zur Messung der Winkelverteilung von Elektronen, die von einem Quantenpunktkontakt emittiert werden, indem wir sie mit einem externen Magnetfeld ablenken. Sodann demonstrieren wir, dass die emittierten Elektronen mit Hilfe einer elektrostatischen Linse effektiv auf einen zweiten Quantenpunktkontakt fokussiert werden können. Im zweiten Kapitel zeigen wir auch die Verstärkung der Kopplung zwischen zwei entfernten Quantenpunktkontakten auf Basis der elektrostatischen Fokussierung ballistischer Elektronen. Unsere Beobachtungen sprechen für eine Elektronendynamik gemäß einem Gaußschen Strahloptikmodell beschrieben mit Hermite-Funktionen. Dies führt zu deutlichen Korrekturen verglichen zu den üblichen Modellen, die Elektronen als ebene Wellen beschreiben. Im dritten Kapitel diskutieren wir die kohärente Kopplung eines Quantenpunktkontaktes mit einem offenen hemisphärischen Resonator. Wir stellen ein Verfahren zur Bestimmung der Elektronenphasen-Kohärenzlänge unter der Annahme von Gauß-Hermit-Moden sowohl des Quantenpunktkontakts als auch des Resonators vor. Das letzte Experiment verwirklicht schließlich eine Lissajous-Schaukel-Ratsche, die eine gerichtete Bewegung von Elektronen erzeugt und die Zeitumkehrsymmetrie auf dem Chip bricht, realisiert in einem in eine Halbleiter-Heterostruktur eingebetteten Quantenpunkt. Zum Abschluss der Arbeit diskutieren wir die Ergebnisse der durchgeführten Experimente im Kontext der Quantentechnologie.

Abstract

Future electronics faces a transition from conventional technology with progress predicted by Moore's law to a quantum technology where quantum tunneling or coherent ballistic transport plays a significant role. This thesis concentrates on several applications of quantum technology. We start with demonstrating an alternative method for engineering the potential landscape in two-dimensional electron systems embedded in GaAs/AlGaAs heterostructures in the first chapter. We present a characterization of this design using field effect, Hall effect, and Aharonov-Bohm measurements to study electrostatic, dynamic and coherence properties and also show the general feasibility of our approach for future quantum applications. In the second chapter, we examine optimization of the electron transport between two distant quantum point contacts. We present a technique to measure the angular distribution of electrons emitted from a quantum point contact by deflecting it with an external magnetic field. In the second chapter, we also demonstrate coupling enhancement between two distant quantum point contacts by electrostatic focusing of ballistic electrons. Our observations favor electron dynamics according to a Gaussian beam optics model assuming Hermite functions rather than the frequently used plane electron wave model. In the third chapter, we discuss the coherent coupling of a quantum point contact with an open hemispherical resonator. We present a method to determine the electron phase coherence length based on Gaussian-Hermite modes of both quantum point contact and a cavity. Finally, the last chapter introduces a Lissajous rocking ratchet realized in the quantum dot embedded in the semiconductor heterostructure. It creates directed motion of electrons and breaks time-reversal symmetry on-chip. At the end of the thesis, we discuss results of performed experiments in the context of quantum technology.

Contents

Inhaltsangabe	i
Abstract	iii
Motivation and Introduction	1
1 Mesoscopic Field-Effect Devices in Depleted Two-Dimensional Electron Systems	3
1.1 2DES fundamentals and electrical field effect	3
1.2 Lithography techniques	5
1.3 Sample design	6
1.4 Field effect characterization	8
1.5 Electron transport in 2DES	9
1.5.1 The Drude model	10
1.5.2 Hall measurements: carrier density and mobility	10
1.6 Electron dephasing in mesoscopic systems	12
1.6.0.1 Aharonov-Bohm effect and dephasing in quasi-1D channels	12
1.7 Conclusions	17
2 Ballistic Electron Optics with Quantum Point Contacts	19
2.1 Quantum Point Contacts	19
2.1.1 QPC conductance	20
2.1.2 Adiabaticity criteria	22
2.1.3 Landauer-Büttiker formalism	22
2.1.4 Casimir-Onsager relation	23
2.1.4.1 Two-terminal device	25
2.1.4.2 Three-terminal device	25
2.1.5 Validity of the Casimir-Onsager relation	25
2.2 Measurement setup	26
2.2.1 He ³ evaporation cryostat	26
2.2.2 Experimental setup and devices	26
2.2.2.1 Ground connection	27
2.2.2.2 Gate wires	27
2.2.2.3 Current wires	27
2.2.2.4 Magnet power supply	28
2.2.3 Sample design and connections	29
2.3 Single QPC characterization	30
2.4 Two QPCs in series	33

2.5	Magnetic deflection experiment	36
2.5.1	Linear response regime	37
2.5.2	Theoretical model	38
2.5.2.1	Modematching: overlap integral	39
2.5.3	Comparison between theory and experiment	41
2.5.4	Deviations between theoretical predictions and measurements	42
2.5.4.1	Classical and coherent scattering	42
2.5.5	Searching for defects in the 2DES	45
2.6	Focusing with the electrostatic lens	47
2.6.1	Geometrical optics of ballistic electrons	47
2.6.2	Energy calibration of the lens gate	48
2.6.3	Effect of the electrostatic lense on the ballistic electron transmission	52
2.6.4	Coherent ballistic electron optics	54
2.6.5	Geometrical optics and Gaussian beam model	56
2.6.6	Comparison between theory and experiment	57
2.7	Combined electrostatic and magnetic focusing	59
2.8	Conclusions	61
3	Coherent Coupling of an Open Ballistic Electron Resonator to a Quantum Point Contact	63
3.1	Dephasing in an open 2DES	63
3.2	Combined system of a QPC and a cavity	64
3.2.1	Theoretical model	68
3.2.2	Comparison between theory and experiment	69
3.3	Conclusions	70
4	Lissajous Rocking Ratchet based on a Quantum Dot	71
4.1	Quantum dots	71
4.2	Breaking time-reversal symmetry in nanoelectrical circuits	74
4.2.1	Rectifier	75
4.2.2	Turnstile and adiabatic pump	75
4.2.3	Ratchet: definition and types	77
4.2.3.1	Flashing ratchet: spatial asymmetry	77
4.2.3.2	Rocking ratchet: time-reversal broken symmetry	78
4.2.4	Ratchets based on quantum dots in semiconductor structures	79
4.3	Measurement setup	80
4.3.1	Dilution fridge and the setup	80
4.3.1.1	rf wires	80
4.3.1.2	Gate and current wires	81
4.3.1.3	Current amplifier offset	82
4.3.2	Sampleholder and the sample	83
4.4	Calibration of the QD	85
4.5	Radio frequency calibration: adiabaticity requirement	88
4.6	Lissajous rocking ratchet	91
4.6.1	Current symmetries	93
4.6.2	Theoretical approach	95
4.6.3	Contribution of a single QD level	96
4.6.4	Comparison between the theory and experiment	99
4.7	Separation of current components	102

4.8	Applications and alternative realizations	105
4.9	Conclusions	107
Summary and outlook		109
A	Appendix	111
A.1	Fabrication parameters	111
A.1.1	Wafer material	111
A.1.2	Optical lithography parameters	112
A.1.3	Electron beam lithography parameters	112
A.1.4	Sample designs	113
A.2	Calibration measurements	114
A.2.1	Calibration of the single QPC resistance	114
A.2.2	Resistance of two QPCs in series	114
A.2.3	Coherent effects in magnetic deflection and electrostatic focusing experiments	115
A.2.4	QD calibration	117
A.3	Experimental raw data	118
A.4	Theoretical model description	122
A.4.1	Transmission through coupled QPCs	122
A.4.1.1	Harmonic oscillator eigenstates in the QPCs	122
A.4.1.2	Free 2DES with magnetic field in WKB approximation	122
A.4.1.3	Propagated wavefunction and transmission through two QPCs in series	123
A.5	Python simulation code	124
A.5.1	Anharmonic QPC eigenmodes	124
A.5.2	Gaussian beam propagation in Fabry-Perot resonator	125
Bibliography		131

Motivation and Introduction

Modern electronics emphasizes miniaturization. Perhaps the most remarkable technological progress has come from reductions in the size of transistors, thereby increasing the number of transistors per chip. This number is predicted by the eponymous Moore's law [1] to double in about 18 months. However recently transistor technology approaches characteristic device sizes comparable to that of molecules, and correct description of the carrier dynamics requires the inclusion of quantum mechanical effects. Nowadays quantum tunneling is widely used in tunnel field-effect transistors (FET) or tunneling diodes as well as in the floating gate operation in the flash memory technology [2]. In today's processor technology tunneling causes unwanted leakage currents, the main dissipation process and the limiting factor for the processor frequency [3]. Due to this limitation, industrial companies cannot fulfill Moore's law anymore without enhancing device and calculation complexity [4]. Future technology will make use out of quantum effects without paying the price of the complexity increase. The quantum technology increases the level of control on the carrier transport and acts as a fundamental basis for applications in fast and high-performance devices.

Usage of ballistic electron transport facilitates further electronic device optimization. Ballistic transport of electrons was first demonstrated in semiconductor structures with the development of molecular beam epitaxy (MBE) [5] over lengths of the order of micrometers at temperatures of liquid Helium. Recently ballistic electron effects were also observed at room temperatures [6]. We can treat ballistic electrons as quantum-mechanical waves, which can reflect, refract and scatter during propagation and thus are similar to electromagnetic waves [7]. To study the coherent properties of ballistic electrons, we can assume interference and diffraction experiments. Here we aim at the fundamental understanding of ballistic and quantum effects to lay the grounds for future devices realizations.

In the thesis, we discuss the role of electron quantum coherence, ballistic electron transport, and tunneling properties as well as production methods of nanoelectrical devices in the agenda of the quantum technology. We show experiments based on mesoscopic devices in a two-dimensional electron system (2DES) embedded in GaAs/AlGaAs heterostructures at cryogenic temperatures $T < 4$ K. The focus is enhancing control of electron dynamics in mesoscopic devices fabricated in GaAs/AlGaAs heterostructures.

We organize the thesis as follows: in the first chapter, we show an alternative method of creating potential landscapes via carrier repopulation of a depleted 2DES. We start with a discussion of the electrical field effect, followed by the sample fabrication process. Next, we discuss electron scattering mechanisms in a 2DES and characterization examples of the created structures via our alternative method. At the end of the chapter, we focus on electron dephasing in a GaAs/AlGaAs 2DES. In the second chapter, we discuss transport through two serial quantum point contacts (QPCs) with the coupling by ballistic electrons being enhanced by electrostatic

focusing. We model our multiterminal system using the Büttiker approach. In the first series of measurements, we explore the lateral distribution of electrons emitted by a QPC using a magnetic deflection experiment. We present a semi-analytical model and discuss our results in the following sections. In the second series of experiments, we study electron focusing by an electrostatic lens and demonstrate coupling enhancement between two distant QPCs. We compare two different models: geometrical optics and Gaussian beam optics to explain our experimental results. In the third chapter, we show the coherent coupling of a QPC with an open hemispherical resonator. We present a method to determine the electron phase coherence length based on Gaussian-Hermite modes of both QPC and a cavity. In the fourth chapter, we realize a Lissajous rocking ratchet based on driving a quantum dot (QD) with two independent forces. We start by discussing how to break the time-reversal symmetry in mesoscopic solid-state devices and highlight the examples of a rectifier, a pump, and a ratchet. In the next section, we concentrate on the case of a ratchet realized in a single QD, present its characterization and discuss electron transport through the ac driven QD. We offer the theoretical model based on a master equation approach and focus on the symmetry properties of the Lissajous rocking ratchet in the following sections. At the end of the chapter, we briefly explain a few alternative implementations of the Lissajous ratchet and its possible applications. The thesis closes with a summary and outlook.

Chapter 1

Mesoscopic Field-Effect Devices in Depleted Two-Dimensional Electron Systems

In this thesis, we use samples based on a two-dimensional electron system contained in a GaAs/Al-GaAs heterostructure. This chapter describes the formation of a 2DES, its physical properties and the techniques to further confine the electrons. In brief, we present an alternative method for engineering the potential landscape in a 2DES based on the electric field effect. We experimentally study the electronic properties of mesoscopic samples created with our design, including the tunability of carrier density, mobility, and phase coherence and give a short theoretical discussion for each of them. We submitted the results of this chapter to Physical Review Applied [8].

1.1 2DES fundamentals and electrical field effect

To create a 2DES, we can use a heterostructure containing layers of different materials with different bandgaps. Each layer of the heterostructure is a thin epitaxial film produced for different materials with MBE. One way to achieve high-quality crystals is utilizing materials of the same lattice structure and similar lattice constants during the growth procedure. A good choice is GaAs/Al_xGa_{1-x}As, $0 < x < 1$ with different ratios of aluminum and gallium that offers concentration combinations with the desired properties [9]. In Fig. 1.1(a) we show an example of a δ -doped GaAs/AlGaAs based heterostructure with a schematic profile of the conduction band. The different bandgaps of GaAs and AlGaAs result in a triangular potential well with the first subband energy below the Fermi energy. Charge carriers from the dopants populate the energy states in the potential well that confines carriers in two dimensions [10].

One can further constrain electrons in one or zero dimensions in a controlled manner by creating potential barriers in a 2DES. The electric field effect is a powerful tool for this task. When used with multiple individual gates it provides full tunability while being compatible with high mobility wafers. Alternative methods for structuring a 2DES include etching [11–13] and surface oxidation techniques [14, 15]. While they ensure additional possibilities in combination with in-plane side gates [16] or metal gates [17], etching and oxidation techniques alone lack tunability. More importantly, they are restricted to wafers with a shallow 2DES causing a close proximity of

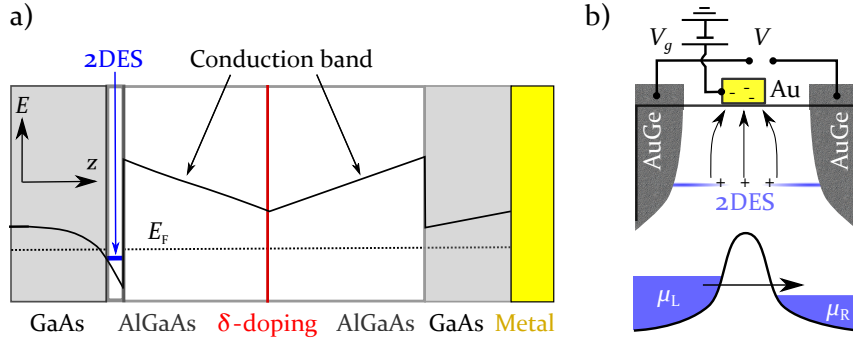


Figure 1.1: a) Sketch of the conduction band in different layers (marked with colour) of a GaAs/AlGaAs heterostructure. b) Electrical field effect sketch in the sample containing a 2DES (blue horizontal line) and surface metal gate (yellow). At the bottom we illustrate the resulting potential profile, when negative voltage is applied to the gate.

surface states and doping atoms limiting the carrier mobility [18] and the electrostatic stability at the nanoscale (related with the $1/f$ spectrum of charge noise [19–21]). Applications based on the quantum mechanical coherence of localized carriers require superior control and stability favoring the field effect.

A straightforward and the most common approach to shape potential landscapes by the field effect, starting from an extended 2DES, is based on the controlled local depletion of the 2DES beneath individual surface gates by applying negative voltages V_g to them [see Fig. 1.1(b)]. This approach works perfectly for relatively small structures with simple topology such as few coupled quantum dots [22, 23] or quantum point contacts. However, an individually tunable one-dimensional array of N quantum dots requires at least $\sim 2N$ metal gates, while even more gates are needed for a two-dimensional array or for increased tunability. Failure of a single gate would alter the current path and typically make the entire device useless. Furthermore, non-trivial topologies such as an Aharonov-Bohm ring, allowing carriers to move in a circle around a depleted center, require voltage biasing of a center gate without depleting the surrounding carriers. This has been achieved by implementation of three-dimensional air bridges [24, 25]. However, the fabrication of air bridges is rather complex and limited to relatively big structures. In a different approach PMMA had been used to locally reduce the electric field beneath a global top gate and thereby define AB rings with limited tunability [26, 27].

By locally diffusing in layers of AuGe we contact the 2DES in order to apply source-drain bias V across the barrier. In case of a single barrier separating source and drain contacts it shifts the chemical potentials μ_L, μ_R of the Fermi seas on both sides of the barrier in respect to each other and a tunnelling current can flow [lower panel of Fig. 1.1(b)]. This example describes a typical transport measurement scheme in a FET, where a full range of parameters such as barrier height, gate shape or coupling parameters for complex multigate structures are encoded in the measured current and can be probed for different combinations of source-drain and gate voltages.

1.2 Lithography techniques

We use optical and electron beam lithography (EBL) to pattern mesoscopic structures on the surface of a heterostructure. In this section, we describe the fabrication process, while we list the specific fabrication parameters in the Appendix (A.1). We cut an approximately $5 \times 5 \text{ mm}^2$

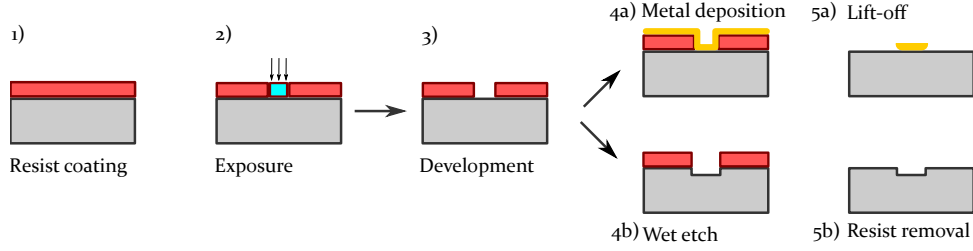


Figure 1.2: Sketch of the lithography process with positive resist. Step 1) The sample (grey) is spin-coated with a photo- or electron-sensitive resist (red). Step 2) The resist is locally exposed (blue areas) to either ultraviolet light through a mask or to a positioned electron beam. Step 3): During development, the exposed parts of the resist are dissolved. Step 4a) For metal deposition, the metal (yellow) is evaporated and deposited on the resist and sample surface. Step 4b) The surface areas of the wafer are etched where the resist was removed. Step 5a) The resist is removed, and the desired structure remains. Step 5b) The resist with metal on top is removed by a lift-off process, and the metal deposited on the wafer surface remains.

sized piece out of the wafer and clean it to improve surface quality. There are five main steps of production from the bare wafer to the finished sample including a nanostructure. All of these steps involve separate lithography processes during which we write a pattern into a resist layer on top of the sample surface. Steps divide into coarse and fine structures lithography. For coarse structures, UV photolithography based is used as a conventional method while for fine structures electron beam lithography (EBL) based on Raith E-line device is employed. The minimum size of structures we build is limited by the wavelength of the radiation for the photolithography and by the resist resolution for the EBL.

We sketch the lithography process in Fig. 1.2, for a detailed description the reader is advised to reference [28]. After spin-coating, the positive resist is exposed through a shadow mask or by scanning exposed areas with an electron beam to pattern the desired structures. Then the resist is dissolved at the exposed areas with a development chemical. In the next step either metal (e.g., Ti/Au) is deposited on the structured surface or it is etched away with diluted sulfate acid, see appendix (A.1) for details. In the following, lift-off process removes the resist at the patterned locations. The periphery of a final sample design is shown in Fig. 1.3. First so-called mesa layer (“table” in Spanish) is defined. We etch away GaAs/AlGaAs layers beyond the depth of the 2DES and leave the mesa area (illustrated in Fig. 1.3 with blue color) unchanged.

We create ohmic contacts to the 2DES by evaporating layers of AuGe/Ni/AuGe locally onto the wafer surface. Then the wafer is heated for approximately 140 s at 480°C to diffuse in Ge which moves much faster than Au or Ni into the AlGaAs layers. Ni acts as a diffusion barrier and is used to control exact timing of the diffusion process. Another role of Ni is also an adhesion material, to improve the adhesion of AuGe on GaAs. Au and Ni stay on the wafer surface, which then allows subsequent contacting with the bond wire. Contacts consist of rectangular pads with a meander edge structure to ensure a lower resistance through a large contact area after thermal

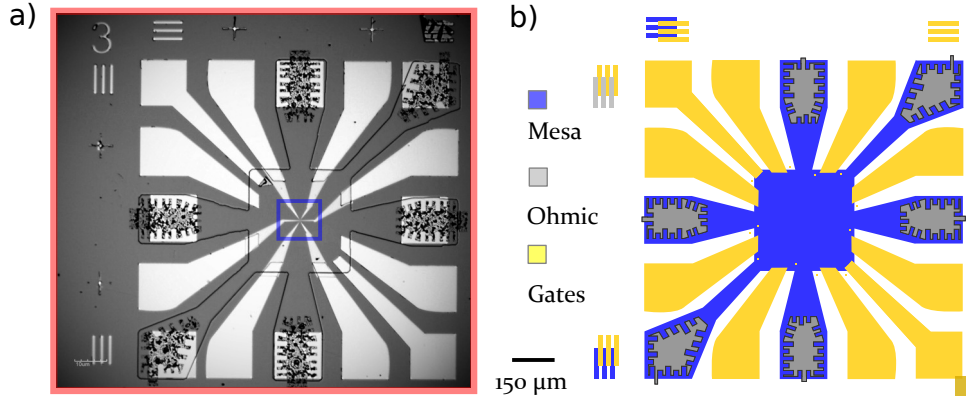


Figure 1.3: a) Microscope image of the finished chip layout. The central area framed by a blue square contains the nanostructure. b) Optical lithography layout of a typical sample.

diffusion [28]. The contact optimization resulted in minimum 250 Ohm resistance of each Ohmic contact. Finally, we define golden gates in the last step of the optical lithography. The gates, shown in Fig. 1.3, consist of a 5 nm titan adhesion layer at the interface to the sample surface and a 35 nm golden layer. We use them to connect later to the nanostructures fabricated via electron beam lithography. In a side project performed by Sebastian Konrad in his bachelor thesis, we have studied the high-frequency properties of this gates through crosstalk and impedance matching [29].

The nanostructure itself is too small for optical lithography and is fabricated by EBL at the last step. We take particular care at the dose test of the desired designs and the writing order of the design elements in the EBL machine (with the details in the master thesis by Hannes Seeger [30]). In Fig. 1.3(a) the blue square contains the fabricated nanostructure. An extra fabrication step, a global top gate is built on top of the nanostructure, to tune the carrier concentration beneath it. For this purpose, an isolating layer that electrically separates the top gate and previously defined nanostructures is needed. We fabricate this layer by crosslinking the poly(methyl methacrylate) (PMMA) resist. When exposed to a very high dose, the molecular chains of PMMA crosslink among each other by secondary electrons and become insoluble in the used chemicals [31]. Production steps of the top gate are similar to the one described in Fig. 1.2 and listed in in the Appendix (A.1).

1.3 Sample design

In this section we probe an alternative method to define complex nanoelectronic circuits based on the field effect, offering full tunability of high-quality devices. Compared to common strategies our method simplifies the production of ring topologies and offers the prospect of scalability while limiting the danger of general failure. Our idea, sketched in Fig. 1.4(a), is based on globally depleting the 2DES using a single top gate while we place nanoscale screen gates between the top gate and the 2DES to locally shield the effect of the top gate and thereby regain free carriers. We electrically isolate the top gate from the screen gates using an about 100 nm thick layer of cross-linked PMMA [31, 32]. In our sample the 2DES at the interface between AlGaAs and GaAs is separated from the surface by 5 nm of GaAs (capping layer) followed by 70 nm of

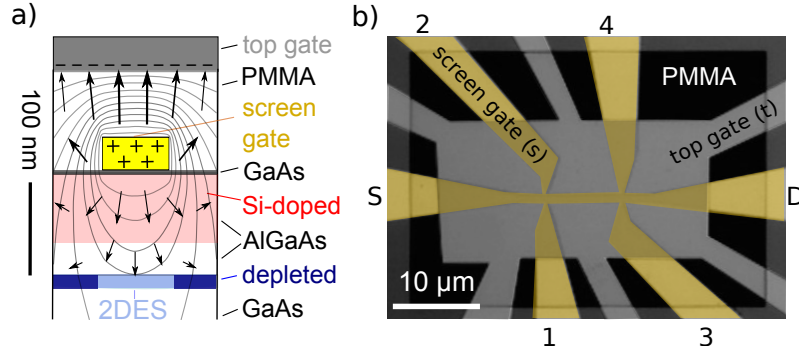


Figure 1.4: a) Effect of a screen gate: the top gate (gray) is biased at $V_t = -1$ V, the screen gate at $V_s = 0.1$ V and the 2DES (light blue) is grounded. The dark blue regions are fully depleted. The electrostatic potential (shown as equally spaced equipotential lines, arrows indicate the field strength) has been calculated by self-consistently solving the Poisson equation using $\epsilon = 2$ for cross-linked PMMA and $\epsilon = 12.8$ for AlGaAs. For the calculation, we considered charges on the gates and in the 2DES but neglected the effect of positively charged doping ions which are immobile at cryogenic temperatures. b) False-colored optical microscope image of a Hall bar sample. Yellow color indicates the screen gate (s) covering 2DES while the top gate (t) is shown in gray.

homogeneously Si-doped $\text{Al}_{0.36}\text{Ga}_{0.64}\text{As}$ and 35 nm of undoped $\text{Al}_{0.36}\text{Ga}_{0.64}\text{As}$ [33]. Details of the heterostructure can be found in the Appendix (A.1). The carrier density and the detailed geometry of the confinement potential depend on the electric field at the 2DES and can be fine-tuned by adjusting the individual gate voltages. In Fig. 1.4(a) we sketch the screening effect on a grounded 2DES for an example of a positively charged screen gate beneath a negatively charged top gate. Global top gates had been used previously for various purposes including the decrease of telegraph noise [20] or for accumulation of carriers in undoped quantum wells [34, 35]. In these examples gates on the GaAs surface are used to locally deplete the 2DES while in our case carriers accumulate beneath the screen gate.

In Fig. 1.4(b) we display a scanning gate microscope (SEM) image of an actual Hall bar sample. The top gate (t) is shown in light grey and the screen gate (s) colored yellow; the isolating cross-linked PMMA manifests itself as a squared slightly darker region extending across most of the image. By charging the top gate negatively with respect to the grounded 2DES and a grounded back gate at the bottom of the 540 μm thick wafer we deplete the 2DES beneath the top gate where the screen gate doesn't shield it. Below the top gate the shape of the screen gate corresponds to the approximate form of the 2DES beneath. The screen gate in Fig. 1.4(b) defines a Hall-bar with the source (S) and drain (D) and four side contacts used as voltage probes (1,2,3,4). The top gate includes a large center square and six arms which electrically isolate the conducting leads in the periphery of the Hall-bar. In our Hall-bar the free carriers are located directly beneath a metal gate, which results in two critical differences to traditional devices: the direct vicinity of metal can reduce the disorder potential as charged defects are partially screened by electron rearrangement at the metal surface. At the same time, the metal will tend to screen the electron-electron interaction in the 2DES below. In this chapter, we do not explore this reduced Coulomb interaction but instead, demonstrate the general feasibility of our method.

1.4 Field effect characterization

For the characterization measurements, we place the sample in a vacuum tube filled with Helium-gas as a thermal bath. We suspended the tube in liquid Helium-4 at the base temperature of $T = 4.2\text{ K}$. The sample was mounted on a chip carrier while the whole system had an option of applying magnetic fields along the tube axis. We sketch the electrical circuit diagram of the measurement setup in Fig. 1.5. We used Yokogawa 7651 to apply gate voltages and a combination of

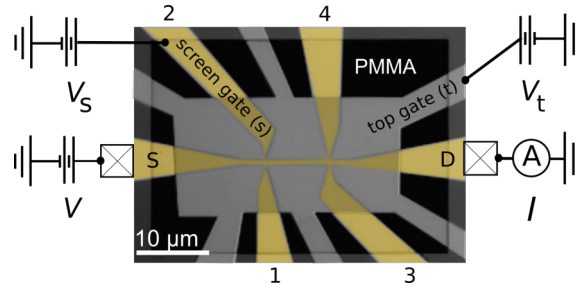


Figure 1.5: Electrical circuit diagram of the measurement setup with the SEM photo of the sample in the center. Contacts 1,2,3,4 are left floated, while we applied voltage across the SD contacts, and measure the current at contact D. We also applied voltages V_s and V_t to the screen gate and the top gate.

current preamplifier DL Instruments 1211 and multimeter Agilent 34411A to detect source-drain current. We didn't apply electric filtering for the hall-bar measurements in the next sections, see [36] for details of the measurement setup. We summarize the setup parameters for wiring in Table (1.1) For a first characterization of our device we present in Fig. 1.6 the current flowing be-

Component	Resistance (Ω)	Capacitance to ground (F)
Double shielded coax	$\simeq 1$	$> 100\text{ p}$
Manganin twisted pairs	> 50	$> 500\text{ p}$
Σ	> 51	$> 600\text{ p}$

Table 1.1: Resistances and capacitances in the electrical wiring.

tween source and drain contacts (while the side contacts are left floating, see Fig. 1.5) in response to a source-drain voltage of $V_{SD} = 0.84\text{ mV}$ as a function of both top gate and screen gate voltages V_t and V_s . The lines of constant current display a kink at $V_t \equiv V_t^d = -1.48\text{ V}$, marked by a dashed horizontal line in panels a) and b), indicating complete depletion of the 2DES for $V_t < V_t^d$. The almost constant slopes of the lines of constant current for $V_t < V_t^d$ suggest a constant ratio of the capacitances between the Hall bar and the two respective gates, $C_s/C_t = dV_t/dV_s$ which we plot in Fig. 1.6(d) versus V_s . This coupling ratio takes the large value of $C_s/C_t \simeq 75$ at $V_s \simeq -200\text{ mV}$ near depletion where it indicates an efficient screening of the top gate by the screen gate. The gradual increase to $C_s/C_t \simeq 45$ at $V_s \simeq 300\text{ mV}$ indicates a growing influence of the top gate at more positive V_s . It suggests that the Hall bar becomes wider at more positive V_s while the potential profile at the Hall bar edges steepens. Consequently, the combination of top- and screen gate voltages can be used to tune the Hall-bar edges and the shape and stability of quantum Hall edge states [37]. Reliable predictions could be achieved employing a Poisson-Schrödinger solver

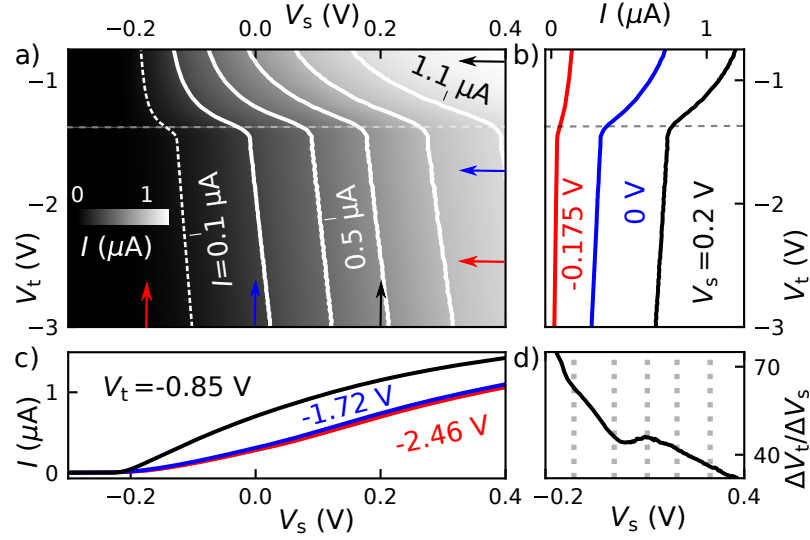


Figure 1.6: a) Current I through the Hall bar at $V_{SD} = 0.84 \text{ mV}$ (gray scale and lines of constant current at an interval of $0.2 \text{ } \mu\text{V}$) as a function of top gate V_t (y-axis) and screen gate V_s (x-axis) voltages. The horizontal dashed line at $V_t \equiv V_t^d = -1.48 \text{ V}$ indicates the onset of depletion of the 2DES below the top gate away from the screen gate. b) and c) Vertical and horizontal cuts $I(V_t)$ and $I(V_s)$ from panel a (fixed voltages V_s and V_t , respectively, are indicated by color coded arrows). d) The slope dV_t/dV_s of the constant current lines versus V_s at $V_t = -2.5 \text{ V}$. Vertical dashed lines indicate intersections with constant current lines in panel a.

such as nextnano³ [38], while breakdown measurements of the quantum Hall effect would provide an experimental test [37]. Both ideas go beyond the scope of the chapter but are topics for the future.

From measured ratios of capacitances we can quantify the shielding of the top gate by the screen gate: we therefore determine the ratio C_s/C_t^0 with C_t^0 being the capacitance between the top gate and the 2DES without screen gate in between. For a first estimate we compare the depletion voltages of the respective gates $C_s/C_t^0 \simeq V_t^d/V_s^d \simeq 1.48/0.2 \simeq 7.4$. For an alternative estimation of C_s/C_t^0 we determine the carrier density of the 2DES at grounded gates, $V_t = V_s = 0$, based on Hall measurements to be $n_s^0 \simeq 1.45 \times 10^{11} \text{ cm}^{-2}$. Using a plate capacitor model accounting for two dielectric layers of equal thickness, PMMA and AlGaAs, we then find the dielectric constant $\epsilon_{\text{PMMA}} \simeq 2.0$ where we used the literature value $\epsilon_{\text{AlGaAs}} = 12.8$ and the measured depletion voltage $V_t^d = -1.48 \text{ V}$. Our plate capacitor model then predicts $C_s/C_t^0 \simeq 1 + \epsilon_{\text{AlGaAs}}/\epsilon_{\text{PMMA}} \simeq 7.4$ in excellent agreement with our first estimate. As a result, we find $C_t^0/C_t = (C_s/C_t)/(C_s/C_t^0) \simeq 75/7.4 \simeq 10.1$ at $V_s = -0.2 \text{ V}$, i.e. the screen gate reduces the coupling of the top gate to the 2DES roughly by one order of magnitude. Clearly, this result depends on the geometry details and the applied voltages.

1.5 Electron transport in 2DES

We aim at evaluating the quality of the 2DES in nano circuits created with our method and discuss the electron dynamics in the 2DES. Transport in mesoscopic systems can be classified in different regimes by comparing the device sizes with characteristic scattering lengthscales [39]. We start with the single particle scattering time τ_s that is a measure of how long an electron remains in

any given momentum eigenstate. The scattering rate $1/\tau_s$ for the single-particle excitations is given by:

$$\frac{1}{\tau_s} = \int dk' W_{kk'}, \quad (1.1)$$

where $W_{kk'}$ represents the probability matrix element of the system to transform from momentum state k to k' . For a degenerate Fermi liquid the single particle scattering length l_s can be defined as $l_s = v_F \tau_s$, where v_F is the Fermi velocity. The momentum scattering time τ_m is defined as the time a carrier moves before collisions randomize its momentum (direction). The scattering rate $1/\tau_m$ can be approximated as:

$$\frac{1}{\tau_m} = \int dk' W_{kk'} (1 - \cos \theta_{kk'}) \quad (1.2)$$

where $\theta_{kk'}$ is the angle between the electron momentum before and after a scattering event. The integral is weighted by $(1 - \cos \theta_{kk'})$, since large-angle scattering events are more probable to randomize the direction of motion. In a typical remotely-doped GaAs/AlGaAs heterostructures the majority of scattering happens from ionized impurities spatially separated from the 2DES. As a result scattering is dominated by small-angle scattering, and $\tau_m \gg \tau_s$ [40].

The mean free path l_m is the average distance an electron travels before its initial momentum is destroyed $l_m = v_F \tau_m$. By comparing l_m with the dimensions L, W of the sample sketched in Fig. 1.7 different transport regimes can be determined. For the case that the elastic mean free path l_m is smaller than the dimensions L, W of the sample ($l_m \ll L, W$), the carriers exhibit diffusive transport. For the case $l_m > L, W$ we assume that electrons propagate ballistically.

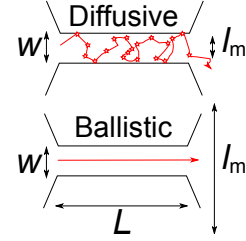


Figure 1.7: Sketch of ballistic and diffusive transport in mesoscopic systems with width W and length L . Red line represent electron trajectories and black line defines the channel.

1.5.1 The Drude model

We can describe the diffusive regime for $L, W \gg l_m$ using the Drude model [10]. In the presence of an in-plane electrical field electrons acquire an average drift velocity:

$$v_{\text{drift}} = -\mu E, \quad (1.3)$$

where the electron mobility is $\mu = \frac{e\tau_m}{m}$, m represent the effective electron mass in GaAs ($m = 0.067m_e$) and e is the elementary charge. The resistivity ρ , may be expressed as

$$\rho = \sigma^{-1} = \frac{m}{e^2 n_s \tau_m}, \quad (1.4)$$

by using the Einstein relation $-en_s v_{\text{drift}} = \sigma E$, where σ is the conductivity.

1.5.2 Hall measurements: carrier density and mobility

For our device we first measure carrier density and mobility based on the Hall-bar introduced above. As reference we use the “nominal” mobility and carrier density averaged over the wafer measured directly after growth at the cryogenic temperature of $T = 4\text{ K}$ using the Van-der-Pauw method [41]. They are $\mu = 0.7 \times 10^6 \text{ cm}^2 \text{ V}^{-1} \text{ s}^{-1}$ and $n_s = 2.27 \times 10^{11} \text{ cm}^{-2}$, corresponding to

a mean free path of $l_m = 5.5 \mu\text{m}$. In our actual sample we determine the carrier density (averaged over the width of the Hall bar) by measuring the classical Hall voltage $V_H \propto 1/n_s$ [10] and the mobility by measuring the longitudinal resistivity in the limit of tiny magnetic fields $B \rightarrow 0$ ($R_{13} = R_{24} \propto \rho_0 \propto (n_s \mu)^{-1}$), both at $T \simeq 4.2 \text{ K}$. We sketch the electrical circuit diagram of the measurement setup in Fig. 1.8(.). For all the measurements we keep the source-drain current con-

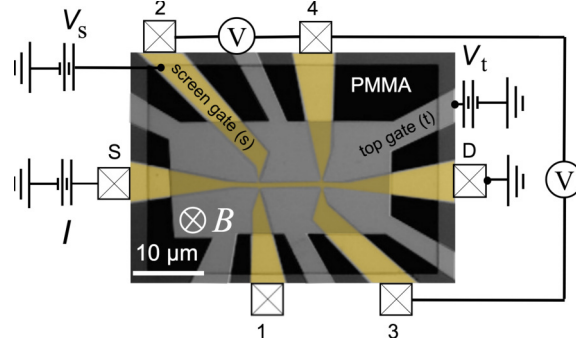


Figure 1.8: Electrical circuit diagram of the measurement setup. In a Hall measurement current is applied between source (S) and drain (D) contacts and voltage is detected at the probes numbered 1, 2, 3, and 4. Magnetic field B is applied out-of-plane of the sample.

stant with a current source Keithley 6221 and measure voltages with Agilent 34411A multimeters. We used the same electrical wiring as described in section (1.4). In Fig. 1.9 we present our results

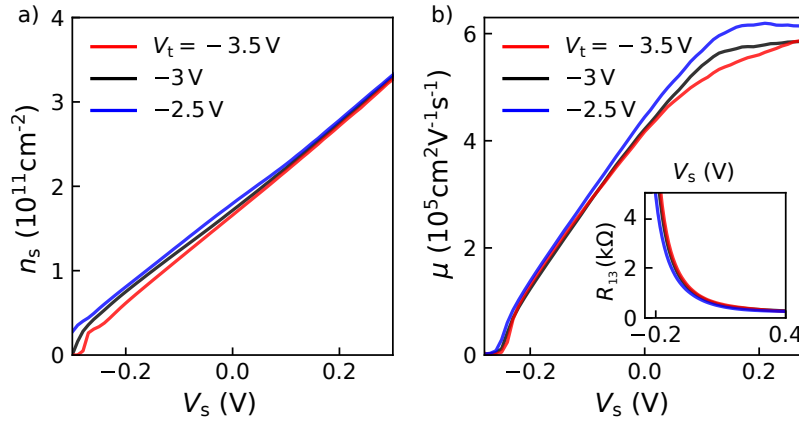


Figure 1.9: Hall measurements: Electron carrier density n_s in panel a) and mobility μ of the 2DES in panel b) versus screen gate voltage V_s for various top gate voltages $V_t < V_t^d$. The inset presents the actually measured longitudinal resistance $R_{13}(V_s)$ at $B \rightarrow 0 \text{ mT}$.

as a function of screen gate voltage V_s and for various top gate voltages $V_t < V_t^d$, i.e. where the 2DES beyond the Hall-bar is fully depleted and the Hall-bar is well defined. Both, the carrier density and mobility depend only little on the top gate voltage but are widely tunable by varying the screen gate voltage. For $V_s < 100 \text{ mV}$ we observe a linear decrease of both, n_s and μ , with decreasing V_s indicating an approximately constant capacitance C_s between 2DES and the screen gate and a resistivity $\rho_0 \propto n_s^{-2}$ (equivalent to $\mu \propto n_s$). We note, that gate voltage independent capacitances (as our C_s) between gates and the 2DES are not guaranteed as this property depends on the wafer material. Leveling of mobility μ at $V_s > 0.1 \text{ V}$ while n_s still increases we can explain

assuming that larger n_s no longer enhance screening of electrical field or that mobility is limited by the screening independent of carrier scattering. In our sample, at $V_s = 0$ carrier density and mobility are reduced by approximately a factor of two compared to the “nominal” values of the pristine wafer. However, the “nominal” values can be recovered by applying positive V_s . This result suggests, that wafers with a higher doping level could be advantageous for applications requiring a high mobility or a highly tunable carrier density.

1.6 Electron dephasing in mesoscopic systems

We also probe dephasing properties of electrons in a 2DES defined with our method. The related time-scale, phase coherence time τ_ϕ determines how long a charge carrier may travel before losing its phase memory [42].

In the diffusive transport regime [43] the phase coherence time τ_ϕ depends on the corresponding lengthscale, phase coherence length l_ϕ as:

$$l_\phi = \sqrt{d_e \tau_\phi}, \quad (1.5)$$

where the diffusion coefficient, d_e , is related to the Fermi velocity v_F and the elastic scattering time τ_m :

$$d_e = 1/2 v_F^2 \tau_m. \quad (1.6)$$

For the ballistic transport regime we can assume $l_\phi = v_F \tau_\phi$.

1.6.0.1 Aharonov-Bohm effect and dephasing in quasi-1D channels

We employ magnetoconductance fluctuations in a ring geometry for estimating phase-coherent properties of the 2DES [43]. We illustrate the principal setup in Fig. 1.10, where a ring encloses an area S and connects two electron reservoirs with chemical potential μ_s and μ_d . The two alternative electron pathways through the ring, as sketched in Fig. 1.10 with red lines give rise to the electron interference at the crossover point with phase difference

$$\phi_1 - \phi_2 = \delta\phi = \oint \vec{k} d\vec{r} - \frac{ne}{\hbar} \oint \vec{A} d\vec{r}, \quad (1.7)$$

where \vec{A} is vector potential, \vec{k} is the electron wavevector and $\oint \vec{A} d\vec{r} = \vec{B} \vec{S}$ is magnetic flux through the ring. The first term $\delta\phi_{es} = \oint \vec{k} d\vec{r}$ sums up all phase shifts related to the existence of multiple paths (as for universal conductance fluctuations [44–46]) or geometry (such as the electrostatic phase shift due to geometrical asymmetry or electron wavevector between the left and right arms of the ring [47]). The second term $(ne/\hbar) \oint \vec{A} d\vec{r}$ represents the magnetic phase is $2\pi n$ times the number of enclosed magnetic flux quanta, where n corresponds to the interference of the trajectories that make n half-revolutions around the ring. Assuming equal transmission amplitudes t_0 for both branches we can calculate current through the ring

$$I \propto |(t_1 + t_2)|^2 \propto 2t_0^2(1 + \cos(\delta\phi)), \quad (1.8)$$

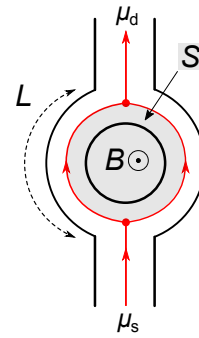


Figure 1.10: Sketch of the Aharonov-Bohm ring with perpendicular magnetic field B applied. Electron trajectories are shown in red.

where $t_{1,2} = t_0 \exp(-i\phi_{1,2})$ is transmission of the arm of the ring. The current oscillations phenomenon has been proposed in 1959 by Aharonov and Bohm and is called Aharonov-Bohm effect [48]. Sharvin and Sharvin made the first observation of the effect in a solid in a long metal cylinder [49]. In the ring geometry, it was investigated by Webb et al. [50]. The Aharonov-Bohm (AB) oscillations can be thus formally described as

$$I = \bar{I} \left[1 + v \cos \left(\frac{e}{\hbar} BS + \delta\varphi_{\text{es}} \right) \right], \quad (1.9)$$

where \bar{I} is the current averaged over B , $v = I_0/\bar{I}$ the visibility of the AB oscillations with amplitude I_0 .

Our method introduced above offers a straightforward way to fabricate conducting pathways with a ring topology. In Fig. 1.11 we present a photograph of a sample containing seven quasi-one-dimensional Aharonov-Bohm (AB) rings of various sizes and shapes in a parallel configuration connected to two-dimensional leads. We can measure the conductance of an individual ring by depleting the 2DES below the top gate and below all ring-shaped screen gates beside the one of the AB-ring of interest. To explore the phase coherence of the carriers, we here concentrate on the smallest ring (rightmost in Fig. 1.11) which we also present as a scanning-electron microscope picture in Fig. 1.12(b). We also show the electrical circuitry of the measurement setup in

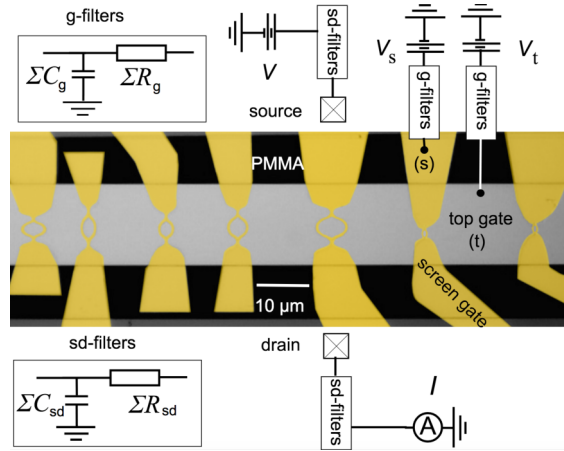


Figure 1.11: False-colored optical microscope image of the Aharonov-Bohm sample with seven individual AB rings and electrical circuit diagram of the measurement setup. We colorize the screen gates in yellow and the top gate in gray. Unused AB rings are depleted by applying sufficiently negative V_s (not shown in the sketch). We used filtering sketched in the insets for both gate wires (g-filter) and source-drain wires (sd-filter), where resistances and capacitances of the circuitry can be found in tables (1.2) and (1.3). Details of the setup and filtering are discussed in master thesis by Bachsoliani [36].

Fig. 1.11. The setup parameters for wiring and filtering for gate wires and for source-drain wires are listed in tables (1.2) and (1.3). In Fig. 1.12(a) we present an example of AB oscillations, measured in a dilution refrigerator Oxford Instruments Kelvinox at a lattice temperature of 25 mK. Here we plot the current I flowing through the smallest ring in response to a source-drain voltage of $V = 0.1$ mV versus the perpendicular magnetic field B . The measured period of the AB

Component	Resistance (Ω)	Capacitance to ground (F)
Double shielded coax	$\simeq 1$	$\simeq 100\text{p}$
Low temperature sd filtering	1 k	500p
Cu coax sd wires	< 200	250p
Filter box sd wires	2.2k	1.8 n
Double shielded coax	$\simeq 1$	100p
$\Sigma(\text{sd wires})$	$\simeq 3.4\text{k}$	$\simeq 3.31\text{n}$

Table 1.2: Resistances and capacitances in the source-drain wires for AB-experiment.

Component	Resistance (Ω)	Capacitance to ground (F)
Double shielded coax	$\simeq 1$	$\simeq 100\text{p}$
Room-temperature gate filtering wires	100k	1 μ
Cu/NbTi loom gate wires	< 10	300p
Low-temperature gate filtering	330k	230 n
Double shielded coax	$\simeq 1$	100p
$\Sigma(\text{gates})$	$\simeq 432\text{k}$	$\simeq 1.2\mu$

Table 1.3: Resistances and capacitances in the gate wires for AB-experiment.

oscillation in Fig. 1.12(a) of $\delta B \simeq 7.9\text{mT}$ corresponds to the enclosed area of $S = h/eB \simeq 0.5\mu\text{m}^2$, coinciding with the area framed by the dashed line in Fig. 1.12(b). In order to observe the AB-oscillations shown in Fig. 1.12(a) it was necessary to almost completely deplete the carriers in the AB-ring by applying V_s close to the depletion voltage V_s^d . This hints at a channel width so wide that it allows for multiple paths (in each arm) contributing with individual phases to the conductance which effectively reduces the visibility of the AB-oscillations [51]. As a rule of thumb, for our geometry an enclosed area difference of about 1% would suffice to generate a phase shift of π at $B \simeq 200\text{mT}$. The almost depleted ring sufficiently reduces the number of possible paths to reach a visibility of few percent. Taking the Hall-bar measurements above as a reference for the applied gate voltages we expect a carrier density of $\sim 8 \times 10^9\text{cm}^{-2}$ and a mean free path in the order of $1\mu\text{m}$ which is the same order of magnitude as the arm length of our AB-ring of $L \simeq 1.5\mu\text{m}$. However, screening is reduced along the almost depleted AB-ring, such that the mean-free-path is likely shorter. Hence, we conclude that the electron dynamics in our AB-ring is located somewhere between the quasi-ballistic and the diffusive regime. One way to reach the ballistic regime in future devices will be to further reduce the intrinsic channel width such that quasi-one-dimensional channels can be realized at relatively large carrier densities. A further reduction of the screen gate width by a factor of four is easily achievable by electron-beam-lithography.

In Fig. 1.13(a) we present AB-oscillations of the current $I - \bar{I}$ as a function of B and V_s while in panel b we show an exemplary depletion curve plotting the current $\bar{I}(V_s)$ averaged over B . The latter strongly oscillates as observed for Coulomb blockade oscillations, the current becomes small but stays finite in the Coulomb valleys. Such behavior can be explained assuming two quantum dots in parallel [52], i.e., one dot in each arm of the AB-ring as indicated in the inset. The exact position of the quantum dots is thereby unknown. The overall resistance of $R \simeq 120\text{k}\Omega \gg h/e^2$ at the two distinct current maxima below $V_s - V_s^d = 10\text{mV}$ is in agreement with the assumption of two parallel dots giving rise to well-established Coulomb blockade oscillations. The two-terminal AB-oscillations in Fig. 1.13(a) feature (i) continuous phase shifts at finite B , confirming the contribution of multiple paths in each arm, and (ii) phase jumps as a function of

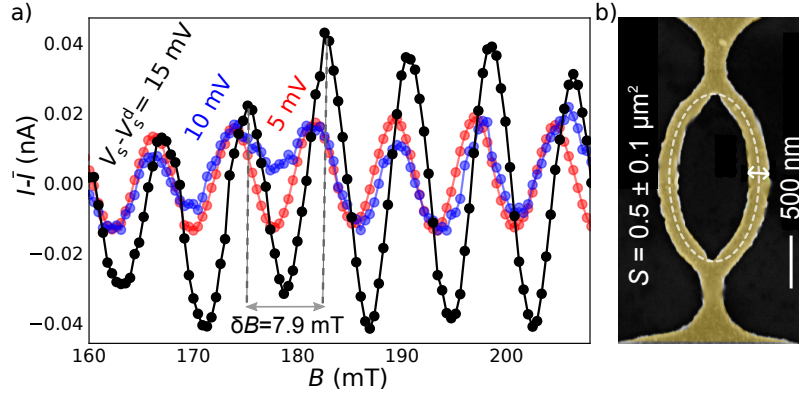


Figure 1.12: a) Measured current $I - \bar{I}$ as a function of perpendicular magnetic field B for three values of $V_s - V_s^d$ near depletion and $V_t = -3$ V. (At V_s^d the carriers beneath the screen gate are depleted.) The bath temperature is $T = 25$ mK and the source-drain voltage $V = 0.1$ mV. b) Scanning electron microscope image of the measured AB-ring. The screen gate is shown in yellow. The dashed white line embraces the area of $S = 0.5 \mu\text{m}^2$ corresponding to the measured magnetic field period of $\delta B = 7.9$ mT, see main text. The white double arrow indicates an error in S of $\pm 0.1 \mu\text{m}^2$ corresponding to a maximum error in δB of ± 1.5 mT. This value reflects the experimental uncertainty in the tilt angle between the 2DES and the magnetic field of $\pm 1^\circ$ (B is the field component perpendicular to the 2DES).

V_s . Both observations confirm the existence of quantum dots in the arms of the AB-ring (phase jumps have been previously observed for one dot in one arm) [53, 54]. Note that our ring is too small to explain the observed phase jumps employing the electrostatic AB-effect [47].

In the following we will discuss the dephasing as a function of temperature and source-drain voltage. In an ideal two-terminal AB-ring composed of one-dimensional arms dephasing by energy broadening is absent at modest energies. The reason is phase rigidity [54–58] allowing only phase shifts by multiples of π which would require either very different arm length or an unreasonably large energy window. Such an ideal AB-ring would be a perfect device to study the electron-electron interaction [59–61] remaining as possible dephasing process. However, realistic AB-rings as ours host multiple paths compromising the phase rigidity such that the temperature or source-drain voltage dependence of the dephasing at relatively small energies is dominated by energy broadening [62–65]. The measured temperature and source-drain voltage dependence of the visibility are presented in Fig. 1.14 for $V_s - V_s^d = 15$ mV where the two-terminal resistance is $\simeq 60$ k Ω , compare Fig. 1.13(b). Having already established the existence of two parallel quantum dots we now consider two scenarios, namely either ballistic or diffusive transport between the quantum dots. Searching for an answer we fit the measured data in Fig. 1.14 for two idealistic models. The first one assumes diffusive transport in an AB-ring with quasi-one-dimensional arms for which the temperature dependence of the visibility has been obtained from the weak localization theory [66]

$$v(T) = v_0 \left(\frac{E_{\text{Th}}}{k_B T} \right)^{1/2} \exp \left(\frac{-L}{\sqrt{d_e} \tau_\phi} \right), \quad (1.10)$$

with $\tau_\phi = \alpha(k_B T)^{-2/3}$ [67]. This equation takes into account thermal broadening (square root term) and decoherence by scattering of electrons (exponential term). Here $E_{\text{Th}} = \hbar d_e / L^2$ is

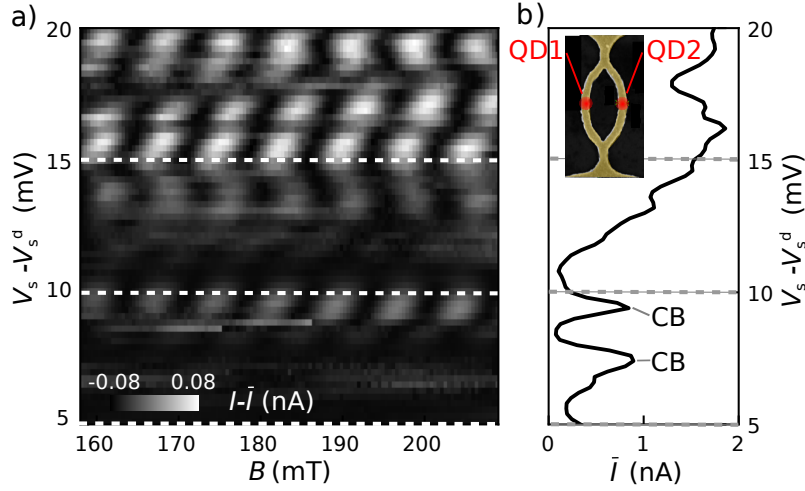


Figure 1.13: a) Current oscillations $I - \bar{I}$ as a function of screen gate voltage and magnetic field at $V_t = -3$ V. b) Coulomb blockade oscillations in $\bar{I}(V_s)$ (averaged over B). Two individual Coulomb blockade maxima are indicated with CB. The bath temperature was $T = 25$ mK and the source-drain voltage $V = 0.1$ mV. The data shown in Fig. 1.12a are plots along the horizontal dashed lines.

the Thouless energy. The according to voltage dependence of the visibility derived from non-equilibrium dephasing models is [68, 69]

$$v(V) = v_0 \left(\frac{e\kappa V}{E_{\text{Th}}} \right)^{1/2} \exp \left(\frac{-L}{\sqrt{d_e \tau_\phi}} \right) \quad (1.11)$$

with $\tau_\phi = \beta(e\kappa V)^{-2/3}$ [70, 71]. The prefactor $\kappa = 0.52$ takes into account that part of the source-drain voltage V drops in the leads of the AB-ring. The red solid lines in Fig. 1.14 are fits to the respective temperature and voltage dependences given by Eq. (1.10) and Eq. (1.11). The diffusive model describes the measured data well for high energies but drastically overestimates the visibility at low T or V . This deviation can be explained with the approximations done in assuming $V = 0$ for fitting the T -dependence and $T = 0$ for fitting the V -dependence. The actual fit-parameters are listed in the caption of Fig. 1.14.

In our second idealistic scenario we assume ballistic transport through the AB-ring. Because the dwell time $\simeq L/v_F$ of an electron moving ballistically through the AB-ring is short compared to τ_ϕ in this case we can neglect the influence of Nyquist noise which leaves energy broadening as only remaining dephasing process [67]. Combining voltage and temperature dependence in first order the ballistic scenario can be described by [72]:

$$v = 2\pi v_0 \frac{k_B T}{|e\kappa V|} \sinh^{-1} \left(\frac{\pi k_B T}{\hbar / \Delta \tau} \right) \left| \sin \left(\frac{e\kappa V}{2\hbar / \Delta \tau} \right) \right|, \quad (1.12)$$

where $\Delta \tau$ defines the difference of the dwell times of a ballistic electron in the two arms of the AB-ring. A single fit to both data sets of Eq. (1.12) representing the ballistic model is shown as black dashed lines in Fig. 1.14. Our ballistic model describes the temperature dependence well but shows qualitative deviations in the voltage dependence (at high voltages). We list the actual fit-parameters in the caption of Fig. 1.14. We find a dwell time difference of $\Delta \tau = 30$ ps. On the

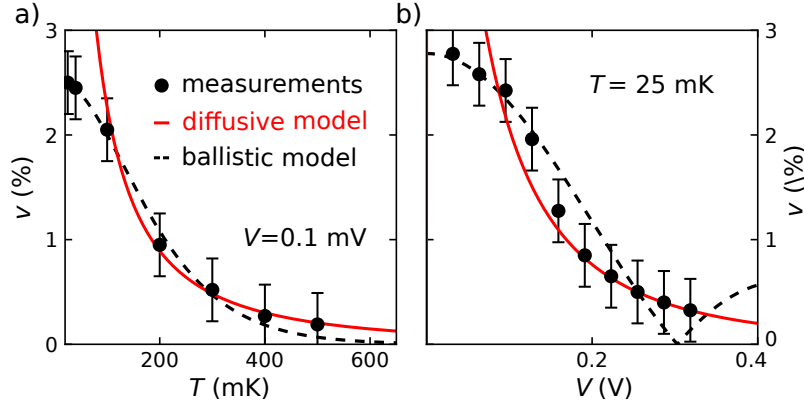


Figure 1.14: Visibility $v(T)$ at $V = 0.1$ mV in panel a) and $v(V)$ at $T = 25$ mK in b); $V_s - V_s^d = 15$ mV and $V_t = -3$ V. Solid red lines are model curves assuming diffusive transport calculated with Eqs. (1.10) in a) and (1.11) in b) for $v_0 = 56\%$, $E_{Th} = 36 \mu\text{eV}$, $\alpha = 0.015 \text{ ps meV}^{2/3}$, $\beta = 0.009 \text{ ps meV}^{2/3}$ and $\kappa = 0.52$. Dashed black lines are calculated assuming ballistic transport with Eq. (1.12) for $v_0 = 2.56\%$, $\Delta\tau = 30$ ps and $\kappa = 0.52$.

one hand, this corresponds to an unrealistically large arm length difference of $\sim 1 \mu\text{m}$ assuming ballistic motion at the Fermi velocity. On the other hand, the existence of a quantum dot in each arm leads to multiple reflections which would enhance dwell times. As a result, without further experimental and theoretical efforts, it is impossible to determine from our data, whether transport through the AB ring is diffusive or ballistic. The almost complete depletion might cause diffusive transport in the AB-rings which is necessary to reduce the number of one-dimensional channels preventing a higher visibility. We believe that AB-rings with narrower arms but higher carrier density will in future help to reach ballistic transport and to reduce the chance of the formation of quantum dots.

1.7 Conclusions

Within the first chapter we have explored an alternative method to define mesoscopic circuits in heterostructures based on the electric field effect. The idea is to deplete most of the 2DES area utilizing a global top gate. Only at those regions where carriers are needed screen gates placed below the top gate are used to shield the effect of the top gate locally. The resulting circuits are highly tunable on the nanoscale as demonstrated in the presented experiments. Importantly, our method has the advantage of reducing the complexity of gate defined nanostructures. In more detail, it allows a straightforward way to realize conducting paths with ring topology and offers a way to design complex structures with a smaller number of gates compared to the conventional technology based on multiple depletion gates. Our Aharonov-Bohm measurements demonstrate phase coherence comparable to that in conventional AB-rings in semiconductors which makes our method suitable for quantum information applications. While not shown here the close vicinity of a metal gate to the carriers is expected to lead to a reduction of the Coulomb interaction between carriers.

Chapter 2

Ballistic Electron Optics with Quantum Point Contacts

Quantum point contacts are short and narrow constrictions in a 2DES with a width in the order of the Fermi wavelength. They display an astonishingly rich spectrum of complex phenomena from the well understood one-dimensional conductance quantization [73] to many-body interaction effects such as the so-called 0.7-anomaly [74, 75]. In our experiments, electrons are injected by a first QPC and travel ballistically towards a second QPC. Previous experiments on coupled QPCs [76] were discussed using a hard-wall confinement potential and didn't include the discussion of realistic QPC eigenmodes in contrast to our study. Another critical difference to some of the historical experiments [77] is that we don't float the intermediate region between the QPCs but leave it as an open and grounded 2DES. We also present electron focusing experiments with an electrostatic lens similar to previous attempts [78, 79] but with an optimized setup.

2.1 Quantum Point Contacts

To define a QPC in a 2DES, we apply negative voltages V_{QPC} to two gates placed on top of the sample surface and separated by a small gap as sketched in Fig. 2.1(a). We deplete the 2DES below the gates and tune the width of the constriction by decreasing V_{QPC} further beyond the depletion voltage until the constriction is completely pinched off. The resulting potential profile can be approximated as the saddle-point potential, characterized by its curvatures ω_y and ω_x sketched in the Fig. 2.1(a).

$$U(x,y) = U(0) + 1/2m\omega_y^2 y^2 - 1/2m\omega_x^2 x^2, \quad (2.1)$$

For an incident electron wavefunction ψ the Hamiltonian of the problem writes [80]:

$$\hat{H}(x,y) = \hat{p}^2/2m + U(x,y), \quad (2.2)$$

where $\hat{p}^2/2m$ is the kinetic energy operator. Here we assume the parabolic dispersion for free electrons in 2DES. Separation of variables x and y in the Hamiltonian leads to a one-dimensional harmonic oscillator in the potential $U(y) = 1/2m\omega_y^2 y^2$ and $\hat{H}(y)\Psi(y) = E_n \Psi(y), n = 1, 2, \dots$

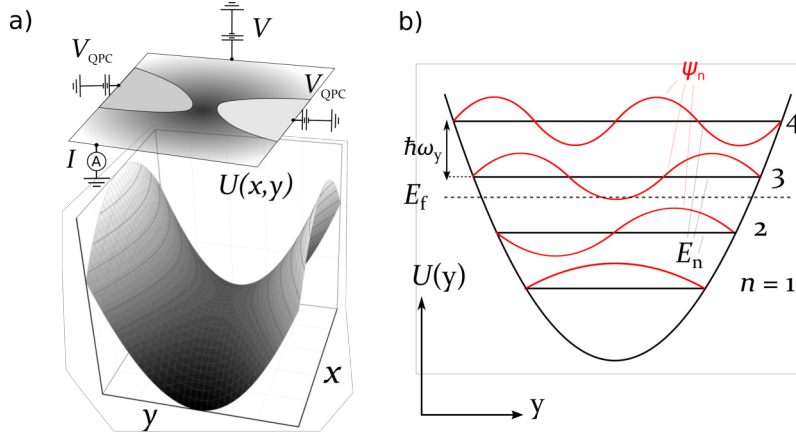


Figure 2.1: a) Top: Sketch of the quantum point contact formed by two metallic gates. Bottom: sketch of the QPC saddle-point potential. b) Sketch of the lateral confinement of the QPC potential at its center (black) and its eigenmodes transversal profile (red)

Eigenmodes of the problem are associated with discrete energy values $E_n = (n - 1/2)\omega_y$. The corresponding wavefunctions $\Psi_n(y)$ with quantum number n are [10]:

$$\Psi_n(y) = \left(\frac{m\omega_y}{\pi\hbar}\right)^{\frac{1}{4}} \frac{1}{\sqrt{2^{n-1}(n-1)!}} H_{n-1} \left(\sqrt{\frac{m\omega_y}{\hbar}} y \right) \exp\left(-\frac{m\omega_y}{2\hbar} y^2\right) \quad (2.3)$$

with the Hermite polynomials H_{n-1} [81]. In Fig. 2.1(b) we illustrate eigenfunctions lateral potential profile and mark the energy values with horizontal black lines.

2.1.1 QPC conductance

In case of ballistic transport a nanodevice's conductance is limited by the scattering on the contacts [10]. One therefore cannot describe conductance in terms of local conductivity as in the case of diffusive transport. Following, we describe the scattering problem of a ballistic QPC by applying the Landauer approach [73, 82] and write its conductance $G = I/V$ as

$$G = \frac{2e^2}{h} \sum_{n=1}^N T_n, \quad (2.4)$$

where T_n is the transmission probability of the n th mode. For idealistic reflectionless contacts and ballistic 1D transport the transmission of every fully occupied mode is $T_n = 1$ such that $G = \frac{2e^2}{h} N$ for N fully transmitting modes, where $h/2e^2 = 12.9 \text{ k}\Omega$. Experimentally the number of occupied modes N can be controlled by tuning the QPC gate voltage V_{QPC} . The resulting 1D conductance quantization predicted by Landauer in 1957 [82] was first measured in 1988 independently by Van Wees et al [83] and Wharam et al [84]. A single mode transmission $T_n(E)$ at a given electron energy E can be calculated following Büttiker [80]

$$T_n(E) = \frac{1}{1 + e^{-\pi\epsilon_n}} \text{ where } \epsilon_n = 2(E - \hbar\omega_y(n - 1/2) - U_0)/\hbar\omega_x \quad (2.5)$$

Here the QPC gate voltage defines the change of the saddle point potential energy $V_{QPC} \propto U_0$. In Fig. 2.2 we illustrate the formula (2.5) for four different ratios of ω_y/ω_x equal to 0.5 (magenta),

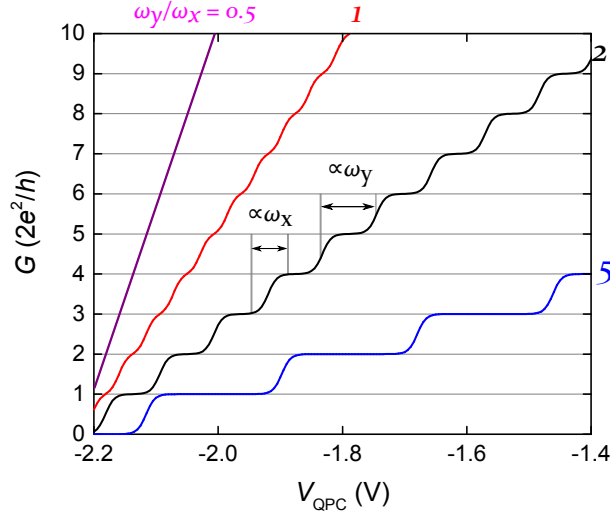


Figure 2.2: Simulated QPC conductance as a function of QPC gate voltage for different ratios of longitudinal and transversal curvatures, ω_x and ω_y , marked with arrows. QPC is biased with finite source-drain voltage V in the linear regime.

1 (red), 2 (black) and 5 (blue). The expression (2.5) describes smooth transitions between conductance plateaus with a step width $\propto \omega_y$ and an edge width proportional to $\propto \omega_x$, as indicated in Fig. 2.2. Experimentally several conditions are required to see quantized conductance in the transmission through a QPC:

- $\omega_x < \omega_y$, otherwise conductance plateaus are too smooth and vanish (red line in Fig. 2.2).
- $k_B T < \hbar \omega_y$, the thermal broadening is smaller than the subband spacing.
- $\delta w_{\text{noise}} < \hbar \omega_y$ the inhomogeneous broadening, e.g. caused by charge noise, is smaller than the subband spacing.

The degree of flatness of the plateaus and sharpness of the steps in the experiments also vary between devices of nominally identical design, indicating that the detailed shape of the electrostatic potential defining the constriction is important [85]. Many uncontrolled factors are affecting this shape, such as small changes in the gate geometry, variations in the pinning of the Fermi level at the free GaAs surface or the interface with the gate metal, doping inhomogeneities in the heterostructure material and trapping of charge in deep levels in AlGaAs [43].

2.1.2 Adiabaticity criteria

A parabolic barrier or more precisely a barrier with the potential $U(x) \propto x^\alpha, \alpha > 2$ guarantees smooth $T(V_{\text{QPC}})$. However if the transition from the QPC centre to the opened 2DES is abrupt there can be considerable reflection of propagating modes at this interface (resulting in Fabry-Perot interference [75, 86]). Such reflection is minimized by adiabatically opening the constriction. When considering the adiabatic transition we have to study the mode coupling at the entrance and exit of the QPC constriction.

Evolving QPC eigenstates change their lateral extensions as indicated in Fig.2.3. The effective mode widths depends on the distance to the constriction centre [87]. At some distance the influence of the charged gates is so small that the electron motion is that of a free particles in 2D. The mode mixing is in the order of the subband splitting $\hbar\omega_y$ at this point [88]. The adiabaticity criterion was first defined by Yacoby and Imry in terms of the constriction geometry [89, 90]:

$$\delta d(x)/\delta x < 1/N(x), \quad (2.6)$$

where $d(x)$ is the constriction width and $N(x) \simeq k_F d(x)/\pi$ is the local number of occupied subbands. If the constriction width changes sufficiently gradually in Eq. (2.6) the transport through the constriction occurs without intersubband scattering. It has been also suggested that for rounded QPC tips the adiabaticity condition can be calculated as [91]

$$\pi^2 \sqrt{2R/d(0)} > 1, \quad (2.7)$$

where R is the tip radius. The QPC conductance is always determined by the narrowest part of the constriction, however, to achieve high QPC transmission for each mode it is essential to minimize the impurity backscattering by keeping the length of the QPC short.

2.1.3 Landauer-Büttiker formalism

In the following experiments we will consider multi-terminal devices. A generalization of the Landauer approach to a multi-terminal case is possible as illustrated in Fig. 2.4. Each of the terminals supports N_i modes and provides an electron reservoir at a given chemical potential μ_i . The Landauer formula [73, 82] can be written for multiterminal resistances as proposed by Büttiker [92]: Let $t_{ij,\alpha\beta}$ define the complex coefficient for scattering from mode β in terminal j to mode α in terminal i . The total transmission probability from terminal j to terminal i is then given by

$$T_{ij} = \sum_{\alpha=1}^{N_i} \sum_{\beta=1}^{N_j} |t_{ij,\alpha\beta}|^2. \quad (2.8)$$

Conservation of current implies $N_i = \sum_j T_{ij}$, where the sum extends over all reservoirs. We took into account the backscattering modes by assuming $T_{ii} = R_i$

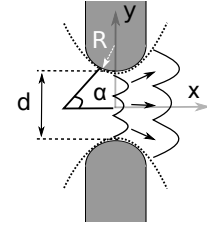


Figure 2.3: a) Illustration of the QPC mode evolving through the QPC. QPC tips are round, transition from the QPC center to the 2DES is adiabatic.

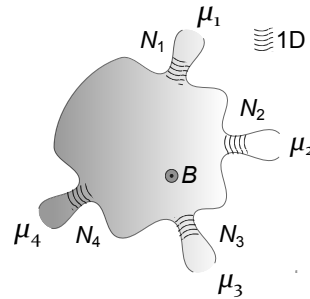


Figure 2.4: Sketch of a multiterminal device used to explain the Landau-Büttiker formalism. Each reservoir is in thermal equilibrium at a chemical potential μ_i . A terminal supporting N_i 1D modes connects reservoirs to a central scattering region.

The reservoir i at chemical potential μ_i above E_F injects into terminal i a current $\tilde{I}_i = 2e/hN_i\mu_i$. A fraction $\tilde{I}_{j,i} = \tilde{I}_i T_{ji}/N_i$ is transmitted into terminal i while a fraction $\tilde{I}_{i,i} = \tilde{I}_i T_{ii}/N_i$ is back reflected. The net current I_i in the terminal i is reduced by the injected current $\sum_j \tilde{I}_j$ from other terminals and thus given by:

$$I_i = \left(N_i \mu_i - \sum_j T_{ij} \mu_j \right) \frac{2e}{h} (-1), \quad (2.9)$$

where the factor -1 takes into account that we assume technical current direction, that is convenient for a direct comparison with experiments. The equation above is known as the Landauer-Büttiker formula. It provides a system of linear equations that may be solved to determine the transmission properties of a sample. Alternatively it allows a direct comparison with specific transport measurements. For instance, if all contacts but 1 and 3 are left floating and a constant current I_{31} is driven from terminal 1 to 3, then the Landauer-Büttiker formula can be used to find the 4-probe resistance, $R_{13,24}$.

$$R_{13,24} = \frac{\mu_3 - \mu_4}{-eI_{31}}, \quad (2.10)$$

In the original formulation, the scattering in the conductor was assumed to be elastic, but Büttiker subsequently showed that the formalism could be extended to include inelastic scattering [57].

2.1.4 Casimir-Onsager relation

To explain the symmetry properties of current for multiterminal devices in external magnetic fields similar to Casimir-Onsager reciprocal relations in thermodynamics [55, 56] we can use the Landauer-Büttiker formula [57]. In the following derivation, we will use two matrix operators: Hermite conjugation $*$ and matrix transposition T [81]. We discuss canonical symmetries of the scattering matrix $S = t_{ij,\alpha\beta}$, those are unitarity and time-reversal symmetry. The unitary symmetry is related with the conservation of currents. It is illustrated for a two-terminal case in Fig. 2.5. We can express the unitarity for the first terminal:

$$\sum_{\alpha\beta} |t_{11,\alpha\beta}|^2 + \sum_{\alpha\beta} |t_{12,\alpha\beta}|^2 = N_1, \quad (2.11)$$

where N is the number of modes in terminal 1. Generally for a multi-terminal device unitarity of the scattering matrix can be calculated as $SS^{*T} = SS^\dagger = 1$ or in a summation form:

$$\sum_j \sum_{\alpha\beta} t_{ij,\alpha\beta} t_{ij,\alpha\beta}^\dagger = 1_i, \quad (2.12)$$

where 1_i is a vector with dimension i , α, β denote mode numbers and i, j are terminal numbers.

Second, we study the invariance of the scattering matrix in presence of non-zero magnetic field $B \neq 0$: $S(B) = S^T(-B)$. The symmetry of the Schrodinger equation implies that the time-reversed wavefunction Ψ^* is identical to the original wavefunction Ψ with the reversed direction

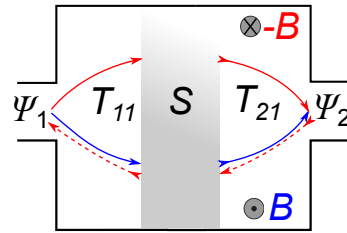


Figure 2.5: Scattering problem sketch for a two-terminal device. T_{21} denotes the transmission, S the scattering and T_{11} the reflection matrix. Solid/dashed lines indicate possible trajectories for electrons for the direct/time-reversed propagation at finite magnetic field B (blue) and $-B$ (red).

of magnetic field $\Psi(B) = \Psi^*(-B)$ [10]. For the two-terminal problem illustrated in Fig. 2.5 the wavefunctions Ψ_1 and Ψ_2 can be related as

$$\Psi_2(B) = S(B)\Psi_1(B) \quad \text{or equivalently as} \quad \Psi_1^*(-B) = S(-B)\Psi_2^*(-B) \quad (2.13)$$

This can be directly seen by conjugating the first equation $\Psi_2^*(B) = S^*(B)\Psi_1^*(B)$ finally we get $S^*(B)S(-B) = 1$. Applying the unitary condition $SS^{*T} = SS^\dagger = 1$ we finally get $S(B) = S^T(-B)$. Time-reversal symmetry of the scattering matrix gives rise to the according symmetry of the transmission matrix:

$$\sum_{\alpha\beta} [t_{ij,\alpha\beta}(B)]^2 = \sum_{\alpha\beta} [t_{ji,\alpha\beta}(-B)]^2 = T_{ij}(B) = T_{ji}(-B) \quad (2.14)$$

Next we consider a four-terminal configuration sketched in Fig. 2.6, where a current I_1 is forced to flow between terminals 1 & 3 and another current I_2 applied between terminals 2 & 4. Solving Eq. 2.9 under the conditions $I_1 = -I_3$ and $I_2 = -I_4$, where I_i is the current into the respective contact, results in [57]:

$$I_1 = \alpha_{11}(V_1 - V_3) - \alpha_{12}(V_2 - V_4) \quad (2.15)$$

$$I_2 = -\alpha_{21}(V_1 - V_3) + \alpha_{22}(V_2 - V_4), \quad (2.16)$$

where $V_i = \mu_i/e$ and with

$$\alpha_{11} = (e^2/h)[(1 - T_{11})D_1 - (T_{14} + T_{12})(T_{41} + T_{21})]/D_1, \quad (2.17)$$

$$\alpha_{12} = (e^2/h)(T_{12}T_{34} - T_{14}T_{32})/D_1, \quad (2.18)$$

$$\alpha_{21} = (e^2/h)(T_{21}T_{43} - T_{23}T_{41})/D_1, \quad (2.19)$$

$$\alpha_{22} = (e^2/h)[(1 - T_{22})D_1 - (T_{21} + T_{23})(T_{32} + T_{12})]/D_1, \quad (2.20)$$

and

$$D_1 = T_{12} + T_{14} + T_{32} + T_{34} = T_{21} + T_{41} + T_{23} + T_{43}, \quad (2.21)$$

From $T_{ij}(B) = T_{ji}(-B)$ it follows that diagonal elements obey the symmetries $\alpha_{11}(B) = \alpha_{11}(-B)$ and off-diagonal $\alpha_{21}(B) = \alpha_{12}(-B)$ [57].

In a four terminal measurement we measure voltage at (2,4) pair of terminals and $I_2 = I_4 = 0$. Then we can express resistance $R_{13,24}$ as a function of $V_2 - V_4$

$$R_{13,24} = (V_2 - V_4)/I_1 = \alpha_{21}/(\alpha_{11}\alpha_{22} - \alpha_{12}\alpha_{21}) \quad (2.22)$$

Now we switch the current and the voltage leads but keep magnetic field fixed and take $I_1 = 0$.

$$R_{24,13} = \alpha_{12}/(\alpha_{11}\alpha_{22} - \alpha_{12}\alpha_{21}) \quad (2.23)$$

The sum of these resistances is symmetric under magnetic field reversal as a result of the symmetry of the $\alpha_{21}(B) = \alpha_{12}(-B)$ and we get:

$$R_{13,24}(B) = R_{24,13}(-B). \quad (2.24)$$

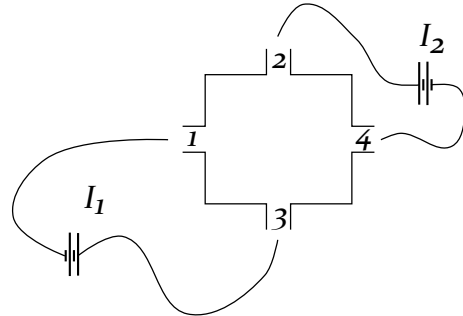


Figure 2.6: Sketch of the measurement when the current is forced to flow between pairs of terminals (1,3) and (2,4).

or the 4-probe resistance is invariant under exchange of the current and voltage leads if the direction of the applied field is also reversed. Now we can determine six resistances

$$R_{mn,kl} = (h/e^2)(T_{km}T_{ln} - T_{kn}T_{lm})/D_2, \quad (2.25)$$

where m, n, k, l are the terminal numbers, and $D_2 = (h/e^2)^2(\alpha_{11}\alpha_{22} - \alpha_{12}\alpha_{21})/D_1$ is symmetric in magnetic field. Finally we can write the general reciprocity relation [57]

$$R_{mn,kl}(B) = R_{kl,mn}(-B), \quad (2.26)$$

. The reciprocity relation is unaffected by adding reservoirs to the system and is not restricted to elastic scattering [57]. In the following chapter we deal with two and three terminal systems. Therefore we discuss the application of the approach outlined above for some special cases.

2.1.4.1 Two-terminal device

Current conservations in a two-terminal system gives $N_1 = T_{11} + T_{12}$ and $N_2 = T_{22} + T_{21}$ for the first and second terminal respectively. From the symmetry of the transmission through the system $T = T_{12} = T_{21}$ we can deduce that the two-terminal resistance $R = (\mu_1 - \mu_2)/eI$ is also symmetric under magnetic field reversal:

$$R(B) = R(-B). \quad (2.27)$$

2.1.4.2 Three-terminal device

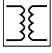
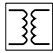
In the three-terminal measurements, we keep terminal 3 always grounded with $\mu_3 = 0$ and apply voltage $(\mu_1 - \mu_2)/e$ from terminal 1 while measuring current I through the terminal 2. Büttiker showed that addition of a lead to a multi-terminal conductor doesn't change the reciprocity relation for the two terminal resistance and is equivalent to the introduction of inelastic scattering into conduction process [57]. Therefore we can write the symmetry of the measured resistance $R_{12} = (\mu_1 - \mu_2)/eI$

$$R_{12}(B) = R_{21}(-B) \quad \text{or} \quad I(B) = -I(-B). \quad (2.28)$$

2.1.5 Validity of the Casimir-Onsager relation

In the diffusive transport regime, the reciprocity relation (2.24) for the resistance follows from the Casimir-Onsager relation also for the resistivity tensor $\rho(B) = \rho^T(-B)$. However, the reciprocity holds only in the linear response limit of infinitely small currents and voltages. Hence deviations from (2.24) can occur experimentally caused by higher order resistance terms which can arise from quantum interference or classically in a strongly driven system [93]. At small deviations the voltage response may be expanded as $V(I) = R_{(1)}I + R_{(2)}I^2 + R_{(3)}I^3 + \dots$ and Onsager relations are not fulfilled for $R_{(2)}$ and higher. In the case of long phase coherence time deviations persist down to tiny voltages in the order of $V \simeq \hbar/e\tau_\phi$ [43]. Magnetic impurities can be another source of deviations from reciprocity if the applied magnetic field is not sufficiently strong to reverse the magnetic moments on field reversal.

2.2.2.1 Ground connection

Avoiding ground loops is an important requirement of low-noise measurement. A usual solution for the ground connection is the powerline, and the ground resistance highly depends on the electrical circuit of the building. However, ground levels can be different for different power sockets or connection spots. Our goal is complete separation of the measurement ground coupled to the source-drain connection of the sample from the other grounds used for instruments and a PC. This ground also serves as a reference for applied voltages. One possible solution is using the isolating transformers that decouple supply ground of the instruments from the measurement ground (sketched with  in Fig. 2.7). The isolator helps to avoid ground loops by interrupting them. We sketch the ground connections with solid black wires in Fig. 2.7. The externally grounded cryostat (with a low-resistance wire) provides a common measurement ground (i) for all wires and devices connected to the cryostat. To avoid ground loops we didn't electrically connect the surrounding dewar and its frame to the cryostat and therefore ground it separately (ii). We also connected the magnet power supply to a separate ground (ii). We define the common measurement ground (i) via the shield of the BNC cable that carried it to electrical instruments. For multimeters and preamplifiers, we used isolation transformers to isolate them from the power supply to avoid the ground loops via the powerline (iii). However, transformers were unnecessary for voltage sources which are galvanically isolated from the powerline. We controlled the whole setup by Lab-View programs using GPIB interfaces (dashed black wires in Fig. 2.7) as connection standard between different devices. We also isolated the measurement computer from the setup by using galvanic USB isolator (CESYS USB Isolator). Finally, we decoupled the magnet power supply via a GPIB isolator from the other GPIB wires. Both isolators are shown with  symbols in Fig. 2.7.

2.2.2.2 Gate wires

We used the gate wires to apply dc voltages to the gates of the sample (blue in Fig. 2.7). As only dc signals were applied we implemented filters with 1.5 Hz cut-off frequencies to achieve efficient noise filtering. We show a circuit diagram in the labeled box of Fig. 2.7. We also used double shielded coax cables as a low noise solution to connect the dc-voltage sources (Yokogawa 7651) via a switching box to the room temperature filters at the cryostat. A feed-through capacitor Tusonix T053 built into the metallic filter box is shielding any high-frequency noise propagating as electromagnetic waves along the wires.

2.2.2.3 Current wires

We used the current wires (solid red wires in Fig. 2.7) for two configurations: in series with QPCs and directly connected to the opened 2DES with resistances $< 200 \text{ Ohms}$. For the ballistic experiments, we have not added any filter components for both to keep resistances and shunt capacitances as low as possible in the source-drain wires. Filtering the second also causes an additional voltage drop on the 2DES that we want to avoid. We used a DL Instruments 1211 model preamplifier to detect currents in our setup. The signal from the amplifier was read out by an Agilent Multimeter 34411A. The setup parameters for wiring and filtering are summarized in Tables (2.1) and (2.2).

Component	Resistance (Ω)	Capacitance to ground (F)
Double shielded coax	$\simeq 1$	100 p
Filter box	100 k	1 μ
Double shielded coax	$\simeq 1$	100 p
Manganin twisted pairs	$\simeq 50$	$\simeq 500$ p
Σ	$\simeq 103$ k	$\simeq 1$ μ

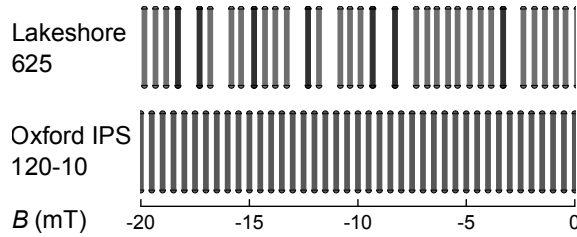
Table 2.1: Resistances and capacitances in the gate wires.

Component	Resistance (Ω)	Capacitance to ground (F)
Double shielded coax	$\simeq 1$	100 p
Manganin twisted pairs	$\simeq 50$	$\simeq 500$ p
Σ	$\simeq 2$ k	$\simeq 400$ p

Table 2.2: Resistances and capacitances in the current wires.

2.2.2.4 Magnet power supply

For the magnetic field measurements, we exploited a magnet integrated into a dewar fabricated by Oxford Instruments and two different power supplies: Lakeshore 625 and Oxford IPS 120-10. In the following sections, we perform several measurements at step sizes less than 1 mT which is close to the accuracy and resolution for the set and readout of both magnet power supplies. For the correct analysis of 2D color scale plots in this chapter, the equidistance of points is essential. The point represents a colored pixel at the 2D plot, and the plotting software makes equal pixel size for every point in a 2D sweep, that realistically can fluctuate due to the limited device accuracy and resolution. In Fig. 2.8, we show an exemplary plot recorded with each power supply to compare the step equidistance. Here we sweep the magnetic field with the step size of 0.5 mT, vertical bars represent measurement points for the used two magnet power supplies. In the specifications of both, we found the same readout resolution of 0.0085 mT. The set-point accuracy of the Oxford device, however, turned out to be higher, permitting sweeps with equidistant steps of 0.5 mT. For the Lake Shore device, a test sweep at the same step size

**Figure 2.8:** Comparison of both power supplies, assuming step equidistance for a continuous sweep of the magnetic field B with step size $\Delta B = 0.5$ mT.

results in a non-equidistant sequence of steps seen in Fig. 2.8. Deviations correspond to the accuracy of the Lakeshore power supply 0.85 mT indicated in the specifications [95]. To summarize, for the general analysis of the measured data arrays in this chapter both devices offered a sufficient output accuracy as well as readout accuracy. To perform magnetic field measurements at stepsizes of $\Delta B \geq 0.5$ mT, we limit the smallest step size for measurements presented in this chapter at 0.5 mT.

2.2.3 Sample design and connections

The sample is located below the He^3 pot and thermally connected to it (by gluing it to the stage with conductive silver epoxy) to obtain the best cooling efficiency. We mount the sample in the center of the magnet located inside the dewar at the coldest part of the cryostat. We engineered the connection from the gates to the macroscopic sample holder and lines with gold wires bonded to the sample via using a wedge-bonder. Golden wires also provide the thermal connection for cooling the 2DES. In Fig. 2.9(a) we show the used sample holder with a sample connected with

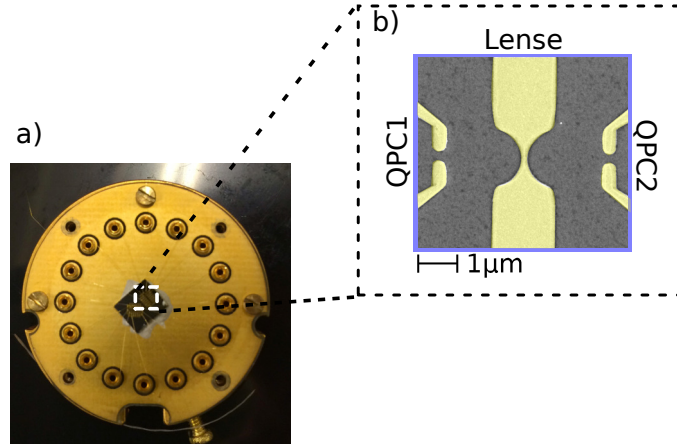


Figure 2.9: (a) Photo of the sample-holder with the sample attached (b) Scanning electron microscope image of the sample surface; the dark grey area contains 2DES 107 nm beneath the surface. Five Ti/Au gates (yellow) are used to define QPC1 and QPC2 and a central lens-shaped gate (yellow) respectively.

bond wires to the golden pins disposed in a circle at the edge of the sample holder. We show the sample design in Fig. 2.9(b) that consists of two pairs of split gates. These gates are employed to define, via the electric field effect, two nominally identical QPCs in series in the 2DES embedded 107 nm below the surface of a GaAs/AlGaAs heterostructure. In the center is an additional lens gate to manipulate electrons moving between QPC1 and QPC2. The sample contains a 2DES with a nominal carrier density of $n_s \simeq 3.1 \times 10^{-11} \text{ cm}^{-2}$ and mobility of $\mu \simeq 2.3 \times 10^6 \text{ cm}^2/\text{Vs}$, corresponding to a mean free path of $l_m \simeq 21 \mu\text{m}$ (see Appendix (A.1) for details). Between the two QPCs with the distance $L \simeq 4.6 \mu\text{m}$ we, therefore, expect ballistic transport. We used the QPC gate design tested by David Borowsky in his master thesis [96] with details showed in the Appendix (A.1).

2.3 Single QPC characterization

In Fig. 2.10(a) we present the setup for the single QPC characterization. We apply voltage V

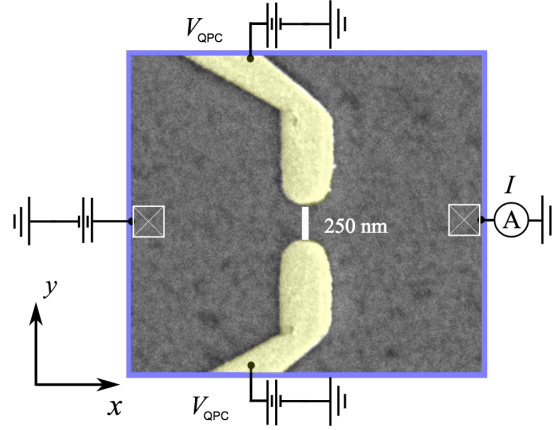


Figure 2.10: a) Sketch of the measurement setup used to characterize single QPCs. We place the SEM photo of the sample in its center. Tips of the golden gates (false-colored with transparent yellow) have adiabatic round design. We deplete the 2DES beneath the gates keep it unchanged under the light grey area. b) Sketch of the saddle point potential described by Eq.(2.29).

from one side of the QPC and measure the current I on the other side as a function of split gate voltage V_{QPC} . We used a single ohmic contact to detect current, while the other five contacts we kept grounded. We will use this configuration in the following ballistic experiments with two QPCs in series. In Fig. 2.11(a) we present pinch-off curves of the two individual QPCs used in the following experiments. The data presented here are shown after subtraction of the lead resistance described in Appendix (A.2). We find well-defined conductance plateaus at integer multiples of the (spin degenerate) conductance quantum $G_Q = 2e^2/h$. The smooth transitions between plateaus indicate perfect adiabatic coupling of the QPCs to the 2DES and the assumption of a parabolic barrier in current direction is appropriate (x -axis in Fig. 2.10a) [97].

We can fit the experimentally measured conductance for both QPCs with Eq. (2.5) and Eq. (2.4) to determine the ratio of transversal and longitudinal potential curvature ω_y/ω_x . However we found that the energy subbands in our QPC are not equidistant in energy that is clear from the inset of Fig. 2.11(b). Here we plot the width of the conductance steps in V_{QPC} that is proportional to the subband energy difference. To account for this problem we can assume slightly anharmonic potential with additional quadratic component of curvature $U(y) = 1/2\omega_y^2(y^2 + \beta_1 y^4)$, where β_1 is the anharmonicity parameter of the potential. We illustrate both harmonic and anharmonic potentials in Fig. 2.12(b). Subband energies and eigenmodes of both harmonic and slightly anharmonic oscillator can be calculated with the help of a tight binding model for a 1D chain with an onsite potential, see Appendix (A.5) for details. We fit the β_1 parameter in order to reproduce the energy dependence from the inset of Fig. 2.11(b) and show results as solid red and black lines there. Corresponding eigenmodes of the oscillator are shown in Fig. 2.12(b). We see that eigenfunctions are slightly less confined in the anharmonic potential at $5 < n < 7$ but almost identical as the corresponding harmonic eigenfunctions at $1 < n < 7$. In

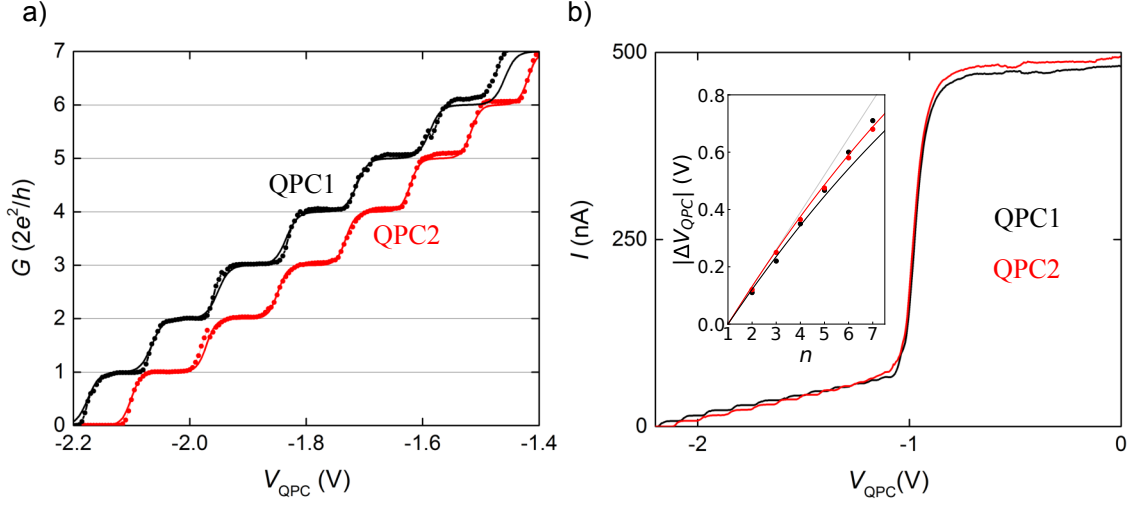


Figure 2.11: a) Dots: Measured conductance $G = I/V$ of a single QPC (QPC1 in black color and QPC2 in red color) as a function of QPC gate voltage V_{QPC} . Solid lines: theoretical fit to the measured data calculated by the formula (2.5). We also place horizontal lines at integers of multiple $2e^2/h$. b) Measured current I as a function of QPC gate voltage V_{QPC} in an extended voltage range of (a). Both (a,b) data was taken at temperature $T = 250\text{ mK}$ and the source-drain voltage $V = -0.7\text{ mV}$. All other gate voltages in Fig.(2.10) are grounded. Inset: Voltage $\Delta V_{\text{QPC}} = V_{\text{QPC}} - V_{\text{QPC}}^0$ at $G = ie^2/h, 1, 2, 3, \dots, 7$, where V_{QPC}^0 is taken at $G = e^2/h$. Points are the measured data and lines are theoretical fits for the anharmonic QPC1 (black) and QPC2 (red) and anharmonic case as a transparent line.

our experiments we will limit discussion to first 7 subbands in all the experiments and assume that we can treat QPC eigenfunctions to have Gaussian-Hermite form up to the 7th conductance plateau of both QPCs. Therefore we can use the extended version of the formulas (2.5) and (2.4).

$$G = G_Q \sum_{n=1}^{\infty} \left(1 + \exp \left\{ -2\pi \frac{(V_{\text{QPC}} - V_{\text{QPC}}^0)/\alpha_1 - (n - 1/2 - \beta_2(n - 1/2)^2)\hbar\omega_y}{\hbar\omega_x} \right\} \right)^{-1}, \quad (2.29)$$

where β_2 is anharmonicity parameter of the subband energy, α_1 is proportional to the gate capacitance and converts the gate voltage V_{QPC} into energy. $V_{\text{QPC}}^0/\alpha_1$ defines the potential energy at the apex of a saddle point potential consisting of a parabolic barrier in current direction, x -axis in panel a, and a slightly anharmonic (i.e. almost parabolic) lateral confinement along the perpendicular y -axis. Table 2.3 contains the result of our calibration.

QPC	ω_y/ω_x	V_{QPC}^0 (V)	$\alpha\hbar\omega_x$ (V)	β_1	β_2
1	2.1 ± 0.1	-2.12	0.06	$-1E-5$	0.009
2	2.1 ± 0.1	-2.04	0.06	$-1E-5$	0.011

Table 2.3: Table of calibrated values of ω_y/ω_x , $\alpha\hbar\omega_x$, β_1 and β_2 for QPC1 and QPC2

Additional broadening can be caused by a source-drain voltage applied $V = -0.7\text{ mV}$ and temperature T . In Fig. 2.13 we plot comparison for the QPC conductance at higher temperature

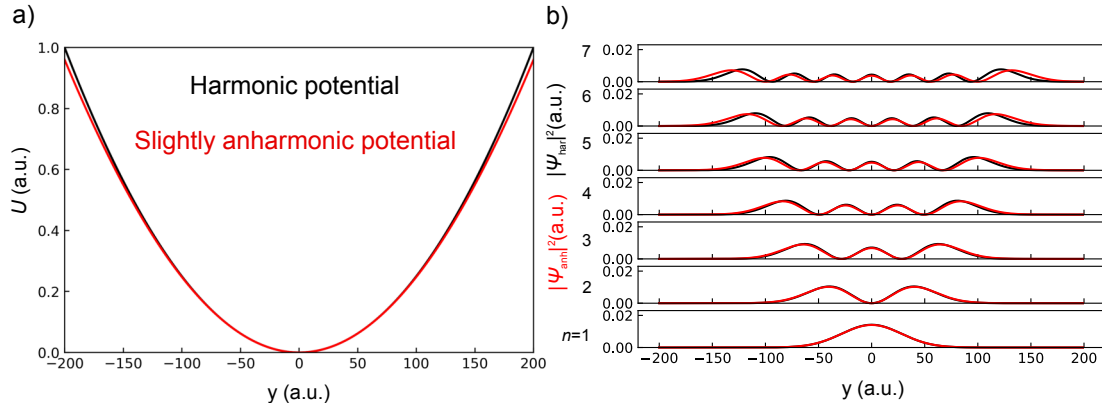


Figure 2.12: a) Oscillator potential profile with (red) and without (black) the anharmonic component. b) Calculated QPC eigenmodes for the harmonic (black) and slightly anharmonic potential (red).

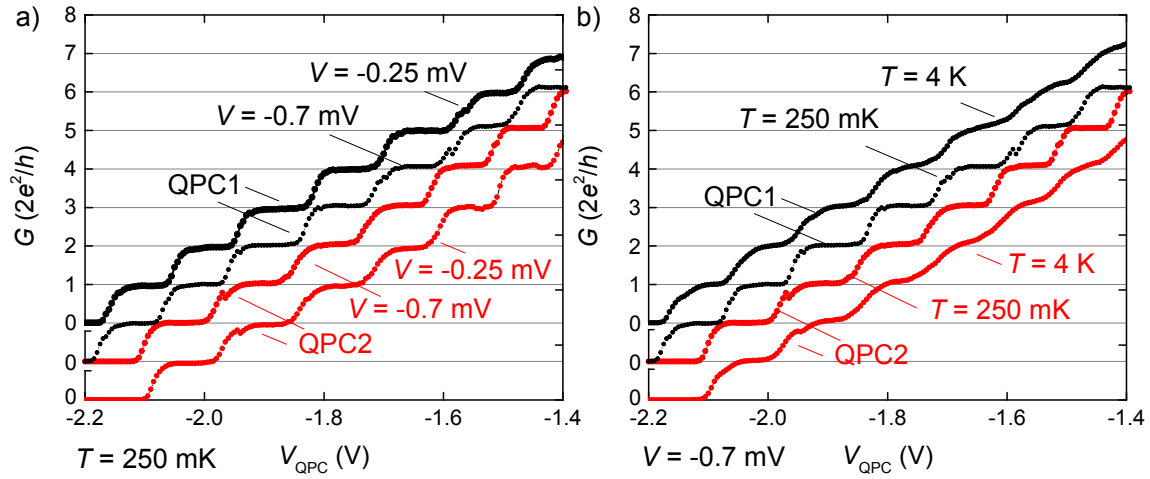


Figure 2.13: a) Measured conductance $G = I/V$ of a single QPC (QPC1 in black colour and QPC2 in red colour) as a function of QPC gate voltage V_{QPC} at two source-drain voltages $V = -0.25$ mV (vertically shifted) and $V = -0.7$ mV. Conductance plateaus are indicated with horizontal lines at integers of $2e^2/h$. b) Measured conductance $G = I/V$ of a single QPC (QPC1 in black colour and QPC2 in red colour) as a function of QPC gate voltage V_{QPC} at two temperatures $T = 250$ mK and $T = 4$ K (vertically shifted).

$T = 4$ K and at smaller source-drain bias $V = -0.3$ mV. QPC Conductance steps are strongly broadened by the temperature and almost don't change their width by applying different source-drain voltage. We can therefore deduce that we can neglect temperature of source-drain voltage broadening for $T = 250$ mK and $|V| < 0.7$ mV for the determination of ω_y/ω_x , $\alpha\hbar\omega_x$, β_1 and β_2 values.

Now we characterize the system of two QPCs in series with the experimental setup shown in Fig. 2.14. QPCs are formed by applying gate voltages V_{QPC1} and V_{QPC2} . The electrostatic lens gate

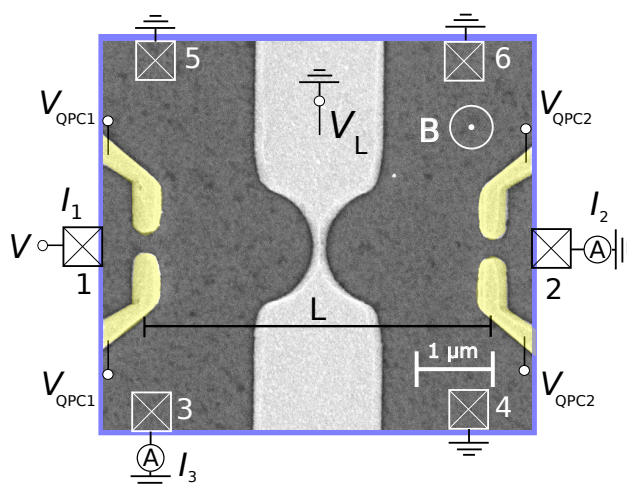


Figure 2.14: Scanning electron microscope image of the sample; the dark grey area contains 2DES. Five Ti/Au gates (a light grey area) are used to define QPC1 and QPC2 and a central lens-shaped gate respectively. We apply voltage V behind QPC1 and measure current I_2 behind QPC2. Four ohmic contacts in the middle of the structure are grounded.

remains grounded to minimize its influence on the measurements presented in this section. Four grounded Ohmic side contacts serve as drains for carries, which are scattered between the QPCs and diffuse to the sides. Applying a small dc voltage $V = -1$ mV across QPC1 (emitter) we record both sides drain I_3 and detector current I_2 flowing through the other unbiased QPC2 (detector). Previous experimental studies of ballistic transport through two opposite point contacts (with conductances G_1 and G_2) were carried out by Wharam et al. [77] and Beton et al. [98, 99]. They discovered that the serial resistance of two QPCs is considerably less than the ohmic sum of the two individual QPC resistances. Subsequent experiments [100] attributed this result to the collimation of the electrons injected by a point contact that enhances the direct transmission probability through the opposite point contact [101]. Two QPCs in series were also investigated for various designs, for example with staggered QPCs [102, 103], for the transition from Ohmic to ballistic adiabatic transport [104] and in the Quantum Hall regime [105]. Recently two QPCs in series in the ballistic regime were used to build multi-valued logic devices [106, 107].

The conductance of the two coupled QPCs G , calculated by Beenakker [108], can be expressed as $G = \max(G_1, G_2)$. In the calculation (expanded by Takagaki et al. [109]) and in the previous two-terminal experiments by Wharam et al. [77, 98, 99] the current I flew only between two QPCs while the additional contacts in between the QPCs were used as voltage probes with zero current through them. To exclude unwanted charge build-up in the area between the QPCs in our experiment we keep the central region grounded. We also designed our QPC gates such that scattered electrons tend to diffuse into the grounded side contacts. Such QPC design reduces the contribution of multiple scattered carriers to the measured detector current. First we discuss the case of zero magnetic field $B = 0$. We perform a similar experiment as described by Shepard

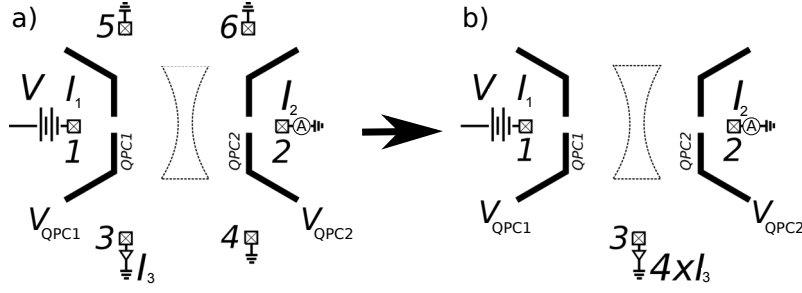


Figure 2.15: (a) The scheme of ballistic electron optics experiment with two QPCs as emitter and detector. We form both QPCs with gate voltages $V_{QPC1,2}$ and apply source-drain voltage V behind one QPC while measuring current I behind the other QPC. We also measure current I_3 through one of the side drain contacts. Four side ohmic contacts in the middle of the structure are grounded. (b) Reduced scheme by assuming all side drain contact resistance R to be the same.

et al. [110, 111]. Following Landauer-Büttiker formalism, the incident electron enters from terminal 1 and is scattered into the one of the six terminals. We assume all side drain contacts to have equal resistance of 250 Ohm, taken into account that we produced all the contacts in one step and used the same design for every contact. Next we reduce the scheme from 6 to 3 terminals by combining all side contacts in one for simplicity of discussion. We illustrate this procedure in Fig. 2.15. Transmission from QPC1 to QPC2 can be determined from Landauer-Büttiker formula (2.4)

$$\frac{h}{2e} \begin{pmatrix} I_1 \\ I_2 \\ I_3 \end{pmatrix} = \begin{pmatrix} T_{11} & T_{21} & T_{31} \\ T_{12} & T_{22} & T_{32} \\ T_{13} & T_{23} & T_{33} \end{pmatrix} \begin{pmatrix} \mu_1 \\ \mu_2 \\ \mu_3 \end{pmatrix} - N_1 \begin{pmatrix} \mu_1 \\ \mu_2 \\ \mu_3 \end{pmatrix}, \quad (2.30)$$

where N_1 is the number of occupied subbands in QPC1. Specifically, we apply a voltage V at reservoir 1, increasing its chemical potential to $\mu_1 = eV$, while $\mu_2 = \mu_3 = 0$. The sum of the currents I_1 , I_2 and I_3 obeys Kirchhoffs law: $I_1 + I_2 + I_3 = 0$. The elements of the first row $T_{i,j}$ of the transmission matrix are directly proportional to the measured currents:

$$T_{1,1} - N_1 = \frac{h}{2e} \frac{I_3}{\mu_1} \quad (2.31)$$

$$T_{2,1} = \frac{h}{2e} \frac{I_2}{\mu_1} \quad (2.32)$$

$$T_{3,1} = \frac{h}{2e} \frac{I_3}{\mu_1} \quad (2.33)$$

In the experiment we have to take into account the following corrections: (i) non-zero lead resistance (250 Ohm) that cause finite chemical potentials μ_2 and μ_3 between the QPCs, (ii) offset voltage from the input of our current amplifier (in the order of $10\mu V$) add to μ_2 and (iii) voltage drop at the emitter contact that influences μ_1 . The finite μ_2 and μ_3 values result in two contributions to I_2 : $\delta I_{21} \propto (\mu_2 - \mu_1)$ and $\delta I_{23} \propto (\mu_3 - \mu_2)$. We subtracted the unwanted contribution for all the measurement data presented in this section with details of calibrations shown in Appendix (A.2).

We present conductance $G = I_2/V$ through both QPCs measured as a function of V_{QPC1} and V_{QPC2} in Fig. 2.16. Most carriers are emitted at an aperture angle [112], consequently, miss the second QPC and contribute to I_3 . Nevertheless the conductance quantization is visible in

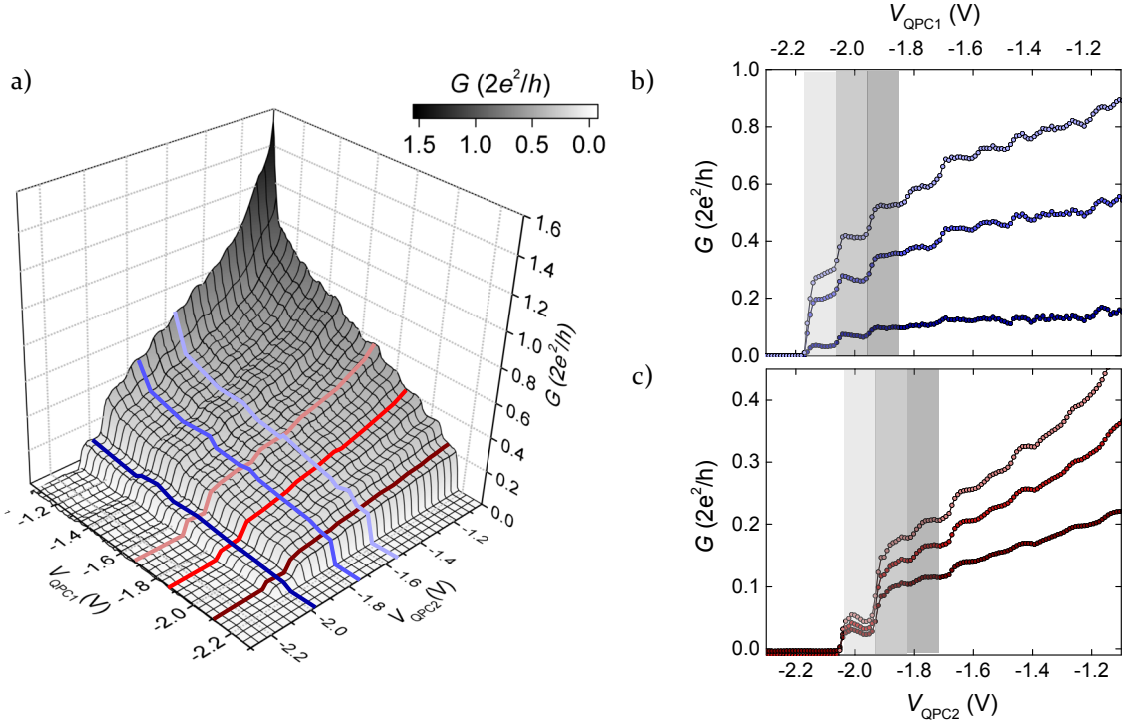


Figure 2.16: a) Conductance G measured for two QPCs in series as a function of V_{QPC1} and V_{QPC2} at $B = 0$. b) Conductance G measured through the device as a function of V_{QPC1} for three various V_{QPC2} marked with shades of blue colour at (a) at $B = 0$. c) Conductance G measured through the device as a function of V_{QPC2} for three various V_{QPC1} marked with shades of red colour at (a) at $B = 0$. Source-drain voltage is $V = -1$ mV at all the plots.

terms of conductance steps for both QPCs [as functions of V_{QPC1} and V_{QPC2} in Fig. 2.16(b) and Fig. 2.16(c)]. The combined transmission through both QPCs is weak and investigated two methods to modulate it: magnetic deflection and focusing with the electrostatic lens. These methods also reveal intrinsic information about the QPC potential profile and help us to probe the 2DES properties in the area between two QPCs.

2.5 Magnetic deflection experiment

In this section we modulate the transmission between two QPCs by applying an external magnetic field B perpendicular to the 2DES. In Fig. 2.17 we illustrate the performed experiment for electrons emitted at zero or a finite angle α . We deflect electrons emitted at a specific angle by the Lorentz force and guide them into the detector constriction, in analogy to bend resistance measurements [86, 113]. The magnetic field allows us to access the angle distribution of the emitted electrons that reflects the lateral structure of occupied modes of the QPC [105, 114]. This experiment is close in spirit to a so-called 'magnetic focusing' experiment [115]. Magnetic deflection of electrons in metals was investigated by Sharvin [116] as a method to measure the shape of the Fermi surface. It was also used to measure surface scattering [117] and electron-phonon interaction [118].

two QPCs by to the 2DES.

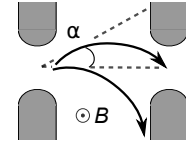


Figure 2.17: Sketch of a magnetic deflection experiment. Magnetic field B bends electron trajectories based on the Lorentz force and deflects them into the detector QPC constriction.

In Fig. 2.18 we present $G(B)$ for both QPCs tuned to identical conductance plateaus at $N_1 = N_2 = N$ from 1 to 7 for each line. We use the measurement setup presented in Fig. 2.14. As insets, we show the reduced scheme of the conductance diagram in Fig. 2.16(a,b). The reduced scheme contains positions of the conductance plateaus on V_{QPC1} with vertical black lines and on V_{QPC2} with horizontal black lines. Every curve on the main plot corresponds to the color filled conductance plateau. We show this scheme in some of the plots in the following sections, as a guide for the eyes. $G(B)$ contains information about the (nominally identical) mode structures of both QPCs and their mutual coupling. We find curves with increasing complexity as the conductance in-

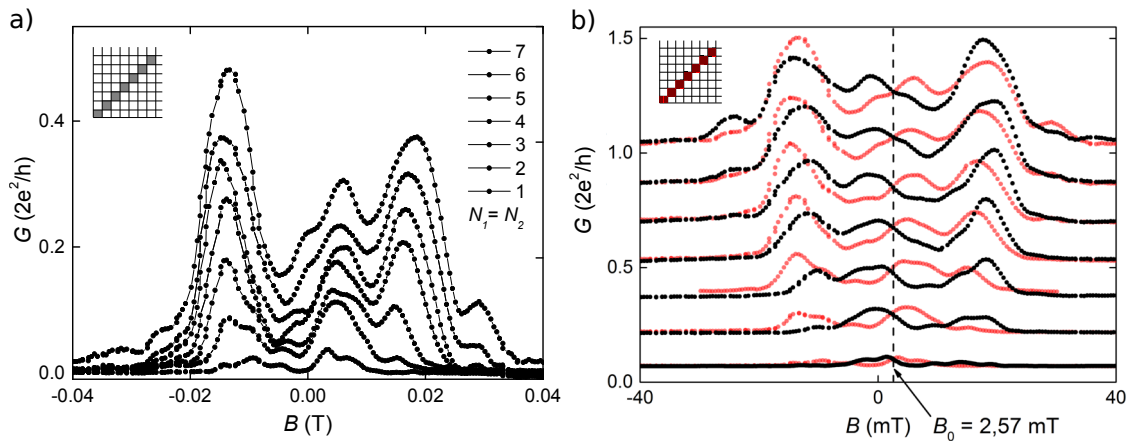


Figure 2.18: (a) Measured conductance G as a function of magnetic field B for different combinations of $G_{\text{QPC1}} = G_{\text{QPC2}} = 2e^2N/h$ starting with $N = 1$ from the bottom. (b) $G(B)$ for both QPCs operating at the same plateau for two configurations of emitter/detector. Red: QPC1 emitter. Black: QPC2 emitter. $V = -1$ mV

creases. In Fig. 2.18(b) we plot the curves of opposite current direction (red color is one direction, black is the other). To do so, we exchanged emitter and detector QPCs, by exchanging positions of the voltage source and the current amplifier. The pairs of curves at identical conductance are mirror symmetric around $B_0 = 2.57$ mT. The observed symmetry confirms the Casimir-Onsager relation discussed in Sec. (2.1.4) for Eq.(2.28). Slight deviations from this symmetry can be at-

tributed to magnetic defects and a residual magnetic field, which is independent of the external magnetic field B and tilted concerning it. Such a magnetic field can be caused by the materials used in the sample holder, for example, Ni. The offset B_0 reveals a residual magnetic field of 2.57 mT parallel to the external field B . We correct this small offset from the following plots.

2.5.1 Linear response regime

One possible problem was Joule heating of the electron system. A larger amplitude of the excitation voltage increases the signal to noise-ratio but also causes heating of electrons in 2DES. The heated 2DES leads to an additional build-up of a thermovoltage across the detector point contact, which is driven by the temperature difference between the heated 2DES in between emitter and detector and the still cold 2DES behind the detector [119]. Another encountered problems were energy broadening at a source-drain voltage of 5 mV corresponding to ≈ 60 K and possible non-linear effects due to excited states, or many-body interaction. To avoid these effects, the applied voltage V to the 2DES should be limited. In Fig. 2.19(a) we show I/V curves for the system of two

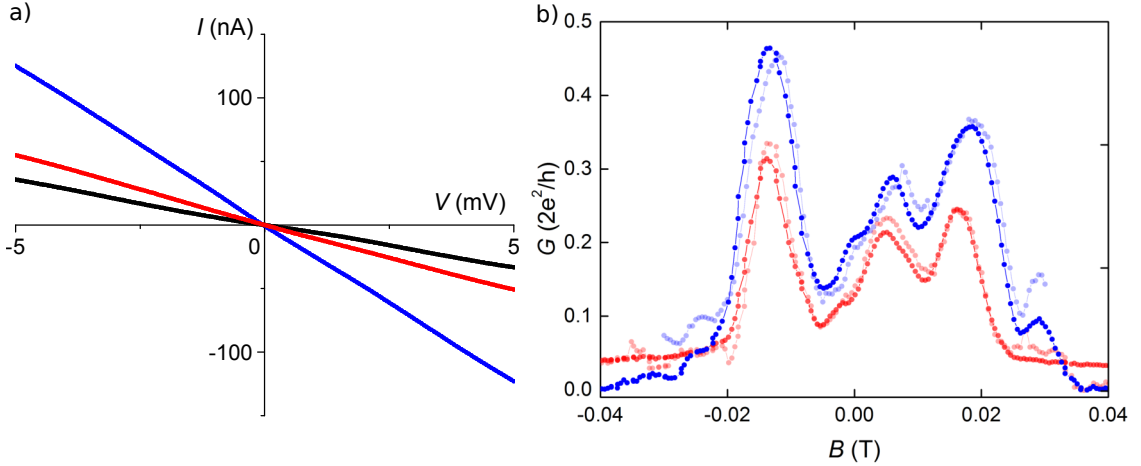


Figure 2.19: (a) Measured conductance G at $B = 2.57$ mT as a function of source-drain voltage V for different combinations of $G_{QPC1} = G_{QPC2} = 2e^2 N/h$, $N = 1$ marked with black colour, $N = 4$ marked with red colour, $N = 7$ marked with blue colour. (b) Measured conductance G as a function of external magnetic field B for both QPCs operating at the same conductance plateau $N = 4$ (marked with red colour) and $N = 7$ (marked with blue colour) for two source-drain voltages, $V = 0.1$ mV (transparent) and $V = 1$ mV (solid line). Both data from (a) and (b) was taken at $T = 250$ mK.

QPCs in series for various combinations of $G_{QPC1} = G_{QPC2} = 2e^2 N/h$, $N = 1, 2, 3, \dots$. We see that we work in the linear response regime up to $V = 5$ mV. In Fig. 2.19(b) we show that all the main local extreme points of the magnetic focusing pattern stay the same for two different voltages of 1 mV and 0.1 mV. Also, the range of the data is preserved. Therefore we found no evidence of heating effects up to $|V| = 1$ mV in our magnetic focusing experiments that is in correspondence too similar experiments in literature [119].

2.5.2 Theoretical model

To reproduce the measured data with simulations, we collaborate with Max Geier and Piet Brouwer from Freie Universität Berlin. They developed a semi-analytical model that assumes adiabatic evolution of the wavefunction in the QPCs and free propagation in the 2DES. The reader is advised to Appendix (A.4) for its full description. Here we present a summary focusing on essential steps of the calculations. The model depends on two fit parameters which model the confinement potential at the crossover points between adiabatic evolution in the QPCs and plane wave propagation in the 2DES. The first fit parameter describes the strength of the confinement at the crossover point and the second parameter specifies the position of the crossover points. The position parameter can be estimated from a distance between the QPCs. All reflections between the QPCs are neglected. In the model, we divide the system into three regions, as

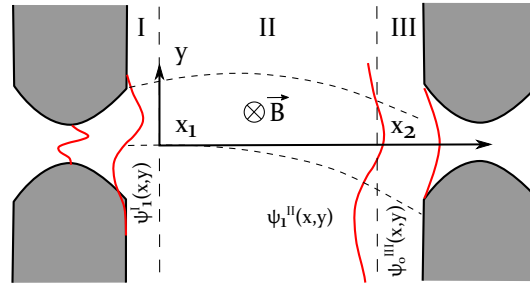


Figure 2.20: Sketch of the theoretical model that describes propagation of the electron wavefunction in three regions: region one describes the QPC1, region II is a free 2DES with perpendicular magnetic field, region III is a QPC2. Along x , the confinement changes adiabatically. Black solid lines illustrate the potential, red - eigenfunctions in the system. Black dashed lines is guide for the eyes to track the propagating wavefunction from QPC1 to QPC2. We chose zero of the coordinate system to be at the crossover point of the first QPC: $x_1 = 0$ and $y = 0$ at the line connected centers of two QPCs.

sketched in figure 2.20. Instead of solving for the eigenstates of the complete 2D model, we solve the equation of motion as the electron wave propagates in x -direction. To achieve this we treat x as a time parameter and keep y as space coordinate. This allows us to describe the system in terms of the eigenstates in y direction that evolve under the Hamiltonian $\hat{H}(x)$ as they propagate through the system.

In this setting we can define the notion of adiabatic evolution: The transitions between two eigenstates $|i\rangle(x)$ and $|j\rangle(x)$ of an evolving Hamiltonian $\hat{H}(x)$ are measured by a matrix element $\langle i | d\hat{H}/dx | j \rangle / [\varepsilon_j(x) - \varepsilon_i(x)]^2$, where $\varepsilon_i(x)$ is the energy of the eigenstate $|i\rangle(x)$. An eigenstate $|j\rangle(x)$ evolves adiabatically, if the change of the Hamiltonian is small on the scale of the energy spacing to all eigenstates of the evolving Hamiltonian, i.e. $\langle i | d\hat{H}/dx | j \rangle / [\varepsilon_j(x) - \varepsilon_i(x)]^2 \ll 1 \forall i \neq j$ and for all x during the evolution.

Region I and III describe the QPCs. The QPCs are modeled by a quadratic confinement potential in y -direction $U(x,y) \propto U_0(x) + m\omega_y(x)^2 y^2/2$ and an offset potential $U_0(x)$. The quadratic potential has Hermit polynomials defined in Sec. (2.1) as eigenstates. Inside the QPCs, the potential changes adiabatically and the strongest confinement $\max_x \omega_y(x)$ determines the experimentally observed spacing ω_y of the conductance steps in the $G(V_{\text{QPC}})$ curves of a single QPC measurement. Going further from the QPCs into the 2DES, the effect of the confining gates reduces,

and the confinement potential widens. We assume the potential to remain parabolic. At some point, the confinement will be too weak to sustain adiabaticity, and adjacent eigenstates will mix. Further away from the QPC, the confinement potential vanishes completely. Here we describe the wavefunction as a superposition of plane wave eigenstates. We model the crossover from adiabatic evolution of the eigenstates to the plane wave based description by an abrupt change of the potential from weak quadratic confinement $\omega_{y1}(x_1 - 0) = \omega_1$ to zero $\omega_{y1}(x_1 + 0) = 0$, which takes place at a position x_1 (crossover point) close to the first QPC. The same is valid for the crossover point x_2 and QPC2 as we treat both QPCs identical in our model and therefore x_1, x_2 and $\omega_{y1}(x_1) = \omega_{y2}(x_2) = \omega_y$. In the 2DES (region II), the electrons propagate freely and are subject to a weak perpendicular magnetic field. Since there are no applied potentials in this region and we assume that there are no impurities in the 2DES, the wave packets evolve undisturbed through the 2DES (there are no transitions between the eigenstates).

The Hermite polynomials broaden as they propagate in region II, but otherwise, preserve their shape in the absence of magnetic fields. Propagation of electron wavepackets is in analogy with the Gaussian beam model in optics. The magnetic field bends the paths of the wavepackets due to the Lorentz force and is included in our model in WKB approximation. The WKB approximation is acceptable for electrons which do not reverse their direction of propagation due to the magnetic field, which is the case as long as the cyclotron radius is larger than half the distance between the QPCs. For our 2DES parameters the cyclotron radius is $r_c = 4.6 \mu\text{m}$ for $B = 20 \text{ mT}$ where it is almost the same as distance between the two QPCs $L = 4.6 \mu\text{m}$. However, because the crossover point is shifted from the center of the QPC the validity condition is fulfilled as we show below.

2.5.2.1 Modematching: overlap integral

To determine the current through two QPCs in series in a perpendicular magnetic field we calculate the transmission T_{n_1, n_2} of an electron emitted from the n_1^{th} mode of the first QPC through the n_2^{th} mode of the second QPC. We start with the evolution of the wavefunction in region I (which is given by the solution of the harmonic oscillator in k-space) to the region II (where we find eigenstates in the free space with non-zero magnetic field using the WKB approximation). Special care will be taken at the crossover points x_1 and x_2 , where the eigenstates of the QPCs are mixed. Next, we find the wavefunction at a given position x_0 between the QPCs that will completely transmit through the second QPC by computing the time-reversed path of electrons emitted from the second QPC. The last step is calculation of the overlap O_{n_1, n_2} for the propagated wavefunction from the first QPC with the time-reversed wavefunction from the second QPC as $T_{n_1, n_2} = |O_{n_1, n_2}|^2$. Matching of both wavefunctions is done at any distance x_0 in region II between the two QPCs. By constructing the wavefunctions as a sum of plane waves in y direction we can compute the overlap directly in Fourier space. The overlap integral can be thus written in the form:

$$O_{n_1, n_2} = \int_{-\infty}^{\infty} dk'_y \frac{1}{\sqrt{\pi 2^{n_1-1} (n_1-1)! 2^{n_2-1} (n_2-1)!}} e^{-k_y'^2} H_{n_1-1}(k'_y) H_{n_2-1}(k'_y) \times \exp\left(-i \frac{\omega_y}{\omega_c} \int_{x'_1}^{x'_2} d\tilde{x} \sqrt{\epsilon - (\tilde{x} - k'_y)^2}\right). \quad (2.34)$$

Here $k'_y = \sqrt{\frac{\hbar}{m\omega_y}} k_y$ with k_y being the wavenumber in y direction, $x' = \sqrt{\frac{m\omega_c^2}{\hbar\omega_y}}$, $\omega_c = eB/m$ being the cyclotron frequency, $\epsilon = 2E/\hbar\omega$ is the electron energy. All the values are given in natu-

ral units and $H_n(k'_y)$ are Hermite polynomials. The factor $e^{-k'_y/2} H_{n_1-1}(k'_y)/\sqrt{2^{n_1-1}(n_1-1)!}\sqrt{\pi}$ describes the weights of the plane waves in the 2DES that are emitted from the n_1 harmonic oscillator eigenstate of the first QPC at the crossover point x_1 . Similarly, $e^{-k'_y/2} H_{n_2-1}(k'_y)/\sqrt{2^{n_2-1}(n_2-1)!}\sqrt{\pi}$ originates from the wavefunction matching at x_2 with the n_2 harmonic oscillator wavefunction of the second QPC. The factor $-i\frac{\omega_y}{\omega_c}\int_{x'_1}^{x'_2} d\tilde{x}\sqrt{\epsilon - (\tilde{x} - k'_y)^2}$ develops during the propagation between the crossover points x_1 and x_2 through the 2DES. Note that we assume the electron energy $\epsilon = E_F$ as we work near $T = 0$.

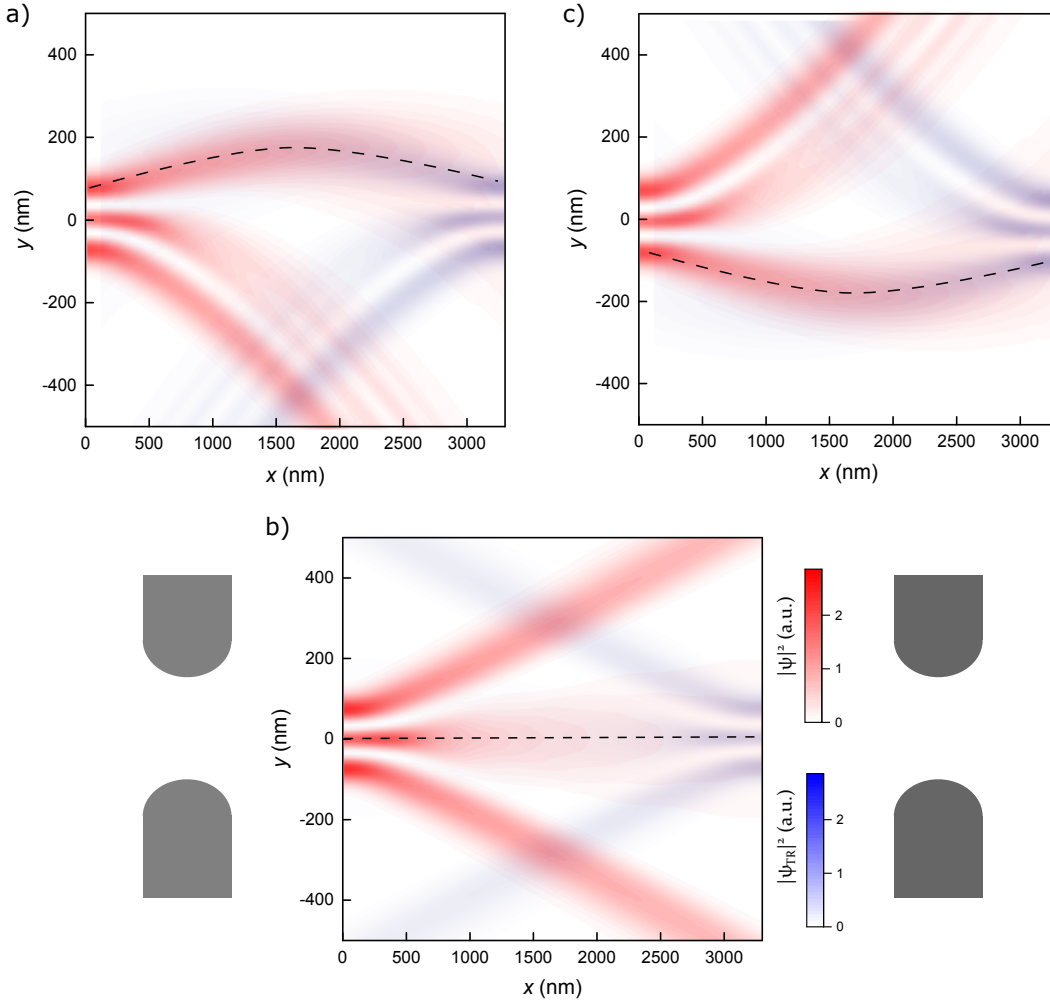


Figure 2.21: Direct (red) and time-reversed (blue) current density profile for an electron emitted in the $n_1 = 3$ level of the QPC at the crossover point set to $x_1 = 0$ for a) $B = 13$ mT b) $B = 0$ mT and c) $B = -15$ mT. The subband splitting $\omega_y(x_1) = 0.21\omega_{y0}$, where ω_{y0} is potential curvature in the center of the QPC. Dashed line indicates the overlapped red and blue area in three plots.

In Fig. 2.21 we illustrate the problem of modematching. Here we plot the current density profile emitted from QPC1 and time-reversed profile emitted from QPC2 for $n_1 = n_2 = 3$ at three different magnetic fields. The overlapped areas (marked with the dashed line) show current density regions contributing to the transmission through the both QPCs. Time-reversed electrons in the 2DES can be treated as holes (with the same effective mass m) in a system with broken time-reversal symmetry. Therefore current density matrix possess time-reversal symmetry for

$B = 0$ [see the Fig. 2.21(b)] and a symmetry in agreement with the Onsager relations for the case of finite magnetic field $T_{12}(B) = T_{21}(-B)$ [see the Fig. 2.21(a,c)] .

All electrons that enter the occupied N_2 modes of the second QPC will transmit, while all others get reflected. In our model we assume that reflected electrons will not reach one of the two QPCs again and neglect interference effects of reflecting waves. The overlap integral directly predicts the transmission T_{n_1, N_2} for an electron emitted from mode n_1 of the first QPC to pass through the second QPC with N_2 conducting modes. It is given by:

$$T_{n_1, N_2} = \sum_{n_2=0}^{N_2-1} T_{n_1, n_2} = \sum_{n_2=0}^{N_2-1} |O_{n_1, n_2}|^2. \quad (2.35)$$

Transmission through the two QPCs, when one QPC has N_1 and the second N_2 occupied modes can be finally calculated as

$$T_{N_1, N_2} = \sum_{n_1=0}^{N_1-1} \sum_{n_2=0}^{N_2-1} T_{n_1, n_2} \quad (2.36)$$

In summary, the main assumptions of the models are: i) we model the crossover between adiabatic evolution and plane wave propagation by an abrupt change of the confining potential and ii) we neglect any reflections between the QPCs.

2.5.3 Comparison between theory and experiment

For the detailed comparison between the experiment and theory we take differences ΔG between measured conductance G for the adjacent conductance plateaus. The corresponding raw data of the measured conductance G_{N_1, N_2} can be found in the Appendix (A.4). We used $\omega_1 = \omega_2 = 0.11\omega_y$ and $x_2 - x_1 = 3.3 \mu\text{m}$ in all following plots. The distance between the crossover points therefore fulfills the validity requirement for the WKB approximation ($x_2 - x_1 < r_c$) in our model. In Fig. 2.22(a) we plot the measured conductance differences $G_{N_1, N_2}(B) - G_{N_1-1, N_2-1}(B)$ for diagonal neighboured conductance plateaus $N_1 = N_2 = N$ in Fig. 2.22(b). Our model predicts

$$\Delta G = G_{N, N} - G_{N-1, N-1} = 2e^2/h(T_{N, N} + \sum_{n_1=1}^{N-1} T_{n_1, N} + \sum_{n=1}^{N-1} T_{N, n}) \quad (2.37)$$

which corresponds to the sum of the calculated transmission coefficients along a horizontal and a vertical line in Fig. 2.22(a) indicated by a corresponding background colour also used in in Fig. 2.22(b). Theory predicts that the number of local current maxima corresponds to the number of modes in the system. To resolve single mode transmission coefficients in figure 2.23, $G(B)$ is plotted for different emitter and detector configurations for the detector fixed at the 7th plateau. We expect to measure single mode transmission as

$$\Delta G = G_{N_1, N_2} - G_{N_1, N_2-1} = \frac{2e^2}{h} T_{N_1, N_2}, \quad N_1, N_2 = 1, 2, 3, \dots \quad (2.38)$$

Similarities with our measured data are apparent albeit the agreement is not perfect. Some of the deviations are more pronounced for odd modes compared to even, for instance, the region around $B = 0$. Total conductance is suppressed by a factor of 1.5 compared to the theoretical case, however, for some of the curves (especially $N_1 = 1, 7$ for any N_2) the expected theoretical conductance values are smaller than the measured conductance.

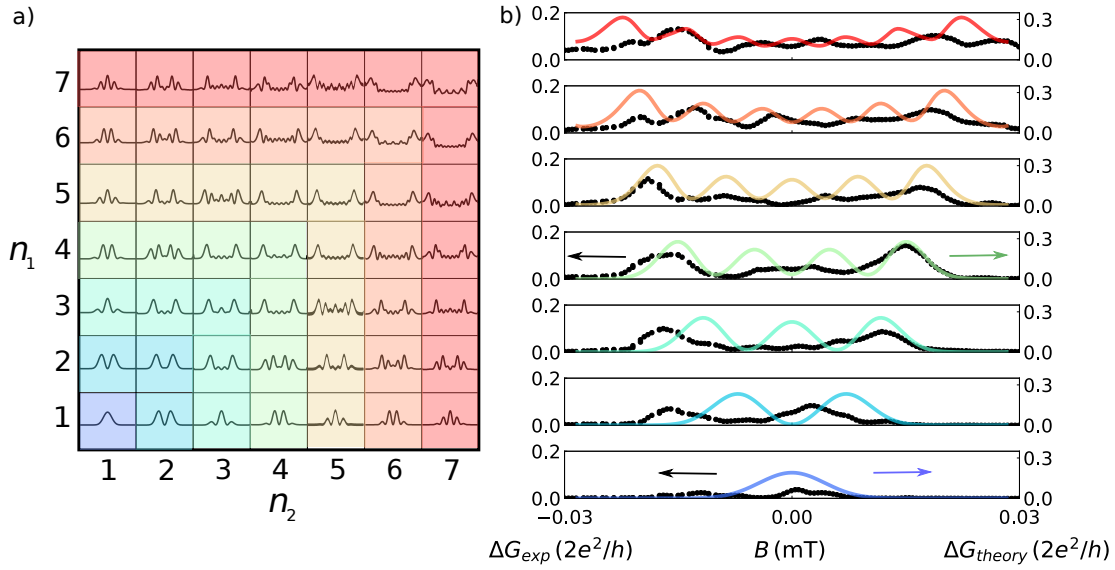


Figure 2.22: (a) Simulated $T_{N_1, N_2}(B)$ for various combinations of emitter QPC1 plateau N_1 and detector QPC2 plateau N_2 . Colour indicates conductance contributions for direct comparison with experiment in (b). (b) Measured $\Delta G(B)$ (with black dots) for equal emitter QPC1 plateau and detector QPC2 plateau $N_1 = N_2 = 1..7$ and simulated ΔG (with color solid lines) for equal emitter and detector plateau $N_1 = N_2$ from 1 to 7. Colour indicates $N = N_1 = N_2$, source-drain voltage is $V = -1$ mV.

2.5.4 Deviations between theoretical predictions and measurements

Several effects can explain deviations: first, the used WKB approximation for the solution of electron free propagation in the 2DES contains the numerical error that grows when increasing the range of magnetic field (for condition $L/2 > r_c$ not holding). Here we treat our model being precise in the region within $|B| < 20$ mT. Second, experimentally we calibrate ω_x and ω_y from the QPC conductance determined by the narrowest region of the confinement potential (in its center). The QPC potential profile far from the center cannot be calibrated using the transmission through the QPC and assumed to be perfectly parabolic in our model. However, the deviation of the real QPC potential shape from the perfect parabolic dependence can cause variations in the measured conductance through the system of 2 QPCs in series. Another existing model [88, 120] of the magnetic deflection experiment assumes hard-wall potential instead of parabolic confinement with different shape of the QPC eigenmodes [76]. Khatua et al. used the QPCs without well-defined conductance plateaus, in contrast, we observe well-defined quantization of the QPC conductance. Their model indicated the existence of strong conductance maxima for all configurations of the QPCs at $B = 0$ and a different shape of the $\Delta G(B)$ curve.

Other possible sources of deviations between theory and experiment are related to electron backscattering, disorder, magnetic defects and residual magnetic field. We will highlight the most important of these factors.

2.5.4.1 Classical and coherent scattering

Elastic electron scattering can be coherent or incoherent depending on scattering length compared to the coherence length of electrons in 2DES [10].

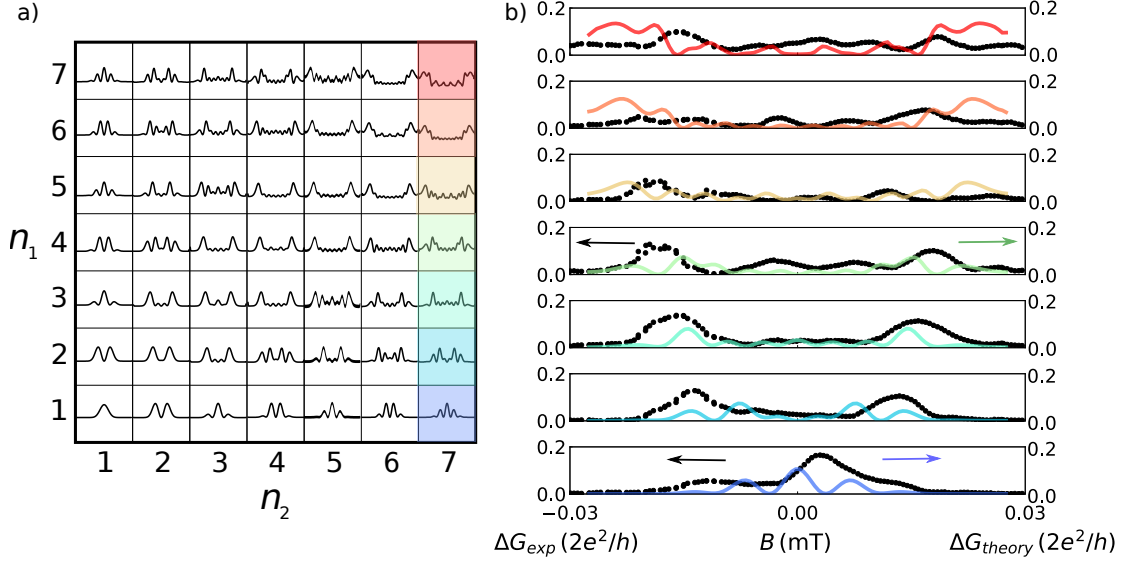


Figure 2.23: (a) Simulated $T_{N_1, N_2}(B)$ for various emitter QPC1 conductance plateaus $N_1 = 1..7$ at a fixed detector QPC2 conductance plateau $N_2 = 7$. Colour indicates conductance contributions for direct comparison with experiment in (b). (b) Measured $\Delta G(B)$ (with black dots) for various emitter QPC1 conductance plateaus $N_1 = 1..7$ at a fixed detector QPC2 conductance plateau $N_2 = 7$. Simulated ΔG (with colour solid lines) for various emitter QPC1 conductance plateaus $N_1 = 1..7$ at a fixed detector QPC2 conductance plateau $N_2 = 7$. Colour indicates $N_1 = 1..7$, source-drain voltage is $V = -1$ mV.

Classical (incoherent) scattering can be described regarding ballistic trajectories between scattering events, while coherent scattering includes interference effects such as standing waves. The latter gives rise to so-called geometry induced weak localization [121, 122]. In Fig. 2.24 we illustrate the coherent scattering. For the rounded QPC tips there exist time-reversed pairs of trajectories (marked with curved arrows in Fig. 2.24) each starting and ending at the same subband of the entrance QPC that can give rise to the coherent reflection. In our experiment, this decreases the zero-field conductance G below the classical value by an amount determined by the electron phase coherence length and temperature. The characteristic magnetic field at which the coherent effect is suppressed is given by a $B_\phi = \hbar e/2S$ where S is the enclosed area of a typical loop. We mark these areas with blue color in Fig. 2.24. For our design we calculate B_ϕ to be $B_\phi < 5$ mT. Our model neglects electron scattering off the ionized donors [123, 124]. The donor states are most probably related to:

- Shallow donor states associated with a normal lattice site and a binding energy of ≈ 7 meV ($d^0 \rightarrow d^+ + e$) [123]
- Deep donor levels with a binding energy of ≈ 160 meV, the negatively charged DX^- centers that arise from lattice distortions at or near the donor site. [123]

In Fig. 2.25 we illustrate scattering off the defects. Both classical (marked with a straight line in Fig. 2.25) and coherent backscattering (marked with a curved line in Fig. 2.25) off the defects contribute to the decrease of the measured conductance through the two QPCs in series. The used GaAs/AlGaAs wafer exploit spatial correlations between donors in different states d^+

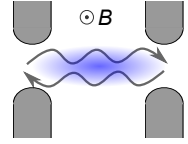


Figure 2.24: Sketch of electron coherent backscattering with QPCs marked as a gray area. Coherent modes, marked by the black lines, can survive within the blue area and are influenced by the external magnetic field B .

and DX^- [125, 126] to reach high mobilities of the 2DES. This creates variations of the carrier density regions of the 2DES [127]. Backscattering occurs from the spots defined by the distribution of donor atoms that is random (marked with red circles in Fig. 2.25) and thus results in inhomogeneous scattering potential in the 2DES [128]. Koonen et al. [123] have shown that the random distribution of donors can be treated as few strong defects using the electron transport in between of the two QPCs. The correlations between donors in different charge states can be altered externally by sample illumination or subsequent warming up and cooling the sample: both effects cause a dissociation of DX^- centers.

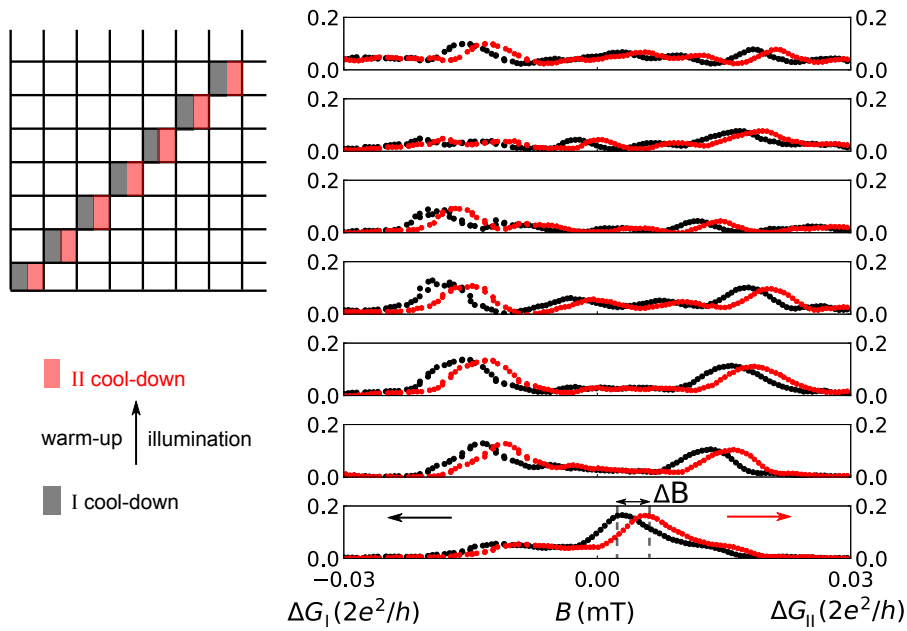


Figure 2.26: Measured $\Delta G(B)$ for changing emitter QPC2 plateau $N_2 = 1$ to $N_2 = 7$ and detector QPC1 fixed at the 7th plateau $N_2 = 7$. Black symbols ΔG_I : the sample was measured during the first cooldown at $V = -1$ mV. Red symbols ΔG_{II} : the sample was measured during the second cooldown at $V = -1$ mV. Top-left inset indicates corresponding QPC conductance plateaus.

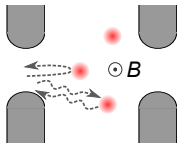


Figure 2.25: Scattering off the defects illustration. Electron trajectories are marked with solid lines. Scatterers are shown with circles.

In Fig. 2.26 we see the current I measured as a function of the magnetic field B for the first and the second cool-down. We illuminated the sample with daylight at room temperature in between the two cool-downs. We observe a shift of conductance curves by the $\Delta B = 3.6$ mT that corresponds to the difference between the residual correspondent field during the first and the second cool-down. Otherwise, all the features and the range of the conductance curve remains the same. A similar observation was also made in ballistic collimation experiments, where a stable scatterer was robust under subsequent illumination and cooldown [129]. Thus we can exclude the contribution of the universal conductance fluctuations related to electron scattering with single impurities, whose effect varies strongly from cooldown to cooldown [123].

2.5.5 Searching for defects in the 2DES

We can conclude the scatterer location by looking at the symmetry properties of the measured conductance curves. Here we discuss a heuristic algorithm for searching the position of defects in the 2DES based on analyzing the symmetry properties of the measured data. For the following discussion, we define the x-axis along the line connecting the centers of two QPCs.

First symmetry of the curves in Fig. 2.23 implies that the possible scatterer breaks the symmetry in B . This statement is illustrated in Fig. 2.27(a). Here we plot current density profiles (1,2,3,4,5,6) for the scatterer positioned on the x-axis (4) and with a slight shift (4,5) from it (with and without magnetic field B applied). We see that a defect located on the x-axis [plots 4 in Fig. 2.27(a)] will not break the symmetry in B while a defect slightly off the axis will do it. In our sample the defect on the x-axis is expected, thus other effects can contribute to the current suppression in the vicinity of $B = 0$. However we can't exclude the existence of few defects in the 2DES between both QPCs.

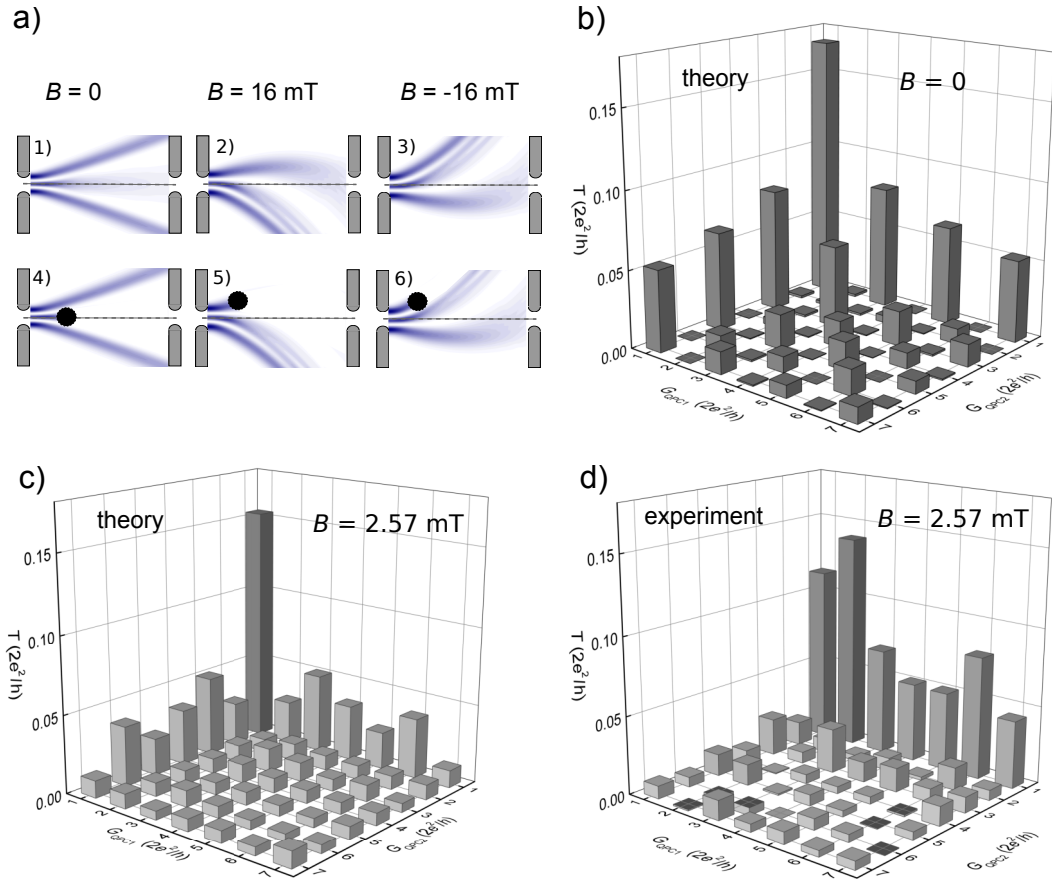


Figure 2.27: a) Current density profile with (4,6) and without (1,3) the defect (marked with black circle). Dashed line represents the x-axis and grey areas - QPCs (b) Calculated T_{n_1, n_2} for $n_1 = 1..7$ and $n_2 = 1..7$ at $B = 0$ mT. (c) Calculated T_{n_1, n_2} for $n_1 = 1..7$ and $n_2 = 1..7$ at $B = 2.57$ mT. (d) Measured T_{n_1, n_2} for $n_1 = 1..7$ and $n_2 = 1..7$ at $B = 2.57$ mT, $V = -1$ mV.

To gain additional information we look at the symmetry properties of the single-mode

transmission matrix T . Theoretically we can calculate every element of this matrix from the overlap integral in Eq. 2.35. T_{n_1, n_2} can be determined experimentally by measuring transmission for various configurations via reverting the formula (2.36) and solving it for single-mode elements T_{n_1, n_2} .

$$T_{n_1, n_2} = T_{N_1, N_2} - T_{N_1, N_2-1} - T_{N_1-1, N_2} + T_{N_1-1, N_2-1} \quad (2.39)$$

First we show the T matrix calculated from Eq. (2.36) at zero magnetic field $B = 0$ in Fig.2.27(b). This matrix has two characteristic properties: T_{n_1, n_2} is reflection symmetric ($T = T^T$) and all elements with odd $(n_1 + n_2)$ are suppressed compared to even $(n_1 + n_2)$. The influence of the magnetic field B is illustrated in Fig. 2.27(c). Here we show the calculated T matrix at a finite magnetic field of $B \neq 0 = 2.57 \text{ mT}$. The resulting matrix is still reflection symmetric ($T = T^T$), however there is no clear separation of even and odd elements any more. We can compare this matrix to the T measured at $B \neq 0 = 2.57 \text{ mT}$ in Fig.2.27(d). In contrast to the predictions the reflection symmetry is also broken in the measured T matrix. This difference can be possibly resolved when assuming a single hard-wall scatterer away from the x-axis, and the deviations at $B = 0$ can be additionally explained by the coherent/incoherent scattering.

2.6 Focusing with the electrostatic lens

In this section, we explore the method to increase transmission through the two distant QPCs using electrostatic focusing assuming a lens for electrons. Electrostatic focusing was studied before for ballistic electrons GaAs/AlGaAs by Stormer et al. [78] and Spector et al [79]. Both groups assumed geometrical optics to describe the effect of the lens on electron trajectories. In contrast here we show that our results are better described by Gaussian beam optics.

2.6.1 Geometrical optics of ballistic electrons

In the classical regime for ballistic electrons with $L < l_m$ and $L \gg l_\phi$ we do not observe interference and diffraction and can describe electronic excitations of the 2DES in analogy to geometric optics considering rays of light. Electron elastic scattering at defects is treated similarly to photon Mie scattering in optics [130]. We define geometrical optics for ballistic electrons using the Snell's law. We hereby assume a constant effective mass throughout the 2DES region and electrons propagating at the Fermi level. Their kinetic energy (the Fermi energy) is for a 2DES directly proportional to the electron density n_s , which can be locally controlled by applying voltages to surface gates. In Fig. 2.28 we show a boundary between an ungated region with carrier density $n_1 = mE_F(0)/(\pi\hbar^2)$ and a gated region $E_F(V) = E_F(0) - U(V)$ with $n_2 = m(E_F(V))/(\pi\hbar^2)$. As long as U is independent of y the y -component of the electron momentum is conserved and

$$k_1 \sin \theta_1 = k_2 \sin \theta_2 \quad k_{1,2} = \sqrt{2\pi n_{1,2}}, \quad (2.40)$$

where k_1 and k_2 are electron momenta. Snell's law of refraction for ballistic electrons propagating across the interface between two 2DES regions with electron densities n_1 and n_2 can thus be written as

$$\tilde{n} = \sin \theta_1 / \sin \theta_2 = (n_2/n_1)^{1/2} = (1 - U(V)/E_F(0))^{1/2}, \quad (2.41)$$

where we used the dispersion relation $E = \hbar^2 k^2 / 2m$ and defined \tilde{n} as refractive index for ballistic electrons. Electrostatic electron focusing can be achieved by engineering curved interfaces

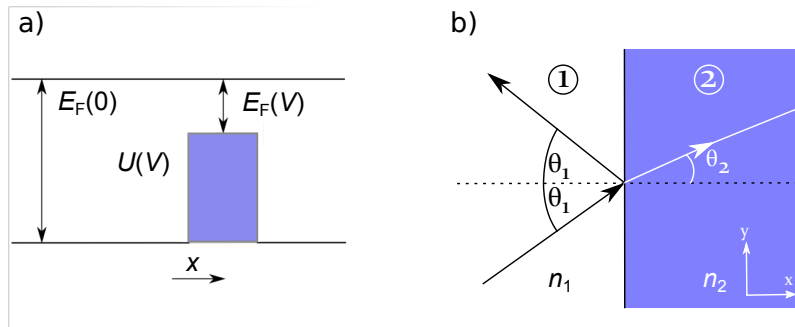


Figure 2.28: (a) Kinetic energies $E_F(V)$ of electrons at the Fermi edge in the ungated and gated (blue) 2DES. (b) Ballistic electron refraction and reflection at a boundary of two regions ungated (1) and gated (2) (blue) that have different electrostatic potentials.

between 2DES areas with carrier densities n_2 and n_1 , in analogy to optical lenses. We consider concave or convex lens-shaped surface gates [78]. As the refractive index of an electron lens \tilde{n}^L can be tuned to be either higher or lower than the refractive index of the undisturbed 2DES \tilde{n}^S , we can assume two different lens designs for focusing of electrons:

- positive voltage is applied to the lens gate, $\tilde{n}^S > \tilde{n}^L$ and the lens should have a biconvex shape similar to the shape of a glass lens used for focusing light.
- negative voltage is applied to the surface gate and $\tilde{n}^S < \tilde{n}^L$. Focusing is achieved for a biconcave lens shape.

When we completely deplete the gated region, it acts as a mirror for electrons. Focusing systems based on electron mirrors are also possible [131].

2.6.2 Energy calibration of the lens gate

To understand electron focusing it is necessary to determine the precise dependence of the electron density $n_s(V_L)$ beneath the lens on the gate voltage V_L . We do it by measuring the reflection of Landau levels from the lens gate as a function of V_L [132–134]. Landau levels have energies $E_i = \hbar\omega_c(i + 1/2)$, where $i = 1, 2, 3 \dots \nu/2$ is the factor of 2 related to the spin degeneracy and ν is the filling factor. In Fig. 2.29(a) we show the measurement setup including a SEM photo of

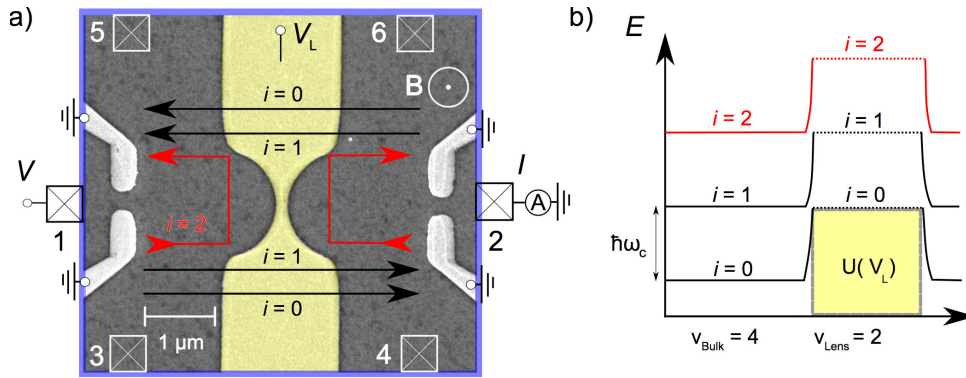


Figure 2.29: (a) Experimental setup for the lens gate calibration. QPC gates are grounded, while we apply V_L to the lens gate. Sketch of transmitted $i = 0, 1$ and reflected $i = 2$ Landau-levels at the lens gate, when the magnetic field B is applied out-of-plane of the sample. (b) Energy diagram of LL for undisturbed and lens potential regions of the 2DES. Depending on the lens voltage, Landau levels underneath the lens are lifted over the Fermi edge and subsequently reflected at the gate, thereby reducing ν_{lens} .

the sample that consists of two QPCs and a lens-shaped gate in the middle. We place the sample in the magnetic field B perpendicular to the sample surface and apply voltage V from one side of the sample divided by the lens gate (contact 1) while measuring the current at the other side (contact 2). Next we vary the lens voltage V_L at constant magnetic field such that B values corresponds to integer filling factors $\nu = n_s h / eB$ in the undisturbed 2DES. We determined the magnetic field values for integer filling factors by a quantum hall measurement. Details of this measurement can be found in the master thesis by Jaan Freudenfeld [135]. Following, we show the measured two-terminal resistance $R = V/I$ as a function of lens gate voltage V_L for integer filling factors ν in Fig.2.30.

For zero lens voltage, V_L the carrier density beneath the gate is the same as in the undisturbed parts of the sample, and the measured resistance R is maximal. Decreasing V_L we lower the carrier density and the filling factor in the gated region. To illustrate this effect we sketch Landau-levels at both gate and undisturbed regions in Fig. 2.29(b). As long as the number of

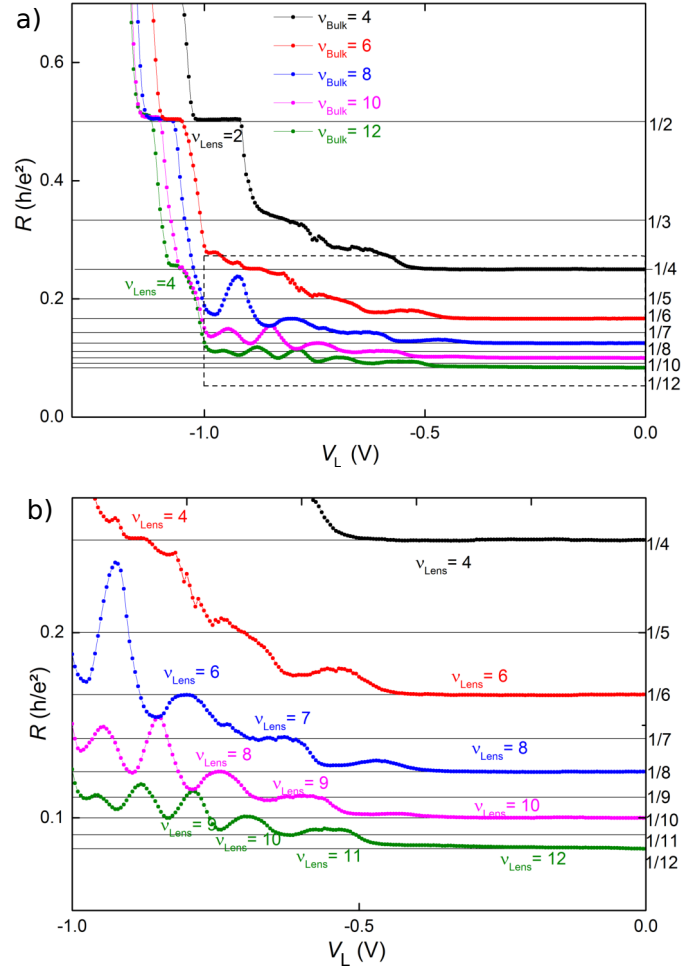


Figure 2.30: a) Two-terminal resistance R of the sample as a function of V_L at finite perpendicular magnetic field B and $V_{\text{QPC1}} = V_{\text{QPC2}} = 0$. b) R as a function of V_L at finite perpendicular magnetic field B . Close-up from the (2.30a) marked with dashed rectangle indicating the data points used for the calibration (with labels).

filled Landau levels in the gated region doesn't change, the transmission should stay constant, and a plateau in the resistance is expected. At the center of the plateau the relation

$$E_F - U(V_L) = i\hbar\omega_c = i\hbar eB/m \quad (2.42)$$

is valid. Here instead we get a resistance maximum instead of a resistance plateau expected from Eq. (2.42) due to quantum tunneling through the narrowest lens region in its center via remaining Landau-levels under the lens [136]. We can determine the values of $U(V_L)$ at the resistance maxima position, and the respective value for several bulk filling factors ν . The pinch-off curve for $B = 0$ yields one additional data point, the gate voltage corresponding to $U(V_L) = E_F(V_L = 0)$ at which current starts to flow across the barrier in a two-terminal setup. Horizontal solid lines in Fig. 2.30 correspond to integer filling factors. With the help of these lines, the tangents with the lens pinch offs and their corresponding V_L can be read off. The labeled points were used for the calibration performed according to equation 2.42.

Finally we show in Fig. 2.31(a) calibrated values of the barrier height $U(V_L)$ as a function

of the applied gate voltage V_L determined for different bulk filling factors. The result of the cali-

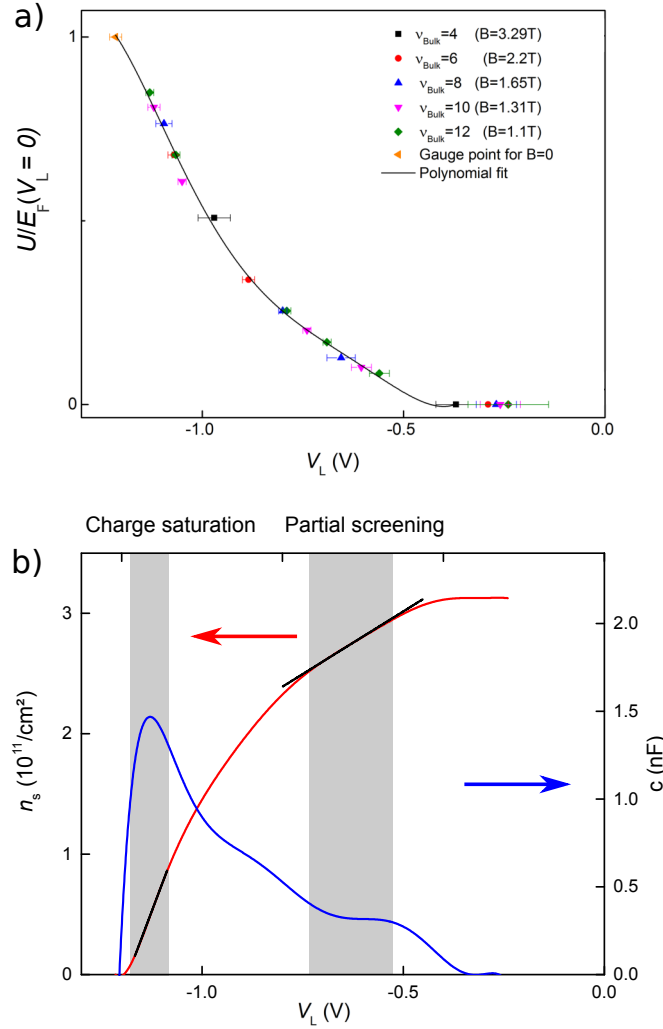


Figure 2.31: (a) Energy $U/E_F(V_L=0)$ as a function of V_L and 5th order polynomial fit of the points in Fig. 2.30. (b) Red curve shows the fit to the carrier density dependence n_s on the lens voltage V_L with two linear regimes (in black): charge saturation and charging of defects. The blue curve shows the differential capacitance c dependence on the lens gate voltage V_L

bration is a non-linear relation (in contrast to other studies [79]) between the voltage applied to the lens and the resulting barrier height. The corresponding carrier density n_s (and lens refractive index \tilde{n}^L) dependence on lens voltage V_L can be calculated from fitted $U(V_L)$ by using the Eq. (2.41). Main error source of the energy values is an error in the determination of correct V_L values. However inaccuracies in the effective mass m used for calculating the energy value and an error in the magnetic field could also contribute to errors. In figure 2.31(b), the carrier density dependence on the lens voltage V_L can be divided into three different regimes:

- $V_L > -0.4\text{V}$: the lens voltage has no influence on the carrier density beneath the lens gate
- $-0.9\text{V} < V_L < -0.4\text{V}$: carrier density depends linearly on lens voltage, charged defects partially screen the electrical field.

- $-1.3\text{ V} < V_L < -0.9\text{ V}$: the defects charge saturates giving rise to a larger slope up to the pinch-off regime

The observed behaviour can be explained by solving the Poisson equation in layers of GaAs/Al-GaAs heterostructure [137]:

$$Q = eV_L = (e^2 d / \epsilon_{\text{GaAs}}) n_s + K \quad (2.43)$$

where d is the thickness of the barrier layer between the gate and the 2DES being $d = 107\text{ nm}$ and ϵ_{GaAs} is the effective dielectric constant of the barrier being $\epsilon_{\text{GaAs}} = 12$ at $T = 4\text{ K}$ [138]. K represents the influence of fixed charges in the barrier layer that are frozen out at low temperatures $T < 20\text{ K}$ [139]. The differential capacitance per unit area $c/S = edn_s/dV_L$ can be then calculated from the slopes dn_s/dV_L of the fits in figure 2.31 as:

$$\frac{c}{S} = dQ/SdV_L = e \frac{dn_s}{dV_L} \quad \text{as} \quad \frac{dK}{dV_L} = 0. \quad (2.44)$$

An effective area of the lens gate can be estimated as $S = 1\mu\text{m}^2$ at the centre of the lens gate. Then the capacitance can be calculated for both regimes in figure 2.31(b) to $c_{\text{saturation}} = 1.48\text{ nF}$ and $c_{\text{screening}} = 0.38\text{ nF}$. The capacitance of a plane capacitor of the same size with distance between the gate and the 2DES being $d = 107\text{ nm}$ and the dielectric constant being $\epsilon_{\text{GaAs}} = 12$ at $T = 4\text{ K}$ [138] was found to be:

$$c = \epsilon_0 \epsilon_r \frac{S}{d} = 0.98\text{ nF} \quad (2.45)$$

which is in agreement with the experimentally obtained results.

2.6.3 Effect of the electrostatic lense on the ballistic electron transmission

The lens gate has a curved shape in its center with curvature radius R and minimum width d . Compared to previously studied layouts [78, 79] we decreased the distance from the QPC to the lens as well as the lens radius. We show the sample layout as well as the measurement setup in Fig. 2.32(a). We measure the two-terminal conductance $G = I_2/V$ in a three terminal configuration, where we combine four grounded side contacts into one. We also measure current I_3 at the side contact 3.

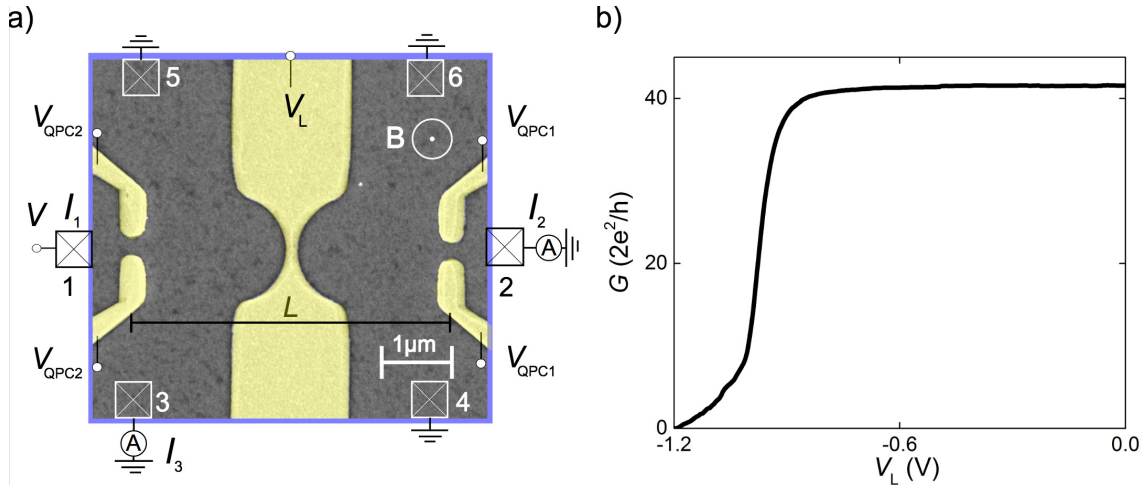


Figure 2.32: a) Sketch of the measurement setup and the SEM image of the sample; the dark grey area contains 2DES. The lens gate and QPC gates are false-colored with yellow color. b) Measured conductance G through the lens gate while both QPCs are grounded $V_{QPC1} = V_{QPC2} = 0$ as a function of V_L .

In Fig. 2.32(b) we first present measured current I through the lens when all QPC gates are grounded $V_{QPC1} = V_{QPC2} = 0$ while applying a source-drain voltage of $V = -1$ mV. We can see that the lens pinches-off for $V_L < -0.8$ V. Next, we probe the effect of the lens refraction on the transmission through both QPCs. We can define two operational regimes of the lens: reflected and transparent. Within the transparent regime ($0\text{ V} > V_L > -1.2\text{ V}$), electrons penetrate the lens gate, experience deflection on the lens/opened 2DES border due to the Snell's law (2.6.1) and reached the second QPC. In the reflected regime ($V_L < -1.2\text{ V}$) the lens acts like a mirror for electrons and formation of standing waves in between the lens gate and the QPC is possible (the regime is shown in Fig. 2.33(a,b)). The reflected regime will be discussed in details in the next chapter, and here we concentrate on the transparent operation mode.

Electrons that leave emitter QPC can either be captured by detector QPC (I_2) or go to the side drain contacts (for example contact 3 and contribute to I_3). In Fig. 2.33(a) we show the measured conductance G as a function of the lens voltage V_L for equal conductance plateaus for both QPCs. For all of them $G(V_L)$ increases as V_L is decreased and reaches a maximum around $V_L = V_f = -0.65\text{ V}$. The maximum always occurs around this voltage independently for various combinations of different QPC plateaus. Beyond this voltage we observe a rapid drop in conductance G down to zero as in Fig. 2.32(b) because of the lens barrier depletion that blocks electrons in the forward direction. In Fig. 2.33(b) we show that changing the direction of current break the time-reversal symmetry and the corresponding curves for the exchanged emitter and

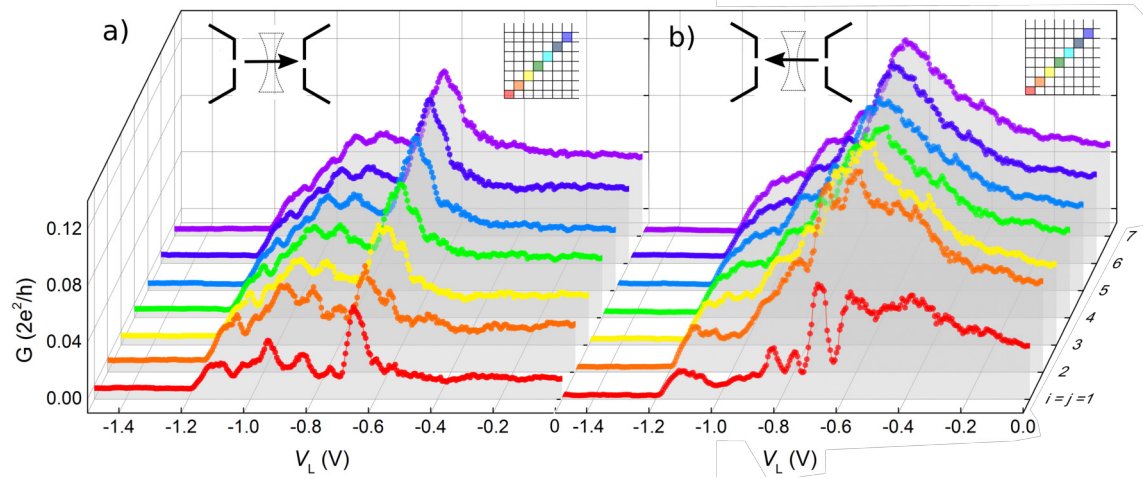


Figure 2.33: a) Measured conductance G for QPC1 used as an emitter and QPC2 for the detector, both are at $N_1 = N_2 = 1..7$ conductance plateaus (marked with color). b) Measured conductance G for QPC2 used as an emitter and QPC1 for the detector, both are at $N_1 = N_2 = 1..7$ conductance plateaus (marked with color). Sketches in the top-left corners indicate direction of current, and in the top-right - position on the QPC conductance map.

detector show different behavior. The discrepancy is related to the residual magnetic field $B = 2.57$ mT that is present while performing electrostatic focusing. The conductance peak can be explained by focusing of laterally diverged electrons emitted from one QPC into the second QPC. Thus we interpret the maximum around $V_L = V_f = -0.65$ V as the focusing peak.

2.6.4 Coherent ballistic electron optics

The general case of coherent non-interacting electrons can be treated assuming the quantum-classical analogy [7]. We study the similarity between the time-dependent Schrödinger equation in a region with spatially varying potential energy U for the photon wavefunction:

$$\frac{\hbar^2}{2m} \nabla^2 \psi + U \psi = 0, \quad (2.46)$$

and the Helmholtz equation

$$\nabla^2 A + k^2 A = 0, \quad (2.47)$$

Equations 2.46 and 2.47 have identical form besides ψ being the scalar photon wavefunction and A describing the electromagnetic TE polarization. Because of the analogous mathematical form between 2.46 and 2.47 it is possible to transfer the known results/techniques used to describe optical phenomena to explain the dynamics of ballistic electrons for $L \ll l_\phi$ [7].

Assuming QPC eigenfunctions being Gaussian-Hermite modes we can therefore use the formulas from the well-known problem in laser physics - gaussian beam propagation [140] illustrated in Fig. 2.34):

$$\psi_n(y, x) = \psi_0 H_n(\sqrt{2}y/w(x)) \frac{w_0}{w(x)} e^{-\frac{y^2}{w^2(x)}} e^{-ikx} e^{-i\frac{y^2}{2R(x)}} e^{-i\theta(x)}, \quad (2.48)$$

where $R(x) = x + \frac{x_R^2}{x}$ is the wavefront radius, $\theta(x) = \tan^{-1}(\frac{x}{x_R})$ is the Gouy phase and $w(x) = w_0(1 + (\frac{x}{x_R})^2)^{1/2}$ is the beam width. The H_n are Hermit polynomials in the 'physicists' form [81]. $x_R = \frac{\pi w_0^2}{\lambda_F}$ is the Rayleigh length, which is defined by the distance by which the width is $\sqrt{2}$ larger than the waist width. The latter is defined by the point where the intensity of the beam

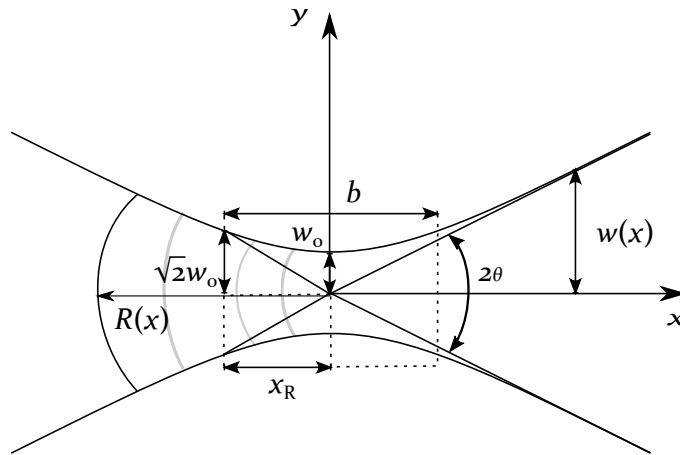


Figure 2.34: Gaussian beam width $w(x)$ as a function of the distance x along the beam.

has dropped to $1/e^2$ of its maximum. As can be seen from Eq. (2.48) the beam has a Gaussian intensity profile in the transverse direction for $n = 0$

$$I(x, y) = \psi \psi^* = \frac{w(x)^2}{w(0)^2} e^{-\frac{2y^2}{w(x)^2}} \quad (2.49)$$

and the minimum beam waist is attained in the focus at $y = 0$. The divergence of the beam is defined as the far-field angle

$$\theta = \lim_{x \rightarrow \infty} \arctan \frac{w(x)}{x} \simeq \frac{\lambda}{w_0 \pi}. \quad (2.50)$$

The more collimated the beam (smaller w_0) the larger is the divergence θ . The distance $b = 2x_R$ between the two points $x = \pm x_R$ is called the confocal parameter or depth of focus of the beam. Let us assume focusing of a Gaussian beam using a lens with the focal length f (see Fig. 2.35). The image size and position can be found from the analogue of the lens equation attributed to Gaussian beam optics derived by Self [141, 142]:

$$\frac{1}{s + (x_R^2)/(s - f)} + \frac{1}{s'} = \frac{1}{f}, \quad (2.51)$$

where s is distance from the object to the lens, s' is the distance from the image to the lens. Compared to geometrical optics there is a Gaussian focal shift [141]. Magnification of the lens is defined as

$$m = w'/w_0 = \frac{1}{\sqrt{(1 - s/f)^2 + (x_R/f)^2}}. \quad (2.52)$$

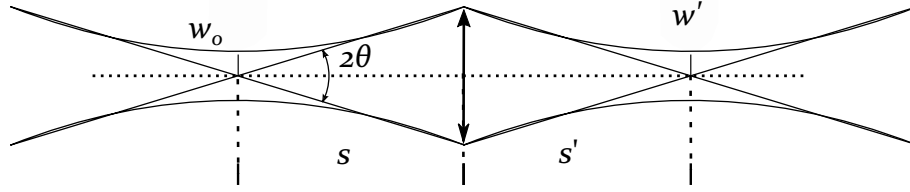


Figure 2.35: Geometry of the imaging of a Gaussian beam by a lens shown for the case of a positive lens and real object and image waists.

2.6.5 Geometrical optics and Gaussian beam model

Next, we compare the focal length for a Gaussian beam with the prediction of ray-optics. A ray-optics model treats electrons as particles moving along straight trajectories unless redirected by the lens [78]. The corresponding imaging equation yields:

$$l = \frac{2r}{1 - n(V_L)} + d \quad (2.53)$$

For ray optics the focal length of a concave lens can be written as:

$$f_l(V_L) = \frac{r}{2(1 - n(V_L))} + d, \quad (2.54)$$

where r is the lens radius and d is the lens width.

The Gaussian-Hermit-like mode profiles discussed before suggest to also assume the Gaussian beam model [141]. An illustration of the beam propagation for the exemplary $n = 3$ mode in our system with and without the lens voltage at zero magnetic field can be found in figure 2.36(a,b). These current density profiles were calculated assuming the same model as was discussed in Sec. (2.5.2). Considering the propagation of a Gaussian electron beam through a lens gives rise to a shift of the focal point compared to the geometrical optics case [141]:

$$f_l = f_0 + \frac{x_R^2(w_0)}{l}, \quad (2.55)$$

The beam waist (for the first mode) $w_0 = 250$ nm exceeds the lithographically defined constric-

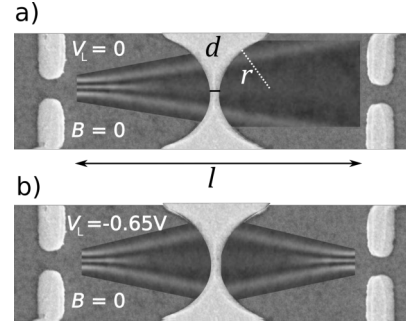


Figure 2.36: Hermit-Gaussian mode propagation between two QPCs with (b) and without lens (a) at zero magnetic field $B = 0$ calculated for the third mode.

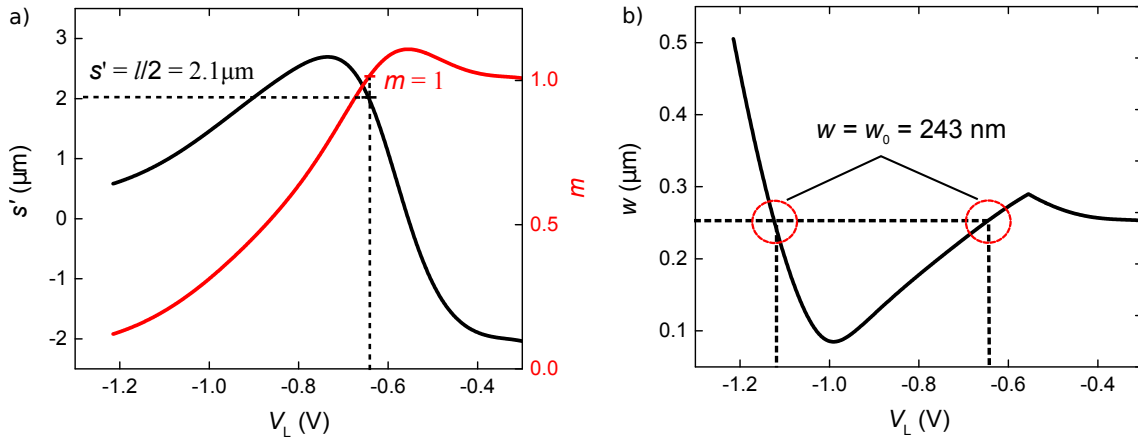


Figure 2.37: (a) Beam waist (image) position s' (black) and its corresponding magnification m (red) as a function of V_L . Focusing with $m = 1$ and $s' = l/2$ is marked with horizontal and vertical dashed lines. (b) Beam width w at the detector position as a function of V_L . Both focal points are marked with red circles.

tion between the two QPC gates because of the flaring effect described previously in Sec. (2.1.2). The expressions for the refractive index (2.41) and its calibration as well as the lens focal length including the Gaussian correction term (2.55) allow us to study beam parameters such as the

(image) waist position s' and the magnification m (ratio of image waist to object waist) as a function of V_L . These quantities are shown in figure 2.37(a): For V_L close to 0 ($n \simeq 1$) we find $s' < 0$ corresponding to a virtual image with the object size, $m = 1$ (that is to say the object itself at a negative distance measured from the lens). At $V_L = -0.55\text{V}$ we have $s' = 0$ and a slightly magnified ($m = 1.1$) image is situated directly on the lens itself. Before at more negative V_L we obtain a real image with growing distance from the lens at decreasing magnification. At the focusing voltage $V_L = -0.65\text{V}$ an image of the same size as the waist at the emitter QPC is obtained at the position of the detector QPC as sketched in figure 2.37(b). A special property of Gaussian beams is the fact that there is a (finite) maximum image waist position unlike for geometrical optics where a pole at the transition from virtual to real image corresponds to a diverging image distance.

2.6.6 Comparison between theory and experiment

For a detailed comparison, we plot in Fig. 2.38(a) previously calibrated lens refractive index with one of the focusing curves at $B = 0$. For our lens geometry, the geometrical optics model predicts electrostatic focusing of ray-like moving electrons at $\tilde{n} = 0.66$ corresponding to $V_L = -1.01\text{V}$ [see left arrow in Fig. 2.38(a)]. In terms of lens focal length f_l , the symmetry between emitter and detector yields a focusing focal length $f_l = f_0 = l/4$. The experimental data in figure 2.38(a) however show focusing at $V_L = -0.65\text{V}$ or $\tilde{n} = 0.93$ respectively [right arrow in Fig. 2.38(a)]. Modelling of electrons in terms of ray optics is thus not in agreement with our experimental results. The focus point position depends on two parameters: distance between the emitter and

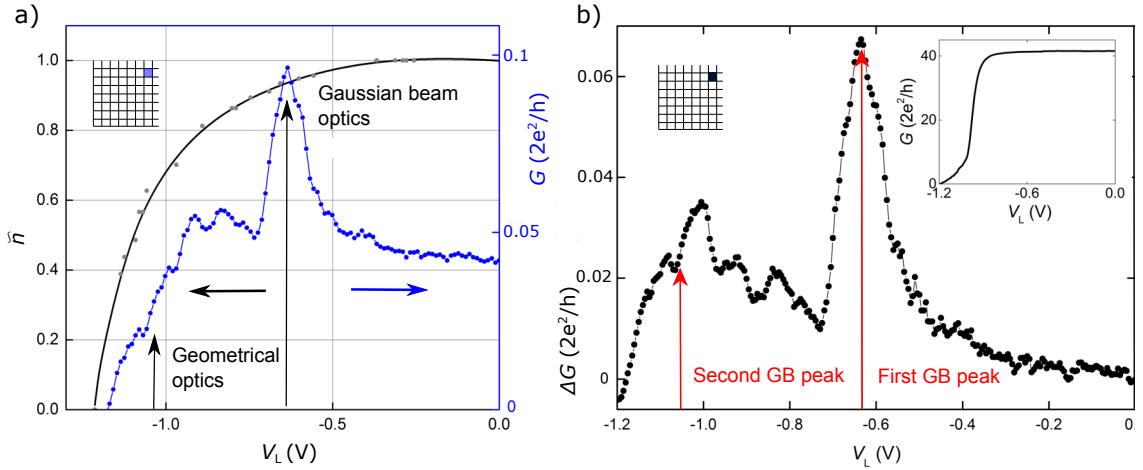


Figure 2.38: a) Grey dots: Lens refractive index calibration points obtained from the calibration and equation (2.41). Black: Spline fit. Blue: $I(V_L)$ for both QPCs set to the 7th conductance plateau and emitter QPC1. b) Measured conductance ΔG as a function of lens gate voltage V_L after subtraction of the baseline (defined in text). Both focusing peaks are clearly seen and marked with vertical arrows. Inset: Measured conductance G when both QPCs are grounded as a function of lens voltage V_L (the baseline). $V = -1\text{mV}$.

detector l and the waist width w_0 according to Eq. (2.55) and the calibration curve in Fig. 2.31. To be consistent with previous results we use the same l as the distance between crossover point in our model that is $x_2 - x_1 = 3.3\text{ }\mu\text{m}$. The crossover points correspond to the position of the beam waist in the model presented here. The beam waist w_0 however is experimentally not accessible. For this reason, we first treat w_0 as a fit parameter in equation 2.55. From the

experimentally found focusing voltage and the corresponding focusing refractive index in figure 2.38a, we obtain $w_0 = 250$ nm at a corresponding Rayleigh range $x_R = 4.4$ μm which is close to the distance between both QPC constrictions $l = 4.6$ μm and by 30% larger than the distance between crossover points $l = x_2 - x_1 = 3.3$ μm . Next we compared the best fitted value of $w_0 = 250$ nm to our experimental data and find good agreement with the beam width from our simulated current density profiles in previous sections.

Another effect that contributes to the decrease in coupling is depletion of the lens barrier. This effect hides a striking feature of the Gaussian beam, the second focal point [marked with red circles in Fig. 2.37(b)]. To revive second focal point we can subtract the normalized depletion curve, measured at grounded QPC gates, that is shown in the figure inset of 2.38(b). The result plotted in Fig. 2.38(b) is a second local maximum in the measured focusing curves, which appears very close to the expected position of the second focusing point at around -1.05 V. Enhancing of

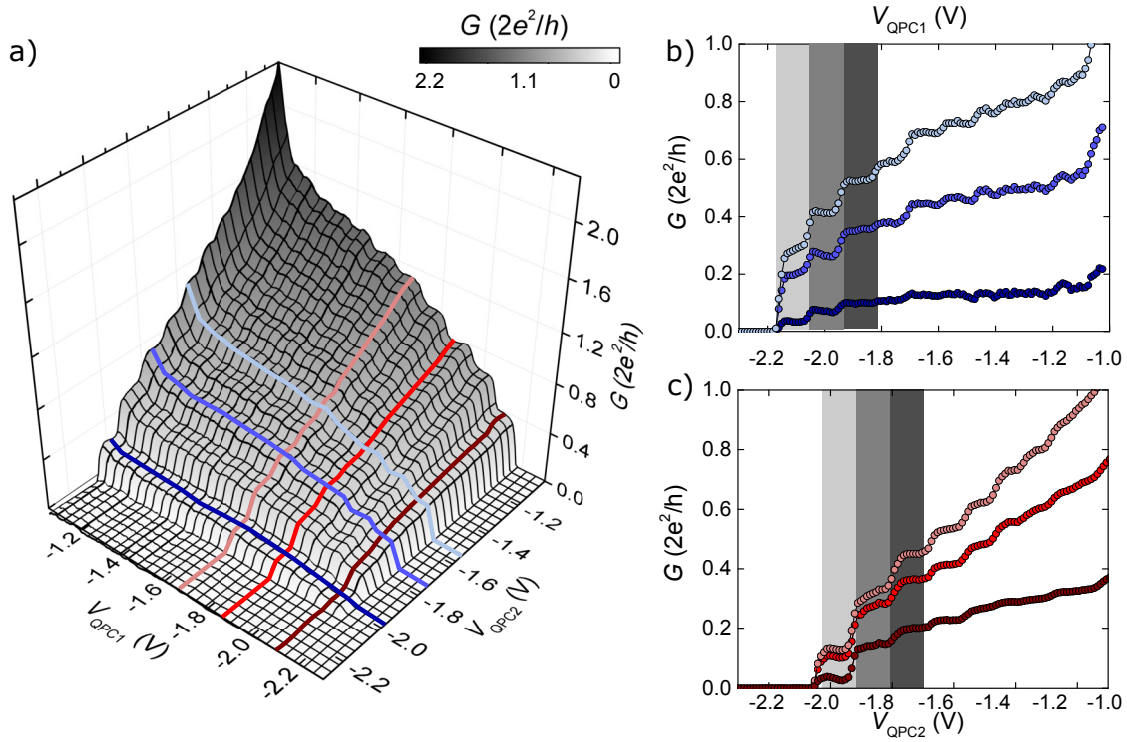


Figure 2.39: a) Conductance G measured for two QPCs in series as a function of V_{QPC1} and V_{QPC2} at $B = 0$, same as in Fig.(2.16) but for $V_L = V_f = -0.65$ V. b) Conductance G measured through the device as a function of V_{QPC1} for three various V_{QPC2} marked with shades of blue colour at (a) at $B = 0$ and $V_L = V_f = -0.65$ V. c) Conductance G measured through the device as a function of V_{QPC2} for three various V_{QPC1} marked with shades of red color at (a) at $B = 0$ and $V_L = V_f = -0.65$ V. Source-drain voltage is $V = -1$ mV at all the plots.

the QPC mode coupling can also be illustrated by plotting conductance G as a function of both V_{QPC1} and V_{QPC2} , as we show in figure 2.39 for the focal lens voltage at small magnetic field $B = 2.57$ mT. At $V_L = 0$ V, the lens optical density corresponds to that of the undisturbed 2DES, and diverging electrons give rise to a relatively low ballistic coupling. We observe weak conductance steps in measured $G(V_{QPC1}, V_{QPC1})$ as presented in Fig. 2.16. Tuning the lens to its focusing voltage $V_L = V_f = -0.65$ V we find the best contrast with well-defined steps over the entire pinch off the range, as illustrated in Fig. 2.39. In this case, ballistic coupling between both QPCs

is maximized. Beyond the focusing voltage, defocusing and a finite reflection coefficient of the lens give rise to a deteriorated contrast and lower ballistic coupling again. The second focusing peak is suppressed due to the vicinity of the QPC depletion point and the 2D conductance map $G(V_{QPC1}, V_{QPC2})$ has weak steps as in Fig. 2.16 at $V_L = 0$

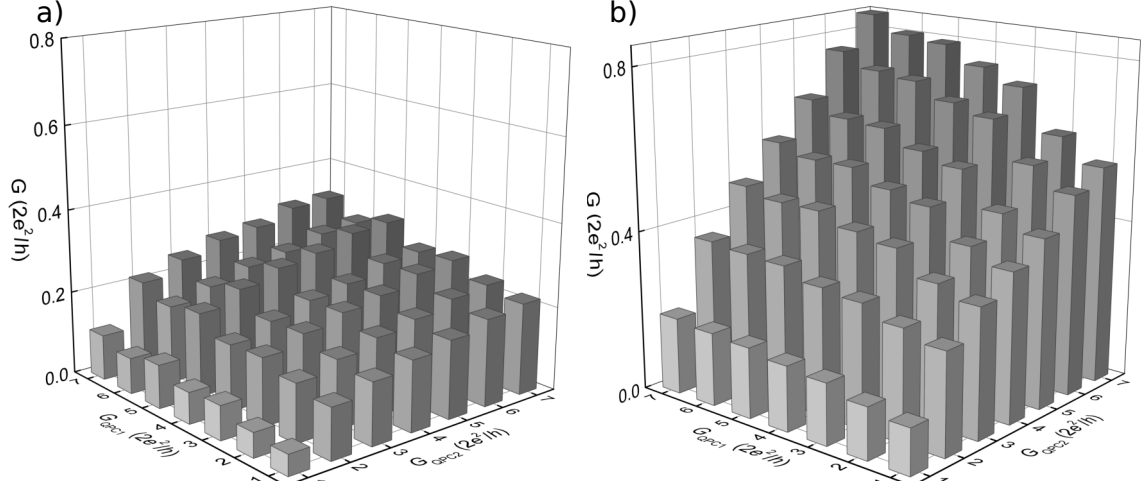


Figure 2.40: Measured conductance G averaged over every conductance plateau for both G_{QPC1}, G_{QPC2} at $B = 2.57$ mT as a function of different combinations of G_{QPC1}, G_{QPC2} at (a) $V_L = 0$ and (b) $V_L = V_f = -0.65$ V

To quantify the effect of the lens, we can compare measured conductance for all QPC mode combinations. In Fig. 2.40 we plot averaged conductance G conductance plateau G_{QPC1}, G_{QPC2} without the electrostatic lense (a) and when we apply focusing voltage to it (b). Here we average conductance over every 2D G_{QPC1}, G_{QPC2} conductance plateau. We detect almost two times amplification of the conductance G signal. We can also estimate the amplification and assume that the lens collimates the effective area of the wavefunction into the detector constriction. As a consequence conductance of the combined system, that is proportional to the square of the wavefunction profile, increases as more of the wavefunction part fits into the detector constriction. The beam width diverges by the factor of $\sqrt{2}$ at the distance of Rayleigh range. Our distance between the emitter and detector L is in the order of the Rayleigh range; naively we can expect enhancement of the signal G_f/G_0 to be at most twice ($G_f/G_0 \approx (w/w_0)^2$). In fact, the intensity of the Gaussian beam of electrons is not distributed uniformly over transversal direction, but in branches defined by extrema of Hermit polynomials. So the enhancing factor will tend to two only for the highest number conductance plateaus (in our case $N_i = 6, 7$). Disorder between the QPCs also suppresses the enhancement factor.

2.7 Combined electrostatic and magnetic focusing

An instructive method to probe the influence of the lens on the coupling between the QPCs is to combine the previously presented magnetic field measurements with electrostatic focusing experiment. To demonstrate this in Fig. 2.41(a) we present the detector conductance as function of B and the voltage applied to the lens gate V_L . In this example both QPCs are tuned to the

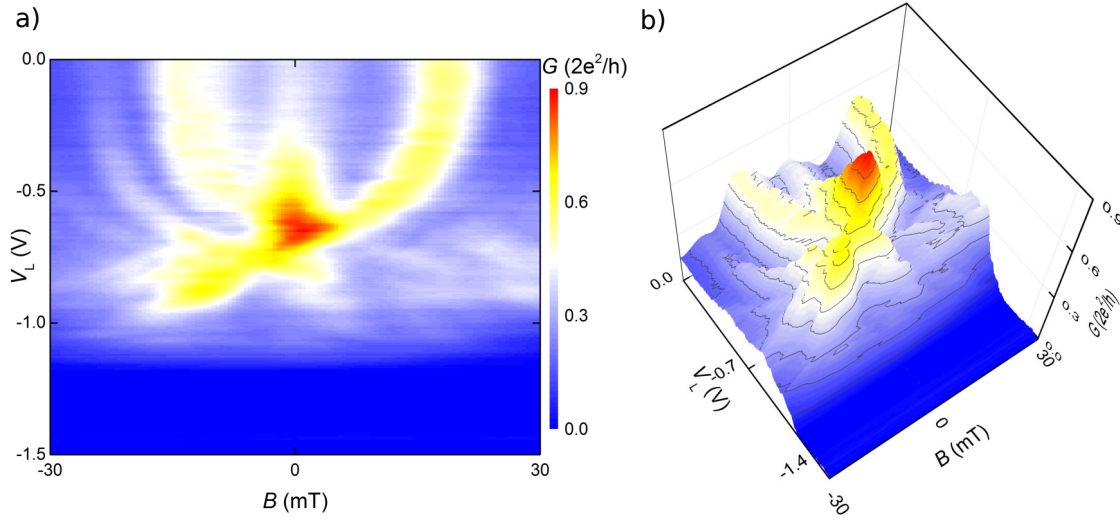


Figure 2.41: (a) Measured conductance G as a function of external magnetic field B and voltage applied to the lens V_L . QPC1 was used as emitter and QPC2 as detector, both tuned to the 7th plateau. (b) 3D profile of the conductance. Maximum value of conductance at $V_L = -0.65$ V and $B = 0$ mT.

7th plateau, hence the horizontal line $G(B)$ at $V_L = 0$ is identical with the uppermost curve in Fig. 2.18(a). As we decrease V_L all conductance maxima move towards smaller B until they merge at $V_L \simeq -0.65$ V. Here the conductance develops a pronounced maximum which even exceeds the sum of the individual maxima at $V_L = 0$. The conductance peak is a strong indication that at $V_L \simeq -0.65$ V our lens indeed focuses carriers between the two QPCs. At even more negative V_L the individual maxima reappear at finite B as now the lens is de-focused again. The measured focusing is not perfect as our lens has astigmatism caused by its imperfect shape. The role of the coherent electron modes is also discussed in the Appendix (A.2.3).

The last relevant argument for the Gaussian beam model of electrons is related to the angular distribution of electrons emitted from the QPC. Attributing the previously discussed $G(B)$ profile to the ray-optics model yields trajectories with emission angles α larger than the opening angle of the lens (solid blue line). Such branches cannot be captured by the lens for geometrical reasons. We however have evidence for the electrostatic focusing of these branches, indicating the observation of weakly diverging Hermite-Gaussian modes according to the Gaussian Beam model. We sketch another argument for using the Gaussian beam model for our measured data in the Fig. 2.42.

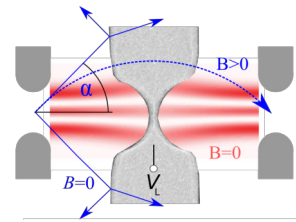


Figure 2.42: Sketch of the electron focusing experiment at finite B for both ray-optics (blue) and Gaussian beam model (red).

2.8 Conclusions

Within the second chapter we investigated the coupling between two distant QPCs via the usage of collimated ballistic electron beams. We presented electrostatic focusing of ballistic electrons emitted and detected by QPCs representing parabolic saddle point potentials. Our magnetic deflection experiments show indications that Hermite functions describe the angle distribution of electrons. We attribute the occurring deviations mainly to defect scattering. We also used an electrostatic lens between both QPCs to refocus the electron beams emitted from a QPC with and without an out-of-plane magnetic field. The lens can be adjusted to enhance the coupling between two QPCs without changing the lateral structure of the ballistic electron modes. Finally, we established a combination of magnetic electron deflection and electrostatic focusing as a new tool for precise manipulation of ballistic electrons. Our observations favor electron dynamics according to a Gaussian beam optics model based on Hermite functions rather than the frequently used plane electron wave model. To summarize we list all the main arguments for using the Gaussian Beam model for ballistic electrons:

- Indications of resolving lateral mode profile with magnetic focusing experiment: Possible deviations from theoretically predicted conductance profiles are caused by the classical/-coherent backscattering from defects and gates.
- Gaussian beam focal shift: the electrostatic focusing experiment result in a shifted position of focal point compared to the focal point in ray optics. The Gaussian Beam model for electron propagation by contrast explains this shift by contrast to ray optics.
- Manipulating electron branches that are inaccessible assuming ray optics for our lens gate design: the electron beam is weakly diverging and propagates according to the Gaussian Beam model.

Chapter 3

Coherent Coupling of an Open Ballistic Electron Resonator to a Quantum Point Contact

Coherent coupling between nanodevices is a key concept for future quantum information circuits. Coupling mechanisms include exchange interaction, extended fields or transport of massive particles. Here we explore the mode coupling between a simple nanostructure, a quantum point contact, and a standing electron wave confined in an open hemispherical resonator. We study linear response transport through the combined system to extract phase information of the quantum point contact modes. Measuring the temperature dependence of the visibility of resonator modes we determine the dephasing of the coupled system, which is dominated by energy broadening at $T < 1$ K. We demonstrate that a proper dephasing analysis is highly model dependent and requires detailed knowledge of the geometry of the mode structure of the coupled system.

3.1 Dephasing in an open 2DES

Phase coherence of ballistic electrons is essential for quantum applications and has been studied in a wide variety of quantum interference experiments in two-dimensional electron systems (2DES) of GaAs/AlGaAs heterostructures. Most fascinating experiments include double slit [143], Aharonov-Bohm [144, 145] or Mach-Zehnder interferometry [146], Fabry-Perot interferometry [147], scanning gate spectroscopy [112, 124, 148] and transport through extended cavities [149, 150], to name a few. However in most of experiments coherent effects can be suppressed due to several mechanisms:

- e-e scattering [151] with energy transfer in the order of $k_B T$. The electron-electron inelastic scattering time can be calculated by the formula [152]:

$$\frac{1}{\tau_{e-e}} \simeq \frac{E_F}{2\pi\hbar} \left(\frac{k_B T}{E_F} \right)^2 \left[1 + \ln(2) + \ln\left(\frac{Q_{TF}}{k_F} \right) - \ln\left(\frac{k_B T}{E_F} \right) \right], \quad (3.1)$$

where $Q_{TF} = m/\epsilon_0\epsilon_{GaAs}\hbar^2$ is the Thomas-Fermi screening vector ($Q_{TF} \simeq 1.9 \cdot 10^8 \text{ m}^{-1}$ in GaAs at cryogenic temperatures), k_F and E_F is the Fermi energy and wavevector accord-

ingly. Validity condition of the formula requires the applied source-drain voltage V to be within the range: $eV \ll k_B T \ll E_F$.

- e-e scattering with small energy transfer (Nyquist noise) [153]. These quasielastic e-e collisions are equivalent to the interaction of an electron with the fluctuating electromagnetic field produced by all the other electrons, i.e. dephasing by the equilibrium Nyquist noise [154]. The Nyquist dephasing rate is given by [155]:

$$\tau_N^{-1} = \frac{k_B T}{2\pi\hbar} \frac{\lambda_F}{l_m} \ln \frac{\pi l_m}{\lambda_F} \quad (3.2)$$

- energy broadening of the Fermi surface. This effect is caused by either finite temperature or finite source-drain voltage and for the first results in a loss of phase coherence after a time $\tau_T = \hbar/k_B T$. The thermal length can be calculated as $l_T = \sqrt{\frac{d_e \hbar}{k_B T}}$ (or $l_T = \hbar v_F/k_B T$ for the ballistic transport regime)
- electron-phonon interaction [156] for temperatures $T > 4\text{K}$. This dephasing time obeys $\tau_{ph} \propto T^{-2}$ dependence [154].

The total dephasing rate can be calculated by using the Matthiessen's rule [155]:

$$\tau_\phi^{-1} \approx \tau_{e-e}^{-1} + \tau_T^{-1} + \tau_N^{-1} + \tau_{ph}^{-1} \quad (3.3)$$

3.2 Combined system of a QPC and a cavity

Recently, the dynamics of ballistic electrons has been compared with that of classical light in the framework of so-called electron optics [157, 158]. While classical motion of electrons is often described in terms of simple ray optics [78, 79, 131], quantum phenomena based on phase coherence require an analogy to wave optics [76, 115, 159]. Here, we present transport measurements of a quantum point contact (QPC) coupled to a mesoscopic hemispherical open resonator (HOR) defined in the 2DES of a GaAs/AlGaAs heterostructure. While previous studies of such coupled systems were restricted to the first fundamental subband of the QPC [160, 161] our experiments cover the complete pinch-off curve of an almost parabolic QPC including seven one-dimensional modes. As we increase the resonator size, we observe the breakdown of well defined deterministic resonances which we interpret as the onset of chaotic behavior. In the deterministic regime, we model the dephasing with increasing temperature and thereby demonstrate the importance of considering the realistic mode structure of two-dimensional resonators.

We use the same electrical wiring and cryogenic techniques as in the previous chapter. The gate layout of our sample is shown in Fig. 3.1(a). Applying negative voltages V_1 and V_2 to the individual gates we locally deplete the 2DES 107 nm beneath the surface to define a QPC embedded in a HOR. In Fig. 3.1(b) we plot a pinch-off curve of our QPC measured at $T = 250\text{ mK}$ without HOR, $V_2 = 0$. It shows smooth and well established conductance plateaus at integer multiples of $G_Q = 2e^2/h$ as a function of gate voltage V_1 . The red line presents a theoretical expectation applying Büttiker's approach for the QPC transmission from Eq. (2.29) with the anharmonicity parameter $\beta_2 = 0.007$. Table 3.1 contains the result of the QPC calibration.

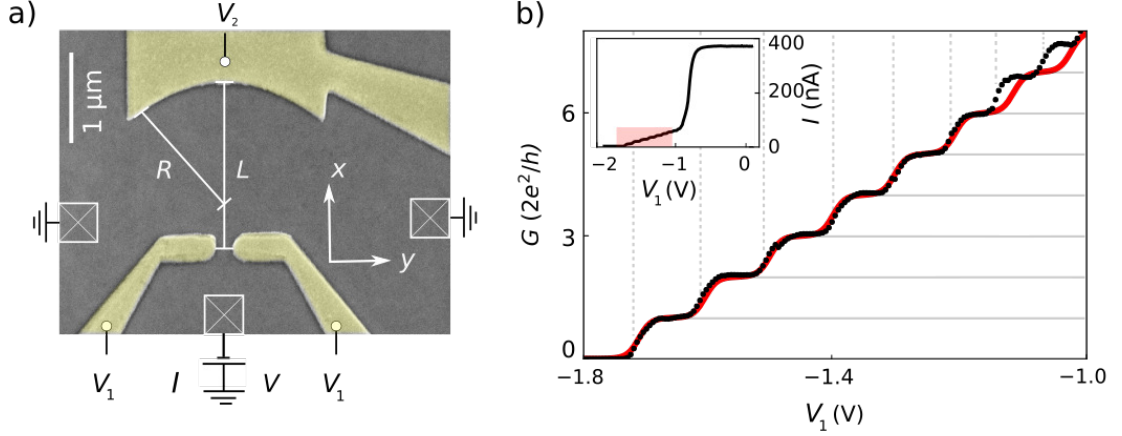


Figure 3.1: (a) Scanning electron microscope image of the sample including a simplified measurement circuit. The GaAs surface of the wafer is shown in gray and Ti/Au gates in yellow. The gates are used to define a QPC by applying a voltage V_1 and an electron reflector by V_2 . An open resonator forms for $V_1, V_2 < -0.8$ V, where the 2DES beneath all three gates is depleted. Ohmic contacts are indicated by white framed crosses. We measure the current I through the QPC in response to a source-drain voltage V applied at the current amplifier at the lower contact while the remaining contacts at the sides are grounded. (b) Pinch-off curve of the QPC at $V_2 = 0$, i.e. with no resonator defined. Black dots are measured with $V \simeq -0.5$ mV while the red line has been calculated with Eq. (2.29). The lead resistance of 270Ω has been subtracted. Horizontal lines indicate integer multiples of $G_Q = 2e^2/h$ and vertical dashed lines correspond to half transmission at $0.5G_Q$ of the respective highest subband. Top-left inset: full range pinch-off curve of the QPC.

ω_y/ω_x	V_1^0 (V)	$\alpha\hbar\omega_x$ (V)	β_1	β_2
1.8 ± 0.1	-1.656	0.06 V	$-0.6E-5$	0.007

Table 3.1: Table of calibrated values of ω_y/ω_x , $\hbar\omega_x$, $\alpha\hbar\omega_x$, β_1 and β_2 for the QPC

To form an open cavity for conduction band electrons, we add a spherical mirror by depleting the 2DES beneath the upper gate in Fig. 3.1(a) applying sufficiently negative voltage $V_2 < -0.8$ V to it. The QPC is located near the cavity's epicenter while the radius of the spherical mirror $R = 1.85 \mu\text{m}$ is slightly shorter than the overall geometric cavity length $L \simeq 2.3 \mu\text{m}$, compare Fig. 3.1(a). L and the QPC transmission can both be fine-tuned by adjusting the gate voltages. The electron dynamics is ballistic inside the cavity as at the Fermi energy of 11.19 meV, the electron mean-free-path is $l_m = 21 \mu\text{m}$ much longer than the resonator's dimensions. Two side contacts electrically ground the cavity with a combined lead resistance of approximately 135Ω . We use a current amplifier (DL Instruments 1211) at the third contact to measure the current flowing from the cavity through the QPC. While for the QPC pinch-off curve shown in Fig. 3.1(a) we used a separate voltage source, now the amplifier also serves as voltage source by adjusting its input voltage offset V . To control the applied voltage, we do this while measuring the current at well-defined resistance, e.g., at $G_{\text{QPC}} = G_Q$ without a cavity ($V_2 = 0$). Combining voltage source and current detector in one instrument helps to achieve a low level of external noise: it minimizes noise produced by connected instruments and makes it more straightforward to avoid noise related to fluctuations of the ground potential. The temperature drift of the electronics is typically $1 \mu\text{V}$ during the duration (typically three hours) of each experiment dominates the uncertainty of the applied voltage.

Depending on the sign of V the QPC emits either electron ($V < 0$) or holes ($V > 0$) into the resonator, but because of the electron-hole symmetry at the Fermi edge the linear response results below are independent of the sign of V . The current flowing at $V = -10 \pm 1 \mu\text{V}$ can be seen in Fig. 3.2(a) as a function of both gate voltages V_1 (QPC gates, y -axis) and V_2 (spherical

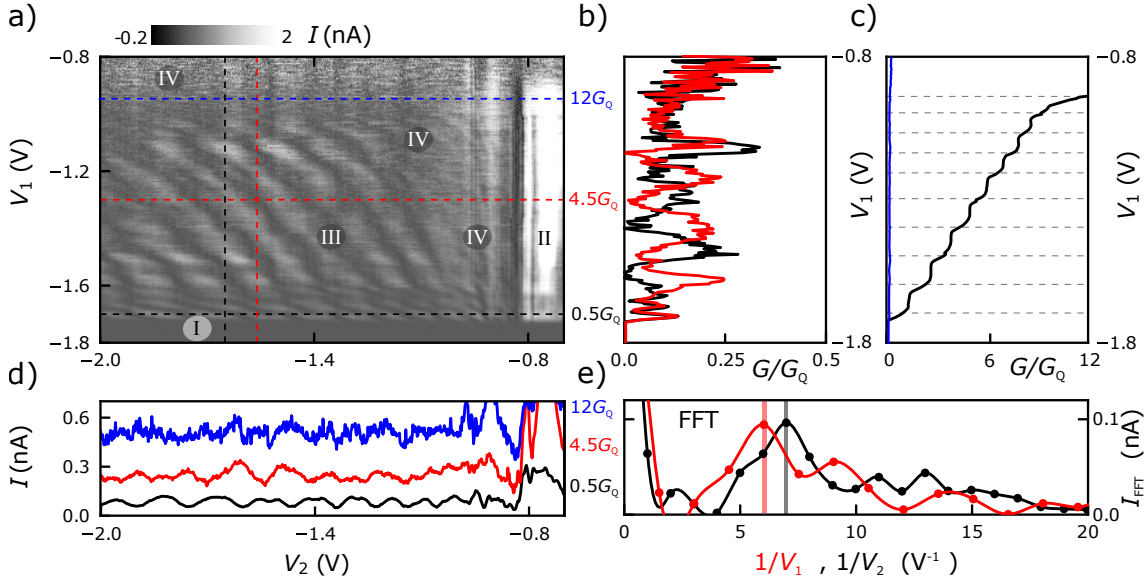


Figure 3.2: a) Measured current I with respect to V_1 and V_2 . Two dashed vertical lines show the position of the cuts in (b) and three dashed horizontal lines - cuts in (d). Four transport regimes are indicated with Roman numbers: first two of them are marked with yellow and red transparent area. b) Measured current I dependence on V_1 at two fixed values (black and red) of V_2 marked in (a) with vertical dashed lines. c) Black curve is the measured conductance G as a function of V_2 for a single QPC in units of $G_Q = 2e^2/h$ (the same data as in Fig. 3.1(b)). Blue curve represents the averaged current dependence $I(V_1)$ over the range of $-2\text{ V} < V_2 < 1.4\text{ V}$. for the combined system of the QPC and the cavity. d) Measured current I as a function of V_1 for three fixed values of V_2 , marked in (a) with horizontal dashed lines. Curves are averaged over the five adjacent lines. e) Fast Fourier Transform (FFT) of measured current $I(V_1)$ and $I(V_2)$. Main peaks are marked with the vertical bars.

mirror, x -axis). For clarity we indicate 4 separate regions, I–IV, in Fig. 3.2(a). In region I defined by $V_1 \lesssim -1.72\text{ V}$ the QPC is pinched off and $I = 0$. The resonator is absent in region II at $V_2 \gtrsim -0.8\text{ V}$ (and $V_1 \gtrsim -0.8\text{ V}$, not shown), because beyond this depletion voltage the barriers below gates become leaky. In region III the resonator has well defined deterministic modes giving rise to a regular stripe pattern of high versus low current. At minimal current carriers emitted from the QPC are efficiently scattered back through the QPC while at high current backscattering is reduced such that more carriers contribute to the current. The stripe pattern is linked to standing electron waves with constructive versus destructive interference of cavity modes at the QPC position. Interestingly, the ordered stripe pattern is absent in region IV, roughly for $V_1 > -0.9\text{ V}$ or $V_2 > -1.2\text{ V}$, but where electrons are still perfectly reflected below the gates. We believe that here we observe a transition from deterministic to chaotic behavior as the cavity extension is tuned too far beyond the focal length of the hemispherical mirror, as discussed further below. The transition can also be seen in $I(V_2)$ in Fig. 3.2(d) plotting horizontal cuts of the panel a) along three identically colored dashed lines. The two lower curves are in region III and exhibit a sinusoidal modulation, while the uppermost curve is in region IV and exhibits oscillations with

a similar amplitude but without a clear period.

In Fig. 3.2(c) we compare the linear response pinch-off curve $G(V_1)$ of the undisturbed QPC at $V_2 = 0$ (black) with corresponding data in region III (blue) where the QPC is coupled to the open resonator. (For better comparison the data are averaged between $-2\text{ V} \leq V_2 \leq 1.4\text{ V}$). Strikingly, once coupled to the open cavity the linear response conductance stays well below G_Q even where the undisturbed QPC has already $G > 10G_Q$. The strong conductance suppression indicates that most carriers emitted by the QPC are scattered back through the QPC and do not contribute to the current. In Fig. 3.2(b) we plot two $G(V_1)$ curves at individual V_2 values [vertical cuts in panel a) along dashed lines of identical colors]. $G(V_1)$ oscillates strongly, reflecting the stripe pattern in panel a), where the minima reach $G = 0$. The conductance oscillations origin in the mode structure of the cavity consisting of the mirror gate and the QPC. They are not linked to the conductance plateaus of the undisturbed QPC plotted in panel c). Our discussion suggests a strong, coherent coupling such that the cavity modes and the QPC modes become indistinguishable. In a first simplified model, we assume a Fabry-Perot type one-dimensional (1D) resonator. We introduce the effective resonator length $L_{\text{eff}} = L - \Delta L_1 - \Delta L_2$, where $\Delta L_1(V_1)$ and $\Delta L_2(V_2)$ account for the lateral depletion regions next to each gate and grow approximately linearly with $-V_1$ and $-V_2$. In a Fabry-Perot resonator, the period of interference oscillations corresponds to half of the Fermi wavelength, $\lambda_F = h/\sqrt{2m^*E_F} \simeq 45\text{ nm}$ in our case. To accurately determine the oscillation period we have performed fast Fourier transformations (FFT) of $I(V_1)$ and $I(V_2)$ presented in Fig. 3.2(e). From the main maxima $I_{\text{FFT}}^{\text{max}}$ indicated by vertical lines in Fig. 3.2(e) we find with $dL_{\text{eff}}/dV_{1,2} = I_{\text{FFT}}^{\text{max}} \lambda_F/2$ the cavity size dependences $dL_{\text{eff}}/dV_2 \simeq 179\text{ nm/V}$ and $dL_{\text{eff}}/dV_1 \simeq 139\text{ nm/V}$.

The increase of the size of the open cavity with gate voltages should result in a transition from deterministic to chaotic behavior: for an ideal resonator with infinite Q -factor we would expect the formation of chaotic modes whenever the focus point of the hemispherical mirror is outside of the cavity [140], in a naive picture for $R < L_{\text{eff}}$ in Fig. 3.1(a). In our sample, as we increase the resonator size L_{eff} we indeed observe a transition from a well defined stripe pattern in region III to a regime characterized by strong reproducible fluctuations which are not periodic, indicated in Fig. 3.2(a) as region IV. We observe the actual transition where R is still slightly smaller than L_{eff} . This discrepancy from the naive model has two reasons: first, our open resonator has a finite Q and the related broadening of individual modes impedes the formation of chaotic behavior. Second, the focus point of our cavity is at a larger distance from the mirror gate compared to R , if we account for its realistic mode structure.

Disorder and imperfect mode coupling lead to deviations from the idealized picture discussed above. In particular, the current measured through the QPC coupled to a resonator requires carrier scattering out of the resonator and into the two grounded side contacts. Note, however, that the Q -factor of our resonator is dominated by losses through the QPC for the data shown in Fig. 3.2(a). The above mentioned imperfections also give rise to additional fluctuations, apparent in $I(V_1, V_2)$ in Figs. 3.2(a), (b) and (d). Within the deterministic regime III, these fluctuations are reproducible and, thus, can be viewed as a fingerprint of the actual mode structure of the coupled system. The first 1D subband of the QPC with $G \leq G_Q$ in Fig. 3.2(c) results in a more complex mode structure with an additional minimum in visibility along with an extra phase shift of $\simeq \pi$, see Fig. 3.2(a). This feature can either be related to the 0.7-anomaly or is caused by disorder related localization. To come to a definite conclusion a more detailed investigation would be necessary. It demonstrates, however, that in principle interaction effects which give rise to phase shifts such as the 0.7-anomaly can be studied in our setup [97]. For $V_2 > V_2^d$, region IV, the 2DES below the mirror gate is not yet depleted such that no resonator forms. In region III,

roughly, for $V_1 \gtrsim -1$ V or $V_2^d > V_2 \gtrsim -0.7$ V the current is characterized by strong and irregular but reproducible fluctuations in $I(V_1, V_2)$. Here our resonator has a chaotic character [162].

3.2.1 Theoretical model

We can model the propagation of the wavefunction along the optical axis through the center of the QPC to the center of the reflector. The wavefunction can be written in the form:

$$\psi^{1D}(y) = \psi_0^{1D} e^{-iky} \quad (3.4)$$

Electrons in the resonator are reflected by both mirror gate and the QPC gates therefore after n loops the wavefunction can be calculated as $\psi^{1D}(n) = \psi_0^{1D} e^{-in(2kL)}$. Here we neglected phase shift of 2π per loop. Summing up all contributions of the standing wave results in the wavefunction at the QPC gate [163]:

$$\Psi_{total}^{1D} = \sum_{n=1}^{\infty} r^n \psi^{1D}(n) \quad (3.5)$$

Here we treat the mirror gate as a perfect reflector with a reflection coefficient equal to 1. Because only carriers which are not backscattered through the QPC contribute to the measured current for the measured resonances, we can also assume a reflection coefficient of approximately 1 for the QPC. However, disorder scattering, as well as imperfections of the open resonator, resulting in a loss channel. We take this into account by assuming a reflection coefficient of the QPC gates $r < 1$.

The sum above can be calculated analytically and results in the transfer function (Airy function)

$$T_r^{1D}(L_{eff}) = \frac{|(1-r)\Psi_{total}^{1D}|^2}{|\psi_0^{1D}|^2} = \frac{1}{1 + F \sin^2\left(\frac{2\pi L_{eff}}{\lambda_F}\right)}, \quad (3.6)$$

where F is the finesse of the resonator as defined in Ref. [140].

In the second model, we use Hermite polynomials as QPC eigenfunctions from Eq. (2.48) and Gaussian beam model from the section (2.6.4) for the free propagation of the electrons emitted from the QPC. After injection into the cavity, every QPC eigenmode propagates in the free 2DES until reaching the mirror gate.

We assume the reflected wavefunction to have Hermite-Gaussian form with a phase shift by π and different radius of the wavefront $1/R_2 = 1/R_1 - 2/R$, where R_1 is the wavefront radius before the reflection and R_2 after. Superposition of all reflected wavefunctions for any number m of electron loops in the resonator can be written as defined in Refs. [164, 165]:

$$\Psi_{total}^{2D} = \sum_{m=1}^{\infty} r^m \Psi^{2D}(m) \quad (3.7)$$

Transfer function of the cavity can be expressed by integrating over the transversal profile of the electron wavefunction and normalizing it:

$$T_r^{2D}(L_{eff}) = (1-r)^2 \frac{\int_{-\infty}^{+\infty} \Psi_{total}^{2D}(x, L_{eff}) \Psi_{total}^{2D*}(x, L_{eff}) dx}{\int_{-\infty}^{+\infty} \Psi^{2D}(x, L_{eff}) \Psi^{2D*}(x, L_{eff}) dx}, \quad (3.8)$$

The current I can be calculated for both models from the transfer function of the cavity T_r assuming finite losses into the side contacts.

$$I = I_0 T_r(L_{\text{eff}}) \quad (3.9)$$

The electron scattering to the sides contacts, i.e. the dephasing of the resonator, is caused by resonator imperfections including elastic scattering including disorder, roughness of gate surfaces or incomplete modematching. All these effects are temperature independent and are summed up in two fit parameters: the QPC gates reflection coefficient r and the baseline current I_0 . In addition there are two dephasing mechanisms that are temperature dependent: electron-electron scattering and thermal broadening. We can account for them by introducing an imaginary part of the wavevector:

$$k = k_F + ik'' \quad (3.10)$$

with $k'' = 1/l_\phi(T)$ [140]. Here we take a straightforward approach and assume a constant k'' such that

$$\Psi_T^{2D} = \Psi^{2D} \exp(-y/l_\phi(T)), \quad (3.11)$$

where $l_\phi = v_F (\tau_{e-e}^{-1} + \tau_T^{-1})^{-1}$. Substituting Eq. (3.11) into Eq. (3.6) or Eq. (3.8) we can calculate current through the coupled system, that is a periodic function of L_{eff} . It has finite visibility $v = (I_{\text{max}} - I_{\text{min}})/(I_{\text{max}} + I_{\text{min}})$ caused by k'' and r . We can compare this v to the measured data.

3.2.2 Comparison between theory and experiment

To study electron dephasing we measure the temperature dependence of the current $I(T)$. Representative data is shown in Fig. 3.3(a). Here we plot $I(V_2)$ at $G/G_Q = 4$ (fourth conductance

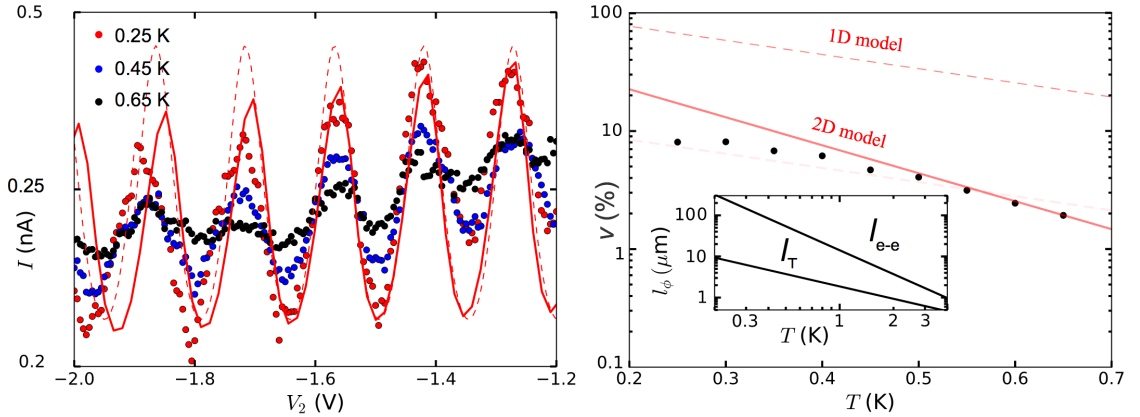


Figure 3.3: a) Dots: Measured current I in the deterministic regime III from Fig.(3.2) as a function of reflector voltage V_2 for various temperatures T at fixed $G_{\text{QPC}} = 4G_Q$. Red lines: simulated current I in the deterministic regime I, solid for the 2D model and dashed for 1D model b) Symbols are the measured visibility values as a function of temperature in semi-logarithmic scale for fixed $G_{\text{QPC}} = 4G_Q$. Lines are theoretical fits, red for the 2D model and black for 1D model. Inset: top line marks the e-e scattering length l_{e-e} and bottom line illustrates the thermal length l_T dependence on temperature.

plateau of the QPC) for three different temperatures. The oscillation period and phase are independent of T as expected as neither thermal broadening nor enhanced scattering affect the

average kinetic energy or wavelength of electrons as long as $k_B T \ll E_F$. The visibility, however, decreases exponentially with increasing temperature as demonstrated in the Fig. 3.3(b). We also indicate $l_{e-e} = v_v \tau_{e-e}$ and $l_T = v_v \tau_T$ as dashed lines in the inset of Fig. 3.3(b).

Now we can compare the measured dependence $I(T)$ with model predictions that the two-dimensional nature of the open resonator has to be taken into account properly in a realistic model. In Fig. 3.3(a) we first plot the calculated current I at various temperatures for the phase coherence length l_ϕ , where $v_F \simeq 2.4 \times 10^5$ m/s, as a solid line in a semi-logarithmic scale. Here we assume a perfectly reflecting mirror while the transmission through the QPC, t_{QPC} , is given by the Büttiker formula [80] and its reflection is $r_{\text{QPC}} = 1 - t_{\text{QPC}} \simeq 0.9$. First we approximate our electron cavity with a one-dimensional Fabry-Perot type resonator and treat electrons as infinite plane waves. This is a standard approach often pursued in literature to describe electron cavities [160, 163]. The resulting $I(T)$ dependence is plotted in Fig. 3.3(a) with red dotted line.

In a more realistic approach, we now model the two-dimensional dynamics in our cavity. The pinch-off curve of our QPC presented in Fig. 3.1(b) indicates an almost perfect parabolic saddle point potential with Hermite functions as eigenfunctions for the carriers. The latter are emitted within a Gaussian beam profile [140, 166]. Consequently, we model the cavity modes also as Hermite functions in a Gaussian beam profile. The radius of the hemispherical mirror is shorter than its distance from the QPC, $R < L$ in Fig. 3.1(a). However, for a Gaussian beam, the focus point of the hemispherical mirror is at $L_e f f \simeq 2.1 \mu\text{m}$, i.e., closer to the QPC. A possible mismatch causes deviations from the cavity eigenmodes from the Hermite functions. In our calculation, we nevertheless assume Hermite functions and account for differences by $0.5 \mu\text{m}$. We show the fit in Fig. 3.3(a) with the solid red line. As we can see from the figure, both theoretical fits exhibit comparable behavior.

Next we present the visibility $v(T)$ calculated from our current measurements $I(T)$ in Fig. 3.3(b) as black circles. It reveals quantitative agreement with the theoretical prediction of the 2D model including its temperature dependence. Assuming unrealistic reflection coefficient of the QPC gates $r = 0.32$ for the 1D model we can fit the visibility values but not for the range of $T > 0.5$ K because of its different exponential dependence on temperature. Hence we can conclude that a one-dimensional Fabry-Perot model overestimates the visibility. In contrast, our measurements agree with theoretical predictions if we consider a realistic model of the electron cavity properly taken into account its two dimensions. They suggest much lower $v(T)$ compared to the theoretical prediction and, also, a stronger temperature dependence.

3.3 Conclusions

In the third chapter, we presented an approach to measure the phase behavior of a nanodevice by coupling to a ballistic cavity. The transmission through the combined system of a QPC and hemispherical resonator shows indications of both quantum interference and QPC mode physics. In this chapter we showed indications of coherent coupling between the cavity and the QPC. We compared two models to describe our data: infinite plane waves and bounded Hermite-Gaussian lateral beam profiles. While these models give the same result regarding transmission through the system they differ in reproducing its dephasing properties: the plane wave model fails to predict dephasing based on energy broadening in ballistic transport regime in contrast to a Gaussian-Hermite model.

Chapter 4

Lissajous Rocking Ratchet based on a Quantum Dot

Breaking fundamental symmetries often give rise to interesting effects and, in particular, breaking the time-reversal symmetry (TRS) is a requirement for many applications such as information processing. In this chapter, we present a familiar with TRS concept based on a QD, nanoscopic structure where electrons are confined in all three dimensions. While different realizations of QD are possible, we deal with lateral QDs defined within a 2DES embedded in a GaAs/AlGaAs semiconductor heterostructure. In our experiment, we break time-reversal symmetry by periodically modulating the quantum dot's barriers. In the next sections, we show the characterization of our QD and discuss that our quantum dot resembles a Lissajous ratchet for complex modulation of both gates. The primary results presented in this chapter are published in Physical Review Letters [167].

4.1 Quantum dots

In the following chapter, we perform experiments with driven QDs, and we start with discussing their transport properties. QD's density of states is discrete, giving rise to a potential map shown in Fig. 4.1(a). The QD is coupled there via tunnel barriers with tunneling rates $\Gamma_{L,R}$ to two electron reservoirs [source and drain marked as L and R respectively, in Fig. 4.1(a)] at cryogenic temperature T . The leads are treated as a degenerate Fermi liquid with chemical potentials μ_L and μ_R shown in Fig. 4.1(a). Tunable barriers [grey in Fig. 4.1(a)] can be achieved by imposing spatially varying electrostatic potentials shifting the energy band locally. The electrostatic confinement potential is provided by the field effect while applying negative voltage on golden gates on the surface (similar to previous chapters).

The system can be characterized by means of the constant interaction model [168]. It parametrizes the mutual Coulomb interaction of electrons inside the dot and their coupling to other charges outside the dot by capacitive coupling constants C_i , see figure 4.1(b). In Fig. 4.1 we show capacitive/resistive simplified scheme of the QD. The main approximation of the model is that the quantum-mechanical energy levels E_n in the QD do not depend on the number of electrons occupying the quantum dot. These energies can be added to the classical electrostatic

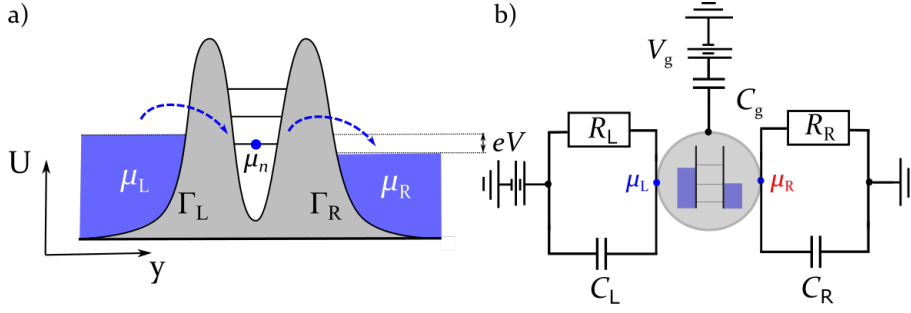


Figure 4.1: Sketch of the QD circuit in a potential landscape representation. Tunnel rates of the barriers that form the dot are $\Gamma_{L,R}$, dot chemical potential levels μ_n are denoted with horizontal lines. (b) The simplified equivalent circuit of a quantum dot coupled to two leads. The QD is sketched in the center: horizontal lines denote chemical potentials and vertical lines barriers. Capacitive couplings are represented by C_i , resistive couplings by R_i . For simplicity, all gates are represented in only one gate C_g with voltage V_g applied to it.

energy U_{es} to obtain the total QD energy U :

$$U = U_{es} + \sum_{i=1}^n E_n, \quad (4.1)$$

The pure classical electrostatic energy of n electrons in the dot is given by

$$U_{es} = \frac{(-en + [C_R V_R + C_L V_L + C_g V_g])^2}{2C_{QD}}, \quad (4.2)$$

where $C_{QD} = C_g + C_L + C_R$. We can now introduce useful concepts for determining the electron ground state of the system as a function of external parameters starting with a chemical potential μ_n

$$\mu_n = \epsilon_n + U_{es}(n) - U_{es}(n-1) = \epsilon_n + \frac{e^2}{C_{QD}}(n-1/2) - \frac{e}{C_{QD}}(V_g C_g + V_L C_L + V_R C_R). \quad (4.3)$$

μ_n of the QD is the energy needed to add the n^{th} electron to the QD if we neglect correlation effects. Note that validity condition requires the system to be considered as the grand canonical ensemble of the QD connected to the leads. The chemical potential of the dot can be modified by changing the applied voltages. A leverage factor $\kappa_\mu = \delta\mu_n/\delta V_i = -eC_i/C_{QD}$ connects the change in voltage to the change in chemical potential. The onsite energy of the QD $\epsilon_0 = -\kappa_g V_g$ shows how energy states of the dot can be tuned with plunger gate voltage V_g . The difference between the chemical potential for n and $n-1$ electrons is defined as charging energy of the QD:

$$E_C(n) = \mu_n - \mu_{n-1} = e^2/C_{QD} + \Delta E \quad (4.4)$$

where $\Delta E = \epsilon_n - \epsilon_{n-1}$ is contribution of the single particle spectrum, that depends on the n . The single quantum dot acts as an artificial atom [169]. Because of the missing positive nuclear charge, numerous different ionization states are possible. We can calculate current through the QD under the independent channel approximation assuming the tunnelling problem through a double barrier [10]:

$$I = 2 \frac{e}{h} \int \sum_n |S_{LR}^n(\epsilon)|^2 \left[f(\epsilon - \mu_L) - f(\epsilon - \mu_R) \right] d\epsilon, \quad (4.5)$$

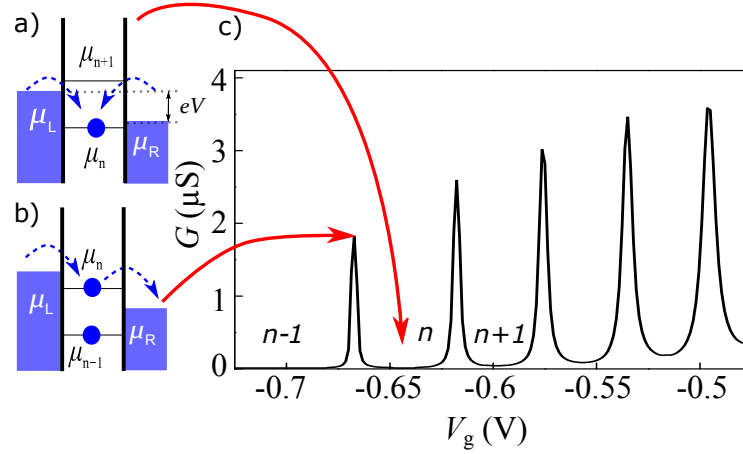


Figure 4.2: a) Reduced scheme of the QD in the Coulomb blockade. Vertical lines denote tunnel barriers, horizontal lines the chemical potentials of the QD for the n^{th} electron. b) Reduced scheme of sequential tunnelling through the QD. c) Simulated conductance G as a function of the plunger gate voltage V_g in the Coulomb blockade regime.

where $S_{LR}^n(\epsilon)$ is the probability that an electron with initial energy ϵ from source lead is scattered to drain lead, $f(x) = [\exp(x/k_B T) + 1]^{-1}$ is the Fermi function for thermal energy $k_B T$. The independent channel approximation assumes each charge state of the quantum dot contributes as independent transport channel to the current. The corresponding scattering matrices S under independent channel approximation read [10]:

$$S^n(\epsilon) = \mathbf{1} - \frac{i\sqrt{\Gamma_L\Gamma_R}}{\epsilon - \mu_n + i(\Gamma_L + \Gamma_R)/2} \begin{pmatrix} \Gamma_L & \sqrt{\Gamma_L\Gamma_R} \\ \sqrt{\Gamma_L\Gamma_R} & \Gamma_R \end{pmatrix}, \quad (4.6)$$

where Γ_L and Γ_R are the dot-lead tunnel rates. Note that $S_{LR}^n = S_{12}^n = S_{21}^n$. In Fig. 4.2(c) calculated current I as a function of the plunger gate voltage V_g is shown. Changing the plunger gate voltage V_g leads to raising up the energy levels of the QD. When the QD energy level fits into the transport window V the current I flows. As V_g is changed the conductance of the dot differs between zero (transitions of the electronic states, sketched in Fig. 4.2(a)) and non-zero (constant charge of the QD illustrated in Fig. 4.2(b)) that corresponds to so-called Coulomb blockade oscillations plot. Experimentally there are few essential requirements for observing Coulomb blockade:

- $E_C > eV$: Transport window V should be sufficiently small otherwise a current flows through the dot by sequential tunneling of electrons.
- $E_C \gg k_B T$: For lateral QDs discussed in this thesis the charging energy is in the order of 1 meV that corresponds to cryogenic temperatures $T < 12$ K. The same requirement for the energy broadening is valid for the applied source-drain voltage $E_C \gg eV$
- $R_{L,R} > 2h/e^2 \simeq 50$ kOhm: The barriers should be sufficiently opaque such that the typical time to charge-discharge the dot, $\frac{R_L R_R}{R_L + R_R} C_{QD}$, fulfils the Heisenberg uncertainty relation.
- $E_C > \delta E$ charging energy should exceed the inhomogeneous broadening. This broadening is caused by the charge noise or imposed by the measurement setup.

4.2 Breaking time-reversal symmetry in nanoelectrical circuits

Breaking the fundamental time-reversal symmetry can be exploited in the quantum computer operation for the reduction of the qubit interaction with the environment. The readout of the qubit state imposes classical measurements on the quantum system [170] and in a variety of readout protocols (for example in solid-state superconducting qubits [171]) both the input and output signals collected on the same spatial channel. For the separation of input and output channels (for instance in microwave reflection based measurements [172]) the readout involves the operation of nonreciprocal devices like circulators (or isolators) [173, 174]. A circulator is a non-reciprocal three- or four-port device [175], in which a microwave or radio frequency signal is entering any port and then only transmitted to the next port in the rotation. We show a circulator sketch in Fig. 4.3. If one of the ports of the circulator is terminated in a matched load, one obtains an isolator [175] in which signals are transmitted in one direction and completely suppressed in the other. Both devices offer selective transmission between given ports and both can be operated actively or passively depending on the underlying physical mechanism.

State-of-art realizations of circulators are based on the Faraday effect and have physical dimensions close to the microwave wavelength employed ($\lambda \approx 30$ cm for $f = 1$ GHz) that violates scalability down to the chip size [176]. Here the time-reversal symmetry is broken via the phenomenon of Faraday rotation based on magnetic materials and fields [175]. An alternative approach makes use of the Quantum Hall effect, i.e., an external magnetic field breaking the time-reversal symmetry of electrical transport [177]. This method suggests an on-chip realization of a circulator and dynamic control of the non-reciprocity of the transmitted signal: the direction of circulation of the signals can be tuned in real time by varying the magnetic field [178]. However, both ideas use a permanent magnet to bias the magnetic field, which may channel unwanted flux into the superconducting qubit. From the active solutions, we can highlight the realization of the circulator on transistors and varactor diodes [175, 179]. Active realizations supply power but can be operated dynamically. Significant drawbacks of the transistor-based active circulators are the power limitation and the signal-to-noise degradation [180], which are critical while operating quantum information devices.

An alternative realization of the circulator is provided by ratchets [181], devices that combine non-equilibrium conditions and asymmetry. These systems don't require bulky magnet assemblies, while providing an on-chip solution where the non-reciprocity of electrical transport is dynamically tunable. In this section we will review such mesoscopic on-chip devices that create directed motion of electrons and break symmetry in 2DES embedded in semiconductor heterostructure [182–184]. For clarity we first sort out the related concepts of a quantum rectifier, a pump and more general ratchet by its applications and realizations.

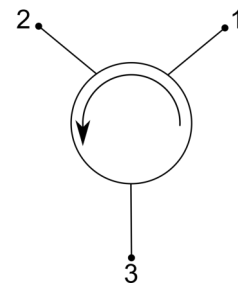


Figure 4.3: A conventional symbol for a three-port circulator indicating counterclockwise circulation ($1 \rightarrow 2 \rightarrow 3$). A signal entering any port is transmitted only to the next port in rotation

4.2.1 Rectifier

One way to break the time-reversal symmetry is imposing a spatially asymmetric element into the device. Such a passive device, an electron rectifier, converts alternating current into the one-directional current. The electron rectifier was demonstrated by Song et al. for 2DES based on modulation-doped GaAs/AlGaAs heterostructure in electron ballistic regime [185]. In Fig. 4.4 we

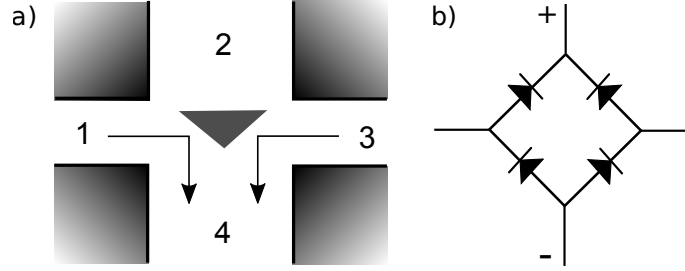


Figure 4.4: (a) Sketch of the central part of a ballistic rectifier. The grey areas are etched away, forming the triangular antidot in the middle and four channels: 1,2,3,4. The current is applied between 1,3 and the output voltage is measured between 2,4. The device operates similarly to a bridge rectifier based on diodes (b).

show simplified sketch of the experiment. They inserted an asymmetric scatterer into the center of a ballistic cross-junction that consists of the two narrow channels 1,3 used as source and drain terminals to source and measure current and the two wide channels 2,4, used to measure the voltage drop. The typical electron trajectories illustrated by the arrows in Fig. 4.4 suggest for non-zero source-drain current I_{13} an accumulation of electrons in the lower lead, i.e., a negative voltage between 2 and 4. This effect is the consequence of broken symmetry along the 1-3 axis. However, the symmetry between 2,4 is still conserved, and the output voltage V_{24} remains the same if the sign of the source-drain current I_{13} is changed and the corresponding four-terminal resistance

$$R_{13,24}(I_{13}) = R_{13,24}(-I_{13}), \quad (4.7)$$

where $R_{13,24} = V_{24}/I_{13}$. The device is operated similarly to a bridge rectifier 4.4(b) with diodes but with a different nature of the nonlinearity in the $I - V$ characteristics. The ballistic rectifier also can be used for the detection of feeble signals without the need of an external bias. Song et al. [186] showed the existence of a rectification DC current in a ballistic rectifier operated with an ac voltage. Note that Onsager relations discussed previously in Sec. (2.1.4) also, hold for non-linear devices but in a more generalized form, by assuming transmission coefficients to be functions of the lead currents [185].

4.2.2 Turnstile and adiabatic pump

The time-reversal symmetry can be broken by exploiting time modulation of the system with external forces. The choice of the modulation frequency distinguishes active devices between operated adiabatically and non-adiabatically. This condition is imposed by the timescales of the modulation compare to the characteristic timescales to reach equilibrium in the system. Here we discuss modulated devices based on QDs embedded in semiconductor heterostructures. We drive the barriers of the QD to the left and right lead Γ_L, Γ_R with frequency Ω . If $\Omega \ll \Gamma_L, \Gamma_R$ we treat operation regime as adiabatic.

A turnstile is defined as a modulated device based on QD with broken time-reversal symmetry by applying a non-zero source-drain voltage. We sketch the operation of a turnstile based on a single QD in Fig.4.5. The modulation of the barriers in the turnstile happens in anti-phase to compensate the movement of the QD chemical potential. To get quantized current from the device, the chemical potential should lie in the transport window, defined by the source-drain voltage (see blocks in Fig. 4.5). At the first half-cycle of the operation left barrier is lowered and electron loads from the left lead into the dot. The right barrier is raised due to the phase difference, preventing any tunneling events with the right lead. At the second half-cycle, the barriers are vice versa and an electron tunnels from the QD through the low right barrier giving rise to the current from the left to the right lead. A turnstile device was proposed by Odintsov [187] and realized in a pioneering work by Kouwenhoven et al. [184]. Kouwenhoven measured quantized current response from a turnstile tuned to the few-electron regime when a discrete number of electrons are transferred through the QD for each modulation cycle [184].

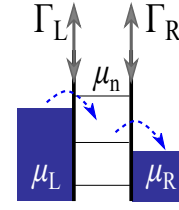


Figure 4.5: Sketch of the turnstile operation. Vertical arrows indicate gate modulation, horizontal - direction of current.

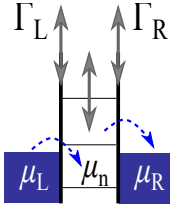


Figure 4.6: Sketch of the adiabatic pump operation. Vertical arrows indicate gate modulation, horizontal - direction of current.

A modulated device based on QD that creates a direct current, where modulation of the QD chemical potential is not compensated is called a charge pump. The charge pump doesn't require any external source-drain voltage for operation and is illustrated in Fig.4.6. The time-reversal symmetry is broken by imposing asymmetry on the driving, i.e., the phase difference between two modulation signals.[188]. The phase difference created a time-delay for the loading-unloading processes in the QD that together with the movement of the QD chemical potential create a non-zero current through it. Now the barriers are operated similarly to the turnstile, but during the loading half-cycle, chemical potential is lower than the chemical potential of the left lead. Then it is raised to a higher value making tunneling through the lowered right barrier energetically favorable. Electron pump devices have been engineered in GaAs/AlGaAs heterostructures [189] as well as in other semiconductor materials, for example in Si by Rossi et al. [190].

Under strict adiabaticity conditions an adiabatic pump requires at least two parameters to produce a non-zero dc current [191]. In our case these two parameters are independent driving of the two QD barriers. An operation of the pump is possible while driving only one-barrier and keeping the other constant in the non-adiabatic regime. In this regime driving also causes modulation of the chemical potential of the QD and the system is driven out of the equilibrium. The non-adiabatic pump operation is shown in Fig.4.7. In the non-adiabatic pump loading, half-cycle is the same as in adiabatic species, but unloading happens by pushing electrons over a fixed barrier. It is crucial that raising the chemical potential of the dot happens faster than tunneling out of the QD. Otherwise, the extra charge will be lost back to the source immediately once μ_n is raised above μ_L (this is a non-adiabatic requirement). Non-adiabatic electron pumps prove their suitability for being used as a metrological standard for the definition of Ampere [192]. In this chapter, we will not describe non-adiabatic pumps but concentrate on adiabatic two-parameter pumping procedure. This pump species will be later discussed in all details based on a realization in our device.

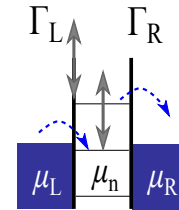


Figure 4.7: Sketch of the non-adiabatic pump operation. Vertical arrows indicate gate modulation, horizontal - direction of current.

4.2.3 Ratchet: definition and types

The ratchet combines different properties discussed previously for a pump and a rectifier: non-equilibrium fluctuations and broken spatio-time symmetry to generate directed motion. In a comprehensive review [181] Hänggi and Marchesoni divided ratchets into two classes: flashing ratchets [193], in which the shape of the ratchet potential varies in space, and rocking ratchets [194], in which the ratchet potential is subject to an (periodic [195]) external force with a time-average of zero.

4.2.3.1 Flashing ratchet: spatial asymmetry

A thought experiment originally proposed by Smoluchowski [196], and later expanded upon by Feynman in his Lectures on Physics [197], illustrates the impossibility of rectifying thermal fluctuations with a system in equilibrium, even if it contains a source of asymmetry. It shows a flashing ratchet and uses a pulsating spatially asymmetric potential to turn fluctuations into work. The second principle of thermodynamics rules out directed motion at thermodynamic equilibrium, thus the generation of a current requires non-equilibrium. We follow ratchet de-

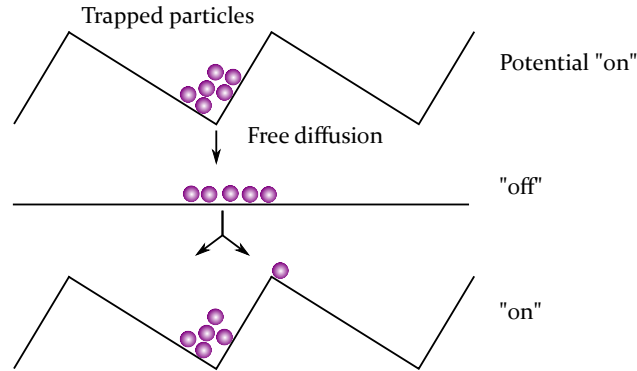


Figure 4.8: Working principle of the flashing ratchet. The operation consist of three sequential steps, when turned on and off potential results in a ratchet current to the right.

scription for Brownian particles [194] as straightforward and easy to understand example. Consider a sample of Brownian particles in a (static) asymmetric periodic potential. If the potential is “flashed” that is, if it is turned on and off repeatedly [198], it is sufficient to set the Brownian particles into directed motion, as sketched in Fig. 4.8. At the initial situation when the potential turned on the Brownian particles localized at the bottom of a given well. Then the potential is turned off, and the Brownian particles will symmetrically diffuse in space. Next, the potential is turned on again, and the Brownian particles are retrapped in both the original well and in the neighboring ones. However, as the potential is asymmetric, the retrapping will lead to an asymmetric situation, with the number of particles trapped in the wells at the left of the original well different from the number of particles trapped in the wells at the right of the starting location. In this way, the center of mass of the particle cloud will move, and directed motion is obtained. Note that the flashing ratchet does not violate the second law of thermodynamics because work is done on the system while turning on the potential.

4.2.3.2 Rocking ratchet: time-reversal broken symmetry

While a flashing ratchet turns undirected diffusion into directed motion by repeatedly switching an asymmetric potential on and off a rocking ratchet breaks the spatiotemporal symmetry using applying periodic forces.

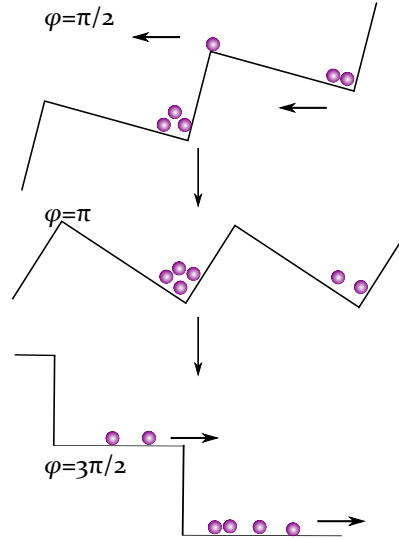


Figure 4.9: Working principle of the rocking ratchet. The potential profile is influenced by an external time-periodic force, time evolution corresponds to phase ϕ change. Three different time moments at $\phi = 0.5\pi$, $\phi = 0.75\pi$ and $\phi = 0.25\pi$ illustrate the observed net drift of Brownian particles to the right.

Figure 4.9 shows an operational cycle of a rocking ratchet for Brownian particles. An asymmetric potential tilted up and down symmetrically is shown at three different moments in time during one period T of operation (that corresponds to the phase change by 2π): $\phi = \pi/2$ tilted up, $\phi = \pi$, at zero tilt, and at $\phi = 3\pi/2$, tilted down. When the asymmetric potential is rocked up and down Brownian particles are more likely to have sufficient energy to traverse the barriers to the right at $\phi = 3\pi/2$ in figure 4.9, than to the left at $\phi = \pi/2$. On average, a current of particles will flow to the right in the rocking ratchet shown in Figure 4.9.

4.2.4 Ratchets based on quantum dots in semiconductor structures

A good example of a quantum ratchet is a double quantum dot (DQD) the device, introduced by Kraphai et al. [182]. Figure 4.10(a) shows a SEM image of the device. The double dot and a QPC are separated by the negatively biased central gate to prevent any leakage currents, see Fig.4.10. The QPC is employed as a nonequilibrium energy source. If the internal symmetry of the double quantum dot is broken (see insets in Fig.4.10) the double quantum dot acts as a flashing ratchet.

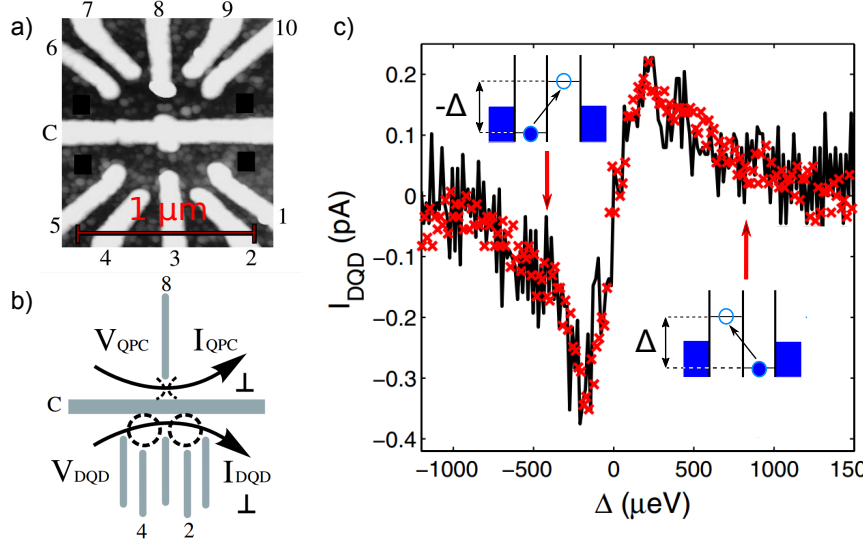


Figure 4.10: a) AFM micrograph of a double-quantum-dot device. Metal gates are marked with light color, black squares are the source and drain regions. The red scale bar marks a length of $1\ \mu\text{m}$. b) Schematic diagram of the device: A biased quantum point contact QPC and the asymmetric double quantum dot DQD is shown as two dashed circles. The asymmetry is induced via gate voltages at the plunger gates 2 and 4. c) Measured current through the double quantum dot I_{DQD} as a function of its detuning Δ for $V_{\text{QPC}} = -1.55\ \text{mV}$ (symbols) and $3.3I_{\text{DQD}}$ for $V_{\text{QPC}} = -1.55\ \text{mV}$ (solid line). An elastic contribution to I_{DQD} is subtracted. The two insets sketch the corresponding inelastic tunneling processes which drive the ratchet current. Reproduced from [182].

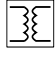
For weak interdot tunneling, detuning of the quantum dot energy levels results in the localization of an electron in one dot, so that elastic electron transfer to the other dot is energetically forbidden. On the insets the interdot tunnelling processes are sketched for the right-to-left transition $[m, n+1] \rightarrow [m+1, n]$, with asymmetry energy $\Delta = E_{m+1, n} - E_{m, n+1}$, and for the opposite left-to-right transition with energy $-\Delta$. Because of inelastic interdot tunneling inside the Coulomb-blockaded double quantum dot, there is a non-zero net ratchet current. This current is plotted in Fig. 4.10(c) as a function of the detuning of the dots Δ . A finite ratchet current is present if the electron energy states in the dots are detuned asymmetrically, i.e., when $\Delta \neq 0$. In contrast, an ionization of one dot toward its adjacent lead, followed by recharging from the same lead, does not result in a net current. The non-equilibrium energy quanta, emitted by the QPC electrons and absorbed by the electrons in the DQD, are likely acoustic phonons, but could also be photons or 1D-plasmons [182].

4.3 Measurement setup

The measurements presented in this chapter are based on low-temperature physics close to the electronic ground state in nanostructures with feature sizes around 100 nm. To reach the QD ground state we performed the experiments at cryogenic temperatures around $T = 50$ mK. The small energy scales of the phenomena examined also limit the excitation voltages that may be applied to samples. In this section, we will describe the used cryogenic setup and discuss electronic and noise considerations relevant to our work.

4.3.1 Dilution fridge and the setup

We used an Oxford TLM 400 dilution refrigerator for resolving typical characteristic energies of the QD that is usually in the order of several $100 \mu\text{eV}$. The basic operating principle of helium dilution refrigerators is the following: when a mixture of He^3 and He^4 is cooled below a critical temperature (0.86 K), the mixture separates into a He^3 -rich, concentrated phase and a dilute phase. Because of the enthalpy difference between the two phases, it is possible to obtain cooling by evaporating He^3 from the concentrated phase into the dilute phase. The reader is advised to Ref. [94] for more detailed explanation. The used cryostat is a top-loading version which consists of a long sample stick, which can be slid from the room temperature top of the cryostat down to the base temperature mixing chamber. This engineering solution provides with the fast exchange of the samples (within one hour) at the cost of high He^4 consumption (50 L per 2 days).

An essential requirement for ratchet measurements in QDs is minimizing noise pickup into the source-drain line that can cause unwanted symmetry breaking of the measured current. To reach a measurement sensitivity with the noise level below $1 \mu\text{V}$ in the source-drain line, we reduced the external noise as much as possible. Our main strategy is to use low-pass filters for all but the rf wires and carefully design our room temperature assembly of instruments and cables to avoid pickup of noise or ground loops. We show the used experimental setup sketch in Fig. 4.11. We show the cryostat as a circle in the center of the Fig. 4.11. All cables inside the cryostat are heatsinked at several points in the cryostat (at $T = 4, 1.5$ K and 300 mK marked with three transparent concentric circles in Fig. 4.11) that provide efficient cooling of the 2DES via the measurement wires. We used the same strategy of avoiding the ground loops as in 2.2, the details can be found in Fig. 4.11. Solid black lines represent the ground connection in Fig. 4.11. The cryostat provided the common measurement ground (i) and the magnet power supply was connected to the ground of the dewar (ii). Ground (iii) was used as technical supply ground for all the devices. To effectively isolate both grounds from each other galvanic isolators were used marked in Fig. 4.11 with the pictogram . The setup was controlled by computer via the GPIB protocol by the framework of Labview-based programs. The connection scheme of GPIB cables is shown in the lower panel of Fig. 4.11) with dashed black lines.

4.3.1.1 rf wires

To generate a high-frequency signal up to 1 GHz, we used an arbitrary waveform generator Tektronix AWG5014B. rf wires are shown with magenta color in Fig. 4.11. For the rf signals, we use lossy semi-rigid stainless steel coax cables inside the cryostat. To combine dc gate voltages with rf modulations we use Mini-Circuits ZFBT-4R2GW bias-tees at the cryostat entrance at

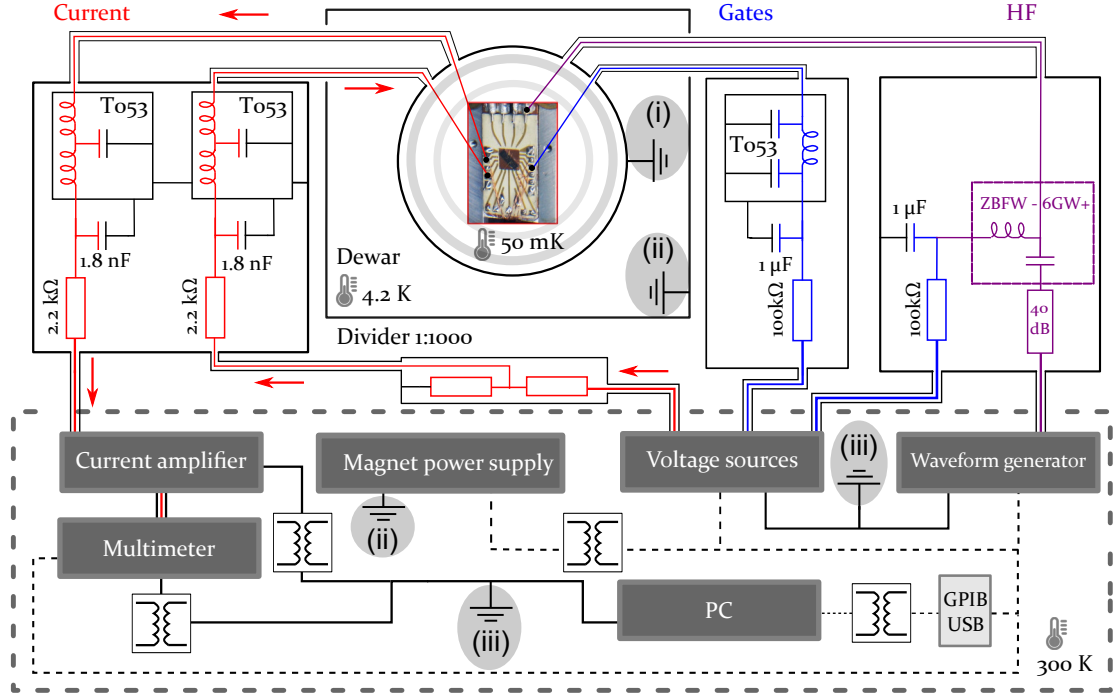


Figure 4.11: Sketch of the experimental setup and the electrical connections. The dewar is sketched in the center as a black box, with a circle that represents a dilution fridge inside. Active electrical devices that are controlled by the PC or send data to the PC are grouped in the bottom of the scheme. Passive elements such as filters and bias-tees are marked with the appropriate color for the gate wires (blue), current wires (red) and distinguished additionally with arrows indicating input/output. rf wires are indicated with magenta color. Thermal anchoring of the wires is indicated at different temperatures with transparent concentric circles inside the fridge.

room temperature. As a DC voltage source, we used Yokogawa 7651. On the rf-side of the bias-tee, we added additional 20 dB attenuators. Signal attenuation allows us to work with higher output signals of the rf generator which provides a higher signal-to-noise level. In table 4.1 we summarize the parameters of the rf wires.

4.3.1.2 Gate and current wires

Gate wires are shown with blue color and current wires with red in Fig. 4.11. We use a combination of π - or T-filters to reduce high-frequency noise and standard RC-filters to reduce noise at lower frequencies. The gate voltage filters have a cutoff frequency of 1.6 Hz. For the current wires we use filtering with the cut-off frequency of 30 kHz in combination with a Voltage divider (1000 : 1) on the source side directly at the cryostat, see Fig. 4.11. The high cut-off frequency makes our filters compatible with lock-in measurements at lower than cut-off frequencies. A requirement is that ohmic resistance of the wires (including the filter) should be much smaller than the sample resistance which ranges from 1 M Ω to few G Ω in our QD measurements.

Component	Resistance (Ω)	Capacitance to ground (F)
Double shielded coax	$\simeq 1$	$> 100\text{ p}$
Filter box	100k	$1\ \mu$
Double shielded coax	$\simeq 1$	$> 100\text{ p}$
Stainless steal coax	$\simeq 200$	$\simeq 250\text{ p}$
Bias tee	2.2k	
Σ	$\simeq 102.4\text{ k}$	$\simeq 1\ \mu$

Table 4.1: Resistances and capacitances in the rf wires.

Component	Resistance (Ω)	Capacitance to ground (F)
Double shielded coax	$\simeq 1$	$> 100\text{ p}$
Filter box	100k	$1\ \mu$
Double shielded coax	$\simeq 1$	$> 100\text{ p}$
Constantan loom wires	$\simeq 200$	$> 100\text{ p}$
Σ	$\simeq 100\text{ k}$	$\simeq 1\ \mu$

Table 4.2: Resistances and capacitances in the gate wires.

The setup parameters for wiring and filtering are summarized in the Table 4.2 and 4.3.

4.3.1.3 Current amplifier offset

We used a combination of preamplifier DL instruments amplifier 1211 model and a multimeter Agilent 34411A to detect source drain currents within the range of pico to nanoamps and obtain the best signal-to-noise ratio for our measurement. The current amplifier schematically is shown in Fig. 4.12 [199].

The output voltage V_{output} is approximately proportional to the input current I and the gain resistance R_{gain} :

$$V_{\text{output}} = IR_{\text{gain}} \quad (4.8)$$

The nonlinear active components of the operational amplifier can generate a voltage between the two inputs V_{off} . Because this input offset acts as a voltage source in our experiment we try to adjust it to $V_{\text{off}} = 0$. To minimize the unwanted V_{off} , our amplifier provides an offset adjust potentiometer. Fig. 4.12 depicts its working principle. By changing the resistance of the potentiometer R_2 with wiper or screw R_1 we compensate the offset voltage with the voltage drop from the supply line. Generally the effect of the input offset voltage can be described in the

Component	Resistance (Ω)	Capacitance to ground (F)
Double shielded coax	$\simeq 1$	$> 100\text{ p}$
Filter box	2.2k	1.8n
Double shielded coax	$\simeq 1$	$> 100\text{ p}$
Constantan loom wires	$\simeq 200$	$> 100\text{ p}$
Σ	$\simeq 2.4\text{ k}$	$\simeq 1.8\text{ n}$

Table 4.3: Resistances and capacitances in the current wires.

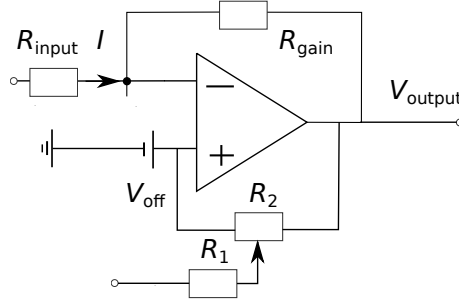


Figure 4.12: Current Amplifier circuit diagram with a potentiometer to correct input offset voltage.

formula [200]:

$$V_{\text{output}} = IR_{\text{gain}} + V_{\text{off}}(T, t) \left(\frac{1}{R_{\text{gain}}} + \frac{1}{R_{\text{input}}} \right) R_{\text{gain}} \quad (4.9)$$

We have adjusted V_{off} before each measurement via a zero set screw at the amplifier with an accuracy of about $10 \mu\text{V}$.

Input offset voltages vary with temperature T with the temperature coefficient named TC_{VOS}, or more commonly, drift. According to DL Instruments 1211 specifications, its temperature drift is $< 10 \mu\text{V}/\text{K}$. The offset drift also depends on the offset value. For example, the drift penalty for a FET input op-amp is in the order of $4 \mu\text{V}/^\circ\text{C}$ for each millivolt of the offset voltage. [201]. We stabilized the ambient temperature during our measurements to avoid strong drifts and achieved stability of $\Delta T = 1 \text{ C}$. The offset voltage also changes over time due to aging, which is usually specified in $\mu\text{V}/\text{month}$ or $\mu\text{V}/1000 \text{ hours}$. Offset time drift is proportional to the square root of the elapsed time. Thus we limit the measurement time of each plot shown in the chapter with 3 hours. We did have a quite stable offset voltage within that time window. However, we cannot exclude that drift by $1 \mu\text{V}$ happened during measuring 2D plots, which required the longest measuring time. Later we use the offset voltage as a fit parameter in our theoretical model, and we determine it from our data as good as $1 \mu\text{V}$. Table 4.4 summarizes all the gained information concerning the offset in our setup. With all these precautions we are able to reduce

Device model	Minimal value	Temperature drift	Time drift
DL Instruments 1211	$10 \mu\text{V}$	$10 \mu\text{V}/\text{K}$	$18 \mu\text{V}/1000 \text{ hours}$

Table 4.4: Input offset information for DL Instruments 1211

the level of our gate or source-drain voltage noise to below $10 \mu\text{V}$.

4.3.2 Sampleholder and the sample

The sample containing the nanostructure was mounted on the radio frequency sample holder shown in Fig. 4.13. The wafer was glued with conducting silver epoxy to a gold plated copper surface thermally connected to the mixing chamber of a dilution refrigerator at a base temperature of $\simeq 50 \text{ mK}$. The sample and sample holder are in direct contact with $\text{He}^3\text{-He}^4$ mixture for their high thermal coupling to the mixing chamber. The close-up of the Fig. 4.13 shows the nanostructure with the source-drain channel. A $1 \mu\text{m}$ wide channel (blue) containing a 2DES

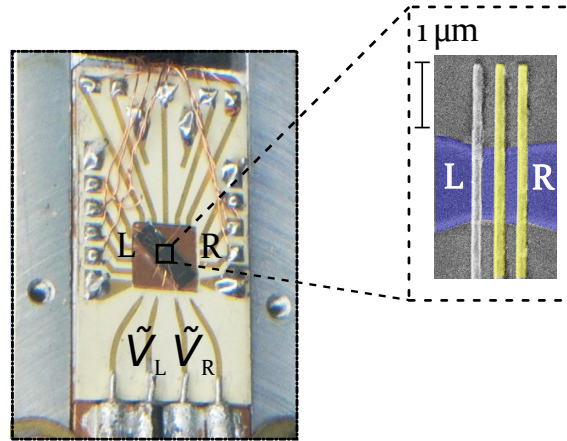


Figure 4.13: Radio frequency sample holder with sample and a scanning electron microscope image of its surface

80 nm beneath the surface has been fabricated by removing part of the wafer (grey). Metal gates used to define and control the barriers (yellow gates in the detailed sample view in Fig. 4.13, the gray gate is grounded) are connected to stainless steel rf coax cables. Electrical connection of the nanostructure is made by wedge-bonding gold wires to designated bond pads. For low crosstalk between different rf lines and good impedance matching between the sample and the bond wires should be short and well separated from other wires. We bonded several wires to one bond pad to improve impedance matching between the sample and electrical circuitry. This approach has a limitation because of the restricted area of the bond pad. It was investigated in bachelor thesis by Sebastian Konrad accompanying this thesis [29].

4.4 Calibration of the QD

We design our sample to place the QD in between of two barriers under the golden gates, indicated with yellow color in Fig. 4.13. First, we calibrate the used QD using the constant interaction model described in Sec.(4.1). A simplified sketch of the device circuit highlighting the capacitive control is presented in Fig. 4.14. We define $I > 0$ for electrons flowing from the right lead to the

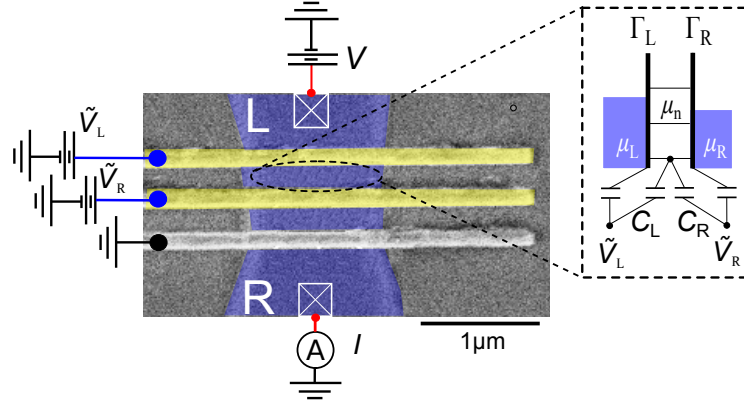


Figure 4.14: Measurement setup for the QD characterization and sketch of the QD circuit in the inset. Tunnel rates, $\Gamma_{L,R}$, and dot levels μ_n (horizontal lines) are capacitively controlled by the gate voltages, V_L and V_R . We neglect the very weak cross couplings $\Gamma_L(V_R) = \Gamma_R(V_L) = 0$. The leads contain a degenerate electron system with chemical potentials, $\mu_{L,R}$. The current is measured at the grounded right lead, while the voltage $V = (\mu_R - \mu_L)/e$ is applied on the left lead.

left lead and deal with two gates: left and right, that form the quantum dot and at the same time can act as the plunger. We substitute the voltage $\tilde{V}_{L,R}$ applied to the gates with $V_{L,R}$ to simplify the discussion, such that our working point on both gate voltages is at $V_L = V_R = 0$ mV. The offset is given by the relation:

$$V_L = \tilde{V}_L + 202 \text{ mV} \quad (4.10)$$

$$V_R = \tilde{V}_R + 91 \text{ mV} \quad (4.11)$$

Values with the tilde are absolute and without are relative. For a first orientation we present in Fig. 4.15(a) a stability diagram of our QD measured at finite dc voltage $V = (\mu_R - \mu_L)/e = 100 \mu\text{V}$ applied between its two leads (at chemical potentials $\mu_{L,R}$). Plotted is the current I as a function of relative gate voltages V_L and V_R applied to the left (L) versus right (R) gate [yellow in the figure 4.13]. We choose $n = 0$ for the QD level closest to the working point.

For $\mu_R \gtrsim \mu_n \gtrsim \mu_L$ the Coulomb blockade is lifted and current flows along broadened lines oriented perpendicular to the bisection line (dashed red line in Fig.4.14). With increasing $V_{L,R}$, the barriers coupling the QD to both leads shrink causing I to grow. On the bisecting line, the QD is symmetrically coupled to both leads (bottom-left and top-right sketch at figure 4.15(a)) but as the distance to the bisecting line is increased, one barrier shrinks and the other one grows (bottom-right and top-left sketch at figure 4.15(a)), causing I to decrease. In Fig. 4.15(b,c) we illustrate this statements and plot the current along the bisecting line (dashed red line in Fig.4.14) and perpendicular to it line indicating the current maximum (dashed black line in Fig.4.14). To characterize

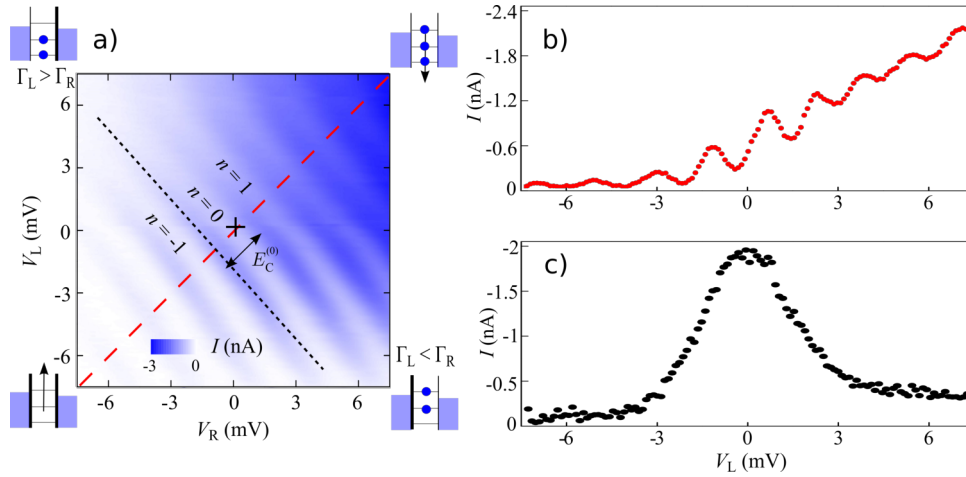


Figure 4.15: a) Current $I(V_L, V_R)$ as a function of V_L and V_R . A double arrow indicates the charging energy $E_C^{(0)}$ at the working point (black cross). Sketches show the configuration of the barriers of the QD. The thick vertical line is a high barrier; thin is a low barrier. Horizontal lines represent energy states of the QD. b) 1D cut through the bisecting line (red, dashed) of the figure a). Measured current as a function of the gate voltage V_L . c) 1D cut through one of the maxima lines (blue, dashed) of figure (a). Measured current as a function of the gate voltage V_L .

the QD we show in Fig. 4.16(a) the current I through the QD as a function of the voltage applied to the left gate V_L and the source-drain voltage V for $V_R = -2.5$ mV. Note that varying the right instead of the left gate would result in a comparable plot. It shows the white dots along the $V = 0$ horizontal indicate the positions of current maxima. As expected, they are located at the crossings of the Coulomb diamonds at $V = 0$. From the dimensions of the Coulomb diamonds (horizontal and vertical arrows) we estimate the charging energies $E_C(n)$ and the capacitive coupling κ_i , where [at the working point $C_L(0) \simeq C_R(0) \simeq 50$ aF and $C_{QD}(0) \simeq 130$ aF]. $E_C(n) = E_C^0 + n\delta E$ with the onsite energy $\epsilon_0 = -0.04$ meV and at the working point $E_C^0 = 1.27$ meV (solid lines in Fig. 4.16(a)) and an approximately constant leverage factor $\kappa_\mu = 0.38e$. The above relations can be reinterpreted as $\mu_n = nE_C^0 - n(n+1)\delta E/2 + \mu_n^0(n=0)$, where $\mu_n^0(n=0) = 0.41$ meV is the difference between the chemical potential of grounded leads and that of the lowest unoccupied dot-level at $V_L = V_R = 0$.

For Coulomb blockade oscillations it is also possible to calibrate dot-lead tunnel coupling Γ . In Fig. 4.16(b) we plot these data along the bisecting line $V_L = V_R$ of Fig. 4.15(a). The Coulomb blockade oscillations display current maxima, but their smoothed average exhibits an exponential dependence on gate voltages below the working point $V_L = V_R = 0$ devolving into a linear increase above. To capture this averaged behavior with only two free parameters, we assume the dependence as:

$$\Gamma_\alpha(V_\alpha) = \frac{\kappa_\Gamma V_\alpha}{1 - \exp(-\kappa_\Gamma V_\alpha/\Gamma)}, \quad (4.12)$$

where $\alpha = L, R$, while $\Gamma \equiv \Gamma_L^0 = \Gamma_R^0 = 0.13$ meV is the tunnel coupling at the working point and $\kappa_\Gamma \simeq 0.03e$ is the slope for large V_L, V_R . Thus the $\Gamma_{L,R}(V_{L,R})$ are determined by fitting a theoretical prediction to the current along the diagonal in Fig. 4.15. The red solid line in Fig. 4.16(b) represents the prediction based on scattering theory including the finite couplings $\Gamma_L(V_L) = \Gamma_R(V_R)$ as only broadening mechanism. Convoluting this curve with an additional Gaussian broadening of constant width yields a better fit to the measured data (blue line). The Gaussian expresses

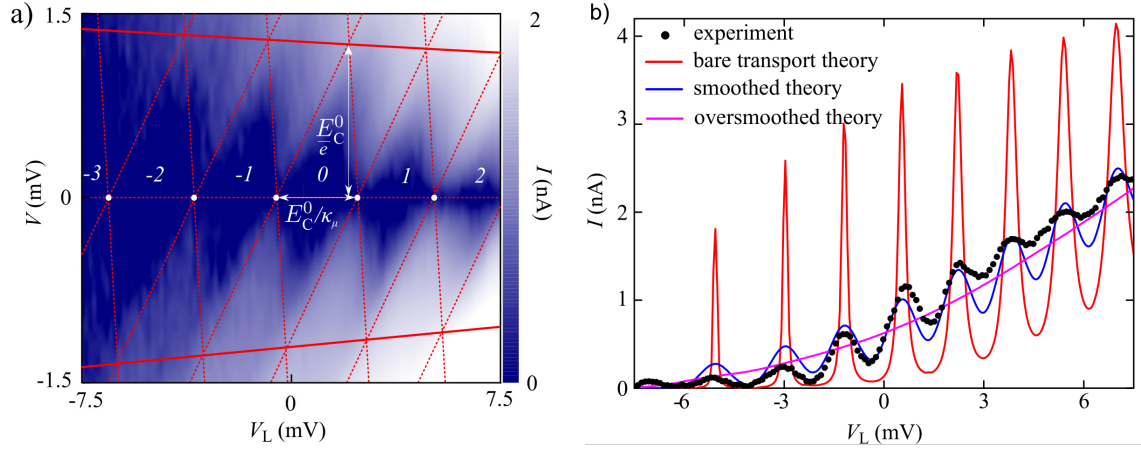


Figure 4.16: a) Calibration of charging energies and capacitive coupling constants. Plotted is measured current as a function of V_L at constant $V_R = -2.5 \text{ mV}$ and source-drain voltage V . b) Calibration of tunnel couplings. Current through the QD for $V = 100 \mu\text{V}$, data from Fig. (4.15) along its bisecting line where $V_L = V_R$ and $\Gamma_L \simeq \Gamma_R$ (black dots). Also shown are two theory curves, all using $\kappa_\Gamma = 0.03e$, $\Gamma = 0.13 \text{ meV}$ in Eq. (4.12), charging energies (see Table (A.6) in the appendix (A.2) and assuming $\Gamma_L = \Gamma_R$: $e\Gamma_{L,R}/h$ according to Eq. (4.12) current calculated with standard scattering theory with finite tunnel barriers as only broadening mechanism (red solid line); calculated current as above but additionally convoluted with a Gaussian inhomogeneous distribution of constant width mimicking slow charge noise (blue line).

an inhomogeneous broadening caused by slow statistical fluctuations of the QD levels (charge noise). In our case, this inhomogeneous broadening is the dominant broadening mechanism. The non-perfect fit is likely a consequence of the increasing relevance of dissipation as the barriers open up. Note that the values of $\Gamma_L(V_L) = \Gamma_R(V_R)$ are predetermined by the integral of the current peaks which are independent of additional broadening. We emphasize this statement by adding to Fig. 4.16(b) theoretical data with an unrealistically high inhomogeneous broadening (magenta curve). The error in determining $\Gamma_\alpha(V_\alpha)$ is related to the deviation of this theory curve from the smoothed average of the measured data (black dots in Fig. 4.16(b)). It is in the order of 10% which has a negligible influence on the theoretical predictions described later. Results of the calibration can be found in the Appendix (A.2).

4.5 Radio frequency calibration: adiabaticity requirement

Now we drive the barriers of the QD Γ_L and Γ_R by modulating the gate voltages \tilde{V}_L and \tilde{V}_R with the radio-frequency f of modulation ($f > 100\text{MHz}$) and the phase shift between two signals ϕ :

$$\tilde{V}_L(t) = \tilde{V}_L + \tilde{V}_L^{\text{rf}} \cos(2\pi f t - \phi) \quad (4.13)$$

$$\tilde{V}_R(t) = \tilde{V}_R + \tilde{V}_R^{\text{rf}} \cos(2\pi f t) \quad (4.14)$$

Figure 4.17 illustrates the experimental setup used for measurement current through the driven QD. A general problem of radio-frequency transport measurement is non-perfect impedance

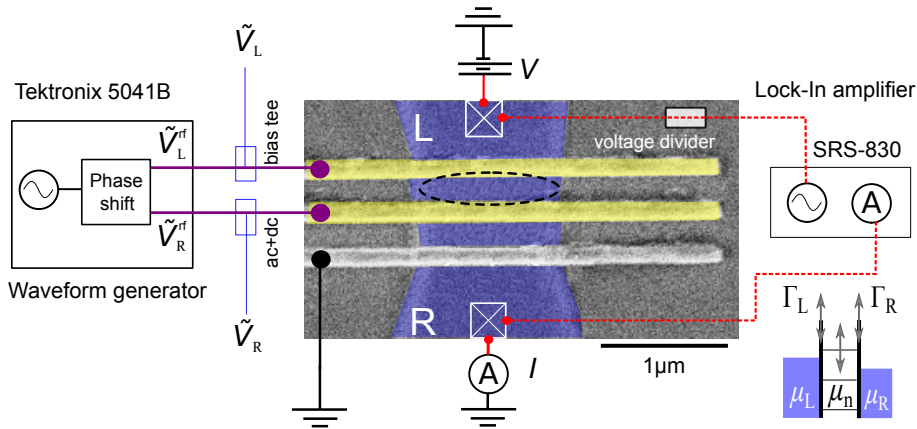


Figure 4.17: Measurement setup for the QD rf calibration and sketch of the QD circuit in the inset. We drive the QD with two rf modulation signals applied to the barriers: \tilde{V}_L^{rf} and \tilde{V}_R^{rf} at frequency f and with phase shift ϕ . Setup was optimized for performing both Lock-in and DC current I measurements. Colour indication of rf, current and gates lines is done as in Fig. 4.11. For the Lock-In measurements we used a voltage divider 1 : 40000.

matching of the signal applied from the waveform generator compared to the signal arrived at the QD. For modulating two gates simultaneously this drawback causes different amplitudes of signals that arrive at two gates for the equal amplitude applied from the device. This effect also gives rise to standing waves caused by reflections of the rf-signal at the sample holder and meters away at the rf generator and as a result additional phase differences between the two modulation signals. In our experiment we measure the dc current I through a driven QD at various frequencies of modulation. During every pumping cycle we expect to load-unload to the QD constant number of electrons, thus in the adiabatic regime we expect to find a pump current $|I| \propto f$, if $V = 0$ [189]. Instead in Fig. 4.18 we observe strong current oscillations which indicate an oscillating modulation amplitude even though the rf signal strength is fixed. Here we show the maximum current within the phase difference between two signals range ϕ from 0 to 2π , when $V = 0$ and modulation frequencies of the barriers are the same.

In order to solve this problem for our ratchet experiments we restricted ourselves to specific modulation frequencies, namely $f = 25, 50, 100, 150, 200\text{ MHz}$. Then we can perform calibration of the gates based on Coulomb blockade oscillations measuring at different frequencies. We exploit plunger function of each barrier and drive it separately while keeping the other barrier constant. When the QD chemical potential is driven with constant frequency each Coulomb

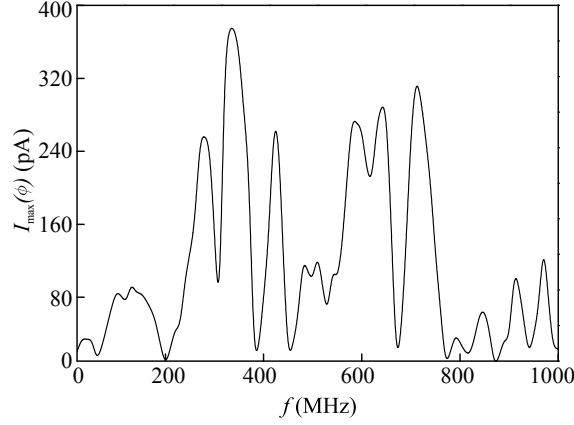


Figure 4.18: Maximum current I_{\max} for phase difference ϕ from 0 to 2π through the unbiased QD plotted as a function of modulation frequency at $k = 1$ and modulation amplitude $A = 3E_C^0$.

resonance splits in two resonances located at the turn around points of driving signal $\tilde{V}_{L,R}(t)$. These splittings are proportional to \tilde{V}_R^{rf} and we therefore expect:

$$A_{L,R} = \kappa_\mu \alpha_{L,R}(f) \tilde{V}_{L,R}^{\text{rf}} / e \quad (4.15)$$

In Fig. 4.19 we demonstrate exemplary for one of the gates the calibration of the modulation amplitude at these frequencies. The calibration was performed with Lock-in amplifier SRS-830 at $V = 0$ with modulation amplitude $\delta V = 1$ V applied from the device through the voltage divider 1 : 40000, measured current represents the static rectification of current in our QD. The flocks of

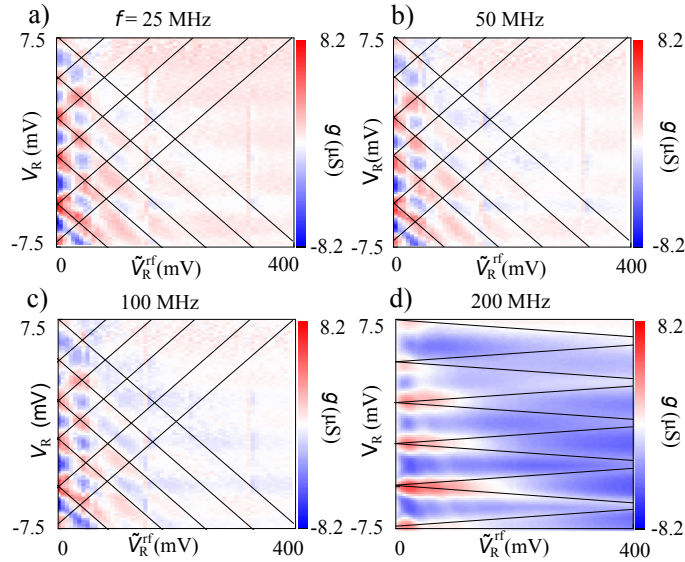


Figure 4.19: Radio frequency calibrations of the right hand side gate for $f = 25, 50, 100, 200$ MHz in panels a-d. Plotted is the differential conductance of the QD as function of $V_R = \tilde{V}_R + 91$ mV and its modulation amplitude \tilde{V}_R^{rf} (where $\tilde{V}_R(t) = \tilde{V}_R + \tilde{V}_R^{\text{rf}} \cos 2\pi f t$) while the left gate voltage is kept constant $V_L = 0$.

parallel black lines with mutually opposite slopes are guide for the eyes indicating current resonances which depart proportional to the increasing amplitude. Their slopes $\alpha_R(f) = \Delta V_R / \Delta \tilde{V}_R^{\text{rf}}$

can be used to calibrate the actual rf modulation amplitude. To account for the frequency dependent calibration in our measurements we compensate the amplitudes at each frequency according to Eq. (4.15). In Fig. 4.20(a) we present $I(\phi)$ at four frequencies for $k = 1$ and identical modulation amplitudes $A = 3E_C^0$ after calibration. The current has been corrected for the frequency dependent transfer functions of the cables by applying the calibration factors $\alpha_{L,R}(f)$ listed in Table A.7 in the Appendix (A.2) according to Eq. (4.15). The same data scaled by $I(f) \rightarrow \frac{100\text{MHz}}{f}I(f)$

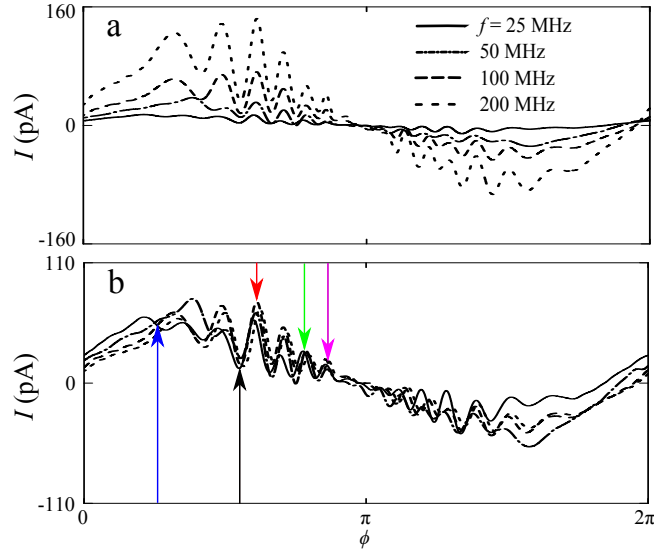


Figure 4.20: (a) Current I as a function of phase difference ϕ for $k = 1$, and $A = 3E_C^0$. (b) Same data as in panel a but scaled by $I(f) \rightarrow \frac{100\text{MHz}}{f}I(f)$.

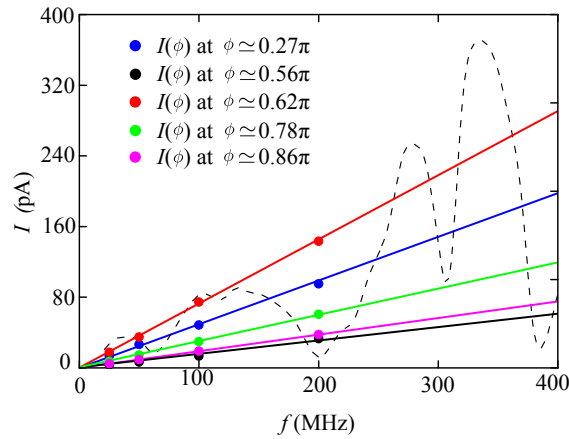


Figure 4.21: Frequency dependence of current before (black dashed line) and after (coloured solid lines) calibration of the modulation amplitude. Coloured symbols indicate current values of specific maxima and minima (constant phase) marked in Fig. 4.20(a) by arrows. The straight lines are a guide for the eyes and verify the expected adiabatic regime.

to the current expected at $f = 100$ MHz are approximately frequency independent [Fig. 4.20(b)]. It corroborates our assumption of adiabatic charge transport. Small deviations, especially those near $\phi = 0$ are probably related to a local disorder potential which compromises the spacial

symmetry. The importance of a correct calibration becomes evident in Fig. 4.21 plotting I_{\max} in direct comparison to the uncalibrated current taken from Fig. 4.18. The dashed line presents uncalibrated data identical to those in Fig. 4.18. Straight lines are the guide for the eyes indicating the adiabatic transport regime. The relative phase between two modulation signals can be determined from the symmetry properties discussed below.

4.6 Lissajous rocking ratchet

Following the calibration explained above we adjust the modulation amplitudes $A_{L,R}$ to be identical. Now we again use the setup from the Fig. 4.17(a) and measure the dc source-drain current I . In our experiment we periodically modulate $V_L(t)$ and $V_R(t)$ to break time-reversal symmetry such that they define trajectories along Lissajous figures centered at the working point:

$$\vec{v}_{k,\phi}(t) = \begin{pmatrix} V_L(t) \\ V_R(t) \end{pmatrix} = A \begin{pmatrix} \cos(2\pi f t - \phi) \\ \cos(k 2\pi f t) \end{pmatrix} \quad (4.16)$$

with $k \geq 1$ (curves with ratios k and $1/k$ can be mapped to each other). For simplicity, we restrict ourselves to integer frequency ratios k (we use $k = 1, 2, 3, 4$ in the experiments). The

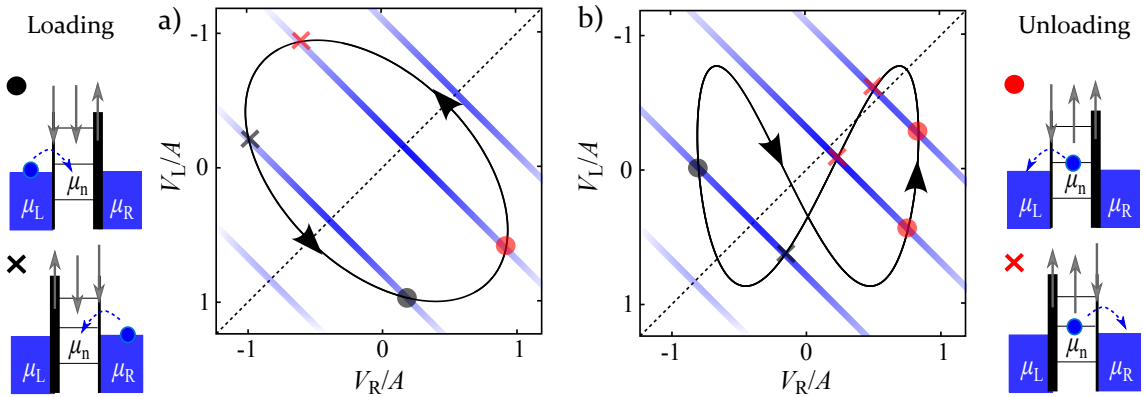


Figure 4.22: Pumping trajectory of the system plotted on reduced sketch of the stability diagram similar to Fig. 4.15 for the $k = 1, \phi = 0.65$. The direction of traversing the loop is shown with red arrows. Simplified sketch of the stability diagram 4.15 with an example Lissajous trajectory of the system for the $k = 2, \phi = 0.85\pi$. Insets are sketches of unloading and loading mechanisms (marked with red crosses). Blue lines depict current maxima in Fig. 4.15. The diagonal dashed line is the bisecting line in Fig. 4.15.

trajectories of the system can cross several charging lines of the stability diagram [see example in Fig. 4.22]. A historical experiment [202] realized an adiabatic electron pump for a two-parameter drive that corresponds to $k = 1$. It was based on periodically modulating the shape of a rather large mesoscopic QD following a general scenario of parametric pumping the QD defined by Brouwer in Ref. [191]. Our first experiment also resembles an adiabatic electron pump defined by Eq. (4.16) with $k = 1$, i.e. identical frequencies. In contrast to Ref. [202] we have considered a smaller QD with a much larger charging energy E_C , hence discrete levels. The latter allows quantized pumping [203] and facilitates a theoretical treatment using the independent channel approximation.

In Fig. 4.22(a) we plot trajectory of the system on stability diagram for the parameters $k = 1$ and $\phi = 0.65\pi$. Traversing the system counter-clockwise we lift the chemical potential of

the QD and end up crossing the charging lines. This position corresponds to the unloading of an electron. In the adiabatic regime (see above) each QD level is unoccupied whenever $\mu_n(t) > \mu_{L,R}$ and its n -electron ground state is occupied for $\mu_n(t) < \mu_{L,R}$. Whenever $\mu_n(t) \simeq \mu_{L,R}$ an electron tunnels into the QD if $d\mu_n/dt < 0$ and out of the QD if $d\mu_n/dt > 0$. With which lead the electron is thereby exchanged depends on ϕ and the ratio Γ_L/Γ_R , which is modulated in time, see Eq. (4.16) and above. These loading/unloading (black/red) events are sketched in the right and left insets of Fig. 4.22 indicating the exchange of electron with the left lead (circle) and the right lead (cross). We show the measured dc current for $k = 1$ in both Cartesian and spherical

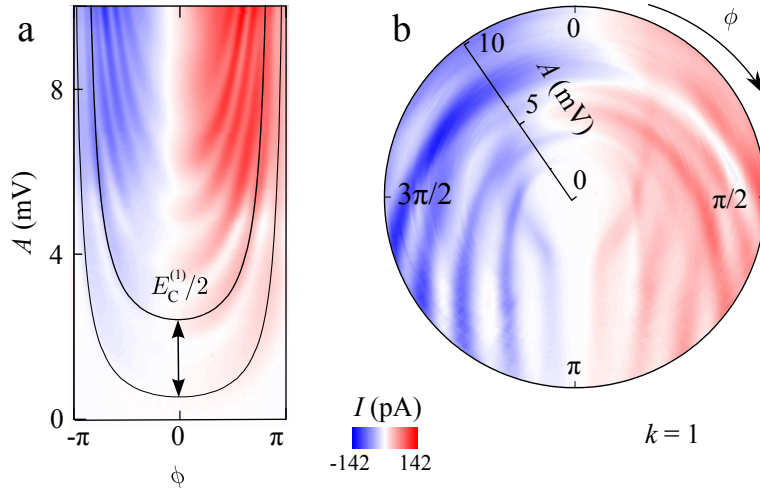


Figure 4.23: Measured current I versus modulation amplitude and phase for (a) $k = 1$ and $f_L = f_R = 200$ MHz in Cartesian and polar representation

coordinates for comparison on Fig. 4.23. The latter can help to emphasize symmetrical properties of the plot and is commonly used for experiments with a phase difference between the signals. We found that at $\phi = 0$ and π the direction of the system trajectory changes, i.e., measured current follows mirror symmetry. The current plotted as a function of A and ϕ also displays clear resonances following lines of constant $A \cos(\phi/2)$ (solid lines). These resonances indicate discrete current contributions of the n -electron QD levels separated by $\kappa_\mu \Delta A = E_C^{(n)}/2$, where the factor 2 accounts for two gates being modulated. During each pumping cycle approximately $\text{int}(2A\kappa_\mu/E_C^{(0)})$ levels fulfill $\mu_n(t) = \mu_{L,R}$ twice. The two-fold symmetry observed in Fig. 4.23 resembles the two-fold symmetry of the according to Lissajous figure presented in Fig. 4.22.

4.6.1 Current symmetries

Now we describe the experiment with driven QD in case of frequency ratio $k > 1$. We start with $k = 2$ with trajectory of the system and the loading/unloading mechanisms sketched in Fig. 4.22(b). The Lissajous figure for the higher k has higher number of loading/unloading events and also higher number of enclosed loops that correspond to the internal symmetry of the Lissajous curve. To emphasize the symmetry properties we shift the working plot to the mixed valance

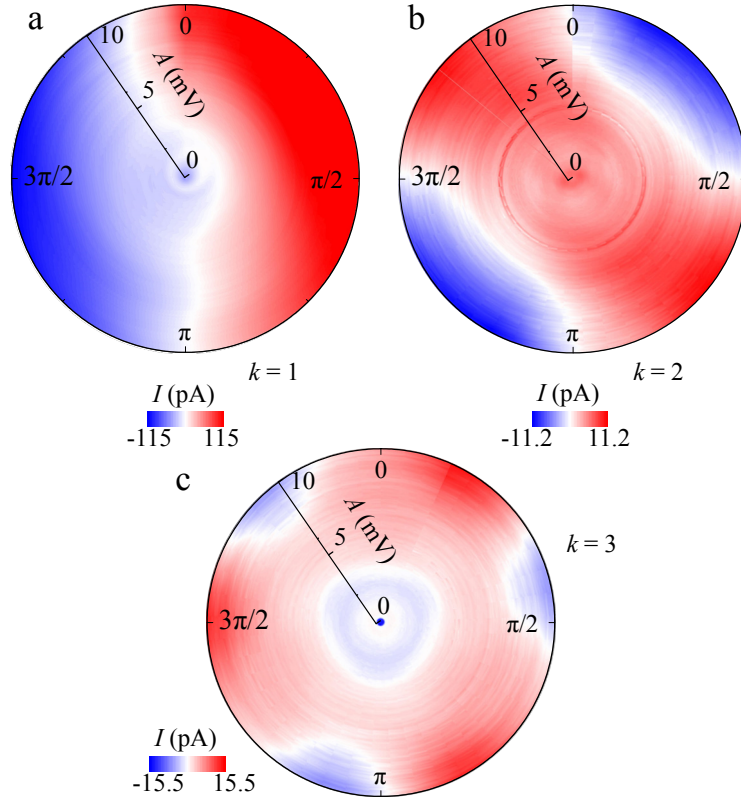


Figure 4.24: Measured current I versus modulation amplitude and phase for (a) $k = 1$ and $f_L = f_R = 100$ MHz, (b) $k = 2$ and $f_L = 50$ MHz $f_R = 100$ MHz, (c) $k = 3$ and $f_L = 50$ MHz $f_R = 150$ MHz. The working point is defined by $\bar{V}_L = 12.5$ mV and $\bar{V}_R = 12.5$ mV near the upper right corner of Fig. 1a. The enhanced dot-lead tunnel coupling washes out most fine structures compared to the data in Fig. 4.25 above.

regime where the Coulomb current peaks overlap strongly ($V_L = 12.5$ mV and $V_R = 12.5$ mV). In Fig. 4.24 we present such data up to $k = 1, 2, 3$ but all in spherical coordinates. The dot-lead tunnel couplings increased and the k -fold symmetry is more evident. The result is a strong broadening which thoroughly washes out most fine structure of the current. Scenario for $k \geq 1$ resembles a rocking ratchet [181] where the current changes direction at $\phi = 0, \pi$, independent of k . For $k = 1$ it gives rise to the two-fold symmetry of a pump observed in Fig. 4.23(a,b).

A ratchet with $k > 1$ has k -fold symmetry (see Fig. 4.25(a,b,c,d)) and goes qualitatively beyond the scope of a pump. For the initial position of the working point ($V_L = 0$ mV and $V_R = 0$ mV) we compare measured data in Fig. 4.25 for $k = 1, 2, 3, 4$. The data contains the k -fold symmetry but also show a complex detailed structure. In every plot of Fig. 4.25 I has $2k$ symmetry points with odd parity, including the phases $\phi = 0, \pi$, where the symmetry is somewhat

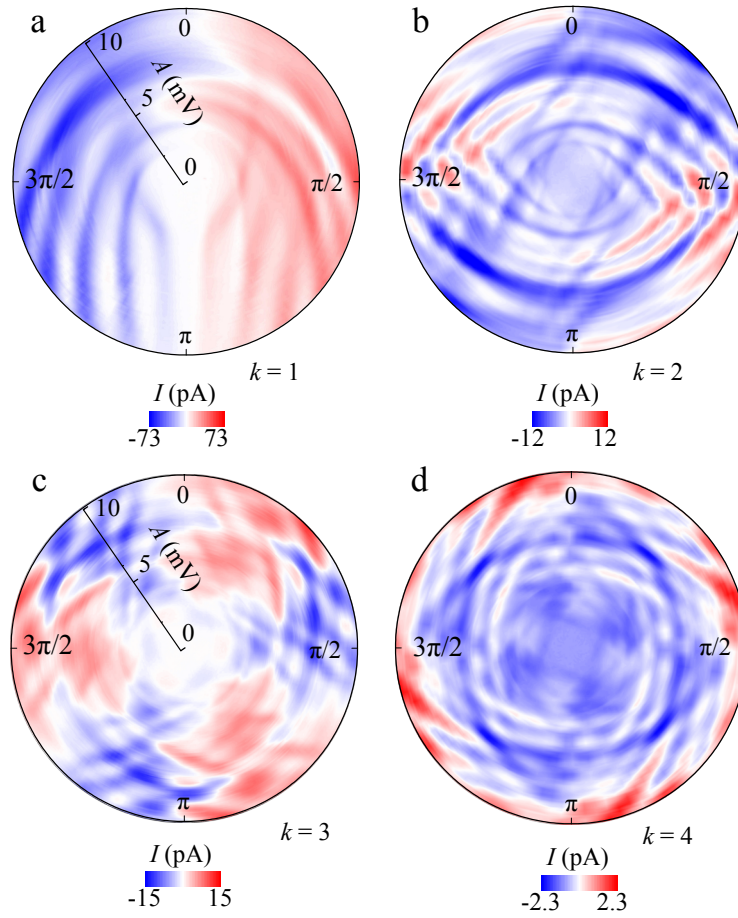


Figure 4.25: Measured current I versus modulation amplitude and phase for (a) $k = 1$ and $f_L = f_R = 100\text{MHz}$, (b) $k = 2$ and $f_L = 100\text{MHz}$ $f_R = 200\text{MHz}$, (c) $k = 3$ and $f_L = 50\text{MHz}$ $f_R = 150\text{MHz}$, (d) $k = 4$ and $f_L = 50\text{MHz}$ $f_R = 200\text{MHz}$.

distorted due to a source-drain dc-voltage and other reasons discussed below. The symmetry can be compromised because of (i) dissipation by transitions within the QD's Excitation spectrum. This, however, would go along with non-adiabaticity which we already excluded; (ii) a spatially asymmetric local disorder potential which influences the ratio Γ_L/Γ_R as the function of n , depending on the electronic probability distribution. This is ignored in our model but can explain deviations from the measured current, particularly near $\phi = 0$ where the $\mu_n(t)$ are modulated strongest and additional spatial disorder causes rectification [183]; (iii) the n -dependence of the charging energy and the choice of the working point; (iv) a dc voltage between the leads ($V \neq 0$). Points (iii) and (iv) are included in our model and discussed in the next section.

4.6.2 Theoretical approach

The theoretical model was constructed by Sigmund Kohler from Instituto de Ciencia de Materiales de Madrid (CSIC). Here we give a summary of the model, and the reader is advised to Ref.[167] for details. A formal description of the general case for any integer k can be summarized as follows: we use an expression for the current obtained with Floquet transport theory [204]. Taylor expansion up to first order in the driving frequency f provides the adiabatic limit of the dc current:

$$I_\alpha = \sum_\beta \bar{G}_{\alpha\beta} V_{\text{off}} + I_\alpha^{\text{rect}} + \frac{Q_\alpha^{\text{cycle}}}{T}, \quad (4.17)$$

where $\alpha = \text{L,R}$. The current can be traced back to the transport properties of the time-independent system for the parameters along the trajectory $\vec{v}_{k,\phi}(t)$, defined in Eq. (4.16). The first term of Eq. (4.17) contains the time-averaged conductance of the QD, \bar{G} . It can be understood as dc current which flows whenever any resonance fulfills the condition $\mu_L \lesssim \mu_n \lesssim \mu_R$ (or $\mu_R \lesssim \mu_n \lesssim \mu_L$).

$$\bar{G} = \int_0^T \frac{dt}{T} G(\vec{v}(t)), \quad (4.18)$$

where the term $G_{\alpha\beta}(\vec{v}(t)) = e^2/h[\delta_{\alpha\beta} - T_{\alpha\beta}(t, \vec{\mu})]$ takes into account the periodic chemical potential $\tilde{\mu}_\alpha = \mu_{\alpha 0} + w_\alpha(t)$. The $w_\alpha(t)$ term arise due to the modulation of the chemical potential in the leads and discussed below. Non-zero dc-current contribution occurs because of the unwanted offset voltage from the input of the current amplifier. Typically such an offset voltage can be adjusted with an accuracy of $\sim 10 \mu\text{V}$ and slowly drifts in time due to its dependence on the ambient temperature (as was discussed in section 4.3.1.3). The second contribution in Eq. (4.17), I_α^{rect} , is a correction that stems from a tiny ac modulation $w_\alpha(t)$ of the lead chemical potentials induced by the capacitive coupling between each gate and its adjacent lead. Despite that the ac bias $w_\alpha(t)$ vanishes on average, its impact becomes rectified and contributes

$$I_\alpha^{\text{rect}} = \int_0^T \frac{dt}{T} G(\vec{v}(t)) w_\alpha(t) \quad (4.19)$$

to the dc measured current, where T is the modulation period. Transmission amplitudes are directly related the corresponding scattering matrices $T_{\alpha\beta}(t, \mu_\alpha) = |S_{\alpha\beta}(t, \mu_\alpha)|$ in the form of Eq. (4.6). The last term in Eq. (4.17) reflects the charge parametrically pumped through source contact during one driving period,

$$Q_\alpha^{\text{cycle}} = \frac{1}{2\pi} \text{Im} \int_0^T dt \left(S(t, \mu_\alpha) \frac{\partial}{\partial t} S^\dagger(t, \mu_\alpha) \right)_{\alpha\alpha}. \quad (4.20)$$

The shape of the driving can be expressed by a closed curve \mathcal{C} in parameter space, $\vec{v}(t) = \vec{v}(t+T)$. Then, if \mathcal{C} is traversed adiabatically slowly, the scattering matrix depends merely parametrically on time, i.e. $S(t, \epsilon) = S(\vec{v}(t), \epsilon)$, where the latter is the static result for the instantaneous value of \vec{v} at time t . This allows one to transform the time integral in Eq. (4.20) to a closed line integral to obtain

$$Q_\alpha^{\text{cycle}} = \frac{1}{2\pi} \text{Im} \oint_{\mathcal{C}} d\vec{v} \cdot \left(S(\vec{v}, \mu_\alpha) \text{grad} S^\dagger(\vec{v}, \mu_\alpha) \right)_{\alpha\alpha}. \quad (4.21)$$

Applying Stokes' theorem, one can transfer this expression into a surface integral to obtain Brouwer's formula [191]. A necessary implication of Eq. (4.17) is the separation of the average current into a dc contribution stemming from the average conductance and an adiabatically

pumped charge. The main difference between these two quantities is their behavior under time inversion of the closed curve \mathcal{C} : while the average conductance is invariant, the pumped charge acquires a minus sign. Below, we will explore this symmetry property for the Lissajous curves applied in the experiment.

4.6.3 Contribution of a single QD level

In our experiment, the QD is driven with an amplitude A ranging from zero to the rather large value $5E_C^0$, so that the onsite energy of the QD may change by several charging energies, and we will consider up to 10 excess electrons. Moreover, we assume that each charge state of the quantum dot contributes as independent transport channel to the current (as we did previously in section (4.1)). The driving must be slow enough that the quantum dots can be assumed to be always relaxed to its many-particle ground state. It is instructive to investigate the contribution of a single resonance to both the average conductance and the charge per cycle. For this purpose, we assume that at a resonance, the dot-lead rates are weakly time-dependent with average values $\bar{\Gamma}_{L,R}$, while $\mu_n(t) \simeq (t - t_0)\dot{\mu}_n$. Then the straightforward evaluation of Eq. (4.18) with the off-diagonal matrix element of S_n yields

$$\bar{G}^n \simeq \frac{e^2}{h} \frac{\bar{\Gamma}_L \bar{\Gamma}_R}{\bar{\Gamma}_L + \bar{\Gamma}_R} \frac{\Omega}{|\dot{\mu}_n|} \quad (4.22)$$

Notice that $\dot{\mu}_n$ is proportional to Ω and, thus, \bar{G}^n is frequency independent. In Fig.4.26 we plot

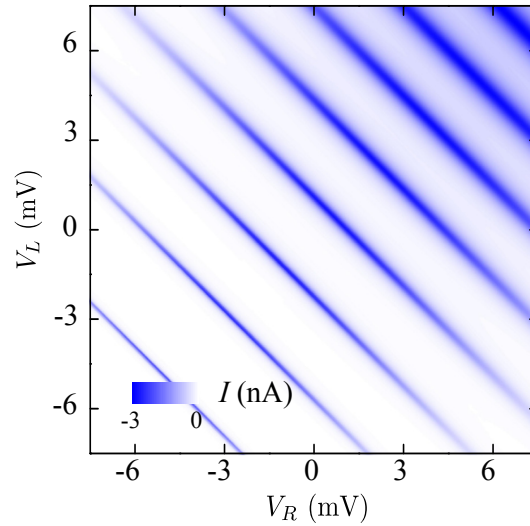


Figure 4.26: Current in the absence of the modulation for bias voltage $V = 200\text{mV}$.

calculated conductance map that reproduces the measured Fig.4.15. The averaged value of tunneling through the dot during one period will be proportional to the area of conductance peaks inclosed by the corresponding Lissajous trajectory of the system.

The pumped charge is essentially determined by the scattering phase in the prefactor of S_n . Assuming again that the $\bar{\Gamma}_{L,R}$ are practically constant at the resonance, we find [203]

$$Q_L^n \simeq \frac{e\bar{\Gamma}_L}{\bar{\Gamma}_L + \bar{\Gamma}_R} \text{sign}(\dot{\mu}_n). \quad (4.23)$$

This means that for $\bar{\Gamma}_L \gg \bar{\Gamma}_R$, an electron enters from or leaves to the left lead depending on the sign of $\dot{\mu}_n$. In the opposite limit, the right lead is relevant and Q_L^{res} is much smaller than the elementary charge. This also emphasizes the role of the parameter dependence of the tunnel rates: In the derivation of Eq. (4.23), we assumed that the $\Gamma_{L,R}$ stays constant when a level crosses the chemical potential of a lead at time $t = t_0$. However, in a complete pump cycle, the level will cross the chemical potential as many times from above as it crosses from below. Thus if $\Gamma_{L,R}$ were constant, the net charge pumped from the left lead to the dot in the whole cycle would vanish. In turn, we will observe significant pumping from the left lead to the right lead if $\Gamma_L \gg \Gamma_R$ when the dot level is lowered, while $\Gamma_L \ll \Gamma_R$ when the level is raised. For our QD system, the pumped currents entering the dot from the left and from the right lead compensate each other so that $Q_L^{\text{cycle}} + Q_R^{\text{cycle}} = 0$. Nevertheless, the vector fields appearing in the integral in Eq. (4.21) may differ by more than their sign, because the integrands are relevant only up to a gradient field which vanishes under the closed line integral. Therefore it is more convenient to discuss the integrand of the symmetrized expression for the pumped charge: $Q^{\text{cycle}} = \frac{1}{2}(Q_L^{\text{cycle}} - Q_R^{\text{cycle}}) = \oint_C d\vec{v} \cdot \vec{a}(\vec{v})$ with the vector field

$$\vec{a} = \frac{i}{4\pi} \sum_n \left\{ (S_n \text{grad } S_n^\dagger)_{LL} \Big|_{\mu_L} - (S_n \text{grad } S_n^\dagger)_{RR} \Big|_{\mu_R} \right\}. \quad (4.24)$$

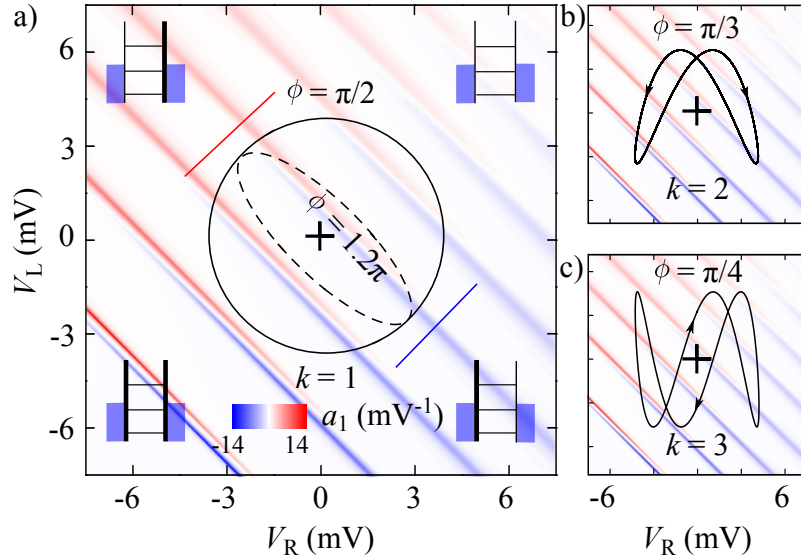


Figure 4.27: Vector field \vec{a} versus gate voltages and typical Lissajous trajectories for $k = 1, 2, 3$ according to Eq. (4.16). QD sketches indicate relative strengths of tunnel couplings.

Figure 4.27 contains example Lissajous curves $\vec{v}_{k,\phi}(t)$: a circle for $k = 1$, a distorted figure eight for $k = 2$ and a triple loop for $k = 3$. For $k = 1$ and ϕ slightly different from π , $\vec{v}_{k=1,\phi}(t)$ is an eccentric ellipse [dashed line in Fig. 4.27] which corresponds to the pumping measurements already discussed in literature [202, 205, 206]. Whenever $\vec{v}_{k,\phi}(t)$ crosses a charging line, $\mu_n(t) = \mu_{L,R}$ and the charge of the QD changes by one electron. If this happens in a red region corresponding to $a_1, a_2 > 0$ with $\Gamma_L > \Gamma_R$ an electron will be exchanged preferably with the left lead. In the blue region with $a_1, a_2 < 0$ and $\Gamma_L < \Gamma_R$, charge exchange with the right lead is preferred. Crossing a blue area from above and a red area from below (see example for $k = 1$) both contribute to $I < 0$, each with half an electron charge per cycle. Our example for $k = 3$ also results in $I < 0$. For $k = 2$, the contributions of the two loops to Q^{cycle} have opposite sign and,

thus, cancel each other to some extent. Therefore, we expect the pump current for $k = 2$ to be generally smaller than for $k = 1$. A generalization of these arguments leads to the expectation that for even k , the pump current should be smaller than for odd k .

Our experimental results indicate that the rf modulation of gate voltages induces a tiny ac bias in the source-drain line. This coupling between the gate voltage and source-drain voltage is sketched in Fig. 4.28. We model it as modulation of the chemical potentials $\tilde{\mu}_\alpha(t) = \mu_\alpha + ew_\alpha(t)$ with a phase shift of $-\pi/2$ (that is typical for a capacitive coupling) compared to the modulation of the gate voltages [described in Eq. (1)]:

$$\vec{w}_{k,\phi}(t) = \begin{pmatrix} w_L(t) \\ w_R(t) \end{pmatrix} = \kappa_{ac} A \begin{pmatrix} \sin(\Omega t - \phi) \\ \sin(k\Omega t) \end{pmatrix}. \quad (4.25)$$

In comparison to the gate voltages in Eq. (4.16), the ac modulation of the chemical potentials, \vec{w} , contains a sine instead of a cosine. Being related to the phase shift this is dynamic rectification and it is very different from rectification caused by static asymmetries of the I - V curve [207]. I^{rect} turns out essential for the quantitative agreement between experiments and theory. The capacitive coupling constant κ_{ac} turns out to be of the order $5 \cdot 10^{-4}$ and is expected to decrease with the modulation frequency, $\kappa_{ac} \propto \Omega^{-1}$. The amplitude of the resulting ac source-drain voltage is of the order $0.1 \mu\text{V}$ for the driving of barriers within the range of 10 mV.

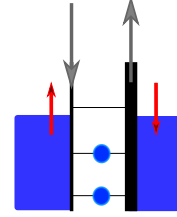


Figure 4.28: Driving of the barriers perturb the motion of the chemical potential in the leads. Vertical lines denote the barriers, horizontal- QD energy states.

4.6.4 Comparison between the theory and experiment

Figure 4.29 compares a typical measurement (lhs) with model predictions (rhs) for $k = 1$ and $\mu_L \simeq \mu_R$. To accurately model our system, we include all experimentally known facts such as $E_C^{(n)}$ and line broadening into our numeric calculations. For the theory data in Fig. 4.29 we have

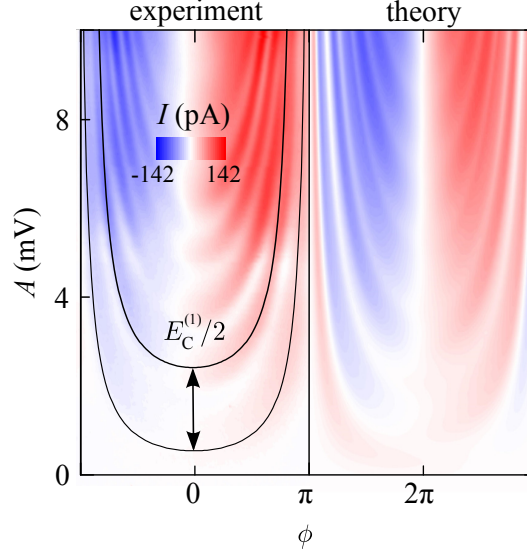


Figure 4.29: Measured (left) versus calculated (right, $V = 1 \mu\text{V}$) $I(A, \phi)$. $V_{L,R}$ are modulated according to Eq. (4.14) with $f = 200 \text{ MHz}$ ($k = 1$). Inset: measured $I(f)$ at $A = 9 \text{ mV}$ for $\phi \simeq 0.3\pi$ (blue) and $\phi \simeq 0.6\pi$ (red).

used $V = 1 \mu\text{V}$ which provides good agreement with the measured data. Below we will see that the symmetry properties of $I(\phi)$ allow us to accurately determine offset voltages. In Fig. 4.30 we compare measured ratchet currents for $k = 2$ and $k = 3$ as function of the modulation amplitude and ϕ . However, the naive expectation $Q^{\text{cycle}} = 0$ for even k is compromised because of the mismatch between the symmetry properties of the Lissajous figures and that of the charge stability diagram [see for instance the upper right panel of Fig. 4.27 for $k = 2$, in which the left loop crosses three and the right loop only two charging lines]. This mismatch is generic for $k > 1$ but its degree depends on the choice of the working point [black cross in Fig. 4.27] and the variation of the gap sizes between charging lines which decrease for increasing n . Under any circumstances, with growing k , there will be an increasing number of contributions with opposite sign, causing an increasing amount of cancellation. As a consequence, even small deviations from our model assumptions will lead to visible differences between calculated and measured data. In particular asymmetries of the confinement potential defining the QD, typically induced by static disorder, will have a stronger effect at larger k . This tendency becomes evident when analyzing the match between theory and experiments in detail: it is superior in Figs. 4.29, below, for $k = 1$ compared to that in Fig. 4.30 for $k = 2, 3$.

The central question is that of the symmetry properties of the dc conductance, the pumped charge and the rectified part of the current as a function of the modulation parameters. We start our symmetry considerations by noticing that the Lissajous figures obey $\vec{v}_{k,\phi}(t) = \vec{v}_{k,\phi+2\pi/k}(t + 2\pi/k\Omega)$, namely that a phase shift of $2\pi/k$ is canceled by a time shift of $2\pi/k\Omega$. This implies

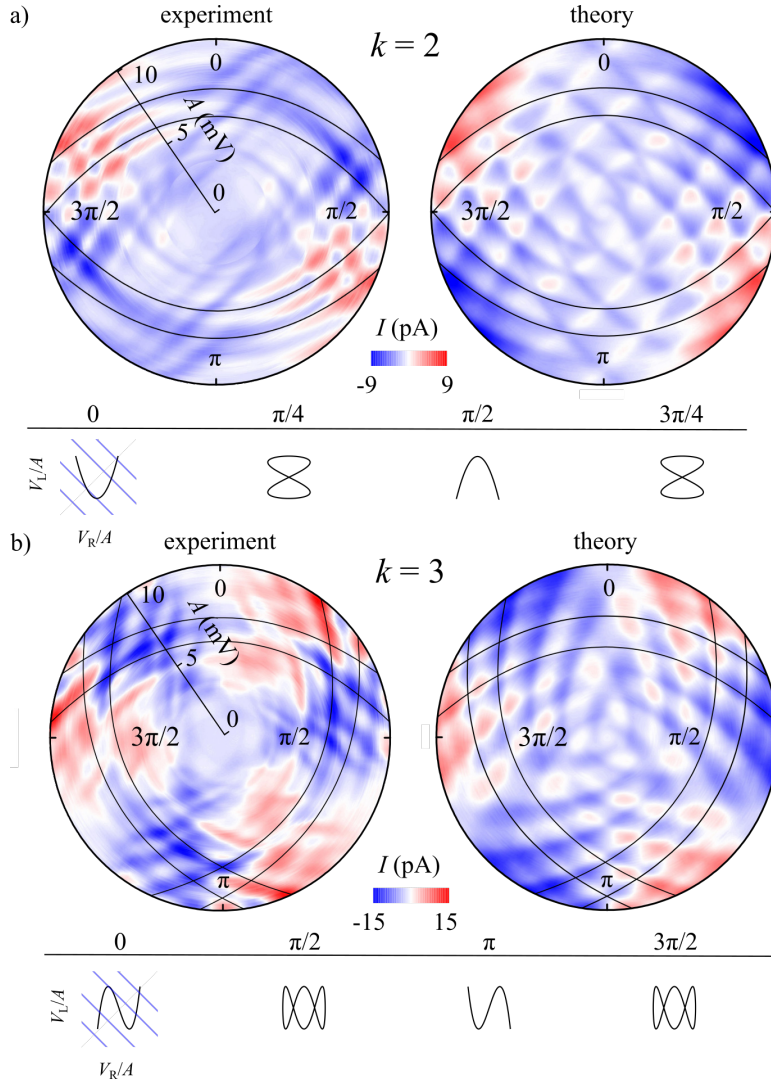


Figure 4.30: Measured (left) and simulated (right) current as a function of modulation amplitude A (radius) and phase difference ϕ (angle) between $V_L(t)$ and $V_R(t)$: (a) $V_L(t)$ at 50 MHz and $V_R(t)$ at 100 MHz ($k = 2$), see Eq. (4.14); (b) 50 MHz and 150 MHz ($k = 3$). Bottom: example Lissajous figures for $k = 2$ and $k = 3$.

that the dc current patterns, being averaged over time, as a function of ϕ possesses a k -fold symmetry in ϕ . A further symmetry property of the three contributions to the current in Eq. (4.17) follows from the behavior of $\bar{G}_{\alpha\beta}$, Q^{cycle} , and I^{rect} under time reversal. It plays a crucial role for adiabatic pumping [191] and ratchet effects. By combining the above k -fold symmetry with time reversal, we will find $2k$ symmetry points at which Q^{cycle} and I^{rect} vanish. For a derivation, we determine for each Lissajous curve $\vec{v}_{k,\phi}$ a time-reversed partner with phase ϕ' which must fulfill the condition

$$\vec{v}_{k,\phi}(t) = \vec{v}_{k,\phi'}(-t + t_0), \quad (4.26)$$

for all times t . The inversion $t \rightarrow -t$ is thereby accompanied by a time offset t_0 , which is permitted by the time periodicity of the integrands in Eqs. (4.19), (4.18), and (4.21). Inserting Eq. (4.16) into Eq. (4.26) yields $\Omega t_0 = 2\pi\ell/k$ and $\phi' = -\phi + 2\pi(\ell/k + \ell')$ where $\ell = 0, 1, \dots, k-1$ and $\ell' = 0, 1$. The special phases $\phi_{\ell\ell'} = \pi(\ell/k + \ell')$ fulfill $\phi = \phi'$ (with t_0 given above), so that the original and the time-reversed Lissajous curves [defined by Eq. (4.16)] lie on top of each other, while they

evolve in opposite direction in time. Thus, the phases $\phi_{\ell\ell'}$ define $2k$ in-equivalent points with time-reversal symmetry. The labeling of the symmetry points is motivated by their derivation, while the alternative designation $\phi_\ell = \ell\pi/k$ with $\ell = 0, \dots, 2k - 1$, is more convenient for the discussions later.

An interesting observation is that there, the Lissajous curve takes the form $V_R(V_L) = \pm \cos[k \arccos(\pm V_L)]$. This defines the k th Chebyshev polynomial [208] which represents a degenerate loop that does not enclose a finite area. As a consequence, Q^{cycle} and I^{rect} (with odd symmetry under time-reversal) vanish. Hence, at the symmetry points the current takes the value $\bar{G}V$ and, in particular, vanishes for $V = 0$. Substituting in Eq. (4.16) the phase ϕ by the

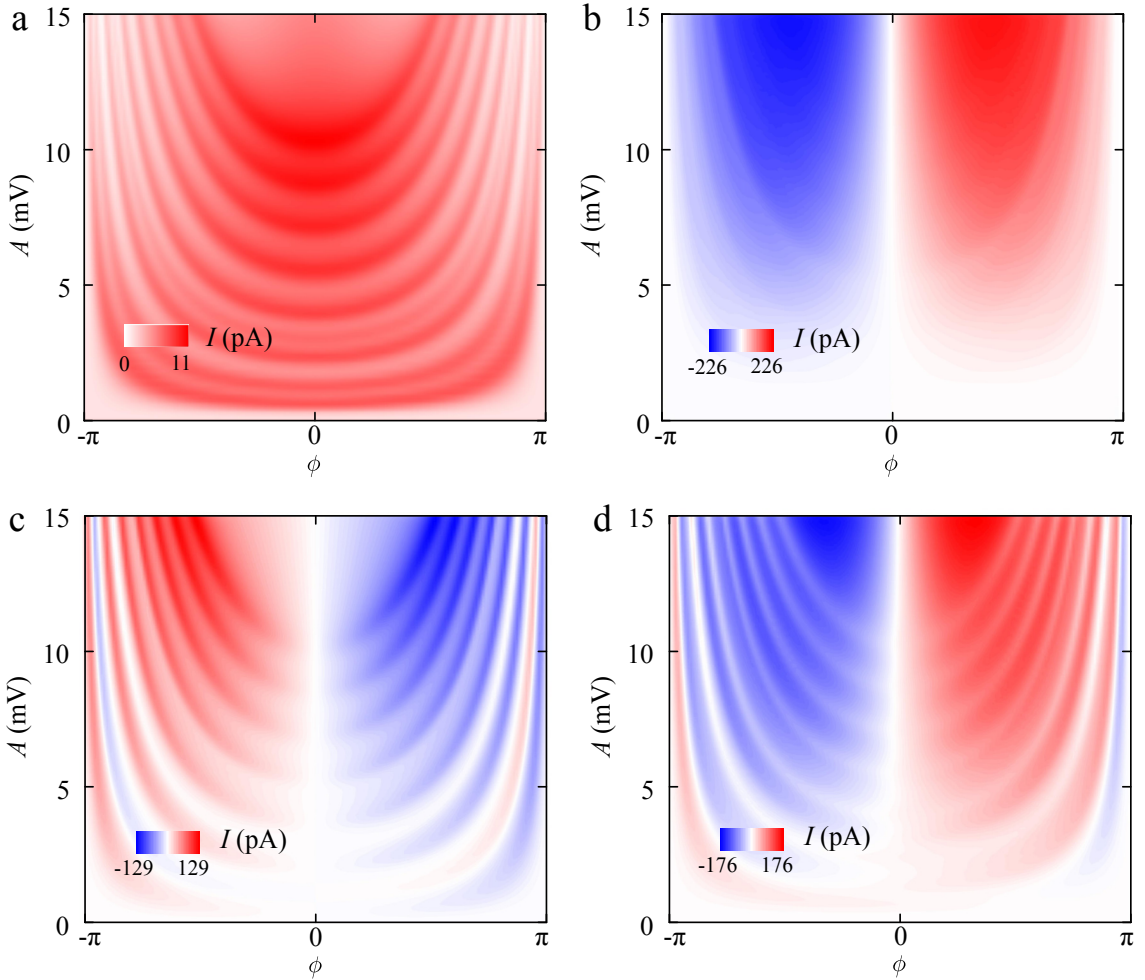


Figure 4.31: Theoretical prediction of the current for $k = 1$, $f_L = f_R = 200\text{MHz}$. The dc tunnel current $\bar{G}V$ (a), the pumped current $Q^{\text{cycle}}f$ (b), and the ac current (c) sum up to the total current plotted in (d).

deviation from the symmetry point, $\Delta\phi = \phi - \phi_{\ell\ell'}$, one can see that time reversal corresponds to $\Delta\phi \rightarrow -\Delta\phi$. Thus, the behavior of the integrals in Eqs. (4.19), (4.18), and (4.21) under time reversal allows us to draw conclusions about the symmetries of $\bar{G}_{\alpha\beta}$ and Q^{cycle} as a function of $\Delta\phi$. To be specific: Since the average conductance Eq. (4.18) is invariant under time reversal, it must be an even function of $\Delta\phi$. By contrast, the charge pumped per cycle, Eq. (4.21), changes

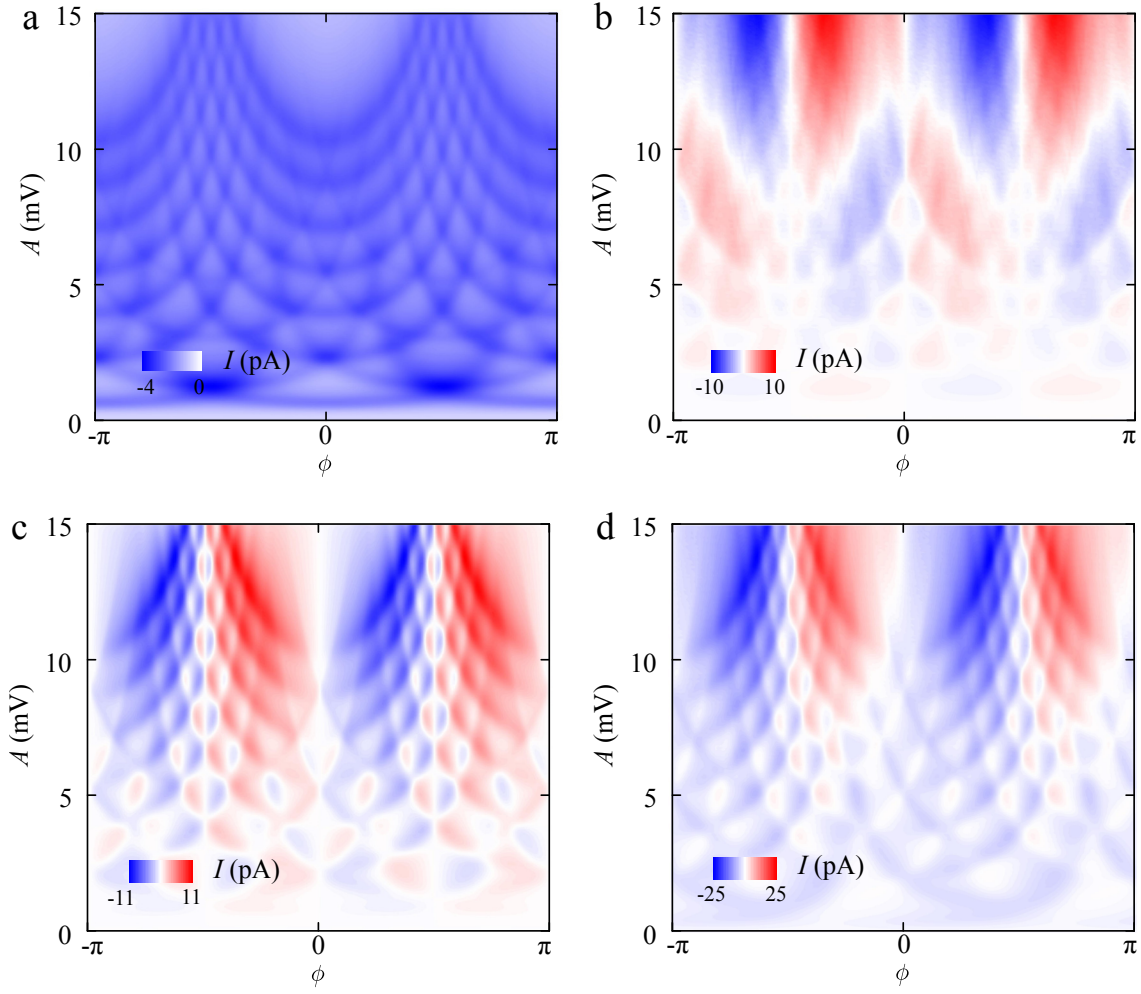


Figure 4.32: Theoretical prediction of the current for $k = 2$, $f_L = 50\text{MHz}$, $f_R = 100\text{MHz}$. The dc tunnel current $\bar{G}V$ (a), the pumped current $Q^{\text{cycle}}f$ (b), and the ac current (c) sum up to the total current plotted in (d).

its sign upon time reversal. Consequently, it must be an odd function of $\Delta\phi$. In short, despite the only k -fold symmetry of the Lissajous curves Eq. (4.16), we find $2k$ in-equivalent phases at which $\bar{G}_{\alpha\beta}$ is symmetric, while Q^{cycle} is anti-symmetric. In Figs. 4.31 and 4.32, we show for $k = 1, 2$ the three contribution to the current in Eq. (4.17), i.e., the dc current $\bar{G}V$, the pump current $Q^{\text{cycle}}f$, and the contribution of the rectified ac bias, I^{rect} . This visualizes the symmetry of the dc current and the anti-symmetry of the second and the third contribution. Notably, for the case of a tiny dc voltage of $V = 1\mu\text{V}$ considered here, the overall behavior [panel (d)] is dominated by the anti-symmetric contributions.

4.7 Separation of current components

To illustrate these symmetry properties we plot in Fig. 4.33 measured versus theoretical $I(\phi)$ -curves at constant amplitudes [e.g. horizontal cuts in Fig. 4.23] for the case $k = 1$. Arrows indicate the phases of which μ_n start to contribute to I . The relative shift between $n = 0, -1$ and $n = 1, -2$, etc. is related to our working point not being centered in the Coulomb gap. As expected, the odd

parity of $Q^{\text{cycle}}f + I^{\text{rect}}$ at $\phi_\ell = 0, \pi, 2\pi$ is apparent in Fig. 4.33(a) for $V \simeq 0$, while in Fig. 4.33(b) for $V \simeq \pm 0.2 \text{ mV}$ the even parity of $\bar{G}V$ dominates. The number of current maxima in Fig. 4.33

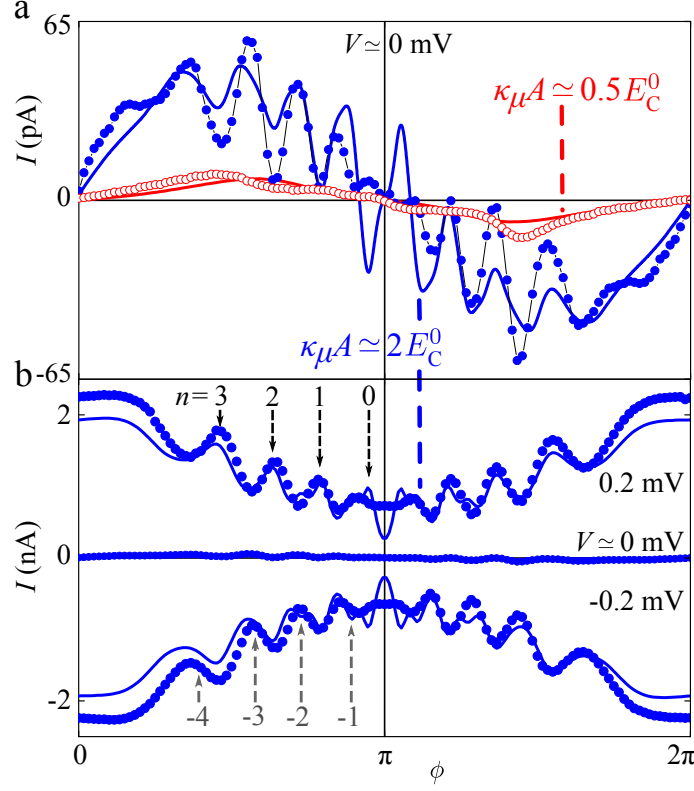


Figure 4.33: Lines depict theory, symbols are measured (offset voltages range from $-1 \mu\text{V}$ to $9 \mu\text{V}$ and are compensated by adjusting V); $k = 1$, $f = 100 \text{ MHz}$. (a) $I(\phi)$ for $V \simeq 0$, $\kappa_\mu A \simeq 2E_C^{(0)}$ (blue) and $\kappa_\mu A \simeq 0.5E_C^{(0)}$ (red). (b) $I(\phi)$ for $\kappa_\mu A \simeq 2E_C^{(0)}$ including curves at finite bias.

gauge the amplitude: At $\phi = \pi$, Γ_L and Γ_R oscillate in anti-phase and the chemical potentials μ_n are static for all k . The modulation of $\mu_n(t)$ grows with $|\phi - \pi|$ and with it the number of QD levels contributing to current, i.e. fulfilling $\mu_n(t) = \mu_{L,R}$ twice during each modulation period. $|I(\phi)|$ increases whenever another QD level starts to participate. At $\phi = 0, 2\pi$, Γ_L and Γ_R oscillate in phase and the number of contributing levels reaches its maximum. For the smaller amplitude (red curve) at most two levels with $n = -1, 0$, for the larger amplitude (blue) up to eight levels with $-4 \leq n \leq 3$ are relevant. To emphasize influence of dc bias contribution to the current we plot it for the broad range of voltages Fig. 4.34. This helps us to conclude mirror symmetry of curves. The transition from even to odd parity observed in Fig. 4.33 starts at source-drain voltages of $\sim 1 \mu\text{V}$ providing a high sensitivity of a driven QD system on a tiny dc bias. Such a strong dependence on a dc-bias has a potentially high influence on the coherent dynamics of driven QDs, an important aspect for quantum information applications. However, the distinct symmetries of the various contributions to $I(\phi)$ provide a direct and reliable method for accurately determining and correcting dc voltage offsets [see, for instance Fig. 4.33].

Before we showed that the current consists of three contributions, namely $\bar{G}V$, $Q^{\text{cycle}}f$, and I^{rect} . As a function of the phase ϕ , the first (dc) contribution is even at the symmetry points,

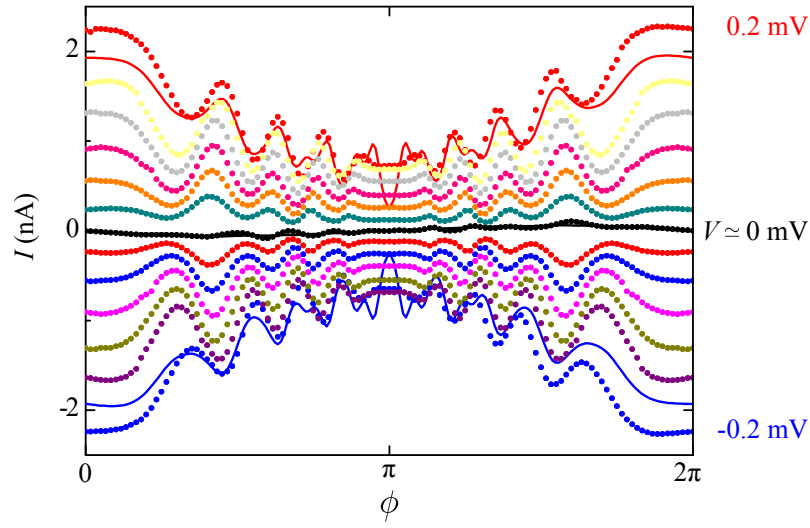


Figure 4.34: Lines depict theory, symbols are measured at $k = 1$, $f = 100$ MHz. $I(\phi)$ for $\kappa_\mu A \simeq 2E_C^{(0)}$ at finite bias for various source-drain voltages $V = i\Delta V$, where $-6 \leq i \leq 6$ is the curve index and a step of $\Delta V = 0.03$ mV.

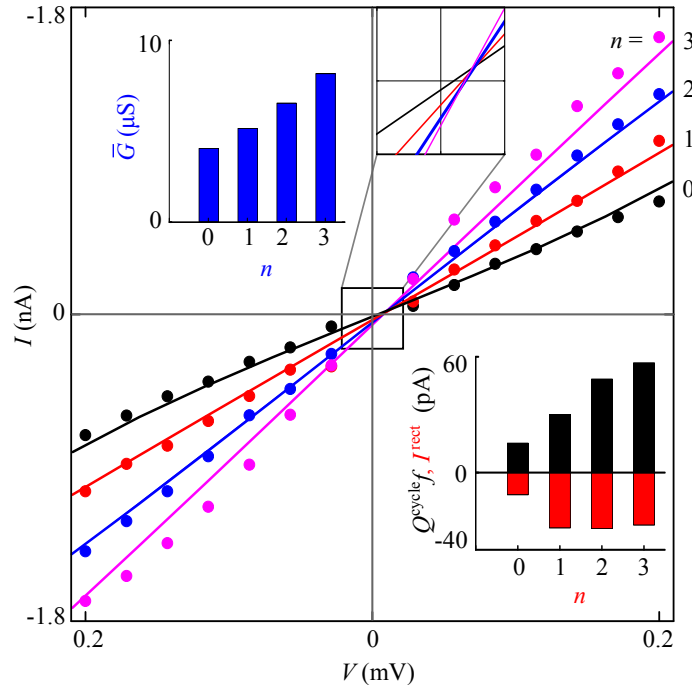


Figure 4.35: I - V characteristics for $\kappa_\mu A \simeq 2E_C^{(0)}$, at current peaks near black arrows in 4.33. Symbols are measured, lines depict theory. The maxima slightly shift proportional to $|V|$. Upper right inset: magnification, theory lines intersect at $V \simeq 9 \mu\text{V}$. Upper left inset: average conductance \bar{G} . Lower inset: I^{rect} (red, negative values) and pump current $Q^{\text{cycle}} f$ (black, positive), both being independent of V .

while the other two (ac contributions) are odd. Also, the dc contribution is proportional to V while the ac contributions are, to lowest order, independent of V . This allowed us to apply a source-drain voltage such that it compensates the offset voltage of the current amplifier and, thus, to determine the point at which $V = 0$. To demonstrate the linear I - V curves we plot

in Fig. 4.35 a selection at the phases marked by black arrows in the upper curve of Fig. 4.33(b). Since $Q^{\text{cycle}}f$ and I^{rect} to lowest order are independent of V , the slopes of these I - V curves are the time-averaged conductances \bar{G} which are plotted in the upper left inset. The index n here corresponds to the highest contributing dot level; n grows by one whenever the phase $|\phi - \pi|$ is increased beyond a current maximum in Fig. 4.33(b). In the adiabatic limit, the ratchet current $Q^{\text{cycle}}f$ increases stepwise with the number of contributing dot levels n (whenever another level starts to contribute). The contribution $\bar{G}V + I^{\text{rect}}$ also depends on the tunnel couplings Γ_α which, however, strongly depend on the gate voltages, see Fig. 4.16(b). As $\Gamma_\alpha(V_\alpha)$ in Eq. (4.12) is a concave function, $\bar{G}V + I^{\text{rect}}$ is always dominated by the contributing QD level with the highest n . The I - V curves in Fig. 4.35 intersect almost at a common point as is best visible from the theory data in the upper right inset. This observation states that the almost V -independent ac current $Q^{\text{cycle}}f + I^{\text{rect}}$ grows with n roughly proportional to $\bar{G}V$. This behavior is expected if the tunnel couplings $\Gamma_\alpha(V_\alpha)$ grow proportional to V_α as indeed approximately the case in our device [see Eq. (4.12) and Fig. 4.16(b)].

The dc current $\bar{G}V$ can be well distinguished from the ac contributions $Q^{\text{cycle}}f$ and I^{rect} due to their different symmetry properties and, hence, can be determined with high precision from phase-dependent measurements such as those in Fig. 4.33(b). The distinction between $Q^{\text{cycle}}f$ and I^{rect} with identical symmetry properties is less precise. However, with the system parameters determined before, the pump current $Q^{\text{cycle}}f$ is already fully determined. By contrast, the rectified current contains an unknown leverage factor that relates the gate voltages to the ac bias they induce between the source and drain leads. We achieved a fair agreement between theory and experiment for a leverage factor of $5 \cdot 10^{-4}$. Having determined this value, we were able to distinguish the two contributions to the current in Fig. 4.33(a). The result is shown in the lower inset of Fig. 4.35 and revealed that $Q^{\text{cycle}}f$ and I^{rect} have the same order of magnitude. While the former grows with the number of resonances crossed by the Lissajous curve, the latter is nearly independent of it.

4.8 Applications and alternative realizations

In our Lissajous rocking ratchet a combination of rf excitations breaks time-reversal symmetry and yields a dc current. It is feasible to decompose the measured dc current into its contributions including an averaged dc conductance stemming from a dc source-drain voltage, a rectification term stemming from an ac source-drain voltage, and the actual ratchet current. The Lissajous rocking ratchet represents an alternative method to access radio frequency information by mutually comparing the frequencies, amplitudes, and phases of rf signals. One of its strength is its ability to encode tiny signals on-chip. As such, Lissajous rocking ratchets could find applications as rf comparator or serve as the detector or filter components, for instance in quantum information applications. An example application could be analyzing a noisy rf signal by comparing it on-chip with a clean rf reference modulation.

In our ratchet setup, the resulting dc current strongly depends on the relative phase, amplitude, and frequency of the two signals. Because the dc response is a non-linear function of the rf signals, it also acts as a multiplier. By measuring a time-averaged dc current, our device filters the time-periodic carrier signal while averaging out the uncorrelated noise. This specific example resembles a lock-in amplifier working on-chip with small signals at radio frequencies. Here, we concentrated on the case of commensurable frequencies (integer k). Non-integer k would give rise to multiple loops most of which canceling each other, hence a much smaller dc

current would occur. The frequency range is limited by the adiabaticity criterion, hence needs to be small compared to the tunnel rates. As the tunnel couplings are adjustable (controlled by the gate voltages) the adiabaticity criterion can be fulfilled for very high frequencies limited only by E_C corresponding to several hundred GHz.

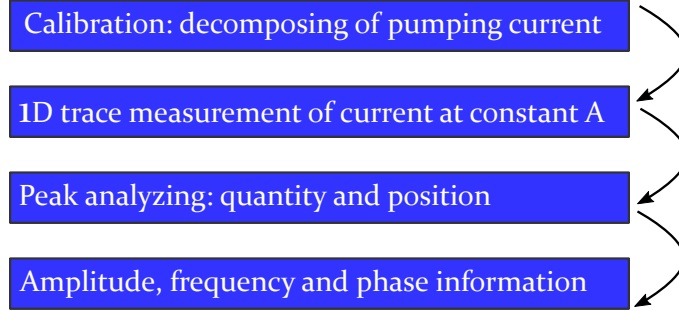


Figure 4.36: Readout protocol developed for the rf comparator based on Lissajous rocking ratchet

Following, we sketch in Fig. 4.36 an explicit example of a possible procedure to use our Lissajous ratchet to measure frequency, amplitude, and phase of an unknown rf sine signal applied to one gate of the QD. We apply a reference sine signal to the other QD gate and measure the current through the QD versus the phase of the reference signal at the fixed amplitude. This data contains information about the unknown signal. To analyze the data we first need to calibrate amplitude and phase of the reference signal as is explained in section (4.7). This calibration allows us to decompose the current into its three contributions (dc, pumping, and rectifying current) defined in Eq. (4.17). The dc contribution allows us to accurately determine V_{off} while the other two contributions both contain information about the unknown rf signal. For our purpose, it is sufficient to analyze the pumping current, $Q_{\text{cycle}}f$ further. Amplitude, phase, and frequency of the pumping current can now be determined by fitting our model to the data. Strengths of our device are its high sensitivity based on a single-electron tunneling current, e.g., $< 10 \mu\text{V}$ amplitudes could be resolved, and its on-chip capabilities. The precision of experiments such as ours depends on the precision of the dc current measurement and the steepness of the resonance which is determined by the linewidth. The latter is inhomogeneously broadened and in our case accounts for 0.2 meV but values of only $5 \mu\text{eV}$ are feasible [209].

Going beyond purely sinusoidal driving and dc detection, a further possible application could be the comparison of tiny rf-pulses as an integrated on-chip component of a future quantum circuit. Then, the averaged dc-current in our present experiments would be replaced by a short signal pulse allowing fast on-chip processing. However, in its present form the averaging dc current and its analysis via a lengthy fit procedure makes commercial lock-in amplifiers or comparators still appear the simpler the choice for classical applications with strong enough input signal levels. Lissajous rocking ratchets are not limited to QD circuits but could be realized in a variety of systems, for instance in macroscopic electronics or mechanics or superconducting circuits. In the following, we propose a possible realization in a nanoelectromechanical system. In Fig. 4.37 we extend the already realized “nano bell” [210] and illustrate what we mean by “nanomechanical Newton cradle”. The device is composed of two cantilevers and a fixed metallic contact (d). The central cantilever is patterned with an isolated metallic island while the left one contains an island but electrically connected to a second lead (s). The islands are positioned such, that the central island can touch both the left and right lead whenever both cantilevers are

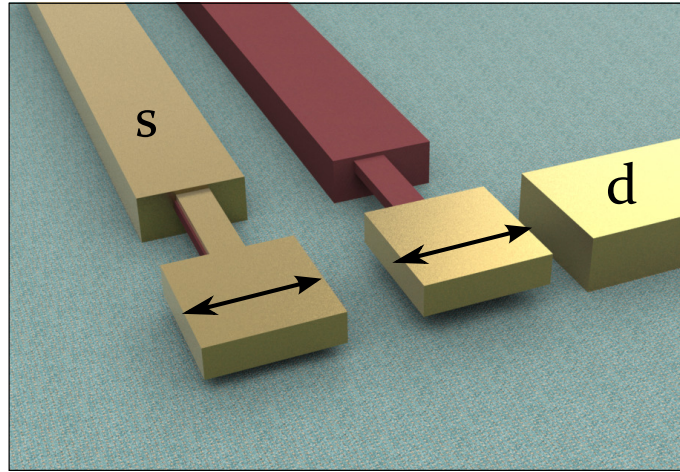


Figure 4.37: Nanomechanical Newton cradle example base on the Lissajous ratchet.

vibrating with sufficiently high amplitude. A voltage can be applied between s and d , and current can be measured. We assume that both cantilevers can be externally driven (at predefined relative phases) at their mutual eigenfrequencies and that the latter are tunable, e.g., via capacitive coupling to additional gates or by using dielectric forces [211]. We also assume that the central island is small enough to allow for single electron transport based on Coulomb blockade, namely that we can treat it as a QD [210]. The electronic levels of the islands are then modulated by the same capacitive coupling that is used to drive the cantilevers mechanically. In such a device the coupling between the islands and that between contact d and the center island is strongly time-dependent, zero most of the time and strong during touching. This system is highly tunable and very close in spirit to our QD circuit: importantly, the time dependence of the couplings and island levels are linked, a central precondition to define a Lissajous ratchet.

4.9 Conclusions

Within the third chapter we offered an approach to break time reversal symmetry, a precondition for useful applications in (quantum) information processing. Experimentally, we concentrate on a specific device, a lateral QD, driven with two forces at different frequencies and with a non-trivial relative phase. The directional motion of the Lissajous rocking ratchet is restored only for certain phases between the signals. To achieve this, it is essential to modulate both the QD-lead couplings and the QD levels. We consider the case of commensurable frequencies where the combined time-trajectories of the modulated voltages are Lissajous figures. Theoretically we apply a realistic transport model which takes into account the relevant QD states and the capacitive coupling between the driven gates and the QD levels, tunnel barriers and lead chemical potentials. We numerically calculate the dc current through the QD within the framework of Floquet scattering theory and find qualitative good agreement with our measured results. Exploring the phase and frequency ratios between the two driving forces we show, that in the regime of adiabatic driving time reversal symmetry can be broken and electrons can be pumped through an unbiased QD. While our experiments used a semiconducting QD, similar rocking ratchets could be realized in different systems, such as superconducting circuits, nano-electromechanical systems or molecular electronics. As a future perspective, the phase, frequency and amplitude sensitivity of a Lissajous ratchet may be exploited for on-chip noise detection or signal analysis

in a wide frequency range. Encoding rf-information on-chip in a dc signal it facilitates the analysis of rf-signals at lab conditions otherwise difficult for rf-detection of tiny signals at ultralow temperatures.

Summary and Outlook

The thesis at hand presents contributions to four fields of quantum technology: first, we demonstrated an alternative method for engineering the potential landscape in a 2DES embedded in GaAs/AlGaAs heterostructures. Second, we studied combined transport through two distant QPCs and thereby revealed the eigenmodes of the QPCs and their propagation through a mesoscopic 2DES. Third, we examined the coupling between a QPC and a hemispherical resonator by coherent ballistic electron modes. Finally, we presented a Lissajous rocking ratchet, based on a single QD, which creates directed motion of electrons and breaks the time-reversal symmetry on-chip. In the following, a summary puts these findings into the frame of quantum technology.

Crucial applications of the quantum technology include high-speed switching devices while routing the signals between these devices is also of significant advantage. Both effects can be combined in ac-driven electron routers, that break the time reversal symmetry [212, 213]. The current generation of electron routers [214] has large dimensions requiring sizes within the used operational wavelength (usually several centimeters) [175] that is incompatible with nano-electrical circuits. Devices such as Lissajous rocking ratchets offer an alternative solution while their size can be scaled down to a few nanometers. These devices combine well-known locomotion mechanisms of biomotors [215, 216] with elliptic Lissajous driving [217]. Here we presented its realization based on an ac driven quantum dot embedded in a semiconductor GaAs/AlGaAs heterostructure. Our Lissajous rocking ratchet encodes frequency, phase and amplitude information of the unknown signals in its dc-output and can be generalized to other fields of physics and biology.

For coupling between different elements of quantum circuits, we can consider coherent ballistic electrons as a fast solution that doesn't require any additional transport systems, like surface acoustic waves or spin waves. In this thesis, we explored coherent coupling between the QPC and the ballistic electron resonator and showed that detailed knowledge of eigenmodes for every element of the combined system is essential for optimized designs of quantum circuits. Coherent ballistic transport is less sensitive to common problems of conventional electronic devices such as scattering or energy relaxation but suffers from electron diffraction processes. Working with weakly diverging ballistic electron beams reduces diffraction effects and thus gives rise to the high coupling between the distant nanodevices. In this thesis, we investigated the propagation of collimated electron beams in the ballistic transport regime. Deflecting electron trajectories by an external magnetic field allowed us to resolve eigenmodes of the system's components and to probe the angular distribution of the emitted carriers. We showed indications of electron beam propagation similar to the Gaussian Beam model from optics.

In quantum circuits, we also need connection elements between the nanodevice and large contact extensions, optimized for minimum reflection. This problem is solved in the existing

transistor architectures like multigate FET [218] or Ultra Thin Silicon on Insulator FET [219, 220] with the help of electrostatic elements similar to optical analogues, such as lenses [221–223], waveguides [158] and mirrors [131]. Here we presented the current increase by focusing the ballistic electron beam into the channel aperture using an electrostatic lens.

Finally, a robust and straightforward engineering approach is needed to produce quantum circuits inside the semiconductor heterostructures. In this thesis, we described an approach to fabricate mesoscopic devices based on the engineering of two metal layers, separated by an insulator film. Our method promises considerable advantages for the definition of complex circuits by the electric field effect as it allows to reduce the number of control gates and simplify device geometries. Prominent examples are carrier systems with ring topology or large arrays of quantum dots. We presented the first exploration of this method pursuing field effect, Hall effect, and Aharonov-Bohm measurements to study electrostatic, dynamic and coherence properties and also show the general feasibility of our approach for future quantum applications.

The obtained results also suggest a broad range of future experiments. Several of those are described in the following: (i) Experiment based on a chaotic quantum dot to determine the phase coherence length for ballistic electron regime is of high interest. Also, new designs of QPCs with high control of the potential profile (for example the three split gate QPCs [75]) engineered by our alternative method can facilitate the study of the coherent coupling between distant QPCs. (ii) The usage of the collimated electron beams makes it possible to control electron transport over vast distances without involving surface acoustic waves transport or utilization of predefined electron channels. The experiment of distant ballistic coupling of quantum dots or qubits could be realized both by using resonant cavities and electrostatic lenses. The possible incorporation of the discussed elements in real quantum information processing circuits, testing their efficiency and influence on coherent properties of a qubit is one of the challenges for the future. Studying the transition from the Fresnel diffraction regime in the near-field to the Fraunhofer regime for ballistic electrons can give rise to exciting applications similar to existing devices known from optics. Other aspects of quantum technology can also be probed, i.e., we can highlight the quantum entanglement that can be tested in the experiment with a beam splitter. It is based on an electrostatic lens that focuses ballistic electrons in two split focal points [223]. (iii) The ratchet physics can be extended into the non-adiabatic regime, where operating conditions are less restricted. Possible realizations can also be explored at room temperature, aiming for commercial products based on on-chip comparing of rf signals while measuring a dc output, similar to a lock-in amplifier.

Appendix A

Appendix

A.1 Fabrication parameters

A.1.1 Wafer material

We used three different wafers in this thesis: wafer A used in chapter I (internal number 11228) was produced in the group of Prof. Andreas Dirk Wieck, University of Bochum. Second wafer B employed in the second and third chapters (internal number mbe8-309) was taken from the group of Prof. Vladimir Umansky, Weizmann Institute of Science, Israel. Third wafer C, used in chapter IV, was produced by Klaus Pierzl from PTB Braunschweig. The layer structures of the

Wafer A material	Thickness (nm)	Wafer C material	Thickness (nm)
GaAs	5	GaAs	10
AlGaAs:Si	70	AlGaAs:Si	50
AlGaAs	35	AlGaAs	30
GaAs	650	GaAs	500
GaAs/AlGaAs superlattice	5/5 (x 10)	GaAs/AlGaAs superlattice	2/2 (x 50)
GaAs	50	GaAs	500

Table A.1: wafer A and C layer structure

wafers A and C are listed in the Tables (A.1).

We summarize the pristine wafer parameters (carrier density n_s , mobility μ , mean free path l_m , Fermi energy E_F and Fermi wavelength λ_F) in table (A.2). The nanostructures used in

Name	$n_s \text{ } 10^{11} \text{ cm}^{-2}$	$\mu \text{ } 10^6 \text{ cm}^2/\text{Vs}$	$l_m \text{ } \mu\text{m}$	$E_F \text{ (meV)}$	$\lambda_F \text{ (nm)}$
A (Wieck)	2.27	0.69	5.4	8.1	52.6
B (Umansky)	3.13	2.28	21	11.2	44.8
C (Pierzl)	2.83	0.32	2.8	10.1	47.1

Table A.2: Wafer parameters

this thesis were produced for the first chapter by Nikolaus Bachsoliani [36] in LMU-Munich, for

the second and third chapter by Jaan Freudenfeld [135] in LMU-Munich and the fourth chapter by Bernd Kastner in PTB-Braunschweig.

A.1.2 Optical lithography parameters

For optical lithography in LMU-Munich, we used the high resolution resist AZ701MIR. Every initial step of the layer was processed with the same parameter combination, while the last step was different for the three layers: Mesa, ohmic contacts, and gates. Used fabrication parameters of the initial step are listed in Table (A.3). The last step of fabrication is described in Table (A.4).

Step	Comment
Spincoating	3 s at 800 rpm, 30 s at 6000 rpm
Prebake	60 s at 90 °C
Exposure	16,5 s at Karl Suss MJB3 mask aligner
Postbake	60 s at 110 °C
Development	30 s in AZ726 Developer, developing stopped in water

Table A.3: Optical lithography processing steps

Layer	Step	Comment
Mesa	Etching	H ₂ O:H ₂ SO ₄ :H ₂ O ₂ (100:3:1) for 100 s @ 0.95 nm/s
Ohmic contacts/Gates	GigaEtch	40 s at 200W before evaporation
Ohmic contacts	Evaporation	60 nm AuGe, 10 nm Ni, 60 nm AuGe
Gates	Evaporation	10 nm Ti, 90 nm Au
Ohmic contacts	Annealing	300 s at 100 °C, 240 s at 360 °C, 140 s at 480 °C
Ohmic contacts/Gates	Lift-off	In DMSO over night, 1 h in Acetone at 40 °C

Table A.4: Specific layer optical lithography processing steps

A.1.3 Electron beam lithography parameters

For the EBL lithography we used PMMA 950K resist with parameters listed in Table (A.5). Crosslinked layer was fabricated with a different dose of $2400 \frac{\mu C}{cm^2}$ at a higher aperture size of

Step	Comment
Spincoating	1 s at 800 rpm, 30 s at 5000 rpm
Prebake	90 s at 170 °C
Exposure	Dose: $60 \frac{\mu C}{cm^2}$, aperture size: 10 μm at Raith E-line system
Development	45 s in MIBK : isopropanol 1 : 3, developing stopped in isopropanol
Evaporation	5 nm Ti, 35 nm Au
Lift-off	6 h in DMSO at 80 °C, 5 minutes in Acetone at RT, isopropanol

Table A.5: Electron beam lithography processing steps

20 μm . Topgate layer was also made thicker than usual gates by adding additional 20 nm of Au in order to avoid metal fracturing at the optical-to-eb1 lithography connection.

A.1.4 Sample designs

We fabricated two samples from the wafer A: A1, and A2; two samples from the wafer B: B1 and B2 and one sample from the wafer C: C1. We show microscope and SEM photos of the samples with marked characteristic sizes in Fig. A.1.

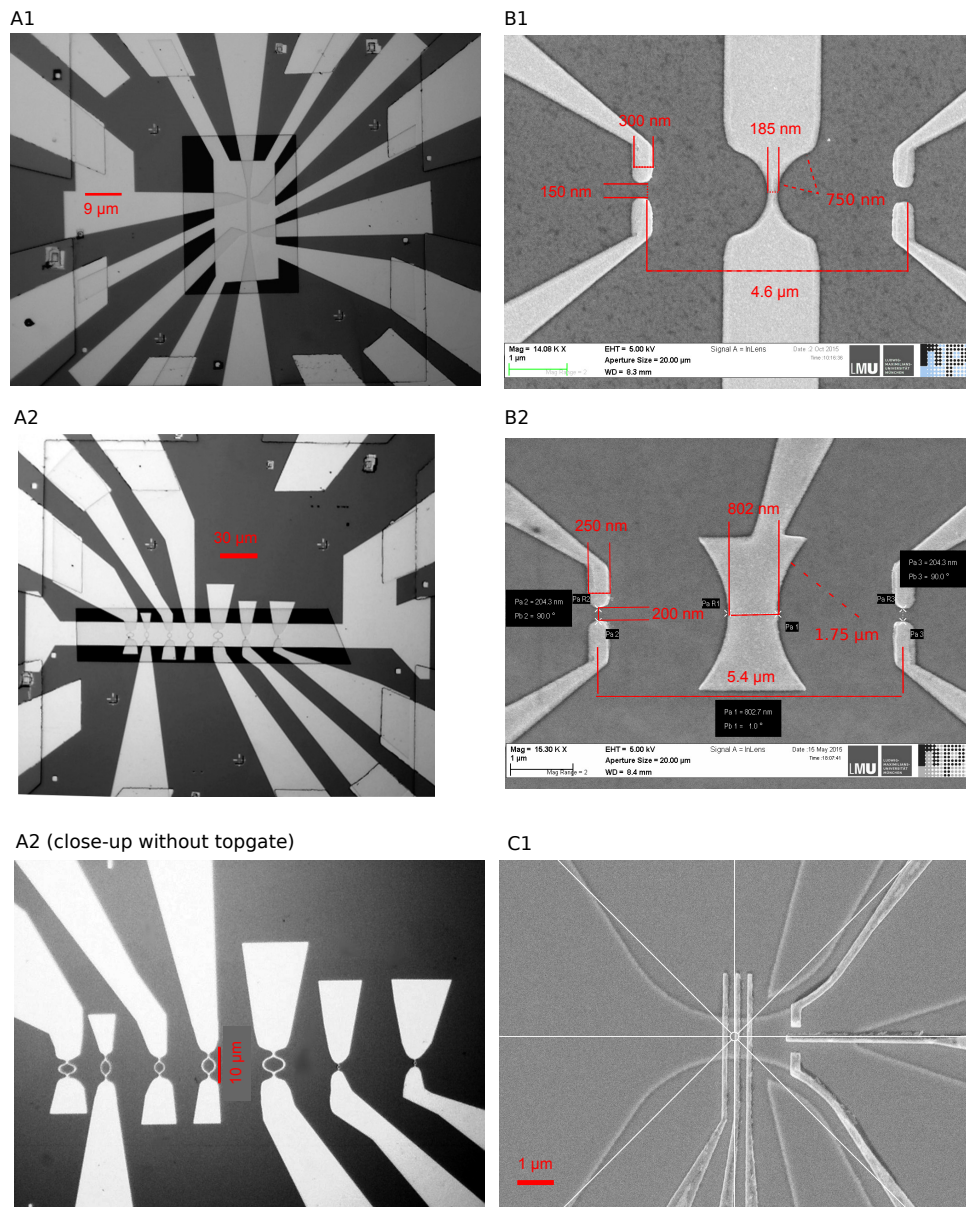


Figure A.1: Microscope images of samples A1,A2 and SEM photo of samples B1,B2 and C1. Sizes are labeled with red colour. The AB-rings in B2 sample are shown in high-resolution without the topgate layer.

A.2 Calibration measurements

A.2.1 Calibration of the single QPC resistance

We performed a two-point measurement to determine a single QPC resistance in chapter II by applying source-drain voltage V to the contact on one side of the QPC and measuring the resulting current I_2 at another contact behind the QPC as a function of V_{QPC} . Measured resistance V/I_1 consists of the resistance of both contacts, the wiring and the two-dimensional electron system that connects both contacts. Assuming grounded side contacts, we simplify the measurement setup in the diagram shown in Fig. A.2. Here the resistance of the wiring connected to an

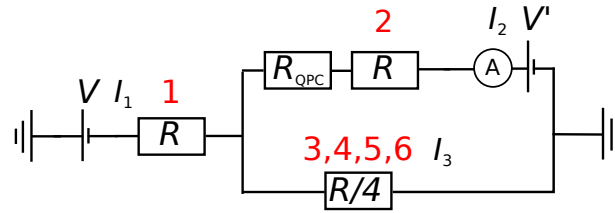


Figure A.2: The setup used for the determination of single QPC resistance corresponds to figure 2.9 with the grounded lens- and second QPC gates. $V = -0,5\text{mV}$ was applied to contact 1 and the QPC-gate voltage dependent current I_2 measured at contact 2. The current I_1 behind source contact splits into five channels (QPC+1-contact channel and four contact-channels that were summarized in one parallel-resistance $R/4$), the voltage drop in the QPC channel is, therefore, the difference of V and the voltage V_1 that dropped at contact one divided by 5.

ohmic contact, the contact-resistance itself and half of the 2DES-channel between two contacts are summarized in a single resistance R which is assumed to be identical for every channel. It was determined in the open channel regime with grounded QPC and lens gates and floating side contacts, yielding $R = 250\ \Omega$. We can write Kirchoff's law for the combination of contacts 1-2 and 1-3,4,5,6.

$$V = I_1 R + I_2 (R_{\text{QPC}} + R_2) \quad V = I_1 R + I_3 R/4 \quad I_1 = I_2 + I_3 \quad (\text{A.1})$$

Solving this set of equations gives us I_2 that can be used to determine the QPC conductance $G_{\text{QPC}} = I_2/V_2$.

$$G_{\text{QPC}} = 5 \left(\frac{V}{I_2} - 6R \right)^{-1} \quad (\text{A.2})$$

We didn't take into account the offset voltage V' from the input of the current amplifier (Ithaco 1211). This offset can be estimated by applying zero source-drain voltage $V = 0$ and measuring current I for closed QPC $R_{\text{QPC}} = \infty$. We found this offset to be $V' < 10\ \mu\text{V}$ that is negligibly small for characterization of a single QPC.

A.2.2 Resistance of two QPCs in series

The same ansatz of equal drain resistance for every contact was used for the measurement of two QPCs in series. We sketch the circuit diagram of the experimental setup in Fig. A.3. We measure the current through both drain contact and one of the side contacts with the current amplifier.

First, we estimated the offset voltage V' by closing the QPC1 and kept QPC2 at $R_{QPC2} = 1 \text{ k}\Omega$ resistance. We found the offset voltage to be $V' = 12 \mu\text{V}$. Then we pinched-off QPC2 and QPC1

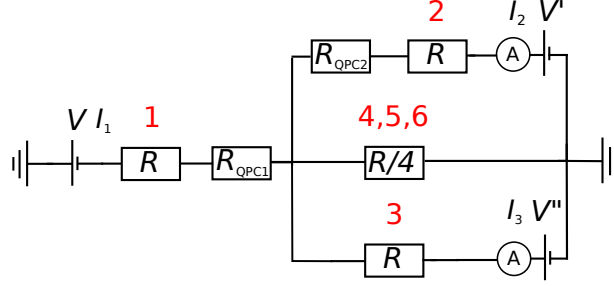


Figure A.3: The setup used for measuring the 2 QPCs in series corresponds to Fig. (3.1) with grounded lens-gate. $V = -0.5 \text{ mV}$ was applied to contact 1 and the QPC-gate voltage dependent current I_2 measured at 2. The current I behind 2 splits into five channels (QPC+1-channel and one side contact-channel with current amplifier and four side contact channels grounded).

$R_{QPC2} = R_{QPC1} = \infty$ and measured the offset voltage of current amplifier $V'' = 4I_3R/3$. Comparable voltage to V'_1 was found to be $V'' = 13 \mu\text{V}$. For the case of non-zero side contact resistance, a voltage can build up in the central region between two QPC causing additional current I_2 to flow through the contact 2. Now we can estimate this correction current from the system of equations

$$I_2(R_{QPC2} + R) + V' = I_3R + V'' \quad (\text{A.3})$$

$$I_2 = \frac{I_3R + V' - V''}{R_{QPC2} + R}. \quad (\text{A.4})$$

For some of the measurements (in Sec. (2.5)) we didn't measure I_3 and didn't have the current amplifier connected; therefore $V'' = 0$ and we can estimate correction current from the following equation:

$$I_1 = \frac{V - V'}{\frac{R'_{QPC2}R/4}{R'_{QPC2} + R/4} + R'_{QPC1}}, \quad (\text{A.5})$$

where $R'_{QPC1} = R_{QPC1} + R$ and $R'_{QPC2} = R_{QPC2} + R$. So finally we have

$$I_2 = \frac{V - V' - I_1R'_{QPC1}}{R'_{QPC2}}, \quad (\text{A.6})$$

This current was removed from all the data shown in chapter III.

A.2.3 Coherent effects in magnetic deflection and electrostatic focusing experiments

First, we discuss experiments from the chapter (3.3) and possible phase-coherent contributions to the measured current. We start with the combined magnetic deflection and electrostatic focusing experiment and plot the detector conductance as the function of B and the voltage applied to the

lens gate V_L for the both QPCs tuned to the first plateau in Fig.A.4. We found some periodic maxima lines that were hidden previously by broad electron branches due to the high conductance. The Periodic substructure of the measured conductance indicates the contribution of backscattering electron trajectories to electron transport. This backscattering effect occurs in both reflected

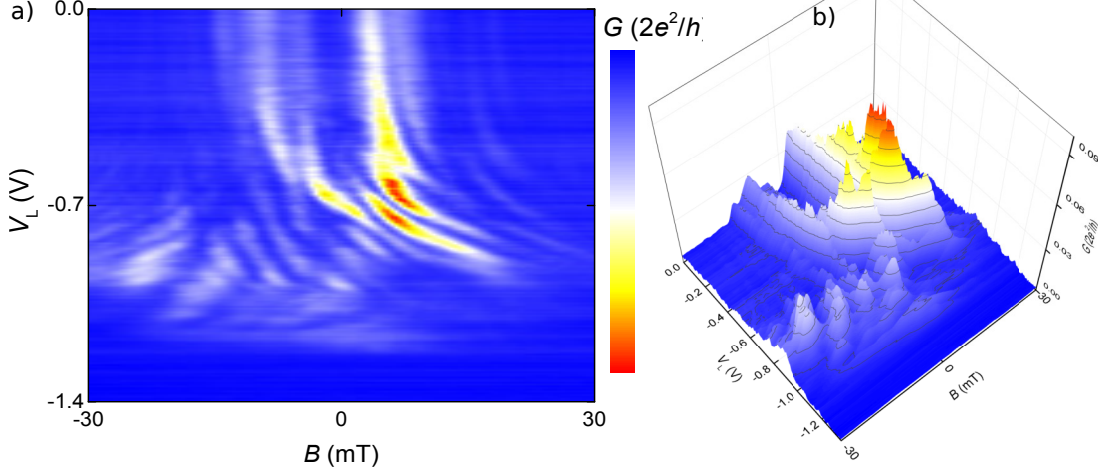


Figure A.4: (a) Measured conductance G as a function of the external magnetic field B and the voltage applied to the lens V_L . QPC1 was used as emitter and QPC2 as the detector; both tuned to the 1st plateau. (b) 3D profile of the conductance. Maximum value of conductance at $V_L = -0.65$ V and $B = 0$ mT.

and transparent regime of the lens. However in most of the experiments discussed above these features were suppressed due to the relatively high source-drain voltage ($V \approx -1$ mV). To probe the effect of the backscattered electrons on the transmission through the two QPCs in series with a lens in between them we perform the same electrostatic focusing experiment as in section (2.6.3) but for various tuning of the emitter QPC1. In Fig. A.5 we showed the influence of the lens gate

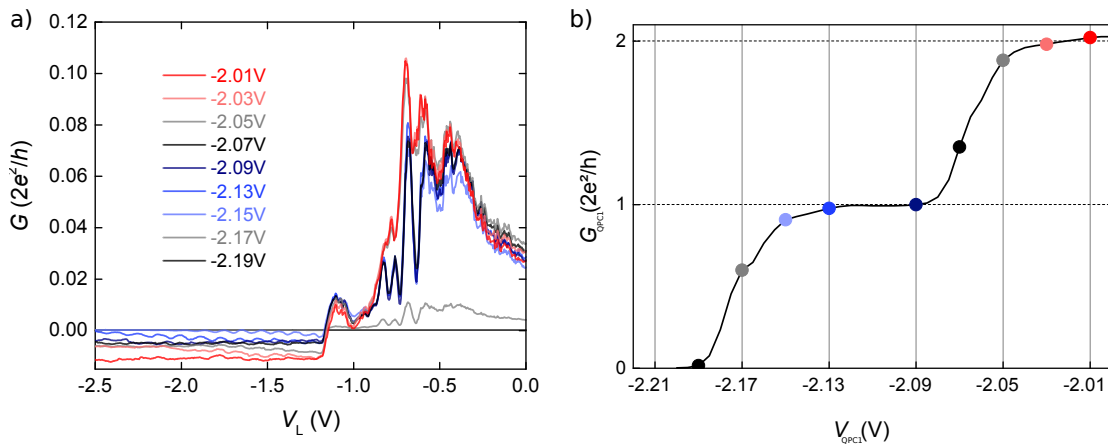


Figure A.5: a) Conductance through two QPC in series and a lens as a function of lens voltage V_L for various detector QPC voltages V_{QPC1} (marked with color), emitter QPC2 was kept at the first plateau. b) Single emitter QPC conductance as a function of QPC gate voltage V_{QPC1} . Emitter tuning used in (a) are marked with identical colors as lines in (a), $V = -1$ mV

for various configurations of the emitter plateau. We found that the conductance profile $G(V_{QP1})$

remains unchanged at varying detector voltages within the first and second plateaus, but shows an abrupt transition between the first and the second detector QPC1 plateau. The change in the

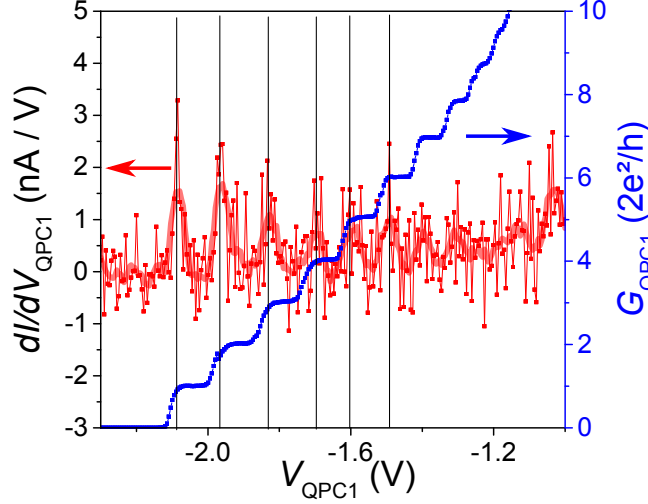


Figure A.6: Averaged conductance derivative on QPC gate voltage V_{QPC1} over the full range of lens voltages. The transparent line indicates spline fit and dots represent calculated conductance. As the guide for the eyes, we also show the emitter single QPC conductance dependence on V_{QPC1} .

conductance profile G for different QPC1 gate voltages V_{QPC1} can be quantified using the conductance derivative over the V_{QPC1} . In Fig. A.6 we plot averaged derivative of the curves of the Fig. A.5 for the whole range of lens voltages. Conductance derivative illustrates the cross-correlation coefficient between the adjacent curves: $\delta G / \delta V_{\text{QPC1}} = [G(V_{\text{QPC1}} + \delta V_{\text{QPC1}}) - G(V_{\text{QPC1}})] / \delta V_{\text{QPC1}}$. It is clear that the change of the conductance profile δG is the same for every conductance plateau and reaches its maximum at the beginning of each conductance plateau. Therefore the observed features in the measured conductance G are connected with the number of injected QPC modes N and not influenced by the coherent backscattering from impurities or gates.

A.2.4 QD calibration

We performed characterization of single quantum dot in chapter IV. The working point was determined as $\tilde{V}_L = -202$ mV and $\tilde{V}_R = -91$ mV. At the working point we found $E_C^{(0)} \simeq 1.27$ meV. In the Table A.6 we summarize the functional dependences along the bisecting line from the figure 4.15.

RF circuitry calibration

In the radio frequency calibration section of chapter IV we presented possible solution of impedance mismatch in our electrical circuitry. The result of the calibration (for both gates) is summarized in the Table A.7. We show here calibration data for the figures Fig. 4.19 presented

Table A.6: Experimentally determined parameters of our QD; from left to right: index number n , chemical potentials at the working point $V_L = V_R = 0$, charging energies $E_C(n) = \mu_n - \mu_{n-1}$, tunnel couplings for the case of symmetric coupling $\Gamma_L = \Gamma_R$ and $V_L = V_R$ such that $\mu_n = 0$, i.e., $\Gamma_{L,R} = \Gamma_\alpha(\mu_n^0/2\kappa_\mu)$

n	μ_n^0 (meV)	$E_C(n)$ (meV)	$\Gamma_{L,R}$ (meV) at $\mu_n = 0$
-3	-3.85	1.39	0.39
-2	-2.25	1.35	0.59
-1	-0.90	1.31	0.82
0	0.41	1.27	1.09
1	1.68	1.23	1.40
2	2.91	1.19	1.74
3	4.11	1.15	2.13
4	5.31	1.11	2.53

Table A.7: Radio frequency calibration factors $\alpha_{L,R}$ at various driving frequencies.

f in MHz	$1/\alpha_L$	$1/\alpha_R$
25	25.2	24.9
50	23.2	23.1
100	27.5	27.2
150	26.3	26.1
200	182.5	178.6

before. The data was taken within the interval of 1 day, therefore the input voltage related to the current amplifier can be quite different in this data plots.

A.3 Experimental raw data

Here we present the raw data used in the chapter II, section (2.4). Fig. A.8 shows conductance as a function of magnetic fields for equal single QPC conductances used for analysis in Fig. 2.22 when QPC1 is emitter and QPC2 is detector. Fig. A.9 shows conductance as a function of magnetic fields for different single QPC1 conductances and QPC conductance fixed at the 7th plateau used for analysis in Fig. 2.23 when QPC1 is emitter and QPC2 is detector. Fig. A.10 shows conductance as a function of magnetic fields for equal single QPC conductances when QPC2 is emitter and QPC1 is detector. Fig. A.11 shows measured conductance as a function of magnetic fields for different single QPC1 conductances and QPC conductance fixed at the 7th plateau when QPC2 is emitter and QPC1 is detector. Fig. A.10 shows conductance as a function of magnetic fields for equal single QPC conductances used for analysis in Fig. 2.26 for two cooldowns.

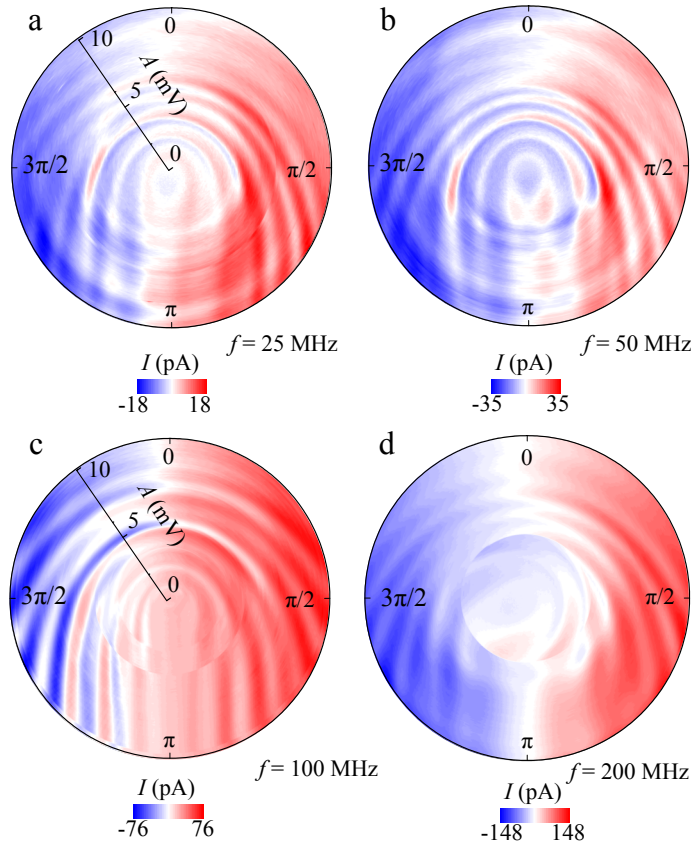


Figure A.7: Measured current I as a function of modulation amplitude A (radius) and phase difference ϕ (angle) between $V_L(t)$ and $V_R(t)$ for $f = 25, 50, 100, 200$ MHz in panels a-d

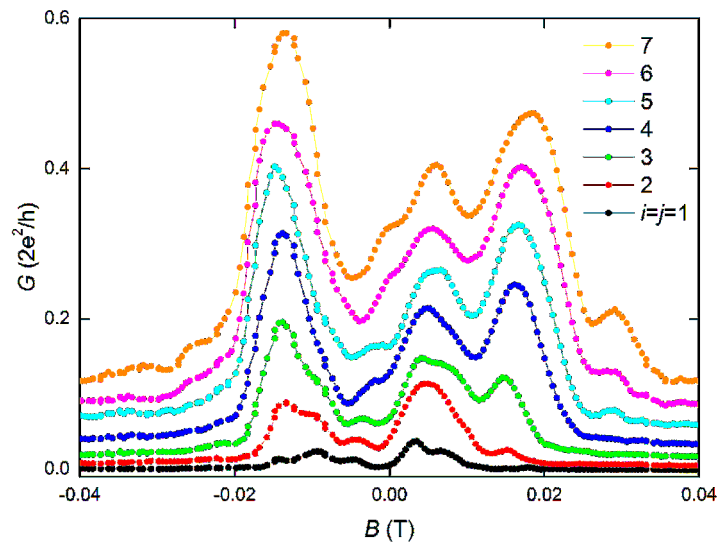


Figure A.8: Measured conductance G as a function of magnetic field B for both QPCs operating at the same plateau $i = j$, $G_{QPC1} = G_{QPC2} = 2e^2i/h$, QPC1 is emitter and QPC2 is detector.

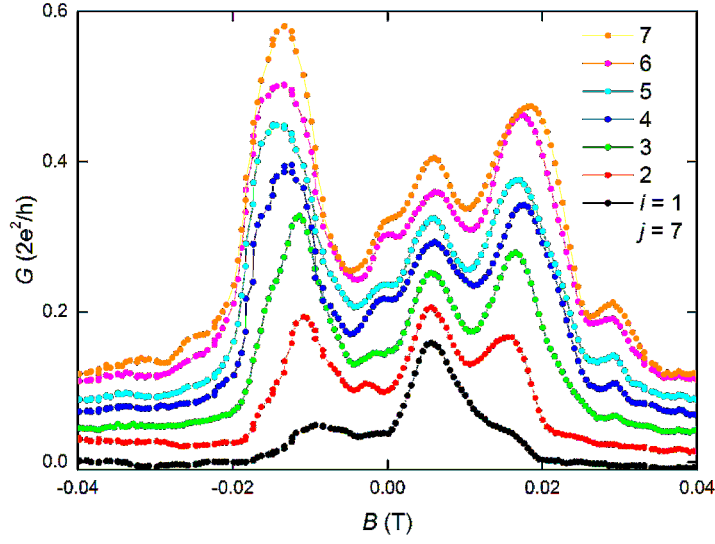


Figure A.9: Measured conductance G as a function of magnetic field B for different combinations of $G_{QPC1} = 2e^2 i/h$ and $G_{QPC2} = 2e^2 j/h, j = 7$, QPC1 is emitter and QPC2 is detector.

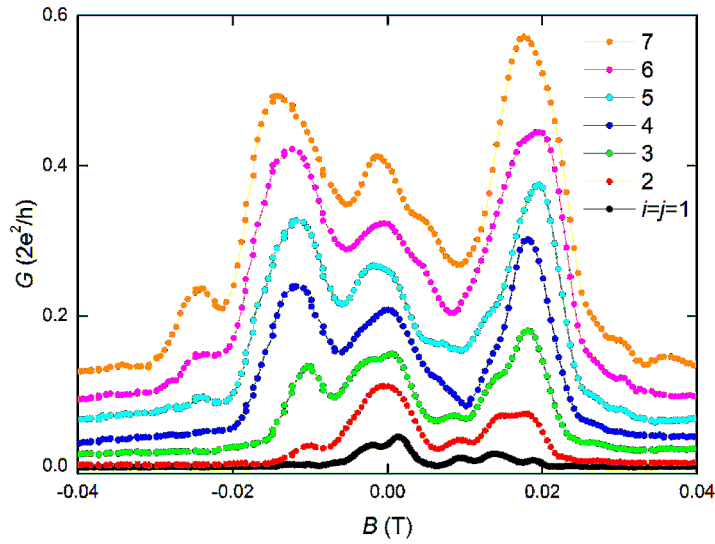


Figure A.10: Measured conductance G as a function of magnetic field B for both QPCs operating at the same plateau $i = j$, $G_{QPC1} = G_{QPC2} = 2e^2 i/h$, QPC2 is emitter and QPC1 is detector.

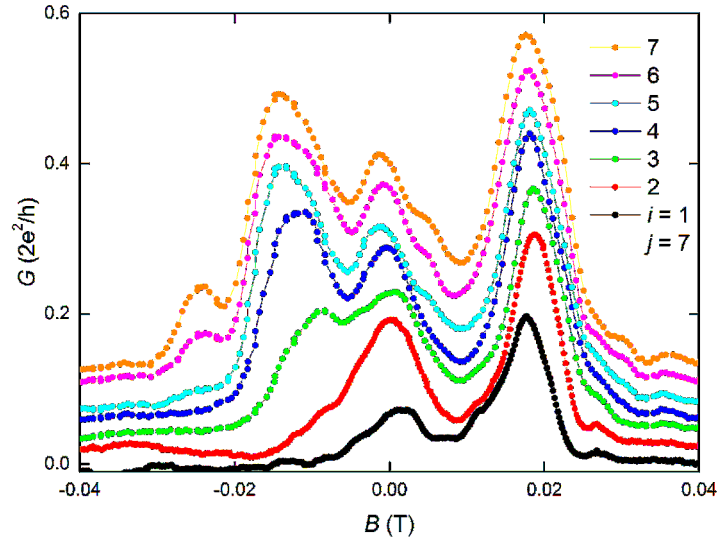


Figure A.11: Measured conductance G as a function of magnetic field B for different combinations of $G_{QPC1} = 2e^2 i/h$ and $G_{QPC2} = 2e^2 j/h, j = 7$, QPC2 is emitter and QPC1 is detector.

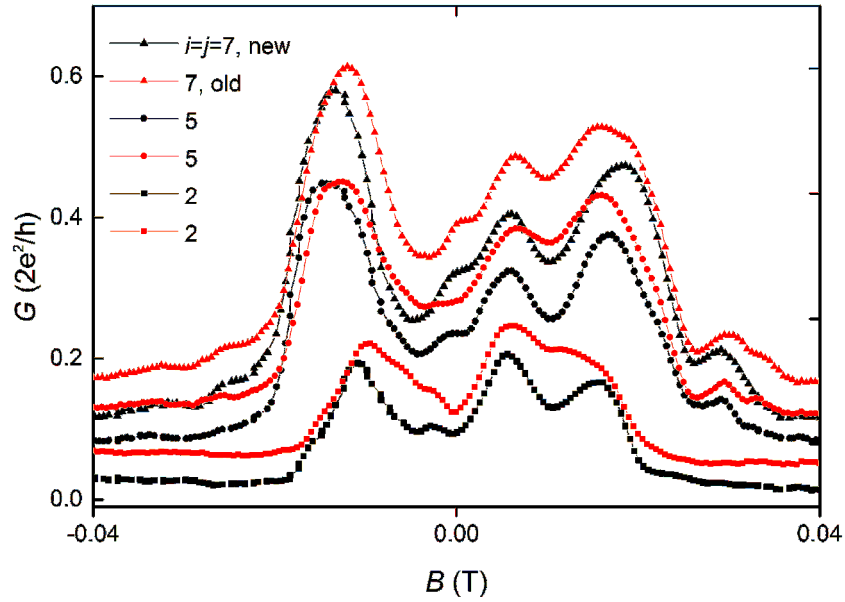


Figure A.12: Measured conductance G as a function of magnetic field B for different combinations of $G_{QPC1} = G_{QPC2} = 2e^2 i/h$ for the first (red) and second (black) cooldown. QPC1 is emitter, QPC2 is detector.

A.4 Theoretical model description

A.4.1 Transmission through coupled QPCs

Here we present the details of the model introduced in Sec. (2.5) of the chapter II.

A.4.1.1 Harmonic oscillator eigenstates in the QPCs

The Hamiltonian in the QPCs in region I and III is a 2DES with quadratic confinement potential,

$$\hat{H} = \frac{\hat{p}^2}{2m} + \frac{m\omega_y(x)^2 y^2}{2} + V_0, \quad (\text{A.7})$$

where $\omega_y(x)$ sets the quadratic confinement potential strength such that $\hbar\omega_y(x)$ is the energy spacing of the harmonic oscillator eigenstates. The chemical potential V_0 sets the number of conducting channels at a given energy E . We assume the quadratic confinement $\omega_y(x)$ changes adiabatically on the scale of the wavelength. When performing the wavefunction matching at the boundary x_1, x_2 with the free 2DES, the weights of the plane wave eigenstates in the 2DES are given by the Fourier transform of the harmonic oscillator eigenstates in the QPCs at x_1, x_2 , $a_{n_1}(k'_y) = e^{-k_y'^2/2} H_{n_1-1}(k'_y) / \sqrt{2^{n_1-1} (n_1-1)! \sqrt{\pi}}$. Here $k'_y = \sqrt{\frac{\hbar}{m\omega}} k_y$ is the wavenumber in y direction in natural units, $H_{n-1}(k'_y)$ are Hermite polynomials and the factor under the square root is normalization. Thus, we solve for the eigenstates directly in momentum space,

$$\psi_{n_i}(k'_y) = \frac{1}{\sqrt{2^{n_i} n_i!}} \frac{1}{\sqrt[4]{\pi}} \exp(-k_y'^2/2) H_{n_i-1}(k'_y), \quad (\text{A.8})$$

where $n_i - 1$ labels the $n - 1$ -harmonic oscillator eigenstate in QPC $i = 1, 2$, $\omega_y i = \omega_y(x_i)$ is the confinement frequency at the boundary of QPC i . Note that in the natural units of k'_y , the confinement frequency $\omega_y i$ at the crossover point x_i of the QPC enters.

A.4.1.2 Free 2DES with magnetic field in WKB approximation

The free 2DES in region II is modeled with the Hamiltonian

$$\hat{H} = \frac{(\hat{p} - q\vec{A}(\vec{r})/c)^2}{2m}, \quad (\text{A.9})$$

where we choose a gauge for the magnetic field as $\vec{A}(\vec{r}) = (0, Bx, 0)^T$. In y -direction, the eigenstates are plane waves. With the ansatz $\psi_{k_y}(x, y) = \psi(x, k_y) e^{ik_y y}$, we can write the differential equation for $\psi(x)$ as

$$\frac{d^2}{dx^2} \psi(x, k_y) = \frac{2m}{\hbar^2} \left[\frac{(m\omega_c x - \hbar k_y)^2}{2m} - E \right] \psi(x, k_y), \quad (\text{A.10})$$

Treating \hbar as a small parameter, we can find the solution for this differential equation from WKB approximation

$$\psi(x, k_y) = \sqrt[4]{\frac{2mE - (m\omega_c x_1 - \hbar k_y)^2}{2mE - (m\omega_c x - \hbar k_y)^2}} \exp\left(i \int_0^x d\tilde{x} \sqrt{2mE - (m\omega_c \tilde{x} - \hbar k_y)^2 / \hbar}\right), \quad (\text{A.11})$$

normalized to unity at $x = x_1$.

The WKB approximation is valid as long as $E \ll (m\omega_c x - \hbar k_y)^2$. The point $E = (m\omega_c x - \hbar k_y)^2$ is exactly when the electrons starting with a given k_y at $x = 0$ reverse their propagation direction along x . Thus, the approximation is valid as long as the distance d between the QPCs is smaller than the cyclotron radius $r_c < v_f / \omega_c$. The approximation is only valid for electrons with small k_y . Electrons with a large negative k_y propagate at an angle such that they need to propagate only a short distance in x -direction for the magnetic field to reverse their direction.

A.4.1.3 Propagated wavefunction and transmission through two QPCs in series

We find how an eigenstate from the first QPC continues in the free region by wavefunction matching at the boundary of the two regions. This procedure is valid for abruptly changing potentials, as sketched in figure 2.20. As the eigenstates of the free region are plane waves in y -direction, the weights of the harmonic oscillator eigenstate with quantum number n_1 propagated in the free region are given by its Fourier transform, equation (A.8). In natural units, $k'_y = \sqrt{\frac{\hbar}{m\omega_{y1}}} k_y$, $y' = \sqrt{\frac{m\omega_{y1}}{\hbar}} y$, $\epsilon = 2E / \hbar\omega_{y1}$ and $x' = \sqrt{\frac{m\omega_c^2}{\hbar\omega_{y1}}}$, this wavefunction thus reads

$$\psi_{n_1}(x', y') = \int_{-\infty}^{\infty} dk_y a_{n_1-1}(k'_y) \sqrt[4]{\frac{\epsilon - (x'_1 - k'_y)^2}{\epsilon - (x' - k'_y)^2}} \exp\left(i \frac{\omega_{y1}}{\omega_c} \int_0^{x'} d\tilde{x} \sqrt{\epsilon - (\tilde{x} - k'_y)^2} + i k'_y y'\right). \quad (\text{A.12})$$

Furthermore, we can calculate the wavefunction of the time-reversed propagation of electrons emitted from the $n_2 - 1$ level of the second QPC:

$$\psi_{n_2}^{TR}(x', y') = \int_{-\infty}^{\infty} dk_y a_{n_2-1}(k'_y) \sqrt[4]{\frac{\epsilon - (x'_2 - k'_y)^2}{\epsilon - (x' - k'_y)^2}} \exp\left(-i \frac{\omega_{y1} 2}{\omega_c} \int_{x'}^{x'_2} d\tilde{x} \sqrt{\epsilon - (\tilde{x} - k'_y)^2} + i k'_y y'\right), \quad (\text{A.13})$$

where the natural units take the same functional form, but the confinement frequency needs to be replaced by the confinement frequency at the entry of the second QPC, $\omega_{y1} \rightarrow \omega_{y2}$. With the time-reversed wavefunction, we can calculate the overlap of electrons emitted from the first QPC with harmonic oscillator eigenstates of the second QPC at any point x_0 in the free region. Since the wavefunctions are plane waves in y -direction, we can compute the overlap directly in

k_y space. In the case of equal confinement at the boundaries $\omega_{y1} = \omega_{y2} = \omega_y$, the overlap is given by

$$O_{n_1, n_2}(x'_0) = \int_{-\infty}^{\infty} dk'_y \frac{1}{\sqrt{\pi 2^{n_1-1} (n_1-1)! 2^{n_2-1} (n_2-1)!}} e^{-k_y'^2} H_{n_1-1}(k'_y) H_{n_2-1}(k'_y) \times \sqrt[4]{\frac{(\epsilon - (x'_1 - k'_y)^2)(\epsilon - (x'_2 - k'_y)^2)}{(\epsilon - (x'_0 - k'_y)^2)^2}} \exp\left(-i \frac{\omega_y}{\omega_c} \int_{x'_1}^{x'_2} d\tilde{x} \sqrt{\epsilon - (\tilde{x} - k'_y)^2}\right), \quad (\text{A.14})$$

where we entered explicitly the form for the prefactor $a_{n_i-1}(k'_y)$. When the confinement at the crossover ω_y is sufficiently small such that all large momenta of order of $\sqrt{\epsilon}$ have negligible weights due to the exponential suppression, the prefactor under the forth root can be approximated as unity. This approximation is done in the formula presented in section 2.5.2.

The transmission for an electron emitted from the n_1 -th level of the first QPC to enter the n_2 -th level of the second QPC is $T_{n_1, n_2} = |O_{n_1, n_2}(x_0)|^2$, independent on the value x_0 between the QPCs chosen. If the second QPC is set to N_2 conducting channels, the electron entering the N_2 lowest levels of the second QPC transmit, while all other electrons get reflected. We assume that these reflected electrons do not enter the second QPC in a cascade of reflections. As stated at the end of section 2.5.2, the total transmission probability for an electron emitted from the n_1 -th level of the first QPC to transmit through the second QPC set to N_2 conducting channels is $T_{n_1, N_2} = \sum_{m=0}^{N_2-1} T_{n_1, m}$.

A.5 Python simulation code

A.5.1 Anharmonic QPC eigenmodes

```

1 import numpy as np
2 from types import SimpleNamespace
3 from matplotlib import pyplot
4 np.set_printoptions(precision=4, linewidth=200)
5
6 def SetUpH(p, doPlot = False):
7     # Simple tight binding model for a 1D chain with an onsite potential
8     def pot(x):
9         pvec = np.zeros(p.L, dtype=float)
10         for cnt, xval in enumerate(x):
11             pvec[cnt] = 2*p.t \
12                 + p.px2*np.power((xval - p.L/2), 2) \
13                 + p.px4*np.power((xval - p.L/2), 4)
14         return pvec
15     if doPlot: pyplot.plot(list(range(p.L)), pot(list(range(p.L))))
16
17     H = np.diag(pot(list(range(p.L))))
18
19     for cnt in range(p.L-1):
20         H[cnt, cnt+1] = -p.t
21         H[cnt+1, cnt] = -p.t
22
23     return H

```

```

24
25 # Parameters for the Harmonic H
26 # L ist the number of sites
27 # px2 is the prefactor of quadratic potential
28 # px4 is the prefactor of the x^4 potential
29 # t is the hopping
30 px2set = 0.0000004
31 p = SimpleNamespace(L = 400, px2 = px2set, px4 = 0.00*px2set, t=1.0)
32 # Parameters for the Anharmonic H.
33 p4 = SimpleNamespace(L = 400, px2 = px2set, px4 = 0.03*px2set, t=1.0)
34
35 # Harmonic H
36 ham = SetUpH(p, False)
37 # Anharmonic H
38 ham4 = SetUpH(p4, False)
39 #pyplot.draw()
40
41 # Compute eigensystems
42 evals, evecs = np.linalg.eigh(ham)
43 evals4, evecs4 = np.linalg.eigh(ham4)
44
45 # Numbers of eigenstates to plot
46 n = range(7)
47
48 # Print eigenenergies
49 print("Eigenenergies harmonic potential");
50 print(evals[n])
51 print("Eigenenergies harmonic potential, normalized to 2 eval[0]");
52 print(evals[n]/(2*evals[0]))
53 print("Eigenenergies anharmonic potential");
54 print(evals4[n])
55 print("Eigenenergies anharmonic potential, normalized to 2 eval4[0]");
56 print(evals4[n]/(2*evals4[0]))
57 print("Difference of the normalized anharmonic eigenvalues");
58 evalsdiff = np.zeros(len(n)-1)
59 for cnt in range(len(n)-1):
60     evalsdiff[cnt] = \
61         (evals4[cnt + 1]/(2*evals4[0])) - \
62         (evals4[cnt]/(2*evals4[0]))
63 print(evalsdiff)
64
65 # Plot wavefunctions
66 f, axarr = pyplot.subplots(len(n), sharex=True)
67 for cntn in n:
68     axarr[cntn].plot(range(p.L), np.abs(evecs[:, cntn])**2)
69     axarr[cntn].plot(range(p.L), np.abs(evecs4[:, cntn])**2)
70
71 axarr[0].set_title("|Psi|^2 for V = x^2 (blue) and V = x^2 + a x^4, a = ... (
    green)")
72 pyplot.show()

```

A.5.2 Gaussian beam propagation in Fabry-Perot resonator

```

1 import scipy
2 import numpy as np
3 import os
4 import matplotlib.pyplot as plt
5 import scipy.integrate as integrate
6 from scipy.integrate import quad

```

```

7 from lmfit import minimize, Minimizer, Parameters, Parameter, report_fit
8 from __future__ import division
9
10 #Physical constants
11 lam=40E-3
12 w0=250E-3
13 z0=np.pi*w0*w0/lam
14 R=2
15 k=2*np.pi/lam
16 mstar=0.067*9.1094E-31
17 hbar=1.0545718E-34
18 e=1.6E-19
19 E=0.002*e
20 omega=E/hbar
21
22 #Gaussian Beam parameters
23 def width(l):
24     return np.sqrt(w0*w0*(1+l*l/(z0*z0)))
25 def radiusin(l):
26     return l+z0*z0/l
27 def radius(m,l):
28     rr=2/np.sqrt((mstar*omega/(2*hbar)))*1E6
29     for i in range(0,m):
30         rr=rr+l+z0*z0/l
31         rr=rr*R/(R-2*rr)
32     return rr
33 def theta(l):
34     return np.arctan(l/z0)
35
36 #Hermite polynomials
37 def H1(x,y):
38     return 1
39
40 def H2(x,y):
41     return 2*(np.sqrt(2)*y/width(x))
42
43 def H3(x,y):
44     return 4*(np.sqrt(2)*(y/width(x))**2-2)
45
46 def H4(x,y):
47     return 8*(np.sqrt(2)*(y/width(x))**3-12*(np.sqrt(2)*(y/width(x))))
48
49 def H5(x,y):
50     return 16*(np.sqrt(2)*(y/width(x))**4-48*(np.sqrt(2)*(y/width(x))**2+12)
51
52 def H6(x,y):
53     return 32*(np.sqrt(2)*(y/width(x))**5-160*(np.sqrt(2)*(y/width(x))
54         **3+120*(np.sqrt(2)*(y/width(x))))
55
56 def H7(x,y):
57     return 64*(np.sqrt(2)*(y/width(x))**6-480*(np.sqrt(2)*(y/width(x))
58         **4+720*(np.sqrt(2)*(y/width(x))**2-120)
59
60 #Wavefunctions
61 m=10
62 kk=0.1
63 #Plane wave propagation
64 def psi0p(y,l,m,kk):
65     psi=np.exp(-1j*(k-1j*kk)*l)
66     return psi

```

```

65 #Gaussian beam propagation
66 def psi1p(y,l,m,kk):
67     psi=w0/width(1)*H1(1,y)*np.exp(-y*y/np.power(width(1),2))*np.exp(-1j*(k-1j*
        kk)*y*y/(2*radius(m,l)))*np.exp(-1j*(k-1j*kk)*l+1j*theta(1))
68     return psi
69 def psi1pin(y,l,m,kk):
70     psi=w0/width(1)*H1(1,y)*np.exp(-y*y/np.power(width(1),2))*np.exp(-1j*(k-1j*
        kk)*y*y/(2*radius(m,l)))*np.exp(-1j*(k-1j*kk)*l+1j*theta(1))
71     return np.power(abs(psi),2)
72 def psi2p(y,l,m,kk):
73     psi=w0/width(1)*H2(1,y)*np.exp(-y*y/np.power(width(1),2))*np.exp(-1j*(k-1j*
        kk)*y*y/(2*radius(m,l)))*np.exp(-1j*(k-1j*kk)*l+3/2*1j*theta(1))
74     return psi
75 def psi2pin(y,l,m,kk):
76     psi=w0/width(1)*H2(1,y)*np.exp(-y*y/np.power(width(1),2))*np.exp(-1j*(k-1j*
        kk)*y*y/(2*radius(m,l)))*np.exp(-1j*(k-1j*kk)*l+3/2*1j*theta(1))
77     return np.power(abs(psi),2)
78 def psi3p(y,l,m,kk):
79     psi=w0/width(1)*H3(1,y)*np.exp(-np.power(y*np.sqrt(2)/width(1),2)/2)*(1/np.
        sqrt(8))*np.exp(-1j*(k-1j*kk)*y*y/(2*radius(m,l)))*np.exp(-1j*(k-1j*kk)*l
        +5/2*1j*theta(1))
80     return psi
81 def psi3pin(y,l,m,kk):
82     psi=w0/width(1)*H3(1,y)*np.exp(-np.power(y*np.sqrt(2)/width(1),2)/2)*(1/np.
        sqrt(8))*np.exp(-1j*(k-1j*kk)*y*y/(2*radius(m,l)))*np.exp(-1j*(k-1j*kk)*l
        +5/2*1j*theta(1))
83     return np.power(abs(psi),2)
84 def psi4p(y,l,m,kk):
85     psi=w0/width(1)*H4(1,y)*np.exp(-np.power(y*np.sqrt(2)/width(1),2)/2)*(1/np.
        sqrt(48))*np.exp(-1j*(k-1j*kk)*y*y/(2*radius(m,l)))*np.exp(-1j*(k-1j*kk)*l
        +7/2*1j*theta(1))
86     return psi
87 def psi4pin(y,l,m,kk):
88     psi=w0/width(1)*H4(1,y)*np.exp(-np.power(y*np.sqrt(2)/width(1),2)/2)*(1/np.
        sqrt(48))*np.exp(-1j*(k-1j*kk)*y*y/(2*radius(m,l)))*np.exp(-1j*(k-1j*kk)*l
        +7/2*1j*theta(1))
89     return np.power(abs(psi),2)
90
91 #Calculating superposition after n-th reflection
92 def psisum0(y,l,r,m,kk):
93     summ0=0
94     for i in range(1,m):
95         summ0=summ0+(1-r)*np.power(r,i)*psi0p(y,l*i,i,kk)
96     #print summ
97     return np.power(abs(summ0),2)
98 def psisum1(y,l,r,m,kk):
99     summ1=0
100    for i in range(1,m):
101        summ1=summ1+(1-r)*np.power(r,i)*psi1p(y,l*i,i,kk)
102    #print summ
103    return np.power(abs(summ1),2)
104 def psisum2(y,l,r,m,kk):
105    summ2=0
106    for i in range(1,m):
107        summ2=summ2+(1-r)*np.power(r,i)*psi2p(y,l*i,i,kk)
108    #print summ
109    return np.power(abs(summ2),2)
110 def psisum3(y,l,r,m,kk):
111    summ3=0
112    for i in range(1,m):

```

```

113     summ3=summ3+(1-r)*np.power(r,i)*psi3p(y,l*i,i,kk)
114     #print summ
115     return np.power(abs(summ3),2)
116 def psisum4(y,l,r,m,kk):
117     summ4=0
118     for i in range(1,m):
119         summ4=summ4+(1-r)*np.power(r,i)*psi4p(y,l*i,i,kk)
120     #print summ4
121     return np.power(abs(summ4),2)
122
123 #Calculating intensity
124 def intens0(l,r,m,kk):
125     return quad(psisum0, -1, 1, args=(l,r,m,kk))[0]
126 def intens1(l,r,m,kk):
127     return quad(psisum1, -1, 1, args=(l,r,m,kk))[0]
128 def intens1in(l,m,kk):
129     return quad(psi1pin, -1, 1, args=(l,m,kk))[0]
130 def intens2(l,r,m,kk):
131     return quad(psisum2, -1, 1, args=(l,r,m,kk))[0]
132 def intens2in(l,m,kk):
133     return quad(psi2pin, -1, 1, args=(l,m,kk))[0]
134 def intens3(l,r,m,kk):
135     return quad(psisum3, -1, 1, args=(l,r,m,kk))[0]
136 def intens3in(l,m,kk):
137     return quad(psi3pin, -1, 1, args=(l,m,kk))[0]
138 def intens4(l,r,m,kk):
139     return quad(psisum4, -1, 1, args=(l,r,m,kk))[0]
140 def intens4in(l,m,kk):
141     return quad(psi4pin, -1, 1, args=(l,m,kk))[0]
142 print (intens4(0.0001,0.9,100,0.1))
143
144 #Fit the Gaussian beam data
145 # load experimental data to be fitted
146 exp1 = np.fromfile("pathtothefile",dtype=float,count=-1,sep=" ")
147 exp1.shape
148 exp1 = np.reshape(exp1, (-1,2))
149 exp2 = exp1.transpose()
150 x=(exp2[0,1:179])
151 data=exp2[1,1:179]
152 #define the size of the resonator
153 z=np.linspace(3.6, 4.2, num=178)
154 res4=np.linspace(4.2, 3.6, num=178)
155
156 #Trying to find the best fit parameters
157 def fcn2min(params, x, data):
158     r = params['r']
159     kk = params['kk']
160     for i in range(1,150):
161         #res2[i]=intens2(x[i],r,m,kk)/intens2in(0.00001,m,kk)
162         res0[i]=intens0(x[i],r,m,kk)
163     return res2 - data
164 # create a set of Parameters
165 params = Parameters()
166 params.add('r', value= 0.9, min=0.7, max=0.99)
167 params.add('kk', value= 0.5, min=0.0001, max=1 )
168 # do fit, here with leastsq model
169 minner = Minimizer(fcn2min, params, fcn_args=(x, data))
170 kws = {'options': {'maxiter':100}}
171 result = minner.minimize()
172 result.params

```

```
173 # calculate final result
174     final = data + result.residual
175 # write error report
176     report_fit(result)
177 # plot results
178     plt.plot(z, data, 'o')
179     plt.plot(z, final, 'r')
180 #save results
181     params2=result.params
182     v = params2.valuesdict()
```


Bibliography

- [1] G. E. Moore, IEEE Solid-State Circuits Society Newsletter **11**, 33 (2006).
- [2] F. Masuoka, M. Momodomi, Y. Iwata, and R. Shirota, *1987 International Electron Devices Meeting*, **33**, 552 (1987).
- [3] S. B. Desai, S. R. Madhvapathy, and S. et al., *Science* **354**, 99 (2016).
- [4] M. S. Islam and L. Vj, *Comm. Mag.* **48**, 112 (2010).
- [5] W. P. McCray, *Nat Nano* **2**, 259 (2007).
- [6] R. Wang, H. Liu, R. Huang, J. Zhuge, L. Zhang, D. W. Kim, X. Zhang, D. Park, and Y. Wang, *IEEE Transactions on Electron Devices* **55**, 2960 (2008).
- [7] D. Dragoman and M. Dragoman, *Quantum-Classical analogies* (Springer-Verlag, Berlin, 2004).
- [8] N. Bachsoliani, S. Platonov, A. D. Wieck, and S. Ludwig, (2017), arXiv:1708.02034 .
- [9] S. Adachi, *Journal of Applied Physics* **58**, 1 (1985).
- [10] S. Datta, *Electronic Transport in Mesoscopic Systems* (Cambridge University Press, 1995).
- [11] R. E. Behringer, P. M. Mankiewich, and R. E. Howard, *Journal of Vacuum Science & Technology B: Microelectronics Processing and Phenomena* **5**, 326 (1987).
- [12] K. Y. Lee, T. P. Smith, C. J. Ford, W. Hansen, C. M. Knoedler, J. M. Hong, and D. P. Kern, *Applied Physics Letters* **55**, 625 (1989).
- [13] E.-A. Moon, J.-L. Lee, and H. M. Yoo, *Journal of Applied Physics* **84**, 3933 (1998).
- [14] R. Held, T. Vancura, T. Heinzel, K. Ensslin, M. Holland, and W. Wegscheider, *Applied Physics Letters* **73**, 262 (1998).
- [15] T. Heinzel, R. Held, S. Lüscher, K. Ensslin, W. Wegscheider, and M. Bichler, *Physica E: Low-dimensional Systems and Nanostructures* **9**, 84 (2001).
- [16] A. D. Wieck and K. Ploog, *Applied Physics Letters* **56**, 928 (1990).
- [17] R. Held, S. Lüscher, T. Heinzel, K. Ensslin, and W. Wegscheider, *Applied Physics Letters* **75**, 1134 (1999).
- [18] W. Walukiewicz, H. E. Ruda, J. Lagowski, and H. C. Gatos, *Phys. Rev. B* **30**, 4571 (1984).

- [19] S. W. Jung, T. Fujisawa, Y. Hirayama, and Y. H. Jeong, *Applied Physics Letters* **85**, 768 (2004).
- [20] C. Buizert, F. H. L. Koppens, M. Pioro-Ladrière, H.-P. Tranitz, I. T. Vink, S. Tarucha, W. Wegscheider, and L. M. K. Vandersypen, *Phys. Rev. Lett.* **101**, 226603 (2008).
- [21] D. Taubert, M. Pioro-Ladrière, D. Schröer, D. Harbusch, A. S. Sachrajda, and S. Ludwig, *Phys. Rev. Lett.* **100**, 176805 (2008).
- [22] D. Schröer, A. D. Greentree, L. Gaudreau, K. Eberl, L. C. L. Hollenberg, J. P. Kotthaus, and S. Ludwig, *Phys. Rev. B* **76**, 075306 (2007).
- [23] F. Forster, M. Mühlbacher, D. Schuh, W. Wegscheider, G. Giedke, and S. Ludwig, *Phys. Rev. B* **92**, 245303 (2015).
- [24] E. Buks, R. Schuster, M. Heiblum, D. Mahalu, and V. Umansky, *Nature* **391**, 871 (1998).
- [25] D.-I. Chang, G. L. Khym, K. Kang, Y. Chung, H.-J. Lee, M. Seo, M. Heiblum, D. Mahalu, and V. Umansky, *Nat Phys* **4**, 205 (2008).
- [26] C. J. B. Ford, T. J. Thornton, R. Newbury, M. Pepper, H. Ahmed, C. T. Foxon, J. J. Harris, and C. Roberts, *Journal of Physics C: Solid State Physics* **21**, L325 (1988).
- [27] C. J. B. Ford, T. J. Thornton, R. Newbury, M. Pepper, H. Ahmed, D. C. Peacock, D. A. Ritchie, J. E. F. Frost, and G. A. C. Jones, *Applied Physics Letters* **54**, 21 (1989).
- [28] G. Petersen, *Decoherence mechanisms of laterally defined double quantum dot qubits coupled to the environment*, Ph.D. thesis, Ludwig-Maximilians-Universität München (2013).
- [29] S. Konrad, *Characterization of electrical circuitry for nanoelectronic transport applications*, Bachelor's thesis, Ludwig-Maximilians-Universität München (2016).
- [30] H. Seeger, *Double-Quantum-Dot Systems for Information Entropy and Hyperfine Interaction Experiments*, Master's thesis, Ludwig-Maximilians-Universität München (2016).
- [31] W. H. Teh and C. G. Smith, *Journal of Vacuum Science & Technology B: Microelectronics and Nanometer Structures Processing, Measurement, and Phenomena* **21**, 3007 (2003).
- [32] I. Zailer, J. E. F. Frost, V. Chabasseur-Molyneux, C. J. B. Ford, and M. Pepper, *Semiconductor Science and Technology* **11**, 1235 (1996).
- [33] A. Wieck and D. Reuter, *Compound Semiconductors 1999: Proceedings of the 26th International Symposium on Compound Semiconductors, 23-26th August 1999, Berlin, Germany* **22**, 51 (2000).
- [34] R. H. Harrell, K. S. Pyshkin, M. Y. Simmons, D. A. Ritchie, C. J. B. Ford, G. A. C. Jones, and M. Pepper, *Applied Physics Letters* **74**, 2328 (1999).
- [35] J. C. H. Chen, D. Q. Wang, O. Klochan, A. P. Micolich, K. D. Gupta, F. Sfigakis, D. A. Ritchie, D. Reuter, A. D. Wieck, and A. R. Hamilton, *Applied Physics Letters* **100**, 052101 (2012).
- [36] N. Bachsoliani, *Field Effect Induced Structures in Depleted Two-Dimensional Electron Systems*, Master's thesis, Ludwig-Maximilians-Universität München (2016).
- [37] A. Siddiki, J. Horas, D. Kupidura, W. Wegscheider, and S. Ludwig, *New Journal of Physics* **12**, 113011 (2010).

- [38] S. Birner, T. Zibold, T. Andlauer, T. Kubis, M. Sabathil, A. Trellakis, and P. Vogl, *IEEE Transactions on Electron Devices* **54**, 2137 (2007).
- [39] R. Waser, ed., *Nanotechnology. Volume 3: Information Technology* (WILEY-VCH Verlag, 2008).
- [40] S. Das Sarma and F. Stern, *Phys. Rev. B* **32**, 8442 (1985).
- [41] L. Van der Pauw, *Philips Research Reports* **13**, 1 (1958).
- [42] T. Ihn, *Semiconductor nanostructures* (Oxford University Press, 2010).
- [43] C. Beenakker and H. van Houten, in *Semiconductor Heterostructures and Nanostructures*, Solid State Physics, Vol. 44, edited by H. Ehrenreich and D. Turnbull (Academic Press, 1991) pp. 1 – 228.
- [44] E. Ginossar, L. I. Glazman, T. Ojanen, F. von Oppen, W. E. Shanks, A. C. Bleszynski-Jayich, and J. G. E. Harris, *Phys. Rev. B* **81**, 155448 (2010).
- [45] S. L. Ren, J. J. Heremans, C. K. Gaspe, S. Vijayaragunathan, T. D. Mishima, and M. B. Santos, *Journal of Physics: Condensed Matter* **25**, 435301 (2013).
- [46] M. A. Castellanos-Beltran, D. Q. Ngo, W. E. Shanks, A. B. Jayich, and J. G. E. Harris, *Phys. Rev. Lett.* **110**, 156801 (2013).
- [47] W. G. van der Wiel, Y. V. Nazarov, S. De Franceschi, T. Fujisawa, J. M. Elzerman, E. W. G. M. Huizeling, S. Tarucha, and L. P. Kouwenhoven, *Phys. Rev. B* **67**, 033307 (2003).
- [48] Y. Aharonov and D. Bohm, *Phys. Rev.* **115**, 485 (1959).
- [49] D. Y. Sharvin and Y. V. Sharvin, *JETP Lett.* **34** (1981).
- [50] R. A. Webb, S. Washburn, C. P. Umbach, and R. B. Laibowitz, *Phys. Rev. Lett.* **54**, 2696 (1985).
- [51] A. J. M. Giesbers, U. Zeitler, M. I. Katsnelson, D. Reuter, A. D. Wieck, G. Biasiol, L. Sorba, and J. C. Maan, *Nat Phys* **6**, 173 (2010).
- [52] R. P. Taylor, A. S. Sachrajda, P. Zawadzki, P. T. Coleridge, and J. A. Adams, *Phys. Rev. Lett.* **69**, 1989 (1992).
- [53] M. Avinun-Kalish, M. Heiblum, O. Zarchin, D. Mahalu, and V. Umansky, *Nature* **436**, 529 (2005).
- [54] A. Yacoby, R. Schuster, and M. Heiblum, *Phys. Rev. B* **53**, 9583 (1996).
- [55] L. Onsager, *Phys. Rev.* **37**, 405 (1931).
- [56] H. B. G. Casimir, *Rev. Mod. Phys.* **17**, 343 (1945).
- [57] M. Buttiker, *IBM Journal of Research and Development* **32**, 317 (1988).
- [58] C. Kreisbeck, T. Kramer, S. S. Buchholz, S. F. Fischer, U. Kunze, D. Reuter, and A. D. Wieck, *Phys. Rev. B* **82**, 165329 (2010).
- [59] S. Washburn, C. P. Umbach, R. B. Laibowitz, and R. A. Webb, *Phys. Rev. B* **32**, 4789 (1985).

- [60] S. Russo, J. B. Oostinga, D. Wehenkel, H. B. Heersche, S. S. Sobhani, L. M. K. Vandersypen, and A. F. Morpurgo, *Phys. Rev. B* **77**, 085413 (2008).
- [61] T. Capron, C. Texier, G. Montambaux, D. Mailly, A. D. Wieck, and L. Saminadayar, *Phys. Rev. B* **87**, 041307 (2013).
- [62] M. Cassé, Z. D. Kvon, G. M. Gusev, E. B. Olshanetskii, L. V. Litvin, A. V. Plotnikov, D. K. Maude, and J. C. Portal, *Phys. Rev. B* **62**, 2624 (2000).
- [63] S. S. Buchholz, S. F. Fischer, U. Kunze, M. Bell, D. Reuter, and A. D. Wieck, *Phys. Rev. B* **82**, 045432 (2010).
- [64] V. S.-W. Chung, P. Samuelsson, and M. Büttiker, *Phys. Rev. B* **72**, 125320 (2005).
- [65] L. V. Litvin, H.-P. Tranitz, W. Wegscheider, and C. Strunk, *Phys. Rev. B* **75**, 033315 (2007).
- [66] S. Washburn and R. A. Webb, *Advances in Physics* **35**, 375 (1986).
- [67] M. Treiber, O. M. Yevtushenko, F. Marquardt, J. von Delft, and I. V. Lerner, *Phys. Rev. B* **80**, 201305 (2009).
- [68] A. Larkin and D. E. Khmel'nitskii, *Journal of Experimental and Theoretical Physics* **64**, 1815 (1986).
- [69] C. Terrier, D. Babic, C. Strunk, T. Nussbaumer, and C. Schönenberger, *EPL (Europhysics Letters)* **59**, 437 (2002).
- [70] A. B. Gougam, F. Pierre, H. Pothier, D. Esteve, and N. O. Birge, *Journal of Low Temperature Physics* **118**, 447 (2000).
- [71] D. P. DiVincenzo and C. L. Kane, *Phys. Rev. B* **38**, 3006 (1988).
- [72] K.-T. Lin, Y. Lin, C. C. Chi, J. C. Chen, T. Ueda, and S. Komiyama, *Phys. Rev. B* **81**, 035312 (2010).
- [73] R. Landauer, *Phil. Mag.* **21**, 863 (1970).
- [74] A. P. Micolich, *Journal of Physics: Condensed Matter* **23**, 443201 (2011).
- [75] F. Bauer, J. Heyder, E. Schubert, D. Borowsky, D. Taubert, B. Bruognolo, D. Schuh, W. Wegscheider, J. von Delft, and S. Ludwig, *Nature* **501**, 73–78 (2013).
- [76] P. Khatua, B. Bansal, and D. Shahar, *Phys. Rev. Lett.* **112**, 010403 (2014).
- [77] D. A. Wharam, M. Pepper, H. Ahmed, J. E. F. Frost, D. G. Hasko, D. C. Peacock, D. A. Ritchie, and G. A. C. Jones, *Journal of Physics C: Solid State Physics* **21**, L887 (1988).
- [78] U. Sivan, M. Heiblum, C. P. Umbach, and H. Shtrikman, *Phys. Rev. B* **41**, 7937 (1990).
- [79] J. Spector, H. L. Stormer, K. W. Baldwin, L. N. Pfeiffer, and K. W. West, *Applied Physics Letters* **56**, 1290 (1990).
- [80] M. Büttiker, *Phys. Rev. B* **41**, 7906 (1990).
- [81] I. N. Bronshtein and K. A. Semendyayev, *Handbook of Mathematics* (Springer-Verlag, Berlin, 1998).

- [82] R. Landauer, IBM Journal of Research and Development **1**, 223 (1957).
- [83] B. J. van Wees, H. van Houten, C. W. J. Beenakker, J. G. Williamson, L. P. Kouwenhoven, D. van der Marel, and C. T. Foxon, Phys. Rev. Lett. **60**, 848 (1988).
- [84] D. A. Wharam, T. J. Thornton, R. Newbury, M. Pepper, H. Ahmed, J. E. F. Frost, D. G. Hasko, D. C. Peacock, D. A. Ritchie, and G. A. C. Jones, Journal of Physics C: Solid State Physics **21**, 209 (1988).
- [85] R. K. Puddy, L. W. Smith, H. Al-Taie, C. H. Chong, I. Farrer, J. P. Griffiths, D. A. Ritchie, M. J. Kelly, M. Pepper, and C. G. Smith, Applied Physics Letters **107**, 143501 (2015).
- [86] G. Timp, Modern Problems in Condensed Matter Sciences **30**, 273 (1991).
- [87] R. N. Gurzhi, A. N. Kalinenko, A. I. Kopeliovich, A. V. Yanovsky, E. N. Bogachek, and U. Landman, Phys. Rev. B **72**, 115332 (2005).
- [88] M. Saito, M. Takatsu, M. Okada, and N. Yokoyama, Phys. Rev. B **46**, 13220 (1992).
- [89] A. Yacoby and Y. Imry, Phys. Rev. B **41**, 5341 (1990).
- [90] M. C. Payne, Journal of Physics: Condensed Matter **1**, 4931 (1989).
- [91] L. I. Glazman, G. B. Lesovik, D. E. Khmel’Nitskiĭ, and R. I. Shekhter, Soviet Journal of Experimental and Theoretical Physics Letters **48**, 238 (1988).
- [92] M. Büttiker, Phys. Rev. Lett. **57**, 1761 (1986).
- [93] P. G. N. de Vegvar, G. Timp, P. M. Mankiewich, J. E. Cunningham, R. Behringer, and R. E. Howard, Phys. Rev. B **38**, 4326 (1988).
- [94] F. Pobell, *Matter and methods at low temperatures* (Springer-Verlag, Berlin, 2007).
- [95] Lake Shore Cryotronics, *User’s Manual Model 625 Superconducting Magnet Power Supply* (2015).
- [96] D. Borowsky, *Transportmessungen zur Untersuchung der 0.7-Struktur in Quantenpunkt-kontakten*, Master’s thesis, Ludwig-Maximilians-Universität München (2011).
- [97] J. Heyder, F. Bauer, E. Schubert, D. Borowsky, D. Schuh, W. Wegscheider, J. von Delft, and S. Ludwig, Phys. Rev. B **92**, 195401.
- [98] P. H. Beton, B. R. Snell, P. C. Main, A. Neves, J. R. Owers-Bradley, L. Eaves, M. Henini, O. H. Hughes, S. P. Beaumont, and C. D. W. Wilkinson, Journal of Physics: Condensed Matter **1**, 7505 (1989).
- [99] P. C. Main, P. H. Beton, B. R. Snell, A. J. M. Neves, J. R. Owers-Bradley, L. Eaves, S. P. Beaumont, and C. D. W. Wilkinson, Phys. Rev. B **40**, 10033 (1989).
- [100] L. W. Molenkamp, A. A. M. Staring, C. W. J. Beenakker, R. Eppenga, C. E. Timmering, J. G. Williamson, C. J. P. M. Harmans, and C. T. Foxon, Phys. Rev. B **41**, 1274 (1990).
- [101] R. Taylor, A. Sachrajda, J. Adams, P. Zawadzki, P. Coleridge, and P. Marshall, Physica B: Condensed Matter **175**, 243 (1991).

- [102] P. C. Main, P. H. Beton, B. R. Snell, A. J. M. Neves, S. P. Beaumont, and C. D. W. Wilkinson, *Semiconductor Science and Technology* **5**, 1189 (1990).
- [103] R. Taylor, A. Sachrajda, J. Adams, C. Leavens, P. Zawadzki, and P. Coleridge, *Superlattices and Microstructures* **11**, 219 (1992).
- [104] L. P. Kouwenhoven, B. J. van Wees, W. Kool, C. J. P. M. Harmans, A. A. M. Staring, and C. T. Foxon, *Phys. Rev. B* **40**, 8083 (1989).
- [105] A. A. M. Staring, L. W. Molenkamp, C. W. J. Beenakker, L. P. Kouwenhoven, and C. T. Foxon, *Phys. Rev. B* **41**, 8461 (1990).
- [106] S. Heedt, A. Manolescu, G. A. Nemnes, W. Prost, J. Schubert, D. Grützmacher, and T. Schäpers, *Nano Letters* **16**, 4569 (2016).
- [107] M. Seo, C. Hong, S.-Y. Lee, H. K. Choi, N. Kim, Y. Chung, V. Umansky, and D. Mahalu, *Scientific Reports* **4**, 3806 EP (2014), article.
- [108] C. W. J. Beenakker and H. v. Houten, *Phys. Rev. B* **39**, 10445 (1989).
- [109] Y. Takagaki and D. K. Ferry, *Phys. Rev. B* **45**, 13494 (1992).
- [110] K. L. Shepard, M. L. Roukes, and B. P. Van der Gaag, *Phys. Rev. Lett.* **68**, 2660 (1992).
- [111] K. L. Shepard, M. L. Roukes, and B. P. van der Gaag, *Phys. Rev. B* **46**, 9648 (1992).
- [112] M. A. Topinka, B. J. LeRoy, S. E. J. Shaw, E. J. Heller, R. M. Westervelt, K. D. Maranowski, and A. C. Gossard, *Science* **289**, 2323 (2000).
- [113] Y. Takagaki, K. Gamo, S. Namba, S. Ishida, S. Takaoka, K. Murase, K. Ishibashi, and Y. Aoyagi, *Solid State Communications* **68**, 1051 (1988).
- [114] L. W. Molenkamp, M. J. P. Brugmans, H. van Houten, and C. T. Foxon, *Semiconductor Science and Technology* **7**, B228 (1992).
- [115] H. van Houten, C. W. J. Beenakker, J. G. Williamson, M. E. I. Broekaart, P. H. M. van Loosdrecht, B. J. van Wees, J. E. Mooij, C. T. Foxon, and J. J. Harris, *Phys. Rev. B* **39**, 8556 (1989).
- [116] Y. V. Sharvin, *Soviet Journal of Experimental and Theoretical Physics Letters* **21**, 655 (1965).
- [117] I. F. Sveklo and V. S. Tsoř, *Soviet Journal of Experimental and Theoretical Physics Letters* **49**, 331 (1989).
- [118] P. C. van Son, H. van Kempen, and P. Wyder, *Phys. Rev. Lett.* **58**, 1567 (1987).
- [119] H. Predel, H. Buhmann, L. W. Molenkamp, R. N. Gurzhi, A. N. Kalinenko, A. I. Kopeliovich, and A. V. Yanovsky, *Phys. Rev. B* **62**, 2057 (2000).
- [120] M. Okada, M. Saito, M. Takatsu, P. E. Schmidt, K. Kosemura, and N. Yokoyama, *Semiconductor Science and Technology* **7**, B223 (1992).
- [121] R. P. Taylor, R. Newbury, R. B. Dunford, P. T. Coleridge, A. S. Sachrajda, and J. A. Adams, *Phys. Rev. B* **51**, 9801 (1995).
- [122] G. Bergmann, *Physics Reports* **107**, 1 (1984).

- [123] J. J. Koonen, H. Buhmann, and L. W. Molenkamp, Phys. Rev. Lett. **84**, 2473 (2000).
- [124] M. A. Topinka, B. J. LeRoy, R. M. Westervelt, S. E. J. Shaw, R. Fleischmann, E. J. Heller, K. D. Maranowski, and A. C. Gossard, Nature **410**, 183 (2001).
- [125] P. T. Coleridge, Phys. Rev. B **44**, 3793 (1991).
- [126] E. Buks, M. Heiblum, and H. Shtrikman, Phys. Rev. B **49**, 14790 (1994).
- [127] A. L. Efros, F. G. Pikus, and G. G. Samsonidze, Phys. Rev. B **41**, 8295 (1990).
- [128] J. A. Nixon and J. H. Davies, Phys. Rev. B **41**, 7929 (1990).
- [129] E. G. Novik, H. Buhmann, and L. W. Molenkamp, Phys. Rev. B **67**, 245302 (2003).
- [130] J. Caridad *et al.*, Nature Communications **7**, 12894 (2016).
- [131] J. J. Heremans, S. von Molnár, D. D. Awschalom, and A. C. Gossard, Applied Physics Letters **74**, 1281 (1999).
- [132] R. J. Haug, A. H. MacDonald, P. Streda, and K. von Klitzing, Phys. Rev. Lett. **61**, 2797 (1988).
- [133] S. Komiyama, H. Hirai, S. Sasa, and S. Hiyamizu, Phys. Rev. B **40**, 12566 (1989).
- [134] D. Taubert, G. J. Schinner, H. P. Tranitz, W. Wegscheider, C. Tomaras, S. Kehrein, and S. Ludwig, Phys. Rev. B **82**, 161416 (2010).
- [135] J. Freudenfeld, *Enhancing the Coupling between two Quantum Point Contacts on Ballistic Electron Focusing*, Master's thesis, Ludwig-Maximilians-Universität München (2016).
- [136] R. J. Haug, J. Kucera, P. Streda, and K. von Klitzing, Phys. Rev. B **39**, 10892 (1989).
- [137] V. Mosser, D. Weiss, K. Klitzing, K. Ploog, and G. Weimann, Solid State Communications **58**, 5 (1986).
- [138] C. Kittel, *Introduction to Solid State Physics 8th edition* (Oxford University Press, 2005).
- [139] S. Takaoka, K. Oto, H. Kurimoto, K. Murase, K. Gamo, and S. Nishi, Phys. Rev. Lett. **72**, 3080 (1994).
- [140] J. H. Peter W. Milonni, *Lasers* (Wiley, 1988).
- [141] S. A. Self, Appl. Opt. **22**, 658 (1983).
- [142] W. H. Carter, Appl. Opt. **21**, 1989 (1982).
- [143] R. Schuster, E. Buks, M. Heiblum, D. Mahalu, V. Umansky, and H. Shtrikman, Nature **385**, 417 (1997).
- [144] M. Avinun-Kalish, M. Heiblum, O. Zarchin, D. Mahalu, and V. Umansky, Nature **436**, 529 (2005).
- [145] M. Yamamoto, S. Takada, C. Bauerle, K. Watanabe, A. D. Wieck, and S. Tarucha, Nat Nano **7**, 247 (2012).
- [146] Y. Ji, Y. Chung, D. Sprinzak, M. Heiblum, D. Mahalu, and H. Shtrikman, Nature **422**, 415 (2003).

- [147] W. Liang, M. Bockrath, D. Bozovic, J. H. Hafner, M. Tinkham, and H. Park, *Nature* **411**, 665 (2001).
- [148] A. A. Kozikov, D. Weinmann, C. Rössler, T. Ihn, K. Ensslin, C. Reichl, and W. Wegscheider, *Phys. Rev. B* **94**, 195428 (2016).
- [149] M. F. Crommie, C. P. Lutz, and D. M. Eigler, *Nature* **363**, 524 (1993).
- [150] J. P. Bird, D. M. Olatona, R. Newbury, R. P. Taylor, K. Ishibashi, M. Stopa, Y. Aoyagi, T. Sugano, and Y. Ochiai, *Phys. Rev. B* **52**, R14336 (1995).
- [151] B. L. Altshuler, A. G. Aronov, and D. E. Khmelnitsky, *Journal of Physics C: Solid State Physics* **15**, 7367 (1982).
- [152] G. F. Giuliani and J. J. Quinn, *Phys. Rev. B* **26**, 4421 (1982).
- [153] A. Yacoby, U. Sivan, C. P. Umbach, and J. M. Hong, *Phys. Rev. Lett.* **66**, 1938 (1991).
- [154] J. J. Lin and J. P. Bird, *Journal of Physics: Condensed Matter* **14**, R501 (2002).
- [155] B. Altshuler and A. Aronov, in *Electron–Electron Interactions in Disordered Systems*, Modern Problems in Condensed Matter Sciences, Vol. 10, edited by A. Efros and M. Pollak (Elsevier, 1985).
- [156] D. Taubert, C. Tomaras, G. J. Schinner, H. P. Tranitz, W. Wegscheider, S. Kehrein, and S. Ludwig, *Phys. Rev. B* **83**, 235404 (2011).
- [157] J. Spector, J. Weiner, H. Stormer, K. Baldwin, L. Pfeiffer, and K. West, *Surface Science* **263**, 240 (1992).
- [158] R. Williams, T. Low, S. Lundstrom, and C. Marcus, *Nat Nano* **6**, 222 (2011).
- [159] S. Chen, Z. Han, M. M. Elahi, K. M. M. Habib, L. Wang, B. Wen, Y. Gao, T. Taniguchi, K. Watanabe, J. Hone, A. W. Ghosh, and C. R. Dean, *Science* **353**, 1522 (2016).
- [160] J. A. Katine, M. A. Eriksson, A. S. Adourian, R. M. Westervelt, J. D. Edwards, A. Lupu-Sax, E. J. Heller, K. L. Campman, and A. C. Gossard, *Phys. Rev. Lett.* **79**, 4806 (1997).
- [161] D. S. Duncan, M. A. Topinka, R. M. Westervelt, K. D. Maranowski, and A. C. Gossard, *Phys. Rev. B* **64**, 033310 (2001).
- [162] C. Yan, S. Kumar, M. Pepper, P. See, I. Farrer, D. Ritchie, J. Griffiths, and G. Jones, *Phys. Rev. B* **95**, 041407 (2017).
- [163] M. Saito, T. Usuki, M. Okada, T. Futatsugi, R. A. Kiehl, and N. Yokoyama, *Applied Physics Letters* **65**, 3087 (1994).
- [164] H. Abu-Safia, R. Al-Tahtamouni, I. Abu-Aljarayesh, and N. A. Yusuf, *Appl. Opt.* **33**, 3805 (1994).
- [165] V. Lorient and P. Gleyzes, *Journal of Optics* **28**, 6 (1997).
- [166] M. Born and E. Wolf, *Principles of Optics* (Pergamon Press, 1970).
- [167] S. Platonov, B. Kästner, H. W. Schumacher, S. Kohler, and S. Ludwig, *Phys. Rev. Lett.* **115**, 106801 (2015).

- [168] L. P. Kouwenhoven, N. C. van der Vaart, A. T. Johnson, W. Kool, C. J. P. M. Harmans, J. G. Williamson, A. A. M. Staring, and C. T. Foxon, *Zeitschrift für Physik B Condensed Matter* **85**, 367 (1991).
- [169] S. Tarucha, D. G. Austing, T. Honda, R. J. van der Hage, and L. P. Kouwenhoven, *Phys. Rev. Lett.* **77**, 3613 (1996).
- [170] M. A. Nielsen and I. L. Chuang, *Quantum Computation and Quantum Information* (Cambridge University Press, 2000).
- [171] J. Clarke and F. K. Wilhelm, *Nature* **453**, 1031 (2008).
- [172] T. Yamamoto, K. Inomata, M. Watanabe, K. Matsuba, T. Miyazaki, W. D. Oliver, Y. Nakamura, and J. S. Tsai, *Applied Physics Letters* **93**, 042510 (2008).
- [173] F. Mallet, F. R. Ong, A. Palacios-Laloy, F. Nguyen, P. Bertet, D. Vion, and D. Esteve, *Nat Phys* **5**, 791 (2009).
- [174] A. Wallraff, D. I. Schuster, A. Blais, L. Frunzio, R.-S. Huang, J. Majer, S. Kumar, S. M. Girvin, and R. J. Schoelkopf, *Nature* **431**, 162 (2004).
- [175] D. Pozar, *Microwave Engineering 4th ed.* (Wiley, New York, 2011).
- [176] A. Kamal, J. Clarke, and M. H. Devoret, *Nat. Phys.* **7**, 1745 (2011).
- [177] W. P. Mason, W. H. Hewitt, and R. F. Wick, *Journal of Applied Physics* **24**, 166 (1953).
- [178] A. C. Mahoney, J. I. Colless, S. J. Pauka, J. M. Hornibrook, J. D. Watson, G. C. Gardner, M. J. Manfra, A. C. Doherty, and D. J. Reilly, *Phys. Rev. X* **7**, 011007 (2017).
- [179] S. Tanaka, N. Shimomura, and K. Ohtake, *Proceedings of the IEEE* **53**, 260 (1965).
- [180] G. Carchon and B. Nanwelaers, *IEEE Transactions on Microwave Theory and Techniques* **48**, 316 (2000).
- [181] P. Hänggi and F. Marchesoni, *Rev. Mod. Phys.* **81**, 387 (2009).
- [182] V. S. Khrapai, S. Ludwig, J. P. Kotthaus, H. P. Tranitz, and W. Wegscheider, *Phys. Rev. Lett.* **97**, 176803 (2006).
- [183] H. Linke, W. Sheng, A. Löfgren, H. Xu, P. Omling, and P. E. Lindelof, *EPL (Europhysics Letters)* **44**, 341 (1998).
- [184] L. P. Kouwenhoven, A. T. Johnson, N. C. van der Vaart, C. J. P. M. Harmans, and C. T. Foxon, *Phys. Rev. Lett.* **67**, 1626 (1991).
- [185] A. M. Song, A. Lorke, A. Kriele, J. P. Kotthaus, W. Wegscheider, and M. Bichler, *Phys. Rev. Lett.* **80**, 3831 (1998).
- [186] A. M. Song, Pär Omling, Lars Samuelson, Werner Seifert, Ivan Shorubalko, and Herbert Zirath, *Japanese Journal of Applied Physics* **40**, L909 (2001).
- [187] D. Averin and A. Odintsov, *Physics Letters A* **140**, 251 (1989).
- [188] H. Pothier, P. Lafarge, C. Urbina, D. Esteve, and M. H. Devoret, *EPL (Europhysics Letters)* **17**, 249 (1992).

- [189] L. P. Kouwenhoven, A. T. Johnson, N. C. van der Vaart, A. van der Enden, C. J. P. M. Harmans, and C. T. Foxon, *Zeitschrift für Physik B Condensed Matter* **85**, 381 (1991).
- [190] A. Rossi, T. Tantt, K. Y. Tan, I. Iisakka, R. Zhao, K. W. Chan, G. C. Tettamanzi, S. Rogge, A. S. Dzurak, and M. Möttönen, *Nano Letters* **14**, 3405 (2014).
- [191] P. W. Brouwer, *Phys. Rev. B* **58**, R10135 (1998).
- [192] B. Kaestner, V. Kashcheyevs, S. Amakawa, M. D. Blumenthal, L. Li, T. J. B. M. Janssen, G. Hein, K. Pierz, T. Weimann, U. Siegner, and H. W. Schumacher, *Phys. Rev. B* **77**, 153301 (2008).
- [193] P. Reimann and M. Evstigneev, *EPL (Europhysics Letters)* **78**, 50004 (2007).
- [194] P. Reimann, *Physics Reports* **361**, 57 (2002).
- [195] R. Bartussek, P. Hänggi, and J. G. Kissner, *EPL (Europhysics Letters)* **28**, 459 (1994).
- [196] M. von Smoluchowski, *Phys. Zeitsch.*, 1069 (1912).
- [197] R. P. Feynman, R. B. Leighton, and M. Sands, *The Feynman Lectures on Physics*, Vol. 1 (Addison Wesley, Reading MA, 1963) Chap. 46.
- [198] J. Rousselet, L. Salome, A. Ajdari, and J. Prost, *Nature* **370**, 446 (1994).
- [199] DL Instruments LLC, *DL Instruments Model 1211: Instruction and Maintenance Manual* (2000).
- [200] Zumbahlen Hank with the engineering staff of Analog Devices, ed., *Linear Circuit Design Handbook* (Newnes, Burlington, 2008).
- [201] Analog Devices Inc, *Tutorial on op-amp input offset voltage and mitigation techniques*. (2009).
- [202] M. Switkes, C. M. Marcus, K. Campman, and A. C. Gossard, *Science* **283**, 1905 (1999).
- [203] V. Kashcheyevs, A. Aharony, and O. Entin-Wohlman, *Phys. Rev. B* **69**, 195301 (2004).
- [204] S. Kohler, J. Lehmann, and P. Hänggi, *Phys. Rep.* **406**, 379 (2005).
- [205] Y. Ono and Y. Takahashi, *App. Phys. Lett.* **82**, 1221 (2003).
- [206] X. Jehl, B. Voisin, T. Charron, P. Clapera, S. Ray, B. Roche, M. Sanquer, S. Djordjevic, L. Devoille, R. Wacquez, and M. Vinet, *Phys. Rev. X* **3**, 021012 (2013).
- [207] S. P. Giblin, M. Kataoka, J. D. Fletcher, P. See, T. J. B. M. Janssen, J. P. Griffiths, G. A. C. Jones, I. Farrer, and D. A. Ritchie, *J. Appl. Phys.* **114**, 164505 (2013).
- [208] I. M. Gradshteyn and I. S. Ryzhik, *Table of Integrals, Series, and Products*, 5th ed. (Academic Press, San Diego, 1994).
- [209] F. Forster, G. Petersen, S. Manus, P. Hänggi, D. Schuh, W. Wegscheider, S. Kohler, and S. Ludwig, *Phys. Rev. Lett.* **112**, 116803 (2014).
- [210] D. R. Koenig, E. M. Weig, and J. P. Kotthaus, *Nature Nano.* **3**, 482 (2008).
- [211] Q. P. Unterreithmeier, E. M. Weig, and J. P. Kotthaus, *Nature* **458**, 1001 (2009).

- [212] B. D. O. Anderson and R. W. Newcomb, *Proceedings of the IEEE* **53**, 1674 (1965).
- [213] G. Viola and D. P. DiVincenzo, *Phys. Rev. X* **4**, 021019 (2014).
- [214] H. N. Chait and T. R. Curry, *Journal of Applied Physics* **30**, 152 (1959).
- [215] R. D. Astumian, *Science* **276**, 917 (1997).
- [216] R. D. Astumian and P. Hänggi, *Phys. Today* **55**, 33 (2002).
- [217] C. Reichhardt and C. J. Olson Reichhardt, *Phys. Rev. E* **68**, 046102 (2003).
- [218] A. Villalon, C. L. Royer, S. Cristoloveanu, M. Casse, D. Cooper, J. Mazurier, B. Previtali, C. Tabone, P. Perreau, J. M. Hartmann, P. Scheiblin, F. Allain, F. Andrieu, O. Weber, and O. Faynot, *IEEE Transactions on Electron Devices* **60**, 1568 (2013).
- [219] S. Berrada, M. Bescond, N. Cavassilas, L. Raymond, and M. Lannoo, *Applied Physics Letters* **107**, 153508 (2015).
- [220] A. Dixit, A. Kottantharayil, N. Collaert, M. Goodwin, M. Jurczak, and K. D. Meyer, *IEEE Transactions on Electron Devices* **52**, 1132 (2005).
- [221] P. Ellinghaus, M. Nedjalkov, and S. Selberherr, *2015 International Conference on Simulation of Semiconductor Processes and Devices (SISPAD)*, , 24 (2015).
- [222] M. Muraguchi and T. Endoh, *Japanese Journal of Applied Physics* **53**, 04EJ09 (2014).
- [223] P. Ellinghaus, J. Weinbub, M. Nedjalkov, and S. Selberherr, *Physica status solidi* **11**, 1700102 (2017), 1700102.

Thanks to :

First of all, Stefan, who gave me an incredible chance to perform extraordinary experiments in the well-equipped and organized lab. Thanks a lot for all the comments that you gave about every step of the research, thanks for my great improvement in writing scientific texts, analyzing the data and developing strategies for my research.

Gunnar Petersen, who taught me how to perform the transport experiments and gave a broad and detailed course in conventional electronics, devices, and cryogenics.

Jaan Freudenfeld, Nickolaus Bachsoliani and Sebastian Konrad for the fantastic time during research together and helping me with results of my thesis. Thanks also for wonderful time apart work, playing kicker and table tennis.

Florian Forster, Matthias Hauck, Jürgen Stefan, Valentin Stierle, the best teamed office I can ever imagine, the best office pranks, and for sure the best Dota team in the LMU.

Max Falkowski, Simon Mates, Johnathan Noe, Jens Repp, Darren Southworth, Matthias Hoffmann, Jessica Lindlau, Manuel Nutz, Thomas Faust, Johannes Rieger, Enrico Schubert, Andrew Neumann and all the students and workers of the nanoelectronics chair in LMU Munich for the friendly and motivating atmosphere at the chair.

Philipp Altpeter for the best possible technical support in the clean room

Stefan Manus for teaching me how to perform soldering and working with HF devices.

Martina Edenhofer (ehem. Jüttner), for helping in every organizational issue.

Dr. Sussanne Hennig and Marilena Pinto from CeNS for giving me an excellent opportunity to participate in the CeNs workshop and helping me during my first weeks in Germany.

My collaborators Dr. Sigmund Kohler, Dr. Bernd Kaestner, Prof. Andreas Wieck for great comments and very fruitful work.

Prof. Riechert and Prof. Grahn for the opportunity to continue my work in PDI.

И наконец, я хочу выразить огромную благодарность моим родителям и моей сестре за неоценимую поддержку во время моего обучения в аспирантуре и написания кандидатской диссертации.